Spring 1-1-2018

On the Design of Solar Gravity Driven Planetocentric Transfers Using Artificial Neural Networks

Stijn De Smet
University of Colorado at Boulder, stijn.desmet@colorado.edu

On the design of solar gravity driven planetocentric transfers using artificial neural networks

by

Stijn De Smet

B.Sc., Delft University of Technology, 2012

M.Sc., Delft University of Technology, 2014

A thesis submitted to the

Faculty of the Graduate School of the

University of Colorado in partial fulfillment

of the requirements for the degree of

Doctor of Philosophy

Ann and H.J. Smead Department of Aerospace Engineering Sciences

2018

This thesis entitled:
On the design of solar gravity driven planetocentric transfers using artificial neural networks
written by Stijn De Smet
has been approved for the Ann and H.J. Smead Department of Aerospace Engineering Sciences

Prof. Daniel J. Scheeres

Prof. Natasha Bosanac

Prof. Jay McMahon

Prof. James D. Meiss

Dr. Jeffrey S. Parker

Date

The final copy of this thesis has been examined by the signatories, and we find that both the content and the form meet acceptable presentation standards of scholarly work in the above mentioned discipline.

De Smet, Stijn (Ph.D., Aerospace Engineering)

On the design of solar gravity driven planetocentric transfers using artificial neural networks

Thesis directed by Prof. Daniel J. Scheeres

The sun's gravity can be used to efficiently transfer between different planetocentric orbits. Such transfers cannot be designed in a two-body dynamical system, nor do analytical methods exist to identify such transfers. This dissertation presents a method to efficiently identify transfers between a specified departure and target orbit. This method is applied to a well known problem: transfers from inclined low-earth orbits to the geostationary orbit.

Motivated by the large observed control authority of the sun for geocentric transfers, a new mission architecture is defined. This architecture allows the injection of multiple spacecraft around Mars in different target orbits, enabled by solar gravity driven orbital transfers. The efficient design of applications for a wide variety of departure and target orbits, requires an understanding of a large area of the phase space. This dissertation showcases how an artificial neural network architecture can accurately predict the solar gravity driven transfers, for a significantly large section of the phase space. The developed architecture is then used to efficiently identify transfers for several different applications. Multiple revolution transfers with maneuvers at intermediate periareions are identified that arrive at Phobos or Deimos. Furthermore, transfers are designed that transfer to both Phobos and Deimos in a single trajectory.

In addition to addressing solar perturbed planetocentric transfers, this dissertation shows how the developed artificial neural network framework can be applied to a different problem, with different dynamics. As an example, the dissertation develops an artificial neural network architecture that can predict heteroclinic connections in the Earth-Moon circular restricted three-body problem.

To my parents, Luc and Lieve,

my sister Ine, and little Hanne

Acknowledgements

Thank you to my committee members, Daniel Scheeres, Natasha Bosanac, Jay McMahon, James Meiss, and Jeffrey Parker for the advising and mentoring throughout my years at CU Boulder.

I would like to thank everyone in the low-thrust trajectory optimization research group led by Jeffrey Parker; Jonathan Herman, Jonathan Aziz, Nathan Parrish, Jeannette Heiligers, and numerous visiting researchers. Within this research group, I learned how to conduct academic research, and I wrote my first conference papers. At the halfway point of my time as a PhD student, I switched to the Celestial Mechanics and Spaceflight Mechanics Laboratory led by Daniel Scheeres. I would like to thank all past and current members of CSML for welcoming me into their lab. I would also like to thank Sarah Melssen, Annie Brookover, Carrie Simon, and Steven Hart, for the administrative and IT support.

Furthermore, I am grateful for the support I have received from a number of organizations. First, Advanced Space, for funding this work. Second, I would like to thank the University of Colorado Graduate School, and the American Astronautical Society for the provided travel grants. Furthermore, this work utilized the RMACC Summit supercomputer, which is supported by the National Science Foundation (awards ACI-1532235 and ACI-1532236), the University of Colorado Boulder, and Colorado State University. The Summit supercomputer is a joint effort of the University of Colorado Boulder and Colorado State University.

Finally, I would like to thank my parents for always supporting me, even if that entailed moving halfway across the globe, and Julia, for keeping me sane in the last year and a halve, especially during the last few months of dissertation writing.

Contents

Chapter

Tables

Table

Figures

Figure

Chapter 1

Introduction and motivation

Orbital transfers are extremely common. Either to transfer between the post-launch and the operational orbit, or to transfer in between different operational orbits. Thus, orbital transfers are very common and an extensive body of literature exists. Two main categories can be identified: methods that solely use maneuvers, and methods that use maneuvers augmented by perturbations.

The first category is commonly used for transfers between different orbits close to the planet's surface. In this orbital regime, the satellite is only marginally perturbed from two-body dynamics. For chemical transfers, approximated by impulsive maneuvers, the optimal location, magnitude and direction of the maneuvers can be obtained approximately from analytical formulae. For low-thrust transfers, the depth of the gravity well in this orbital regime requires very lengthy transfers with many optimization parameters. Recent advances in hybrid differential dynamic programming allows to optimize such transfers [1].

Perturbation based methods are commonly used for transfers further away from the planet's surface. The dynamics in this orbital regime can no longer be accurately approximated by two-body dynamics, since gravitational perturbations of other bodies become significant. Efficient transfers between different orbits using perturbations have been extensively studied. First, a gravitational assist, or flyby, method requires a spacecraft to get in close proximity to the perturbing body. An example is the research by Ocampo, who introduced the idea of lunar flybys for inclined low-Earth orbits to the geostationary orbit [2]. Second, methods have been studied that do not require such close proximity to the perturbing body. A distinction can be made based on design methodology.

A dynamical systems-based methodology uses manifolds; stable and unstable manifolds can be followed to cheaply transfer between different orbits [3, 4]. This methodology has been successfully applied to design low-energy transfers between the Earth and the Moon for the GRAIL mission [5], or between different libration point orbits for the ARTEMIS mission [6].

The second branch of design methodology focuses on the natural force structure, i.e., perturbations. This methodology can be used to design Earth-Moon transfers with ballistic captures as studied by Miller and Belbruno [7], and Yamakawa [8] and applied by the Hiten mission [9]. Solar tides can also be used to design transfers between different, planetocentric orbits. Orbital changes that affect the magnitude of the angular momentum vector can be categorized by the quadrant of the orbit in a rotating frame [8, 10]; including changes in the semi-major axis a, eccentricity e, and thus periapse and apoapse radii r_p and r_a. A simple quadrant representation does not exist for changes that affect the inclination i, argument of periapse ω and/or right ascension of ascending node Ω. Nonetheless, large orbital plane changes are possible. An example is the work by Villac [11, 12, 13, 14], who identified transfers with large inclination changes while maintaining a constant periapse radius. This analysis heavily relies on numerical integration of periapse Poincaré maps in the Hill system. The large computational load limited the discussion to the identification of potential transfers, for a few discrete values of initial inclination, periapse radius and apoapse radius, functioning as snapshots for the entire phase space. Besides designing transfers with fixed r_p and different i, Villac and Scheeres [15] investigated how periapse Poincaré maps in the Hill system can be used to find trajectories that escape Europa. This work was furthered by Paskowitz and Scheeres [16] to find trajectories that do not escape nor impact, for long periods of time. This work was performed in the Jupiter-Europa system, but can be extended to sun-planet systems. An example is the work by Davis and Howell, who investigated the escape-capture evolution of transfers in the Sun-Saturn system [10]. Another example is the patent application of Geryon Space Technologies [17]. This document demonstrates that solar gravity perturbations can be used to transfer from an inclined low-Earth orbit (LEO) to the geostationary orbit (GEO). However, this research is limited to point designs, without developing a systematic way to design such transfers. Such inclined LEO

to GEO transfers can also be designed using a dynamical systems-based methodology in the circular restricted three-body problem (CRTBP) [18, 19]. This methodology requires finding a suitable halo orbit, with a stable and unstable manifold that intersect tangentially with the target LEO and GEO, respectively. The spacecraft departs tangentially from the LEO on the stable manifold, after which it approaches the halo orbit. Then, the spacecraft departs the halo orbit on an unstable manifold, and arrives tangentially to the geostationary orbit. This methodology requires an experienced mission designer to identify halo orbits with suitable manifolds. This dissertation will investigate how Villac's work in the Jupiter-Europa Hill dynamical system [11, 12, 13, 14] can be adapted to systematically find transfers from LEO to GEO that do not explicitly depend on Lagrange point orbit invariant manifolds.

A common impeding factor for all of the methods described above is the lack of closed form solutions for three-body dynamics. Villac derived analytical criteria for planar escaping or captured trajectories, based on the sign of periapse [20]. However, no three-dimensional equivalent exists. Furthermore, he derived an analytical approximation to predict the change between periapses based on knowledge of the apoapse state [11]. However, the apoapse state is not readily known for transfers departing from a specified initial orbit. Thus, no exact analytical solutions exist for orbital transfers exploiting three-body dynamics. Hence, designing transfers in three-body dynamics heavily relies on numerical integration, which can be computationally expensive. Furthermore, third-body dynamics can be very sensitive to the initial conditions. For an evaluation of a large section of the phase space, this sensitivity leads to a high required sampling density. Both factors combined can lead to large computational requirements. Furthermore, the required memory to store a dense sampling of the phase space can be large. Therefore, to the author's knowledge, no global understanding of such transfers exist, captured in an easily accessed database that can be used as a road map for the dynamics within this system. This dissertation demonstrates how machine learning techniques can be used to create this road map.

Machine learning has been successfully applied to a large variety of applications in many different research disciplines. Nonetheless, only a few astrodynamics applications utilized machine learning. Examples are planetary landing pinpoint guidance [21, 22], optimal low-thrust transfers between near-earth objects [23], automated low-thrust initial guess generation within a multi-body regime [24], and automated low-thrust trajectory correction [25]. Furthermore, some research has been conducted to understand the natural response in complicated dynamical systems. Guého et al. [26] researched how machine learning techniques can be used on a problem replicating Keplerian dynamics. Shah and Beeson [27] attempted to approximate invariant manifolds in the Earth-Moon CRTBP. Both studies attempted to predict the full state at all intermediate time steps along the natural flow of a solution. This greatly increases the size of the machine learning problem, and prevents the training of models for the entire phase space. In this dissertation, it is shown how this issue is resolved through the use of periapse Poincaré maps to map the Hill problem dynamics, allowing the identification of transfers of interest within a large section of the phase space.

The evaluation of complex dynamical systems imposes a large computational load. Traditionally, the phase space is investigated in a circular representation of the three-body problem. For some applications, the solutions found in this simpler dynamical system can significantly deviate from the solutions in the real dynamics. An example is the effect of the eccentricity of the celestial bodies' orbits, for instance for capture orbits near Mars and Mercury [28]. Another example is the Sun-Earth-Moon system, or the Jovian system, where more than two celestial bodies interact. Such problems are usually modeled as segments in different CRTBP; a patched three-body model. Examples are the work by Parker [3], Gómez et al. [29], Yagasaki [30], Howell and Kakoi [31], Bokelmann and Russel [32], Bosanac et al. [33], etc. After analyzing the problem in a simple dynamical system, specific transfers that exhibit certain desired characteristics are corrected into a higher fidelity force model using a differential corrector [3]. This dissertation shows how the systematic difference between a low- and higher-fidelity dynamical system can be predicted using machine learning techniques.

Multiple satellites can increase the science or commercial return of a mission, while cost-intensive phases can be shared. Multi-spacecraft missions can be subdivided into two categories. The first category is comprised of missions with communal orbital planes. A well-known example is the GPS constellation of 24-32 satellites on six orbital planes [34]. However, each satellite has a dedicated launch. The Galileo system on the other hand has three orbital planes, with a total of 30 satellites [35]. Up to four satellites in the same orbital plane are launched on a single vehicle [36]. The angular separation along the orbit is obtained through an intermediate phasing orbit [36]. Another example is the BepiColombo mission. This mission to Mercury has two spacecraft, using a common solar electric propulsion (SEP) module for the interplanetary transfer and a common chemical module for Mercury orbital insertion maneuvers [37]. The two spacecraft have a common orbital plane around Mercury but are injected at different orbital altitudes.

For some single-launch missions, the science return is increased when the spacecraft are injected into different orbital planes. Orbital plane changes are energy intensive and are expensive to execute using chemical maneuvers. One solution is the use of SEP. An example is the mission design of MISEN, a proposed mission where three cubesats are injected into three different orbits around Mars [38]. While they share a launch vehicle, they each use their own dedicated SEP system to transfer to Mars and spiral into their dedicated science orbit [39]. Three-body dynamics can also be used as an efficient orbital transfer strategy for multi-spacecraft missions. An example is the THEMIS mission, where five spacecraft are deployed in different orbits, using third-body perturbations by the Sun and Moon, in combination with maneuvers [40]. Another example is the work by Chow et al. [41], who demonstrated that multiple satellites can be deployed in a constellation with differently inclined orbits, using one launch vehicle. This methodology exploits the CRTBP dynamics of Lissajous orbits near the Earth-Moon L1 Lagrange point. Similar to the discussion on LEO to GEO transfers using manifolds, it is expected that a Hill system approach could identify transfers without explicitly relying on manifolds. Therefore, this dissertation investigates if a new Martian, single-launch architecture with different orbital planes at different altitudes can be enabled by highly eccentric, solar perturbed transfer orbits.

1.1 Research statement and goals

Based on the identified knowledge gaps, the research statement can be summarized as:

This research combines dynamical systems theory for complex dynamical systems with modern computational tools; artificial neural networks. This allows the characterization of the response in a dynamical system through a series of simple, analytical evaluations. This new characterization is applied to a new mission architecture for the injection of multiple spacecraft around Mars, and allows for the rapid design of complex transfers.

Three main research goals can be identified to realize this research statement:

(1) Develop a systematic methodology to identify solar gravity driven transfers between a specified departure and target orbit, applied to inclined LEO to GEO scenarios.

(2) Define a new mission architecture for the injection of multiple spacecraft around Mars, enabled by solar gravitational perturbations.

(3) Develop methods to obtain an understanding of the control authority of the gravitational perturbations for a wide variety of departure and target orbits around Mars.

1.2 Dissertation overview

Chapter 2 covers the theoretical background for the dissertation. A literature review of historical approaches to orbital transfers is given, focusing on transfers from inclined LEO to GEO. Furthermore, an overview is given on three-body dynamics and transfers. Finally, a high-level overview is given on machine learning, and more specifically, artificial neural networks (ANN).

Chapter 3 explains how transfers between inclined LEO and GEO can be realized using solar gravity. An algorithm is created to identify transfers departing from different initial inclinations. Furthermore, the stability of these transfers is investigated, as well as the effect of missed and imperfect maneuvers. This chapter designs the transfers assuming the Earth revolves around the Sun in a circular orbit. Despite Earth's small eccentricity of 0.0167, it is shown that this assumption

leads to significant errors for the highly eccentric regime of the spacecraft on the planetocentric transfer orbits.

Chapter 4 introduces a new mission concept, where multiple satellites are deployed around Mars in drastically different orbits. This chapter introduces some key methodologies to establish a global understanding of the control authority of the Sun, for a wide variety of departure and target orbits. This chapter introduces the concept of databases that can be used as a road map for the solar perturbed dynamics around Mars. In this chapter, the database is constructed using numerical integration. The database is build for a limited subset of the phase space, centered around a specific target application. First, the database is computed, under the assumption that Mars' orbit around the Sun is circular. Chapter 3 demonstrates that this circular assumption is invalid. Therefore, the database is constructed for the eccentric restricted three-body problem. The time invariance of this dynamical system greatly increases the number of database entries, even for the limited subset of the considered phase space. This chapter therefore limits itself to identifying the bounds of the phase space where the necessary conditions for specific transfers are met, and transfers could exist.

The research milestone that enables the construction of a database of transfers, in the eccentric problem, and for a large area of the phase space, is the use of ANN. Chapter 5 starts with the development of ANN for the small subset of the phase space considered in chapter 4. Key to success is the introduction of an apoareion scaled version of the circular Hill system, as an approximation to the eccentric Hill system. This scaled version allows to account for the majority of the time-varying effect of the eccentricity, while only increasing the number of database entries by 20%, as compared to the circular approximation. It is observed that the usage of the apoareion scaled Hill system introduces systematic errors in the transfers, compared to the eccentric system. These systematic errors can be captured in a separate ANN. This allows the introduction of a new ANN architecture that can predict the response in the eccentric Hill system. This architecture is then applied on a large area of the phase space, achieving the research goal of a global understanding of the control authority of the Sun. Then, it is demonstrated how this architecture can be used

to train ANN for a totally different application; designing heteroclinic connections between planar Lyapunov orbits in the Earth-Moon, circular restricted three-body problem.

Chapter 6 demonstrates how the developed artificial neural network architecture can be used to determine all initial conditions to target specific final orbits, with multiple revolutions around Mars, and with impulsive maneuvers at intermediate periareions. Furthermore, it is shown how the architecture can be used to analyze the effect of imperfect maneuvers on the identified transfers.

Chapter 7 summarizes the main contributions of this dissertation, and discusses future work.

Chapter 2

Theoretical background

In this chapter, the theoretical background for the dissertation is discussed. First, classical orbital elements are described, followed by an overview on common strategies for transfers between different orbits. Second, the different three-body dynamical systems used throughout this dissertation are described. Third, the used reference frames are introduced, and the conversions between different frames is discussed. Fourth, a brief overview is given on common methods to design orbits and orbital transfers in three-body dynamics. Finally, the theory behind machine learning and artificial neural networks is introduced.

2.1 Orbital elements and orbital element change strategies

An orbit subject to two-body motion, also known as Keplerian motion, is commonly described using either Cartesian, or Keplerian orbital elements. The Cartesian elements are composed of three positions and velocities, described with respect to a reference frame. Under Keplerian motion, the individual position and velocity components change over time. Furthermore, they provide little insight in the orbital type and the orbit's orientation. These issues are circumvented by the use of Keplerian orbital elements, also known as classical orbital elements.

In this section, first, the Keplerian orbital elements are discussed. Second, methods are described to transfer between co-planar orbits. Third, methods are listed to transfer between orbits with a different orbital plane, but identical in-plane parameters. Finally, transfer methods with simultaneous orbital plane and in-plane changes are discussed.

2.1.1 Orbital elements

The Keplerian orbital elements can be divided into two categories: parameters describing the orientation of the orbital plane, and parameters describing the size of the orbit in the orbital plane. Commonly, the orbital plane is described using a set of 3-1-3 Euler angles, as shown in Fig. 2.1. The first rotation occurs around the z-axis by Ω, the right ascension of ascending node. This parameter describes the angular distance between the x-axis and the intersection of the orbital plane with the xy-plane at the ascending node. The second rotation occurs around the local x-axis by angle i, the inclination. This angle describes the tilt of the orbital plane with respect to the xy-plane. The final rotation occurs around the local z-axis by angle ω, the argument of periapse. This angle describes the angular distance from the ascending node to the location of periapse; the closest point on an orbit. The size of the orbit is determined by the semi-major axis a. This parameter is the average of the closest and farthest point of the orbit; periapse and apoapse. The difference between the periapse distance r_p and apoapse distance r_a is dictated by the eccentricity parameter, e. Finally, the true anomaly ν is a measure of the location of an object within the orbit, measured from periapse. For unperturbed Keplerian motion, all parameters except ν are constant.

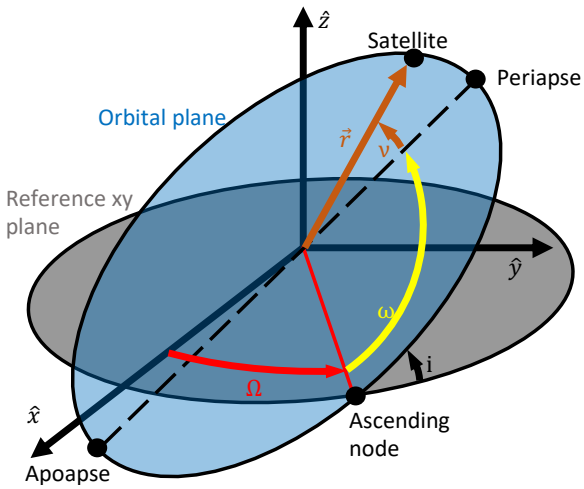

Figure 2.1: Visualization of the classical orbital elements.

Some commonly used parameters can be defined using the six Keplerian orbital elements, and the standard gravitational parameter, μ: the product of the mass of the central body, M and

the gravitational constant, G. A few examples are periapse distance r_p, apoapse distance r_a, semi-latus rectum p, argument of latitude u, true longitude λ, and specific angular momentum vector direction $\hat{\boldsymbol{h}}$ and magnitude h:

$$\begin{aligned} r_p &= a \cdot (1-e) & r_a &= a \cdot (1+e) & p &= a \cdot (1-e^2) \\ u &= \nu + \omega & \lambda &= \nu + \omega + \Omega & & \\ \hat{\boldsymbol{h}} &= \begin{bmatrix} \sin\Omega \sin i & -\cos\Omega \sin i & \cos i \end{bmatrix}^T & h &= \sqrt{\mu p} & & \end{aligned} \tag{2.1}$$

Different terminology exists for the periapse and apoapse parameters, depending on the central body. The periapse for orbits around the Earth, the Sun and Mars are respectively called perigee, perihelion and periareion. Similarly, the apoapses are called apogee, aphelion and apoareion.

2.1.2 Co-planar transfers

In this subsection, the design of co-planar transfers is investigated; i.e., transfers where only the periapse and apoapse radii change. A maneuver at apoapse parallel to the velocity vector only changes the periapse radius. Similarly, a maneuver at periapse parallel to the velocity vector only changes the apoapse radius. To change both parameters in an efficient way, at least two maneuvers are required. Examples are a Hohmann and a bi-elliptic transfer [42] between co-planar circular orbits. The two different approaches are visualized in Fig. 2.2. A Hohmann transfer is a two-burn solution. At periapse, a first maneuver changes the apoapse from r_1 to r_2. This transfer orbit is then followed for half an orbit, up to apoapse. There, a second maneuver reduces the eccentricity to zero, effectively changing the periapse radius from r_1 to r_2. The total required ΔV is

$$\Delta V = \sqrt{\frac{\mu}{r_1}} \left[(\gamma - 1)\sqrt{\frac{2}{\gamma(\gamma+1)}} + \frac{1}{\gamma} - 1 \right], \tag{2.2}$$

where $\gamma = r_2/r_1$ is the ratio between the arrival and departure orbital radii. A Hohmann transfer is not always fuel-optimal. Depending on the γ-ratio, a three-burn bi-elliptic transfer could be more efficient. For this transfer, a first maneuver at periapse changes the apoapse from r_1 to r_a where $r_a > r_2$. This transfer orbit is then followed for half an orbit, up to apoapse. There, a second

maneuver raises the periapse radius from r_1 to r_2. This second transfer orbit is then followed for half an orbit, up to periapse. Then, a third maneuver reduces the eccentricity to zero, effectively changing the apoapse radius from r_a to r_2. For $\gamma < 11.939$, the Hohmann transfer is optimal. For $\gamma > 15.582$, the bi-elliptic transfer is optimal. For intermediate γ-values, the bi-elliptic transfer is optimal for sufficiently large $\zeta = r_a/r_1$ [43]. The total required ΔV is

$$\Delta V = \sqrt{\frac{\mu}{r_1}} \left[(\zeta - 1)\sqrt{\frac{2}{\zeta(\zeta+1)}} + \sqrt{\frac{2(\zeta+\gamma)}{\zeta\gamma}} - \frac{1}{\gamma} - 1 \right] \tag{2.3}$$

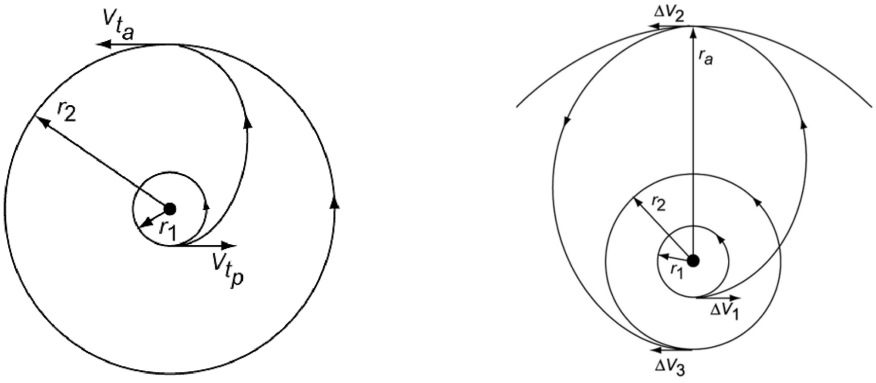

Figure 2.2: Visualization of a Hohmann and a bi-elliptic co-planar transfer (credit Wakker [43]).

2.1.3 Transfers with orbital plane change only

If two orbits only differ in one orbital plane parameter, different approaches exist for different orbital plane parameters. If only the inclination is allowed to change, a maneuver must be performed at the ascending or descending node with an angle from the initial orbital plane equal to $90° + \frac{\Delta i}{2}$. This requires $\Delta V = 2\sin(\frac{\Delta i}{2})V_1$. If only the right ascension of ascending node is allowed to change, a maneuver must be performed at $u = 90°$ or $u = 270°$, i.e. $90°$ away from the ascending or descending node. This requires $\Delta V = 2\sin(i)\sin(\frac{\Delta\Omega}{2})V_1$.

2.1.4 Transfers with orbital plane and in-plane changes

In this subsection, common methods to transfer between orbits with different orbital plane angles and in-plane orbital elements are discussed. As an example, a very common, and well studied

plane change is investigated; the transfer from a low earth orbit (LEO) to the geostationary orbit (GEO). This is an equatorial circular orbit with an orbital radius of 42,164 km. Its orbital period is equal to a sidereal day. Hence, a spacecraft in this orbit stays stationary as seen from a fixed point on the surface. This makes it a popular orbit for numerous applications such as weather and communication satellites. Several strategies exist to minimize the fuel cost for transfers from inclined circular LEO to GEO. An overview of a few strategies will be given, divided into two categories: maneuver based changes and perturbation based changes.

2.1.4.1 Maneuver based methods

Two-burn strategy with Δi optimally distributed over two burns At a node crossing of the initial circular orbit, a first maneuver raises the apogee to the geosynchronous radius and reduces the inclination by Δi_1. This transfer orbit is then followed for half an orbit, up to the apogee at geosynchronous altitude. There, a second maneuver nullifies the eccentricity and inclination. For a given ratio $\gamma = \frac{r_{\text{GEO}}}{r_{\text{LEO}}}$ the total ΔV is [43]

$$\Delta V = \sqrt{\frac{\mu}{r_{\text{LEO}}}} \left[\sqrt{\frac{3\gamma+1}{\gamma+1} - 2\sqrt{\frac{2\gamma}{\gamma+1}}\cos\Delta i_1} + \sqrt{\frac{1}{\gamma}\left(\frac{\gamma+3}{\gamma+1} - 2\sqrt{\frac{2}{\gamma+1}}\cos\Delta i_2\right)} \right] \tag{2.4}$$

The distribution of the inclination changes over the two maneuvers can be optimized to minimize the overall ΔV budget. A few examples for different initial inclinations can be found in Fig. 2.3. For all considered initial inclinations, it is more efficient to perform the majority of the inclination change with the second maneuver.

Three-burn bi-elliptic or super-synchronous transfer Reference [42] introduces the idea of bi-elliptic transfers between two circular, coplanar orbits [42]. A co-planar bi-elliptic transfer with a γ ratio above 11.94 can be more fuel-optimal than a co-planar Hohmann transfer [42]. For the geostationary orbit with orbital radius of 42,164 km, the initial orbital radius must be below 3,531 km. This is well below the Earth's surface. For any realistic r_p value of a LEO orbit, the γ-value is thus lower than 11.94. Therefore, it would appear that a bi-elliptic transfer type is not

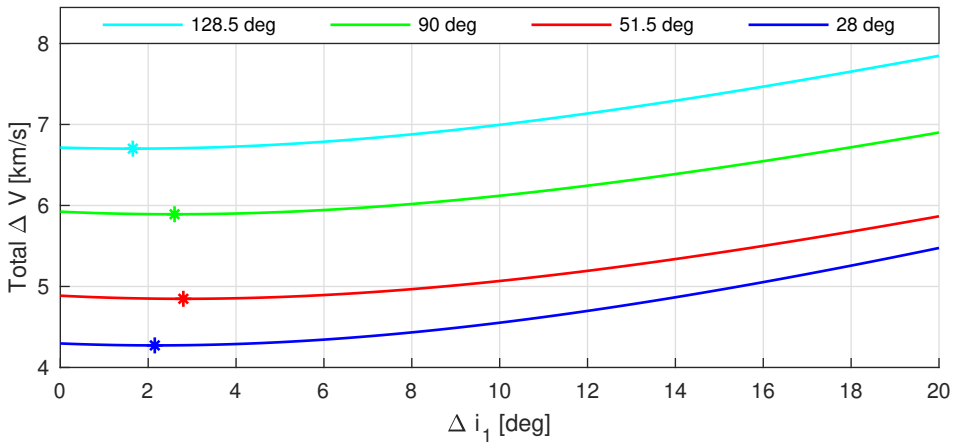

Figure 2.3: Determine initial inclination change to minimize total fuel cost for a two-burn strategy. The different colors indicate different total inclination changes, the asterisks the optimum initial inclination changes to minimize the total fuel cost.

advantageous. However, it is stipulated that for the transfer between circular, inclined orbits, it could be more efficient to "obtain an intermediate point far out, make necessary inclination changes and then return to the required orbit" [42]. This leverages the fact that inclination changes require the least fuel when applied at low velocities, i.e. at a high apoapse. The considered bi-elliptic transfers are composed of two consecutive transfer orbits. In the initial circular orbit, at a node crossing, the first maneuver raises the apogee altitude above the geosynchronous altitude. This transfer orbit is followed for half an orbit, up to apogee. Here, a second maneuver is executed that raises the perigee from the initial value to the geosynchronous altitude. This maneuver also nullifies the inclination. This second transfer orbit is followed up to perigee. There, a third maneuver circularizes the orbit. For given ratios $\gamma = \frac{r_{\mathrm{LEO}}}{r_{\mathrm{LEO}}}$ and $\zeta = \frac{r_{\mathrm{apogee}}}{r_{\mathrm{LEO}}}$, the total ΔV is [43]

$$\Delta V = \sqrt{\frac{\mu}{r_{\mathrm{LEO}}}} \left(\sqrt{\frac{2\zeta}{\zeta+1}} + \sqrt{\frac{2\zeta}{\gamma(\zeta+\gamma)}} - \sqrt{\frac{1}{\gamma}} - 1 + \sqrt{\frac{2}{\zeta}\left[\frac{1}{\zeta+1} + \frac{\gamma}{\gamma+\zeta} - 2\sqrt{\frac{\gamma}{(\zeta+1)(\zeta+\gamma)}}\cos(\Delta i)\right]} \right) \tag{2.5}$$

In theory, the inclination change is free when $r_{\mathrm{apogee}} = \infty$. However, this requires infinite time of flight. The required ΔV for this extreme scenario is computed using

$$\Delta V = \sqrt{\frac{\mu}{r_{\mathrm{LEO}}}} \left(\left(\sqrt{2} - 1\right)\left(1 + \sqrt{\frac{1}{\gamma}}\right) \right) \tag{2.6}$$

On the left-hand side of Fig. 2.4, a few examples are shown of the trade-off between time of flight (apogee radius) and fuel cost for bi-elliptic transfers for different initial inclinations. On the right-hand side of Fig. 2.4, the optimal two-burn strategies for different inclinations are compared to the theoretical minimum of the bi-elliptic transfers. For initial inclinations larger than 38.365°, the optimal two-burn strategy has a higher fuel cost than the theoretical minimum for bi-elliptic transfers. Note that this value is specific for the considered γ-parameter. For this scenario, a value of 6.42 is used, corresponding to an initial periapse altitude of 185 km.

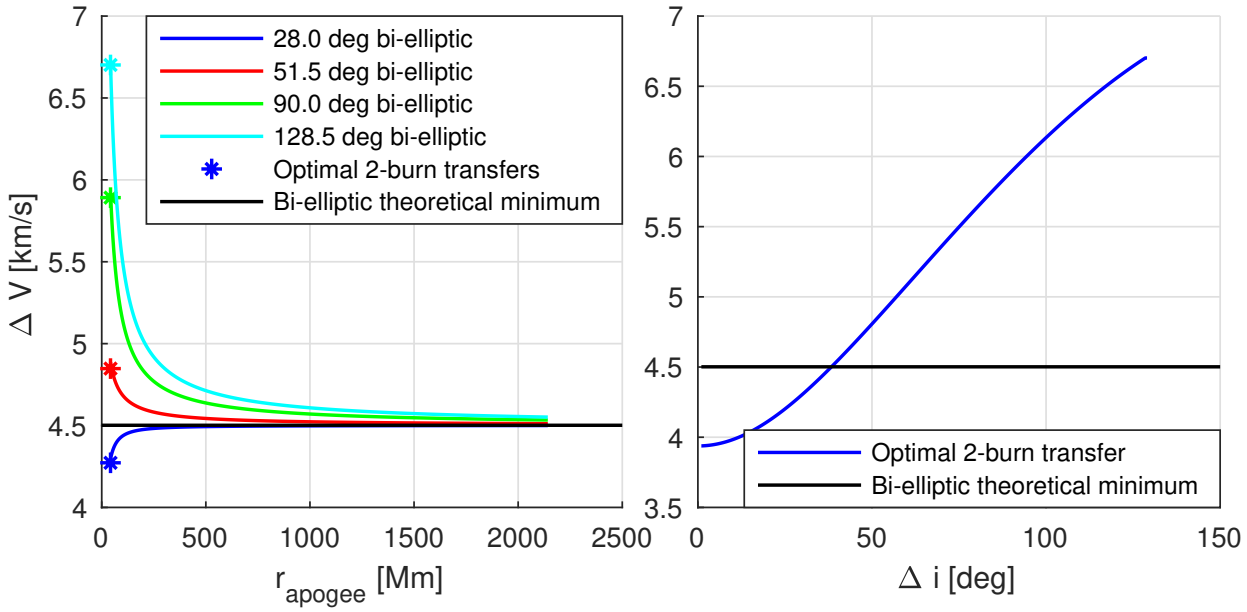

Figure 2.4: Comparison between a two- and a three-burn strategy. Left: ΔV in function of r_{apogee}. Right: ΔV in function of total required Δi.

Continuous-thrust transfers Continuous-thrust transfers are transfers that have maneuvers that occur over a long time frame. A common form uses electrical energy to expel propellant at a very high velocity, which increases transfered momentum per unit of propellant mass. Due to the large required power to expelled mass ratio, current spacecraft power levels only allow for a small mass flow rate. Hence, the achievable thrust and corresponding accelerations are low. To realize the desired orbital changes, the maneuvers are performed over long time periods. Multiple options exist for low-thrust transfers between LEO and GEO. One option is using only low-thrust

propulsion. Starting with a circular orbit deep inside Earth's gravity well, the low accelerations only allow for very gradual orbital changes. Hence, low-thrust transfers from LEO to GEO require many revolutions around the Earth. Optimizing the thrust direction and magnitude on all revolutions leads to a very large optimization problem. Therefore, historically, these transfers have been designed using control laws and not with optimization procedures. An example is the Q-law, which is based on Lyapunov feedback control [44]. Recent breakthroughs in hybrid differential dynamic programming allow to numerically optimize such transfers [1]. An example with 750 revolutions is shown in Fig. 2.5. This transfer requires 7.23 km/s, but only 691 kg of propellant assuming a dry mass of 1000 kg and a specific impulse of 2000 s. On this figure, the orange arcs indicate thrust arcs, the blue indicate coast arcs. A major disadvantage of this method, besides the lengthy transfer times, is the large time spend in the Van Allen belts, a radiation belt around the Earth where energetic charged particles are trapped by Earth's magnetic field. The main Van Allen belt

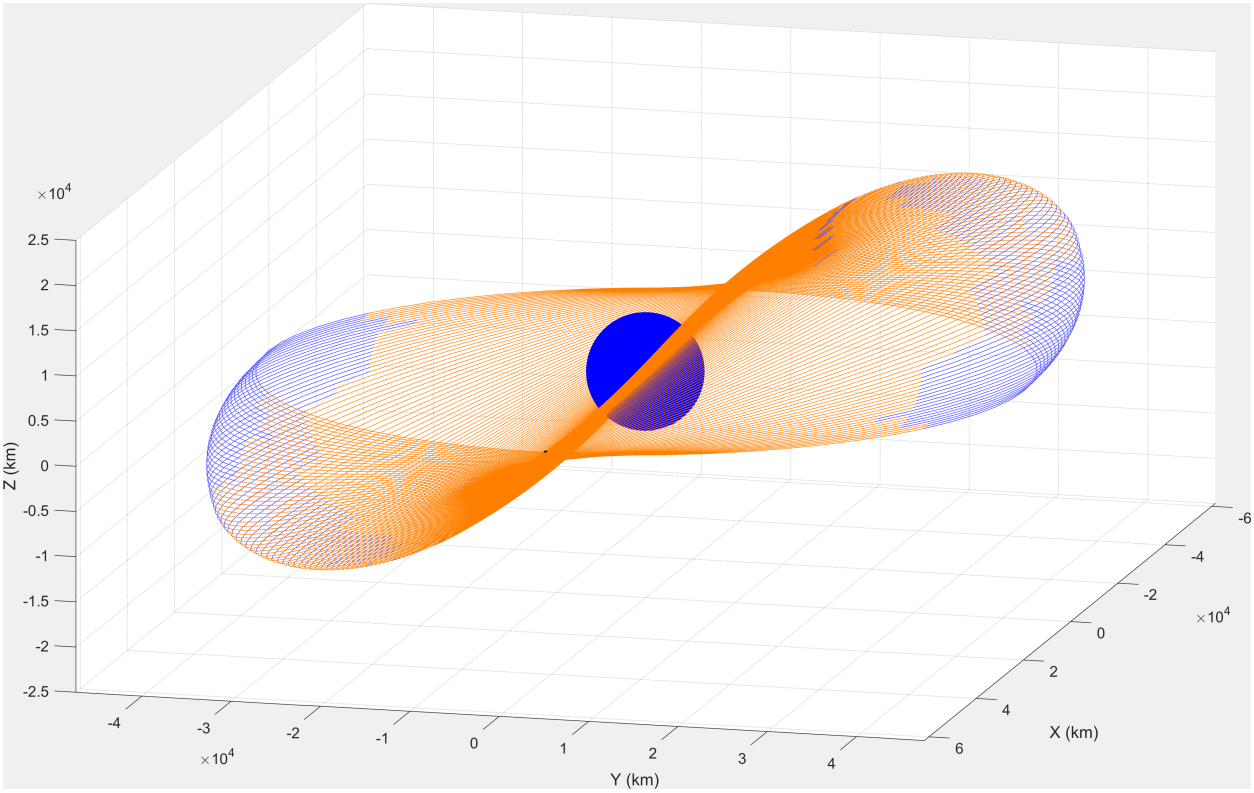

Figure 2.5: A 750-revolution low-thrust transfer from LEO to GEO (credit Aziz [1]).

is situated at altitudes between 1000 km and 6000 km above the Earth's surface. One way of reducing the time spend in the Van Allen Belt is through an initial chemical maneuver that puts the apogee way past the Van Allen Belts. Then, over the course of many revolutions, the perigee is gradually increased. This does not solve the problem entirely, as a considerable amount of time is still spent inside the Van Allen belts [45].

2.1.4.2 Perturbation based methods

Lunar flybys In 1998, a failure in the last stage of the launch vehicle deployed HGS1, also known as AsiaSat3, in a highly inclined, eccentric orbit. The spacecraft did not have enough propellant to transfer to the geostationary orbit using traditional transfer methods. However, the on-board propellant allowed to fly a trajectory with two lunar flybys to ultimately be inserted into GEO [46]. While this transfer saved the mission, more efficient transfers exist using only one lunar flyby. Such transfers are introduced in Ref. [2]. The direct lunar flyby trajectories have a perigee radius at LEO and the apogee radius at the mean lunar distance. To achieve this eccentricity, a maneuver in the velocity vector-direction is made in the low-earth parking orbit. The apogee vector must lie in the lunar orbital plane to target a lunar encounter at apogee. This requires a unique combination for the longitude of ascending node and the argument of perigee, given an initial inclination. To achieve an equatorial orbital plane post-flyby, the flyby must occur when the Moon passes through the equatorial plane; i.e., at the ascending or descending node of the Moon's orbit. An example for a transfer from a 52° inclined 200 km circular LEO can be found in Fig. 2.6. This transfer requires 4.263 km/s and is 8.5 days long. The results of a preliminary, patched-conics analysis can be found in Fig. 2.7 for an initial LEO at 185 km altitude. This approximation provides the general trends, and can be corrected into a more accurate force model using the procedure in Ref. [2]. Designing accurate lunar flybys is not the main goal of this section. Therefore, this correction step is not applied here. This method requires the Moon to be close to a nodal crossing, which only happens twice a month. An alternative using phasing loops has been found that allow daily launches. However, those pass often through the Van Allen Belt.

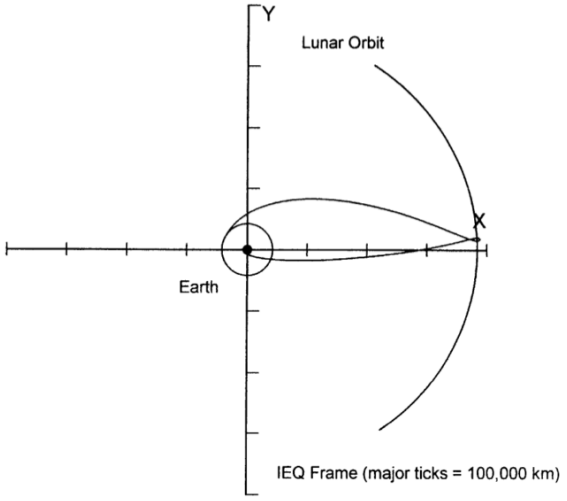

Figure 2.6: Schematics of a geostationary transfer using a lunar flyby (credit Ocampo [2]).

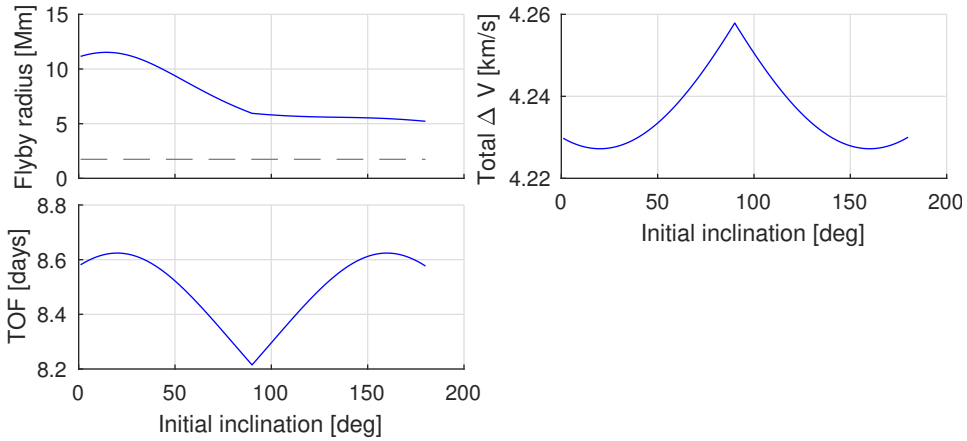

Figure 2.7: Preliminary results of a patched-conics approach to analyze geostationary transfers using a lunar flyby.

Solar tide transfers Solar gravity perturbations can be used to achieve the required Δi and Δr_p. In Reference [17], a point-design transfer starting at $i = 51.5°$ is identified that requires only 2.5% more ΔV than the two-burn transfers from 28.5° [17]. In Section 2.4, the methodology to design such transfers will be briefly explained. In Chapter 3, these transfers will be discussed in more detail.

2.2 Three-body dynamics

Throughout this dissertation, transfers are designed in three-body dynamical systems. As the name suggests, three-body dynamical systems are used to describe the motion of three masses under the gravitational interactions amongst each other. The interest in three-body dynamics was first piqued by classical dynamical astronomy, for instance to describe the motion of the Moon in the Sun-Earth-Moon system. Compared to two-body dynamics, no analytical solution exists for three-body dynamics. Many famous scientists have tackled the problem, developing numerous techniques that are still used in classical mechanics: Euler [47], Lagrange [48], Jacobi [49], Poincaré [50] and Hill [51], to name a few. Different applications require different models to represent the dynamics, with different assumptions. For brevity, this dissertation will not give a detailed description on each of the developed models and their assumptions. However, two specific applications are described, as they lead to the introduction of terminology that will be used throughout this dissertation.

First, Hill described the motion of the Moon in the Sun-Earth-Moon system [51]. Hill used two specific physical properties of this problem; the mass of the Moon and of the Earth are much smaller than the mass of the Sun, and, the Moon and the Earth are spatially close. These assumptions are known as the Hill approximation and allow for a simplification of the equations of motion.

Second, spaceflight introduced a new application for three-body dynamics, where the motion of a spacecraft is described in the Sun-Earth system or Earth-Moon system. In general, the mass of a spacecraft is much smaller than the mass of the other two bodies. This is known as the restricted problem [52], and allows the simplification of the equations of motion.

In the next few subsections, three different dynamical systems are introduced. For each dynamical system, the assumptions used to derive the equations of motion are explained, the reference frame in which the equations of motion are expressed in, and several properties are discussed such as equilibrium points, symmetries and the Jacobi constant, when they exist.

2.2.1 Circular restricted three-body problem

In this subsection, the circular restricted three-body problem (CRTBP) is discussed.

2.2.1.1 Assumptions

The circular restricted three-body problem describes the motion of an object with a negligible mass under the gravitational influence of two large masses M_1 and M_2. The larger of these two, M_1 is called the primary, while M_2 is called the secondary. The primary and secondary are assumed to orbit their center-of-mass in a circular orbit, with radius a, with constant angular velocity N:

$$N = \sqrt{G\frac{M_1 + M_2}{a^3}} \tag{2.7}$$

2.2.1.2 Reference frame

The CRTBP is commonly implemented in a non-dimensional coordinate system using length scale l, time scale τ, and mass scaling ψ.

$$l = a \qquad \tau = \frac{1}{N} \qquad \psi = M_1 + M_2, \tag{2.8}$$

Furthermore, a three-body parameter η is commonly used describing the mass ratios:

$$\eta = \frac{M_2}{M_1 + M_2} \tag{2.9}$$

In Fig. 2.8, the reference frame used for the CRTBP is shown. The origin lies at the center of mass of the two large masses, the x-axis points from the primary to the secondary. The z-axis is parallel to the angular momentum vector of the circular orbit of the secondary around the primary. The y-axis completes the right-handed system. This reference frame rotates around the z-axis with a constant angular velocity N, defined in Eq. 2.7. In this synodic, or co-rotating frame, the coordinates of the primary and secondary are constant and located at $(-\eta, 0, 0)$ and $(1-\eta, 0, 0)$, respectively. Furthermore, r_1 is the distance to the larger primary, and r_2 is the distance to the smaller primary.

$$r_1 = \sqrt{(x+\eta)^2 + y^2 + z^2} \qquad r_2 = \sqrt{(x-1+\eta)^2 + y^2 + z^2} \tag{2.10}$$

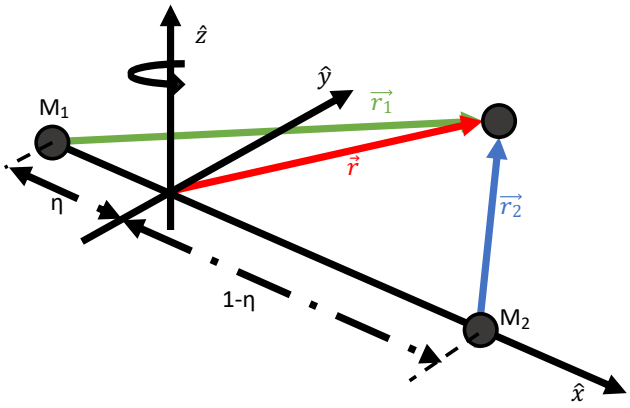

Figure 2.8: Schematics of the reference frame used for the circular restricted three-body problem.

2.2.1.3 Equations of motion

Under the listed assumptions and non-dimensionalization, the Lagrangian L of this system is defined as:

$$L = \frac{\dot{x}^2 + \dot{y}^2 + \dot{z}^2}{2} - \dot{x}y + \dot{y}x + \frac{x^2 + y^2}{2} + \frac{1-\eta}{r_1} + \frac{\eta}{r_2} \tag{2.11}$$

Using the Lagrangian formulation, the equations of motion in the non-dimensional CRTBP frame can be found to be:

$$\begin{aligned} \ddot{x} &= 2\dot{y} + x - (1-\eta)\frac{x+\eta}{r_1^3} - \eta\frac{x-1+\eta}{r_2^3} \\ \ddot{y} &= -2\dot{x} + y - (1-\eta)\frac{x}{r_1^3} - \eta\frac{y}{r_2^3} \\ \ddot{z} &= -(1-\eta)\frac{z}{r_1^3} - \eta\frac{z}{r_2^3} \end{aligned} \tag{2.12}$$

2.2.1.4 Properties

The Lagrangian, L, defined in Eq. 2.11, is time invariant. Thus, from Noether's theorem, it is known that a conserved quantity exists: the Jacobi constant J [53].

$$J = \frac{x^2 + y^2}{2} + \frac{(1-\eta)}{r_1} + \frac{\eta}{r_2} - \frac{\dot{x}^2 + \dot{y}^2 + \dot{z}^2}{2} \tag{2.13}$$

The CRTBP has five equilibrium points, known as Lagrange points. At such points, a body does not experience a net acceleration in the synodic frame. Hence, if a point is placed at this

location with infinite precision, with exactly zero velocity with respect to the synodic frame, it will remain there. The Lagrange points can be found by nulling all velocities and accelerations in Eq. 2.12 and solving for three position components. The location of the five Lagrange points, which all lie on the xy-plane, are shown in Fig. 2.9. Three of these points are known as the collinear points, and lie on the x-axis. L_1 is located between the primary and secondary, L_2 is on the right-hand side of the secondary, and L_3 is on the left-hand side of the primary. Their exact locations can be found by solving:

$$x - \frac{(1-\eta)(x+\eta)}{|x+\eta|^3} - \frac{\eta(x-1+\eta)}{|x-(1-\eta)|^3} = 0 \tag{2.14}$$

Furthermore, two equilateral libration points exist, located at $x = 1/2 - \eta$, and $y = \pm\sqrt{3}/2$.

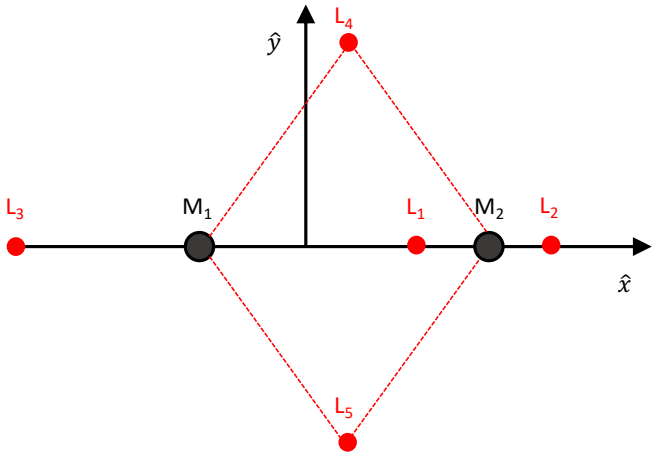

Figure 2.9: Location of the five equilibrium points for the circular restricted three-body problem.

Finally, the CRTBP has several symmetries [3, 54]. If $(x, y, z, \dot{x}, \dot{y}, \dot{z}, t)$ is a solution, then the following are also solutions:

$$(x, y, z, \dot{x}, \dot{y}, \dot{z}, t) \rightarrow (x, y, -z, \dot{x}, \dot{y}, -\dot{z}, t) \tag{2.15}$$

$$(x, y, z, \dot{x}, \dot{y}, \dot{z}, t) \rightarrow (x, -y, z, -\dot{x}, \dot{y}, -\dot{z}, -t) \tag{2.16}$$

$$(x, y, z, \dot{x}, \dot{y}, \dot{z}, t) \rightarrow (x, -y, -z, -\dot{x}, \dot{y}, \dot{z}, -t) \tag{2.17}$$

2.2.2 Restricted circular Hill problem

In this subsection, the restricted circular Hill problem is discussed. For the remainder of this dissertation, this is abbreviated to "circular Hill problem".

2.2.2.1 Assumptions

The circular Hill problem has several assumptions. First, it is assumed that body three is massless. Hence, body one and two are only gravitationally attracted by each other and they orbit their center of mass. Second, it is assumed that this orbit is circular with radius a where one body revolves around the other body with constant angular velocity N:

$$N = \sqrt{G\frac{M_1 + M_2}{a^3}} = \sqrt{\frac{\mu_1 + \mu_2}{a^3}}, \tag{2.18}$$

where μ_1 and μ_2 are the standard gravitational parameters of the larger, and smaller primary, respectively. Using the Hill assumption, where body one is assumed to be much more massive than body two, this can be approximated by:

$$N \approx \sqrt{\frac{\mu_1}{a^3}} \tag{2.19}$$

Finally, under the Hill assumption, the massless object is assumed to remain much closer to the smaller body than to the larger body.

2.2.2.2 Reference frame

The circular Hill system is commonly implemented in a non-dimensional coordinate system using length scale l, and time scale τ.

$$l = \left(\frac{\mu_2}{\mu_1}\right)^{\frac{1}{3}} a \qquad\qquad \tau = \sqrt{\frac{a^3}{\mu_1}} \tag{2.20}$$

In Fig. 2.10, the reference frame associated with the circular Hill problem is shown. The frame is centered at the secondary. The x-axis points from the primary to the secondary. The z-axis is parallel to the angular momentum vector of the secondary's orbit around the primary. The y-axis completes the right-handed system. This reference frame rotates around the z-axis with constant angular velocity N, defined in Eq. 2.19. The non-dimensional coordinates for the primary and secondary are $(-\sqrt[3]{M_1/M_2}, 0, 0)$ and $(0, 0, 0)$, respectively.

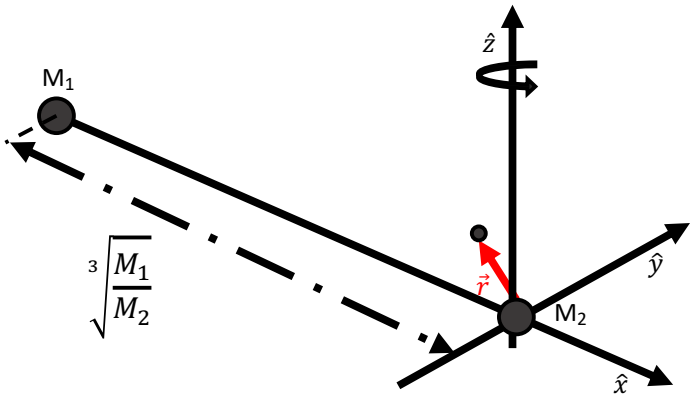

Figure 2.10: Schematics of the reference frame used for the circular and eccentric Hill problems.

2.2.2.3 Equations of motion

Under the listed assumptions and non-dimensionalization, the Lagrangian L of this system is defined as:

$$L = \frac{\dot{x}^2 + \dot{y}^2 + \dot{z}^2}{2} - \dot{x}y + \dot{y}x + \frac{1}{r} + \frac{1}{2}(3x^2 - z^2) \tag{2.21}$$

where r is the L^2 norm of the non-dimensional position vector $\mathbf{r}$ in the circular Hill coordinate frame. Using the Lagrangian formulation, the equations of motion can be found to be [13]:

$$\begin{aligned} \ddot{x} - 2\dot{y} &= \frac{-x}{r^3} + 3x \\ \ddot{y} + 2\dot{x} &= \frac{-y}{r^3} \\ \ddot{z} &= \frac{-z}{r^3} - z \end{aligned} \tag{2.22}$$

2.2.2.4 Properties

The Lagrangian, L, defined in Eq. 2.21, is time invariant. Thus, from Noether's theorem, it is known that a conserved quantity exists: the Jacobi constant J:

$$J = \frac{\dot{x}^2 + \dot{y}^2 + \dot{z}^2}{2} - \frac{1}{r} - \frac{1}{2}(3x^2 - z^2) \tag{2.23}$$

The equilibrium points can be identified by nulling all velocities and accelerations in Eq. 2.22. Only two collinear equilibrium points exist for the circular Hill problem. Both equilibrium points are on the x-axis and are located at $x = \pm\sqrt[3]{\frac{1}{3}}$.

Finally, Villac demonstrated that the circular Hill problem has five symmetries [13]. If $(x, y, z, \dot{x}, \dot{y}, \dot{z}, t)$ is a solution, then the following are also solutions:

$$\begin{aligned}
&(x, y, z, \dot{x}, \dot{y}, \dot{z}, t) \rightarrow (-x, y, z, \dot{x}, -\dot{y}, -\dot{z}, -t) \\
&(x, y, z, \dot{x}, \dot{y}, \dot{z}, t) \rightarrow (x, -y, z, -\dot{x}, \dot{y}, -\dot{z}, -t) \\
&(x, y, z, \dot{x}, \dot{y}, \dot{z}, t) \rightarrow (x, y, -z, \dot{x}, \dot{y}, -\dot{z}, t) \\
&(x, y, z, \dot{x}, \dot{y}, \dot{z}, t) \rightarrow (-x, -y, z, -\dot{x}, -\dot{y}, \dot{z}, t) \\
&(x, y, z, \dot{x}, \dot{y}, \dot{z}, t) \rightarrow (-x, -y, -z, -\dot{x}, -\dot{y}, -\dot{z}, t)
\end{aligned} \tag{2.24}$$

Villac further showed that the latter three symmetries can be translated into classical orbital element space [13]. Note that these orbital elements are expressed with respect to the Hill reference frame, which uses the ecliptic plane as the reference plane.

$$\begin{aligned}
&(a, e, i, \omega, \Omega, M) \rightarrow (a, e, i, \omega + \pi, \Omega, M) \\
&(a, e, i, \omega, \Omega, M) \rightarrow (a, e, i, \omega, \Omega + \pi, M) \\
&(a, e, i, \omega, \Omega, M) \rightarrow (a, e, i, \omega + \pi, \Omega + \pi, M)
\end{aligned} \tag{2.25}$$

2.2.3 Restricted eccentric Hill problem

In this subsection, the restricted eccentric Hill problem is discussed. For the remainder of this dissertation, this is abbreviated to "eccentric Hill problem".

2.2.3.1 Assumptions

The eccentric Hill problem has several assumptions. First, it is assumed that body three is massless. Hence, body one and two are only gravitationally attracted by each other and they orbit their center of mass. Second, it is assumed that this orbit is eccentric with semi-major axis a and

eccentricity e, where one body revolves around the other body with non-constant angular velocity, β. Using the Hill assumption, where body one is assumed to be much more massive than body two, this angular velocity can be approximated by:

$$\beta \approx \frac{\sqrt{a(1-e^2)\cdot\mu_1}}{d^2}, \tag{2.26}$$

where d is the instantaneous distance between the two primaries

$$d = \frac{a(1-e^2)}{1+e\cos\nu_2}, \tag{2.27}$$

where ν_2 is the true anomaly of the secondary in its orbit around the primary. Finally, under the Hill assumption, the massless object remains much closer to the smaller body than to the larger body.

2.2.3.2 Reference frame

The eccentric Hill system is commonly implemented in a non-dimensional coordinate system. The dimensional position and velocity vectors $\mathbf{R}$ and $\mathbf{V}$ are scaled to the non-dimensional position vector $\mathbf{r}$ and $\mathbf{r}'$, its derivative with respect to ν_2 [55]:

$$\mathbf{R} = \alpha d\mathbf{r} \qquad\qquad \mathbf{V} = \alpha\beta(d'\mathbf{r} + d\mathbf{r}'), \tag{2.28}$$

where α is a mass scaling parameter, β is the instantaneous angular rate defined in Eq. 2.26, d is the instantaneous distance between the two primaries defined in Eq. 2.27 and d' is its derivative with respect to true anomaly ν_2 [55]:

$$\alpha = \sqrt[3]{\left(\frac{\mu_2}{\mu_1}\right)} \qquad\qquad d' = \frac{d^2}{a(1-e^2)}e\sin\nu_2 \tag{2.29}$$

All scaling parameters, except α, vary with ν_2 and are thus not constant.

The reference frame used for the eccentric Hill problem is identical to the reference frame for the circular Hill problem, shown in Fig. 2.10, with one major difference. For the circular Hill frame, the angular velocity of the rotation around the z-axis is constant. For the eccentric Hill frame, this angular velocity β, defined in Eq. 2.26, is not constant. The non-dimensional coordinates for the primary and secondary are $(-\sqrt[3]{M_1/M_2}, 0, 0)$ and $(0, 0, 0)$, respectively.

2.2.3.3 Equations of motion

Under the listed assumptions and non-dimensionalization, the Lagrangian L of this system is defined as:

$$L = \frac{x'^2 + y'^2 + z'^2}{2} - x'^2 y + y'^2 x + \frac{1}{1 + e\cos\nu_2}\left(\frac{1}{r} + \frac{1}{2}\left(3x^2 - z^2\right)\right), \tag{2.30}$$

where r is the L^2 norm of the non-dimensional position vector $\mathbf{r}$ in the eccentric Hill coordinate frame. Using the Lagrangian formulation, the dynamics of the eccentric Hill system can be derived, with the derivatives taken with respect to true anomaly ν_2, and not with respect to time, as described by Scheeres and Marzari [55]:

$$\begin{aligned} x'' - 2y' &= \frac{1}{1 + e\cos\nu_2}\left(\frac{-x}{r^3} + 3x\right) \\ y'' + 2x' &= \frac{1}{1 + e\cos\nu_2}\left(\frac{-y}{r^3}\right) \\ z'' + z &= \frac{1}{1 + e\cos\nu_2}\left(\frac{-z}{r^3}\right) \end{aligned} \tag{2.31}$$

2.2.3.4 Properties

Due to the dependency on $\cos\nu_2$, the Lagrangian in Eq. 2.30 is time variant. Thus, no Jacobi constant exists for the eccentric Hill problem. Similar to the circular Hill problem, two equilibrium points exist for the eccentric Hill problem. Those equilibrium points have the same non-dimensional coordinates as the circular Hill problem. However, due to the time dependent length and time scales, their real physical location shifts. The eccentric Hill has the exact same symmetries as the circular Hill system, but using the true anomaly as the time parameter. Furthermore, the orbital element symmetries listed in Eq. 2.25 are identical.

2.3 Reference frames

This section describes several reference frames that are used throughout this dissertation. First, the non-rotating frames will be discussed, followed by a discussion on synodic frames.

2.3.1 Non-rotating frames

In this dissertation, two different types of non-rotating frames are used: mean equator and equinox of J_{2000} frames, and mean orbit of J_{2000} frames. For each type, two implementations are developed, one centered at Earth and one at Mars.

2.3.1.1 Mean equator frames

The mean equator and equinox of J_{2000} frame is a category of reference frames where [3]

- $\hat{x}$: crossing of the planetary equator and ecliptic plane
- $\hat{y}$: completes the right hand system
- $\hat{z}$: planetary North pole

where the equator and ecliptic plane are defined with respect to the reference epoch J_{2000}. From this definition, one can see that the mean equator frame uses the planetary equatorial plane as the xy-plane. The Earth Mean Equator and Mars Mean Equator reference frames are abbreviated to, respectively, EME and MME. The common, center independent, abbreviation is ME.

2.3.1.2 Mean orbit frames

The mean orbit of J_{2000} frame is a category of reference frames where [3]

- $\hat{x}$: crossing of the planetary equator and ecliptic plane
- $\hat{y}$: completes the right hand system
- $\hat{z}$: heliocentric angular momentum of the planet

where the equator and ecliptic plane are defined with respect to the reference epoch J_{2000}. From this definition, one can see that the mean orbit frames use the planetary ecliptic plane as the xy-plane. The Earth Mean Orbit and Mars Mean Orbit reference frames are abbreviated to, respectively, EMO and MMO. The common, center independent, abbreviation is MO.

2.3.2 Synodic frames

Synodic frames are rotating reference frames, that rotate with the same instantaneous angular velocity as the orbital motion of the two massive bodies in the three-body problem. As a result, the coordinates of the primary and secondary are constant in a synodic frame. Depending on the assumptions on this orbit, this angular velocity can be constant or time-varying. Depending on the used dynamical system, a different synodic frame is used. Three different reference frames have been introduced earlier in Subsubsections 2.2.1.2, 2.2.2.2, and 2.2.3.2.

2.3.3 Conversions between reference frames

In this subsection, the conversion between the mean equator, mean orbit and Hill frames are discussed. First, the conversion between Cartesian state elements are discussed, followed by the conversion between orbital elements.

2.3.3.1 Conversion in Cartesian state space

Mean equator and mean orbit This is a simple rotation around the $\hat{\mathbf{x}}$-axis by an angle ε; the obliquity of the ecliptic. This is visualized on the left-hand side of Fig. 2.11

Since both systems are non-rotating reference frames, the transformation is simply

$$\begin{aligned} \mathbf{r}_{\mathrm{MO}} &= [M_1(\varepsilon)]\,\mathbf{r}_{\mathrm{ME}}, \quad \mathbf{r}_{\mathrm{ME}} = [M_1(\varepsilon)]^T\,\mathbf{r}_{\mathrm{MO}} \\ \dot{\mathbf{r}}_{\mathrm{MO}} &= [M_1(\varepsilon)]\,\dot{\mathbf{r}}_{\mathrm{ME}}, \quad \dot{\mathbf{r}}_{\mathrm{ME}} = [M_1(\varepsilon)]^T\,\dot{\mathbf{r}}_{\mathrm{MO}} \end{aligned} \tag{2.32}$$

where $[M_1(\varepsilon)]$ is the single-axis rotation matrix around the first body axis, i.e., $\hat{\mathbf{x}}$ [56].

Mean orbit and Hill This is a rotation around the $\hat{\mathbf{z}}$-axis by angle Θ, the instantaneous angle between MO and Hill's frame. This is visualized on the right side of Fig. 2.11. For the circular Hill

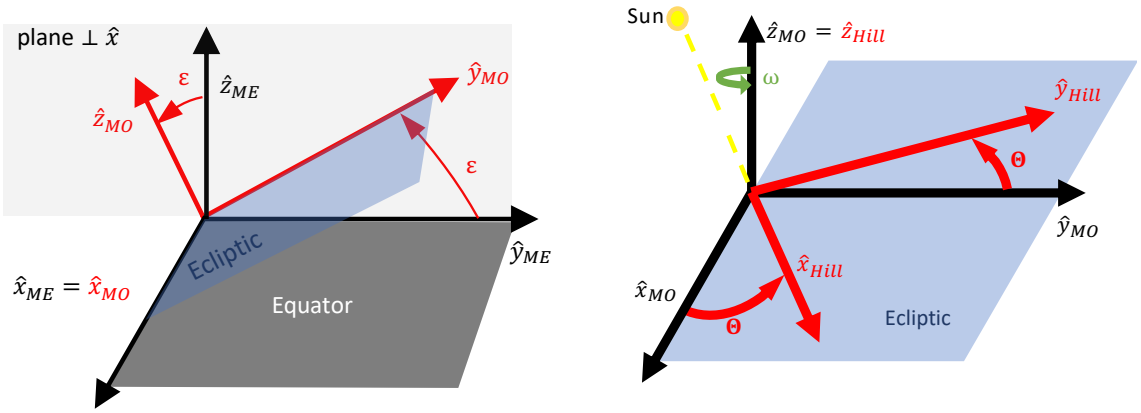

Figure 2.11: Schematics of the conversion from the mean equator to the mean orbit reference frame (left), and the mean orbit frame to the Hill reference frame (right).

frame, $\Theta = \Theta_0 + N(t - t_0)$ where Θ_0 is the angle at a chosen time t_0. For the eccentric Hill frame, this angle is $\Theta = \Theta_0 + \nu_t - \nu_{t_0}$ where the difference between the true anomalies between time t_0 and the current time can be computed using Kepler's equation applied to the orbit of the secondary around the primary. Since those systems do not maintain a constant orientation with respect to each other, but have relative angular rotation rate $\boldsymbol{\omega} = [0\ 0\ N]^T$ for the circular and $\boldsymbol{\omega} = [0\ 0\ \beta]^T$ for the eccentric Hill frame, the transformation can be found using the transport theorem [56]:

$$\begin{aligned} \mathbf{r}_{\text{Hill}} &= [M_3(\Theta)]\,\mathbf{r}_{\text{MO}}, \quad \dot{\mathbf{r}}_{\text{Hill}} = [M_3(\Theta)]\,\dot{\mathbf{r}}_{\text{MO}} - [\tilde{\boldsymbol{\omega}}][M_3(\Theta)]\,\mathbf{r}_{\text{MO}} \\ \mathbf{r}_{\text{MO}} &= [M_3(\Theta)]^T\,\mathbf{r}_{\text{Hill}}, \quad \dot{\mathbf{r}}_{\text{MO}} = [M_3(\Theta)]^T\dot{\mathbf{r}}_{\text{Hill}} - [M_3(\Theta)]^T\,[\tilde{\boldsymbol{\omega}}]^T\mathbf{r}_{\text{Hill}} \end{aligned} \tag{2.33}$$

where $[M_3(\varepsilon)]$ is the single-axis rotation matrix around the third body axis, i.e., $\hat{\mathbf{z}}$ [56], and $[\tilde{\boldsymbol{\omega}}]$ is the skew-symmetric matrix form of the vector $\boldsymbol{\omega}$ [56].

2.3.3.2 Conversion in orbital element state space

Orbital elements are defined with respect to a reference frame. The conversion in orbital elements space can be performed by first converting orbital elements into Cartesian elements, after which one can convert the Cartesian elements into a different reference frame, followed by converting these states back to orbital elements. However, this does not provide much insight, nor are the systematic trends identified. Therefore, in this paragraph, analytical relationships between the orbital elements defined in different reference frames are identified.

Mean equator and mean orbit For a reference frame, the orientation of the angular momentum vector is constant and can be described by:

$$\hat{\mathbf{h}} = \begin{bmatrix} \sin\Omega\sin i & -\cos\Omega\sin i & \cos i \end{bmatrix}^T \tag{2.34}$$

The angular momentum vector described in the mean orbit frame can be rotated into the mean equator frame:

$$\hat{\mathbf{h}}^{\mathrm{ME}} = [M_1(\epsilon)]^T \hat{\mathbf{h}}^{\mathrm{MO}} \tag{2.35}$$

$$\begin{bmatrix} \sin\Omega_{ME}\sin i_{ME} \\ -\cos\Omega_{ME}\sin i_{ME} \\ \cos i_{ME} \end{bmatrix} = \begin{bmatrix} 1 & 0 & 0 \\ 0 & \cos\epsilon & -\sin\epsilon \\ 0 & \sin\epsilon & \cos\epsilon \end{bmatrix} \begin{bmatrix} \sin\Omega_{MO}\sin i_{MO} \\ -\cos\Omega_{MO}\sin i_{MO} \\ \cos i_{MO} \end{bmatrix} \tag{2.36}$$

$$\begin{bmatrix} \sin\Omega_{ME}\sin i_{ME} \\ -\cos\Omega_{ME}\sin i_{ME} \\ \cos i_{ME} \end{bmatrix} = \begin{bmatrix} \sin\Omega_{\mathrm{MO}}\sin i_{\mathrm{MO}} \\ -\cos\epsilon\cos\Omega_{\mathrm{MO}}\sin i_{\mathrm{MO}} - \sin\epsilon\cos i_{\mathrm{MO}} \\ -\sin\epsilon\cos\Omega_{\mathrm{MO}}\sin i_{\mathrm{MO}} + \cos\epsilon\cos i_{\mathrm{MO}} \end{bmatrix} \tag{2.37}$$

From this, one can see the coupling between the two reference frames' orbital elements

$$\begin{aligned} i_{\mathrm{ME}} &= \arccos\Big(-\sin\epsilon\cos\Omega_{\mathrm{MO}}\sin i_{\mathrm{MO}} + \cos\epsilon\cos i_{\mathrm{MO}}\Big) \\ \Omega_{\mathrm{ME}} &= \mathrm{atan2}\Big(\sin\Omega_{\mathrm{MO}}\sin i_{\mathrm{MO}}, \cos\epsilon\cos\Omega_{\mathrm{MO}}\sin i_{\mathrm{MO}} + \sin\epsilon\cos i_{\mathrm{MO}}\Big) \end{aligned} \tag{2.38}$$

The results of the conversion from any ecliptic state to its equatorial state are shown in Fig. 2.12. Three distinct regions are detected based on the i behavior:

$$\begin{aligned} i_{\mathrm{MO}} \in [0^\circ, \epsilon] \quad &\rightarrow \quad i_{\mathrm{ME}} \in [\epsilon - i_{\mathrm{MO}}, \epsilon + i_{\mathrm{MO}}] \\ i_{\mathrm{MO}} \in [\epsilon, 180^\circ - \epsilon] \quad &\rightarrow \quad i_{\mathrm{ME}} \in [i_{\mathrm{MO}} - \epsilon, i_{\mathrm{MO}} + \epsilon] \\ i_{\mathrm{MO}} \in [180^\circ - \epsilon, 180^\circ] \quad &\rightarrow \quad i_{\mathrm{ME}} \in [i_{\mathrm{MO}} - \epsilon, 360^\circ - \epsilon - i_{\mathrm{MO}}] \end{aligned}$$

Every i_{ME} in each of the three regions, except for the bounds, is achieved twice. Once for $\Omega_{\mathrm{MO}} \in (0^\circ, 180^\circ)$ and once for $\Omega_{\mathrm{MO}} \in (180^\circ, 360^\circ)$. The minimum and maximum i_{ME} are achieved at Ω_{MO} of 180° and 0° respectively. The equator can only be achieved for an ecliptic state with $i_{\mathrm{MO}} = \epsilon$ and $\Omega_{\mathrm{MO}} = 180^\circ$. Here, Ω_{ME} bifurcates, as it is singular for i-values of 0°.

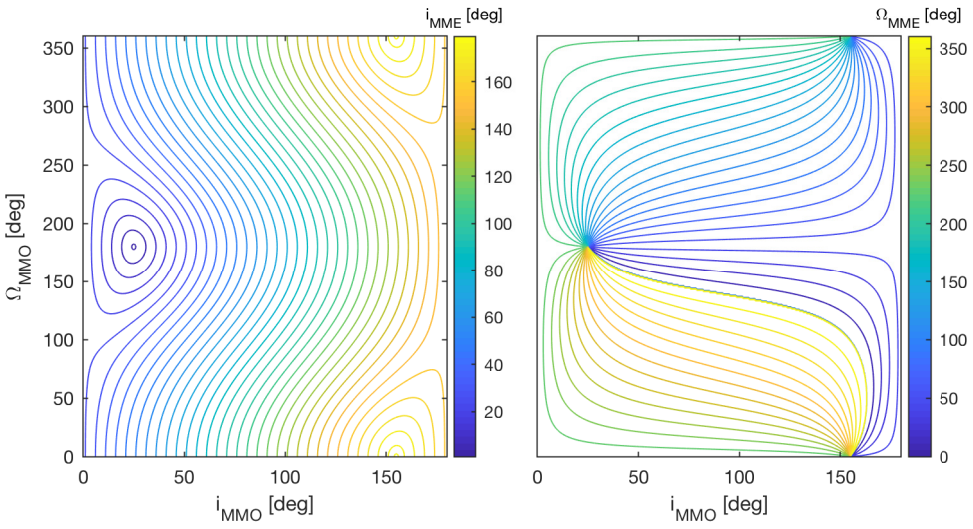

Figure 2.12: Coupling between i and Ω for the equatorial and ecliptic reference frame. As an example, the MME and MMO frames are shown, centered around Mars with angular difference $\epsilon = 25.19°$.

At periapse, the orbital velocity is

$$V = \sqrt{\frac{1+e}{r_p}} \tag{2.39}$$

Eq. 2.32 conserves the magnitude of the position and velocity. Thus, if the conversion is performed at periapse, it can be easily seen that r_p and e are conserved, and thus the semi-major axis.

Mean orbit to Hill The angular momentum vector described in the Hill frame can be rotated into the mean orbit frame:

$$\hat{\mathbf{h}}^{\mathrm{MO}} = [M_3(\Theta)]^T \hat{\mathbf{h}}^{\mathrm{Hill}} \tag{2.40}$$

$$\begin{bmatrix} \sin\Omega_{MO}\sin i_{MO} \\ -\cos\Omega_{MO}\sin i_{MO} \\ \cos i_{MO} \end{bmatrix} = \begin{bmatrix} \cos\Theta & -\sin\Theta & 0 \\ \sin\Theta & \cos\Theta & 0 \\ 0 & 0 & 1 \end{bmatrix} \begin{bmatrix} \sin\Omega_{\mathrm{Hill}}\sin i_{\mathrm{Hill}} \\ -\cos\Omega_{\mathrm{Hill}}\sin i_{\mathrm{Hill}} \\ \cos i_{\mathrm{Hill}} \end{bmatrix} \tag{2.41}$$

$$\begin{bmatrix} \sin\Omega_{MO}\sin i_{MO} \\ -\cos\Omega_{MO}\sin i_{MO} \\ \cos i_{MO} \end{bmatrix} = \begin{bmatrix} \cos\Theta\sin\Omega_{\mathrm{Hill}}\sin i_{\mathrm{Hill}} + \sin\Theta\cos\Omega_{\mathrm{Hill}}\sin i_{\mathrm{Hill}} \\ \sin\Theta\sin\Omega_{\mathrm{Hill}}\sin i_{\mathrm{Hill}} - \cos\Theta\cos\Omega_{\mathrm{Hill}}\sin i_{\mathrm{Hill}} \\ \cos i_{MO} \end{bmatrix} \tag{2.42}$$

From this, one can see that

$$i_{\mathrm{MO}} = \pm i_{\mathrm{Hill}} \tag{2.43}$$

Since $i \in [0, \pi]$

$$i_{\mathrm{MO}} = i_{\mathrm{Hill}} \tag{2.44}$$

Thus, $\sin i_{\mathrm{MO}} = \sin i_{\mathrm{Hill}}$. Dividing both sides of Eq. 2.42 by $\sin i_{\mathrm{MO}}$

$$\begin{bmatrix} \sin \Omega_{\mathrm{MO}} \\ \cos \Omega_{\mathrm{MO}} \end{bmatrix} = \begin{bmatrix} \cos \Theta \sin \Omega_{\mathrm{Hill}} + \sin \Theta \cos \Omega_{\mathrm{Hill}} \\ \cos \Theta \cos \Omega_{\mathrm{Hill}} - \sin \Theta \sin \Omega_{\mathrm{Hill}} \end{bmatrix} \tag{2.45}$$

Using the trigonometric functions $\sin(\alpha+\beta) = \sin\alpha\cos\beta + \sin\beta\cos\alpha$ and $\cos(\alpha+\beta) = \cos\alpha\cos\beta - \sin\alpha\sin\beta$, one can see that

$$\Omega_{\mathrm{MO}} = \Omega_{\mathrm{Hill}} + \Theta \tag{2.46}$$

Eq. 2.33 conserves the magnitude of the position, but not of the velocity. Thus, if the conversion is performed at periapse, r_p is conserved, but the periapse velocity defined in Eq. 2.39, and thus e, and the semi-major axis are frame-dependent.

In conclusion, the i are equal in both reference systems, while Ω simply differs by the instantaneous angle Θ. The e in both systems are different, and thus the r_a for conversions occurring at periapse.

2.4 Common design philosophies for transfers in three-body dynamics

In this section, two different design philosophies are explained. The first philosophy based on dynamical systems theory uses manifolds. The second philosophy focuses on the natural force structure, i.e. perturbations. Before explaining both design philosophies, a commonly used technique, a Poincaré map, is defined.

2.4.1 Poincaré map

A Poincaré map is a method to reduce a system from a continuous trajectory in $\mathbb{R}^n$ to a discrete mapping in $\mathbb{R}^{n-1}$. It is defined as the mapping of the flow of the trajectory between two surface of section crossings. The surface of section is an $n-1$-dimensional hyperplane that is transverse to the flow, and has a specified crossing direction. As an example, imagine an autonomous system, with a planar orbit that is slowly spiraling outwards (Fig. 2.13). The state is uniquely determined by positions x and y, and velocities $\dot{x}$ and $\dot{y}$. Now imagine a plane where $y = 0$, the surface of section. One can easily see there are multiple intersections with this plane, for crossings in a specific direction: $\dot{y} > 0$. The crossings are uniquely defined by x, $\dot{x}$ and $\dot{y}$. The Poincaré map thus reduces the continuous trajectory to discrete points on the y=0-plane. For this example, the Poincaré map is the operator that maps the $(x, \dot{x}, \dot{y})$ states at intersection 1, I_1, to the $(x, \dot{x}, \dot{y})$ states at the next intersection, I_2. Note that a Poincaré mapping is not guaranteed to exist. For instance, a trajectory could have no future intersections with the y=0-plane.

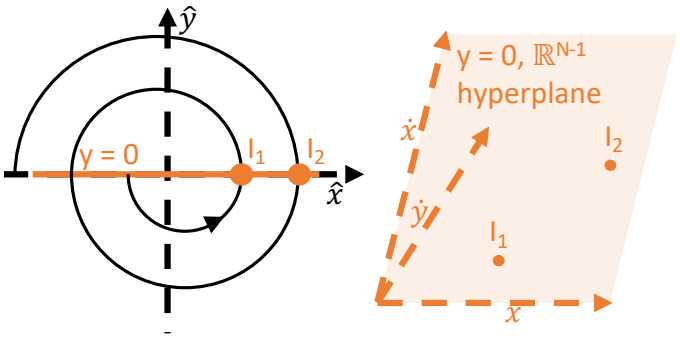

Figure 2.13: Conceptual example of a Poincaré map.

Many different surface of sections can be used. For this dissertation, the transfers of interest change their orbital elements in between subsequent periapses. Therefore, the periapse condition is an obvious candidate for the surface of section. Villac and Scheeres [57] introduced the periapse surface of section for the Hill problem. The following equation defines this periapse surface of section and crossing direction.

$$\begin{cases} \mathbf{r} \cdot \dot{\mathbf{r}} & = 0 \\ v^2 + \mathbf{r} \cdot \ddot{\mathbf{r}} & > 0 \end{cases} \tag{2.47}$$

Haapala and Howell [58] have adapted the periapse surface section for the CRTBP by defining the periapse with respect to the secondary body:

$$\begin{cases} \mathbf{r_2} \cdot \dot{\mathbf{r}} & = 0 \\ v^2 + \mathbf{r_2} \cdot \ddot{\mathbf{r}} & > 0, \end{cases} \tag{2.48}$$

where v and $\ddot{\mathbf{r}}$ are the radial velocity and acceleration of the satellite relative to the secondary body.

2.4.2 Dynamical systems theory

Fuel efficient transfers between different orbits can be identified by connecting stable and unstable manifolds of libration point orbits [3, 4, 59]. This process consists of three steps. First, libration point orbits are determined. Second, unstable and stable manifolds are computed. Third, intersections of the unstable and unstable manifolds on the Poincaré map's surface of section are determined to identify heteroclinic transfers.

In this dissertation, only planar Lyapunov periodic orbits in the Earth-Moon CRTBP around L_1 and L_2 are considered, which are unstable periodic orbits. Those orbits can be identified using the single-shooting method described in Ref. [3] using an initial guess from Grebow [59]. The computation of periodic orbits is performed using a predictor-corrector scheme: an initial state is integrated numerically, after which a deviation from periodicity is observed. The initial state is then corrected using information from the monodromy matrix.

Unstable periodic orbits have stable and unstable manifolds. Those can be computed using the eigenvectors of the monodromy matrix, $\mathbf{v_s}$ and $\mathbf{v_{us}}$, corresponding to the smallest and largest real eigenvalue respectively, evaluated at one fixed point along the orbit. For each point on the periodic orbit, $\mathbf{x}^i$, the initial state of the stable and unstable manifolds, $\mathbf{x_s^i}$ and $\mathbf{x_{us}^i}$, can be computed using the state transition matrix $\Phi_{i,0}$ from the initial point of the periodic orbit, $\mathbf{x}^0$, up to $\mathbf{x}^i$:

$$\mathbf{x_s^i} = \mathbf{x^i} + \epsilon \ \frac{\Phi_{i,0}\mathbf{v_s}}{|\Phi_{i,0}\mathbf{v_s}|} \qquad\qquad \mathbf{x_{us}^i} = \mathbf{x^i} + \epsilon \ \frac{\Phi_{i,0}\mathbf{v_{us}}}{|\Phi_{i,0}\mathbf{v_{us}}|} \tag{2.49}$$

Using these initial points, the manifolds can be computed by numerically integrating the state backwards and forwards in time for the stable and unstable manifolds respectively. The integration is stopped when the next Poincaré surface of section is encountered, as explained in Subsection 2.4.1. This allows the determination of unstable and stable manifolds that have an intersection on the first Poincaré surface of section. The computation of the next Poincaré maps allows to compute intersections on the next Poincaré surface of sections. This methodology has been successfully applied to design low-energy transfers between the Earth and the Moon for the GRAIL mission [5], or between different libration point orbits for the ARTEMIS mission [6].

2.4.3 Natural force structure

Another branch of design methodology focuses on the natural force structure, i.e., perturbations. This methodology can be used to design Earth-Moon transfers with ballistic captures as studied by Yamakawa [8] and applied to the Hiten mission [9]. Solar tides can also be used to design transfers between different, planetocentric orbits. Orbital changes can be categorized by the quadrant of the orbit in a rotating frame, for changes that affect the magnitude of the angular momentum vector, i.e., changes in the semi-major axis a and eccentricity e, and thus periapse and apoapse radii r_p and r_a [8, 60]. In Ref. [60], Davis et al. derive an analytical expression to express the tidal accelerations. For an exaggerated scenario, the solar tidal accelerations are shown in Fig. 2.14. One can see that in quadrant I and III, the tidal acceleration opposes the motion of a

prograde orbit. In quadrant II and IV on the other hand, the acceleration lies in the same direction as the motion of a prograde orbit [60]. This allows to categorize the orbital changes according to the quadrant, as shown in Table 2.1.

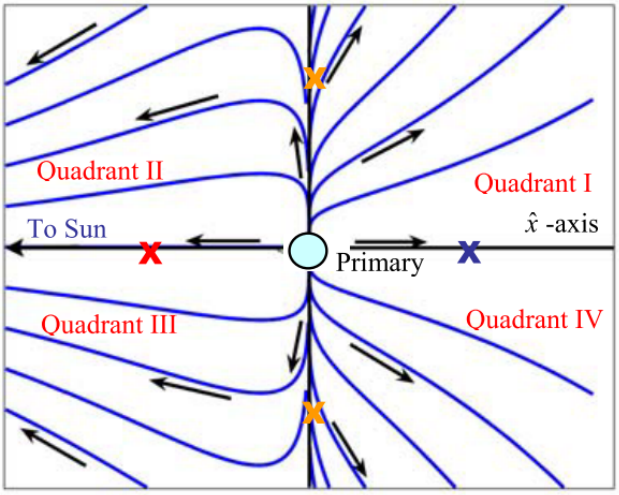

Figure 2.14: Visualization of the solar tidal accelerations in the Sun-Saturn system, in function of the quadrants defined in the rotating frame. The effects are exaggerated by introducing an artificially large primary and magnifying the $\hat{y}$-components (credit: Davis [60]).

Table 2.1: Quadrant categorization for gravitational perturbations in the Hill system. Reproduced from Davis [60].

	Quadrants I and III	Quadrants II and IV
a	$\downarrow$	$\uparrow$
r_p	$\downarrow$	$\uparrow$
e	$\uparrow$	$\downarrow$

For changes that affect the inclination, argument of periapse and/or right ascension of ascending node, a simple quadrant representation does not exist. Nonetheless, large orbital plane changes are possible. An example is the work by Villac [11, 12, 14, 13], who identified transfers with large inclination changes while maintaining a constant periapse radius. This work was performed in the Jupiter-Europa system, but can be easily extended to Sun-planet systems.

2.5 Machine learning

The term "machine learning" was first coined by Arthur Samuel in 1959. He defined this term as "the field of study that gives computers the ability to learn without being explicitly programmed" [61]. Within machine learning, a distinction is made based on the type of data available for training. Supervised learning algorithms have data sets available that contain the exact mapping from input to output parameters. These algorithms mainly focus on learning the underlying relationships between the input and output parameters. Unsupervised learning algorithms on the other hand have only access to training data without explicit mapping between input and output parameters. These algorithms mainly focus on finding structure in the data, and the identification of different subgroups in the data. In this dissertation, the focus lies on supervised learning algorithms. While numerous supervised learning algorithms exist, the general work-flow is always the same and can be divided in several tasks. The work-flow is visualized in Fig. 2.15.

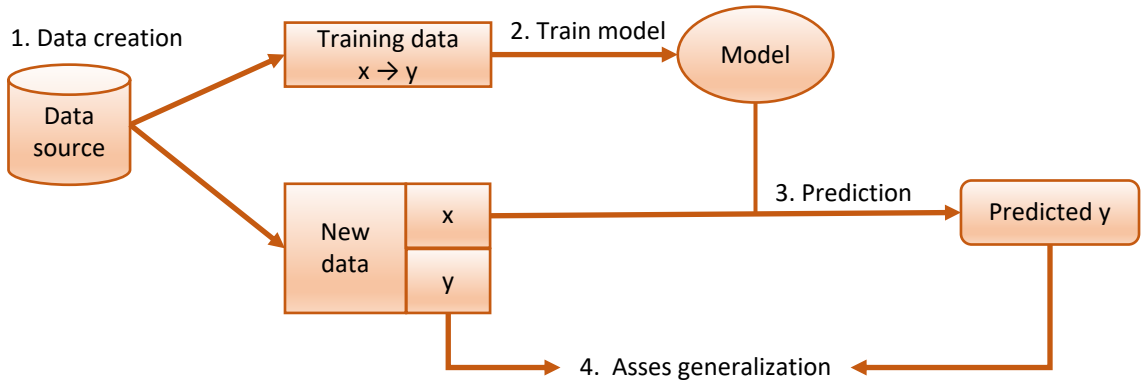

Figure 2.15: General work-flow of a supervised learning algorithm, adapted from Ref. [62].

(1) Data creation: generate the input-output pairs

(2) Training: use the input-output pairs in the training data to train a model.

(3) Prediction: predict the outputs, using a set of new inputs and the trained model.

(4) Asses generalization: compare the predicted outputs with the true outputs. The errors are an indication for the generalization performance of the trained model.

Some common supervised learning techniques are support vector machines [63], naive Bayes classifiers [64], k-nearest neighbor [65], artificial neural networks (ANN) [66, 67, 68], and decision tree methods such as random forests [69]. In this dissertation, artificial neural networks will be used as the chosen machine learning technique. In the next subsections, an answer is given to the following questions:

(1) How do artificial neural networks simulate input-output relationships?

(2) How are artificial neural networks trained?

2.5.1 How do artificial neural networks simulate input-output relationships?

Artificial neurons Rosenblatt introduced the concept of perceptrons in 1957 [67]. A perceptron is a mathematical concept, that computes a weighted average of its inputs, and based on this weighted average, returns a single binary value. This led to the development of artificial neurons; perceptrons with continuous output. Figure 2.16 shows a schematic of an artificial neuron. Artificial neuron k maps n input signals x to a single output value y_k. First, it computes a weighted sum of the inputs and adds a bias term, b_k. Then, a mathematical operation is performed on this weighted average; the activation function ϕ [70].

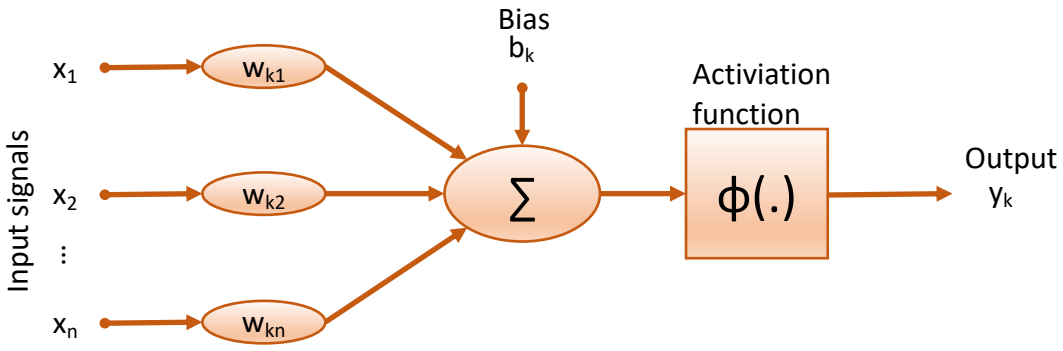

Figure 2.16: Schematics of an artificial neuron, adapted from Ref. [71].

The output of a neuron is thus computed as:

$$y_k = \phi\left(\vec{\mathbf{x}} \cdot \vec{\mathbf{w}}_\mathbf{k} + b_k\right) \tag{2.50}$$

Some examples of commonly used activation functions are a standard logistic function, also known as sigmoid function $S(x)$, and a hyperbolic tangent function $\tanh(x)$ [70]:

$$S(x) = \frac{1}{1+e^{-x}} \qquad \tanh(x) = \frac{e^{x}-e^{-x}}{e^{x}+e^{-x}} \tag{2.51}$$

Artificial neural network An artificial neural network is composed of a collection of artificial neurons. Many variations exist in the way neurons are organized into a network, but all neural networks are composed of multiple layers; an input layer, an output layer, and intermediate layers, called hidden layers. Some common hidden layers are:

- feedforward layer: the output of a neuron is only dependent on its inputs and its weights.
- recurrent layer: the output of the previous evaluation of the neuron is added as an input. This memory term enables the prediction of time series.

For this research, the neural networks predict the response of a Poincaré map; there is only one epoch for which the output states are predicted. Hence, solely feedforward layers are used in this research. A visualization of such a feedforward neural network is shown in Fig. 2.17. The inputs

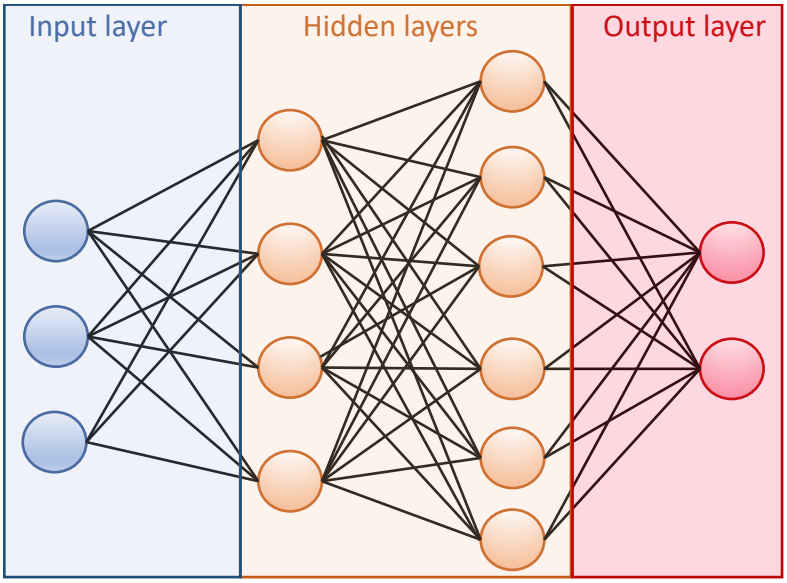

Figure 2.17: Schematics of a 3-4-6-2 feedforward artificial neural network: two input neurons, two hidden layers with 4 and 6 neurons, and 2 output neurons.

of the neural network are propagated forward throughout the network to compute the outputs of the network. This requires knowledge on the weights, unique for each neuron-neuron connection, the bias of each neuron and the chosen activation function of each neuron. For the shown 3-4-6-2 neural network, $(3 \times 4 + 4) + (4 \times 6 + 6) + (6 \times 2 + 2) = 50$ unique weights and biases exist.

2.5.2 How are artificial neural networks trained?

An ANN tries to match the input-output relations observed in data. To do this, a cost function is defined to represent how accurate the ANN is predicting the outputs. Two common cost functions are the mean squared error and cross-entropy cost function. For N training samples and M predicted output parameters, these are defined as:

$$MSE = \frac{1}{N} \sum_{i=1}^{N} \sum_{j=1}^{M} \left(y^i_{\text{pred,j}} - y^i_{\text{truth,j}} \right)^2 \tag{2.52}$$

$$CE = -\frac{1}{N} \sum_{i=1}^{N} \sum_{j=1}^{M} \left(y^i_{\text{truth,j}} \ln \left(y^i_{\text{pred,j}} \right) + \left(1 - y^i_{\text{truth,j}} \right) \ln \left(1 - y^i_{\text{pred,j}} \right) \right) \tag{2.53}$$

The weights and biases of the neurons are randomly initialized. During training, the weights and biases are updated to minimize the cost function. This is done using a back propagation algorithm [72]. There are numerous implementations, each with their advantages and disadvantages [70]. For good generalization performance, a balance must be found between ANN with insufficient neurons that miss trends, and ANN with too many neurons that suffer from over-fitting to the training data [68, 73]. The latter occurs when the minimization procedure tunes the weights in such a way that it almost perfectly captures the provided data, but is inaccurate when applied to new data, not used in the training procedure. To detect overfitting, the data is divided into three sets: a training, validation and test set [68, 73]. The training set is used in the training procedure to minimize the cost function. During the training, the validation set is used to detect overfitting. If overfitting occurs, the cost function on the validation set increases. When this happens, the training procedure is stopped. Finally, there is the test data. This data is not used to train, nor detect overfitting and stopping of the training procedure. Thus, it provides an independent measure to compare the performance of different ANN.

Chapter 3

Transfers from inclined low-Earth orbits to geostationary orbit

3.1 Motivation

The geosynchronous orbit (GEO) is in high demand, yet it requires a considerable amount of fuel to reach. Common launch sites for GEO satellites include the Guiana Space Centre, the NASA Kennedy Space Center and the Baikonur Cosmodrome. Without dog-leg maneuvers after launching into a parking orbit, the minimum inclinations that can be reached for each launch site are 5°, 28.5° and 51.5°, respectively. For launch sites at high latitudes, a large part of the fuel budget needs to be allocated to inclination changes Δi. Several strategies exist to minimize this fuel cost. Some of the methods are discussed in Subsection 2.1.4. In this chapter, transfers will be designed from an initial, highly inclined circular orbit at 185 km altitude to a geosynchronous orbit, which is an equatorial, circular orbit at an altitude of 35,786 km. The patent application of Geryon Space Technologies [17] shows that solar gravity perturbations can be used to provide the required Δi and Δr_p. Point-design transfers starting at $i_{\text{EME}} = 51.5°$ have been found that require only 2.5% more ΔV than the two-burn transfers from 28.5°. The large body of work for conventional strategies for this specific transfer, and the known existence of point-design solutions, makes this transfer a great starting point to develop some of the required computational tools.

This chapter develops a systematic approach to identify transfers, if they exist, for any time of year and initial i_{EME}. Furthermore, the sensitivity of the dynamics to the initial state is quantified through Lyapunov characteristic time analysis. Finally, the sensitivity of the transfers' final i_{EME} and r_p to launch injection errors is analyzed.

3.2 Problem formulation

First, the structure and design variables of the transfer orbits are explained. Second, it is shown how the Hill system's properties can be used to prune the phase space.

3.2.1 Structure and design variables of the transfer orbits

The transfers depart LEO after an in-plane impulse in the velocity-direction to reach the transfer orbit's e_1; index 1 indicates the orbital elements after this first maneuver. At the next perigee, the transfers arrive with $r_{p,2} = r_{\mathrm{GEO}}$ and $i_{\mathrm{EME},2} = 0°$; index 2 indicates the orbital elements prior to the second, in-plane impulse in the anti-velocity direction that circularizes the final orbit. Figure 3.1 shows this strategy, and compares it with the bi-elliptic transfer (Subsubsection 2.1.4.1) for a transfer from an initially polar orbit. The solar-perturbed orbit manages to do the entire plane change without any out-of-plane maneuvers.

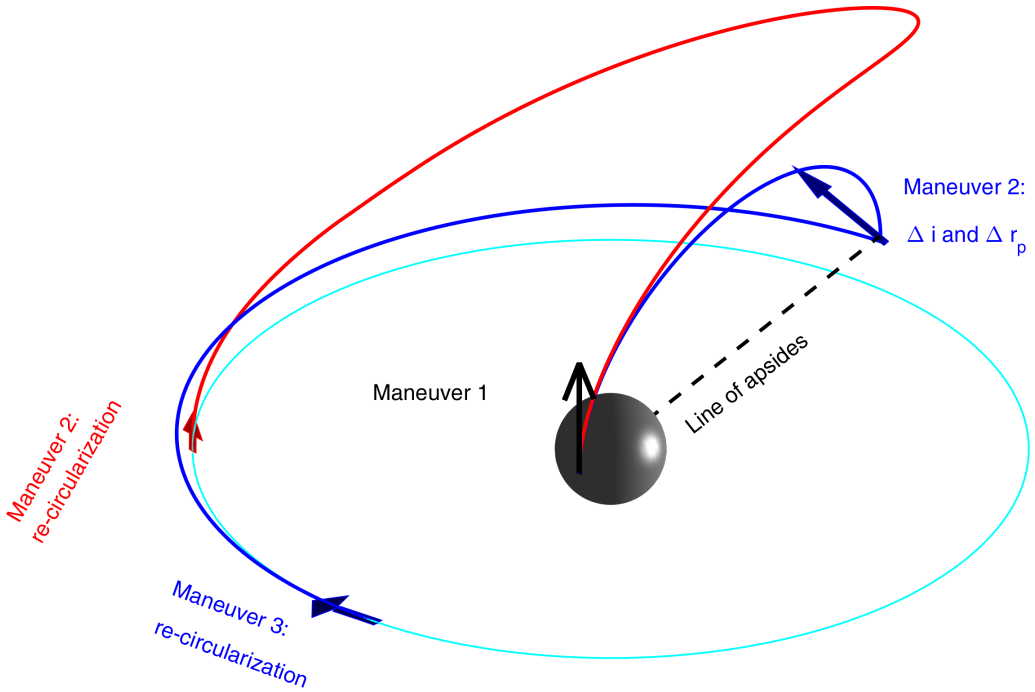

Figure 3.1: Comparison between a bi-elliptic (blue) and solar-perturbed transfer (red) for a scenario departing from an initial polar orbit. Not to scale: red solar perturbed orbit has an apogee radius $\mathcal{O}(10^5\text{-}10^6$ km), cyan target orbit has a radius of 42,164 km.

For this research, the initial $r_{p,1}$ and $i_{\text{EME},1}$ are determined by the launch vehicle and launch site, and are kept constant. This leaves four free design variables: the initial transfer e_1, the initial time t_1, $\omega_{\text{EME},1}$ and $\Omega_{\text{EME},1}$. The first design variable characterizes the size and duration of the transfer orbit, whereas the latter three determine the relative orientation between the Sun and the trajectory, and thus the perturbing accelerations. Given the size of the phase space, and the sensitive maps between design variables and final $r_{p,2}$ and $i_{\text{EME},2}$ values, navigating the state space is not trivial. For each day of the year, the four design variables that satisfy the required Δi_{EME} and Δr_p are determined. To find transfers, intersections must be found between contour lines representing the correct Δr_p and correct Δi_{EME}, at the smallest e_1 at which they occur. By minimizing e_1, the required fuel to inject the spacecraft from LEO into its transfer orbit is minimized.

3.2.2 Phase space pruning

The Earth has a small heliocentric eccentricity of 0.0167. Therefore, the circular Hill problem is used for this application. The circular Hill problem has three spatial symmetries in orbital element space (Eq. 2.25). Only one of those spatial symmetries exists in the EME formulation, whereas the other two are hidden in a more complex combination. If ω_{EME} is a solution, $\omega_{\text{EME}} + \pi$ is also a solution. Therefore, the ω_{EME} design space can be halved: $\omega_{\text{EME}} \in [0, \pi)$. Furthermore, the $\Omega_{\text{Hill}} + \pi$ symmetry is translated into a temporal symmetry. An identical response in the EME system requires identical Ω_{EMO} (Eq. 2.38), which is achieved for the $\Omega_{\text{Hill}} + \pi$ scenario if Θ is adjusted by π (Eq. 2.46); i.e., if the timing changes by half an orbital period. Thus, a solution at time t_0 is also a solution at time $t_0 + 0.5P$, with P the orbital period of the secondary around the primary. Therefore, the temporal design space can be halved: $t \in [t_0, t_0 + 0.5P)$. Note that this temporal symmetry relies on the time-invariance of the circular Hill problem. In conclusion, employing the spatio-temporal symmetries, the solution space can be reduced by a factor of four.

3.3 Transfer design methodology

The methodology is divided into four blocks. First, the mapping from the initial perigee to the next perigee is developed. The next two blocks identify the maximum Δi_{EME} that can be achieved at a specific e_1 and t_1. To do this, the second block finds an initial condition that satisfies the required Δr_p using a single shooting method. The third block uses this to start a continuation method to compute the entire contour of points with the correct Δr_p. On this contour, the local maxima for Δi_{EME} are identified. The fourth block traces out these optima in e_1 until the maximum Δi_{EME} is encountered. Each of those four blocks will be treated in more detail, followed with a discussion on how the four blocks fit into a single algorithm.

3.3.1 Perigee to perigee Poincaré map

The transfers are designed to perform the entire Δr_p and Δi_{EME} in one orbit. Analytical methods exist to predict the change between perigees based on knowledge of the apogee state [11]. As this state is not known a priori, a numerical approach is required: the computation of the Poincaré map using the periapse surface of section defined in Eq. 2.47, using the circular Hill equations of motion in Eq. 2.22.

By definition, the Hill model's xy-plane is the ecliptic plane. However, the transfers nullify their i with respect to the equatorial plane. Because i and Ω are coupled between equatorial and ecliptic reference frames, $i_{\text{Hill},1}$ is not constant for constant $i_{\text{EME},1}$, nor is the required $i_{\text{Hill},2} = 0°$. Therefore, the initial conditions in the equatorial inertial reference system must first be converted to initial conditions in Hill's rotating frame, after which they are numerically integrated. Finally, the end states are rotated back to the inertial frame, to assess the achieved inclination change.

The Poincaré mapping can be performed for different initial conditions. Figure 3.2 shows the inclination and perigee radius changes for the entire range of possible $\omega_{\text{EME},1}$ and $\Omega_{\text{EME},1}$ at $t_1 = 0$ with respect to J_{2000}, with an initial $i_{\text{EME},1} = 51.5°$, a perigee altitude of 185 km and an eccentricity of 0.9856. There are clearly defined contour lines for the inclination and perigee

changes. Their shapes and the location of their extrema do not necessarily overlap. Furthermore, the spatial symmetries in the circular Hill system can be observed.

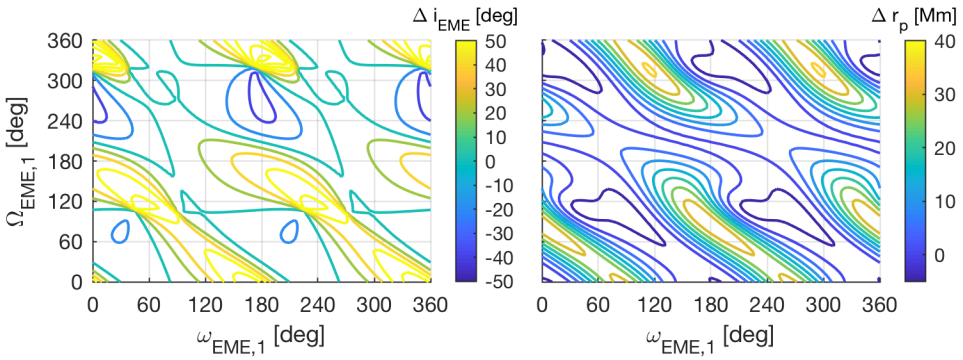

Figure 3.2: Contours for Δi_{EME} and $\Delta r_{p,2}$. Example at t_1=0, $i_{\text{EME},1} = 51.5°$, $e_1 = 0.9856$.

3.3.2 Find point with required perigee raise

The Poincaré map is used to find a set of initial conditions that raises the perigee altitude by 35,601 km from 185 km to GEO altitude. Note that in this subsection, all initial conditions except $\omega_{\text{EME},1}$ and $\Omega_{\text{EME},1}$ are kept constant. First, an initial guess for the orbital parameters is propagated between perigees and the obtained $r_{p,2}$ and $i_{\text{EME},2}$ are stored. A forward finite difference method computes the partials of $r_{p,2}$ and $i_{\text{EME},2}$ with respect to $\omega_{\text{EME},1}$ and $\Omega_{\text{EME},1}$. Then, the required $\Delta\omega_{\text{EME},1}$ and $\Delta\Omega_{\text{EME},1}$ to change the $r_{p,2}$ by $\Delta r_p = r_{p,GEO} - r_{p,2}$ are predicted by solving the following equation:

$$\Delta r_p = \frac{\partial r_p}{\partial \omega} \cdot \Delta\omega + \frac{\partial r_p}{\partial \Omega} \cdot \Delta\Omega = \frac{\partial r_p}{\partial \omega} \cdot \frac{\Delta\omega}{\Delta\Omega}\Delta\Omega + \frac{\partial r_p}{\partial \Omega} \cdot \Delta\Omega \tag{3.1}$$

To obtain the ratio between the two angles, a total angle step $\Delta\Psi = \sqrt{(\Delta\omega)^2 + (\Delta\Omega)^2}$ is selected:

$$\frac{\Delta\omega}{\Delta\Omega} = \pm\sqrt{\left(\frac{\Delta\Psi}{\Delta\Omega}\right)^2 - 1} \tag{3.2}$$

Provided that

$$\alpha = (\Delta\Psi)^2\left[\left(\frac{\partial r_p}{\partial \omega}\right)^2 + \left(\frac{\partial r_p}{\partial \Omega}\right)^2\right] - (\Delta r_p)^2 \tag{3.3}$$

is positive, Eq. 3.1 has two solutions for $\Delta\Omega$. If α is negative, the required perigee change can not be realized for the assumed step size. Increasing $\Delta\Psi$ resolves this.

$$\Delta\Omega_{1,2} = \frac{\left(\partial r_p/\partial\Omega\right)\Delta r_p \pm \left(\partial r_p/\partial\omega\right)\sqrt{\alpha}}{\left(\partial r_p/\partial\Omega\right)^2 + \left(\partial r_p/\partial\omega\right)^2} \tag{3.4}$$

Each solution for $\Delta\Omega$ has two solutions for $\Delta\omega$:

$$\begin{aligned} \Delta\omega_{11} &= \sqrt{\Delta\Psi^2 - \Delta\Omega_1^2} & \Delta\omega_{12} &= -\sqrt{\Delta\Psi^2 - \Delta\Omega_1^2} \\ \Delta\omega_{21} &= \sqrt{\Delta\Psi^2 - \Delta\Omega_2^2} & \Delta\omega_{22} &= -\sqrt{\Delta\Psi^2 - \Delta\Omega_2^2} \end{aligned} \tag{3.5}$$

Because the $\pm$ was ignored in Eq. 3.2, of the four solutions, only two are correct solutions. Plugging the solutions into Eq. 3.1 determines the real solutions. The solution that has the most negative Δi_{EME} gradient is chosen. This procedure predicts the required change in $\omega_{\text{EME},1}$ and $\Omega_{\text{EME},1}$. Then, at this new state, the perigee-to-perigee Poincaré mapping is performed; after which the procedure is repeated until the target perigee raise is reached within a tolerance of 100 km, a 0.28% error on the required perigee raise of 35,601 km.

An example of this procedure is shown in Fig. 3.3. Starting at (250°, 220°), indicated by point 0, and a perigee raise of roughly 10,000 km, the solution jumps to point 1 with a perigee raise of 70,000 km, after which it jumps to point 2, 3, and finally settles on point 4, where the perigee raise is 35,604 km, a 3 km error. This figure also demonstrates that the solution jumps occur in a direction that reduces the final inclination.

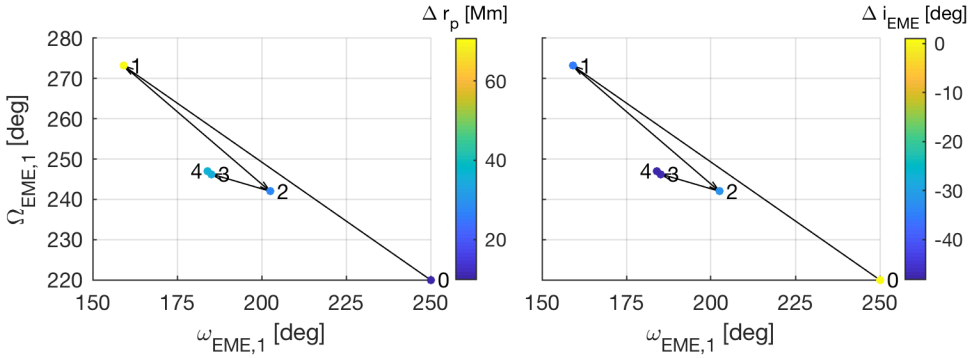

Figure 3.3: Procedural example for finding a point with the required perigee radius change.

3.3.3 Find contour with required perigee raise

The method of the previous subsection provides a starting point to find all combinations of $(\omega_{\text{EME},1}, \Omega_{\text{EME},1})$ that satisfy the perigee raise; again, while keeping all other design variables constant. This will be done using a pseudo-arclength continuation method [74], which is known to be robust around turning points [75]. This method consist of two steps: a predictor and a corrector step. Both are briefly explained in the next paragraphs.

3.3.3.1 Predictor step: tangent method

First of all, a unit vector $\hat{\mathbf{t}}$, tangent to the contour at the current point, must be determined by solving the following:

$$\begin{cases} \left(\partial r_p/\partial\omega\right)\hat{t}_\omega + \left(\partial r_p/\partial\Omega\right)\hat{t}_\Omega & = 0 \\ \hat{t}_\omega^2 + \hat{t}_\Omega^2 & = 1, \end{cases} \tag{3.6}$$

which has solutions

$$\hat{t}_\Omega = \pm\sqrt{\frac{\left(\partial r_p/\partial\omega\right)^2}{\left(\partial r_p/\partial\omega\right)^2 + \left(\partial r_p/\partial\Omega\right)^2}} \qquad \hat{t}_\omega = -\frac{\partial r_p}{\partial\Omega}\left(\frac{\partial r_p}{\partial\omega}\right)^{-1}\hat{t}_\Omega$$

This solution has a sign ambiguity because a tangent direction exists in both directions. Therefore, a choice must be made on the sign of $\hat{\mathbf{t}}$. For the step from the first to the second point, this is arbitrarily chosen. For the next steps, the sign of $\hat{\mathbf{t}}$ is chosen in the direction that maximizes its dot product with the difference between the two previously found points: $\max \pm\hat{\mathbf{t}} \cdot [\omega_{i-2} - \omega_{i-1}, \Omega_{i-2} - \Omega_{i-1}]^T$. This method ensures the continuation along the contour line past a turning point. Based on this method, the direction of the prediction step is fully determined. Then, a step size Δs is chosen with which the new coordinates can be computed. Computing the Δr_p at these new coordinates completes the predictor step.

3.3.3.2 Corrector step: pseudo-arclength constraint

The pseudo-arclength constraint ensures that the dot product between the tangent direction and the difference between the previous converged point $\mathbf{x_{i-1}}$ and the next point $\mathbf{x_i}$ is equal to Δs.

$$\hat{\mathbf{t}} \cdot (\mathbf{x_i} - \mathbf{x_{i-1}}) = \Delta s \tag{3.7}$$

Hence, the corrector step points must all lie on a (n - 1)-dimensional hyperplane, where n is the dimensionality of the state-space. For this application, this results in computing a unit vector perpendicular to the $\hat{\mathbf{t}}$-direction; $\hat{\mathbf{n}}$. The geometric interpretation is shown in Fig. 3.4.

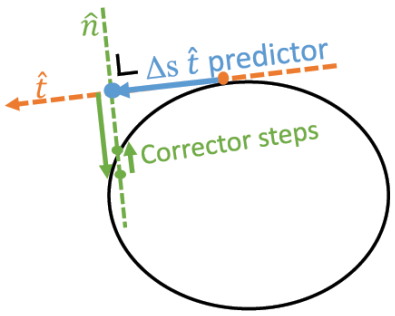

Figure 3.4: Visualization of the pseudo-arclength constraint.

The next step computes the gradient of the perigee raise along the $\hat{\mathbf{n}}$-direction. Using this information, the next corrected state can be predicted. This Newton-method is iterated until convergence. Again, the tolerance is set to 100 km. The number of required iterations is used to adjust the Δs size for the next predictor step.

3.3.3.3 Completing the contour

This pseudo-arclength continuation method is repeated until a closed target Δr_p contour is obtained. A few examples for different eccentricities can be found in Fig. 3.5, where the inclination changes on the perigee-raise contours are shown. The local minima are indicated by red asterisks. It has been verified that the contours indeed stay within a 100 km tolerance of the 35,601 km target. This figure shows that multiple perigee contours can exist and they can merge. Furthermore, one can see that the number of local minima of the inclination change is not constant.

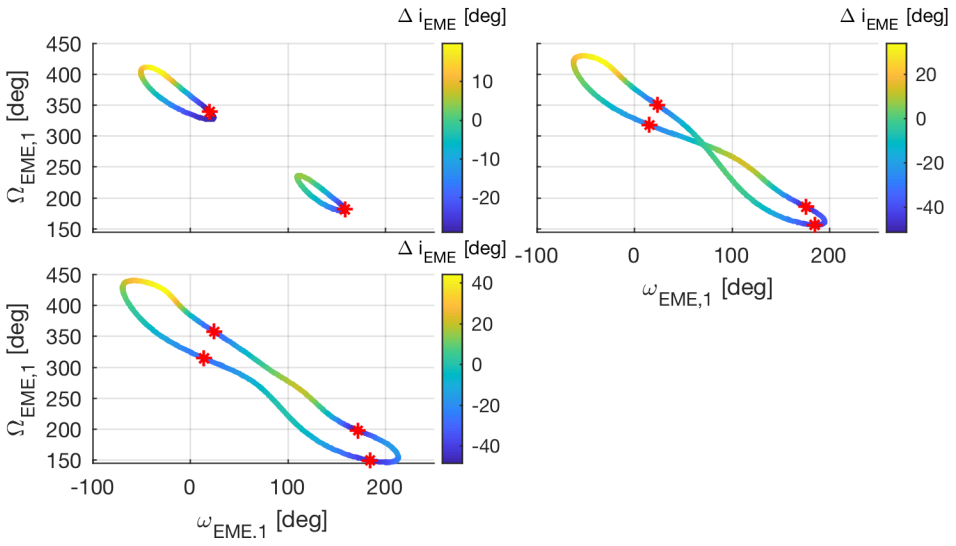

Figure 3.5: Inclination change on the contours with correct Δr_p for different e_1: $e_1 = 0.9860618$ (top left), $e_1 = 0.986618$ (top right), $e_1 = 0.9870$ (bottom left).

To better understand these processes, Fig. 3.6 is created where the perigee contour plots for many e_1-values are depicted. One can see that the contours grow when e_1 increases. At a certain e_1, the two contours meet. Upon increasing e_1 further, they become one big contour. Furthermore, one can see how the local minima, indicated by the black dots, branch of from each other. Starting at one local optima per contour line, a V-pattern arises and the local optima branch off. From

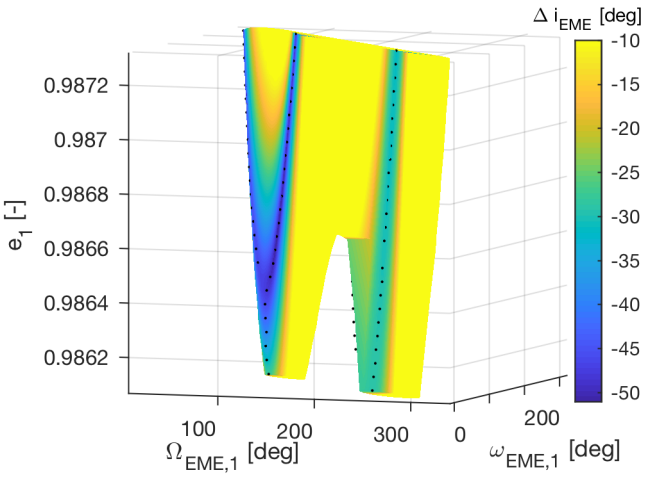

Figure 3.6: Continuum of contours with correct Δr_p for a large number of e_1.

then on, there are two local optima per contour line. When the two contour lines merge into one big contour line, the V-shaped pattern continues, explaining the four local optima on that contour line. For all considered cases, a maximum of four local optima is observed.

3.3.4 Follow inclination gradient on perigee contours

Figure 3.6 shows that the local minima move smoothly. It is thus inefficient to compute complete contours for every e_1. The entire contour(s) is computed for one e_1, the local optima are determined and passed on to the next e_1. First, a point on the contour line for the new e_1 in the neighborhood of the optima of the previous e_1 is found. Then, a pseudo-arclength continuation technique is used, but it is stopped when the new local minima at that e_1 is observed. An example for one local optima is visualized in Fig. 3.7. Note that a few extra steps are performed after observing a local minimum, to reduce sensitivity to numerical noise.

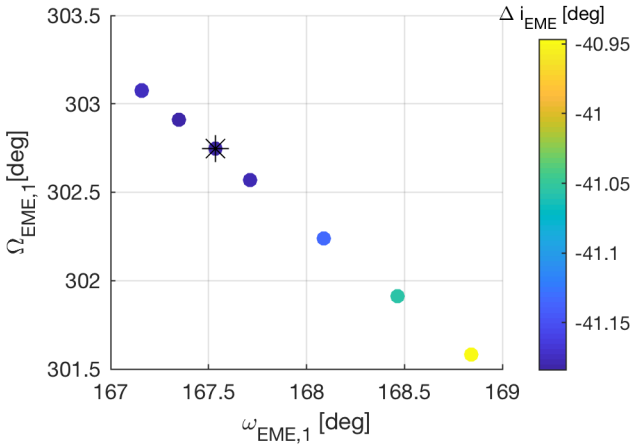

Figure 3.7: Identify local Δi_{EME} minimum on a contour with correct Δr_p for a fixed e_1. The local minimum is indicated by a black asterisk.

Looking back at Fig. 3.6, one can see that local optima branch off from each other and that contours merge. Therefore, it was decided to start at an initial e_1 where the merge has occurred and where four local optima are present. Then, each local optima is traced out in e_1 until the minimum $i_{\text{EME},2}$ is found for that local optima family. Note that a limit of 0.99 has been imposed on the e_1. At such large e_1, the TOF between two perigees becomes very large, and in some cases

infinite, indicating an escape trajectory. An example of this procedure can be found in Fig. 3.8, where the red and black stars are respectively, the local minima on the full contour plot and the minima for each local minima family traced out in e_1.

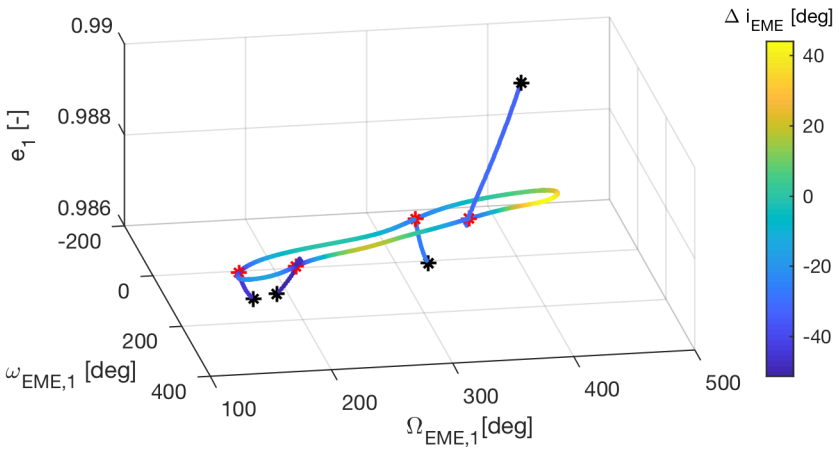

Figure 3.8: For each of the four local minima on the closed contour, the $(\omega_{\text{EME},1}, \Omega_{\text{EME},1})$ location of the local minimum in $i_{\text{MME},2}$ is traced out in e_1.

3.3.5 Final algorithm

For an initial e_1, the full contour is found. It is ensured that there are four local optima and only one closed contour. If this is not the case, e_1 is changed and the new contour is traced out until both criteria our met. Then, for each local optima, the e_1 that results in the minimal $i_{\text{EME},2}$ is determined. Those results, including the optimal e_1, are used as an initial guess for the next day. However, this results in jumps between local optima families. To prevent these jumps, the local optima at the initial e_1, and not the optimal e_1, are passed on to the next day. This ensures staying on the local minimum, but it comes at a higher computational cost.

3.4 Resulting transfers for different initial inclinations

The developed method is applied to several $i_{\mathrm{EME},1}$-values. In Fig. 3.9, one can see how the four local optima (indicated by different colors) evolve over the year for $i_{\mathrm{EME},1}$ of respectively 51.5°, 90° and 128.5°. These $i_{\mathrm{EME},1}$ capture the entire spectrum for launch sites between Baikonur and polar latitudes, as well as the retrograde counterpart for Baikonur. t_1, e_1, $\omega_{\mathrm{EME},1}$ and $\Omega_{\mathrm{EME},1}$ are shown, which in combination with the known $i_{\mathrm{EME},1}$ and $r_{p,1}$, fully determine the initial state. The first row in Fig. 3.9 shows the realized Δi_{EME}. Note that the algorithm is only applied to the first half of the year; the results for the next half are identical through the temporal symmetry explained in Subsection 3.2.2.

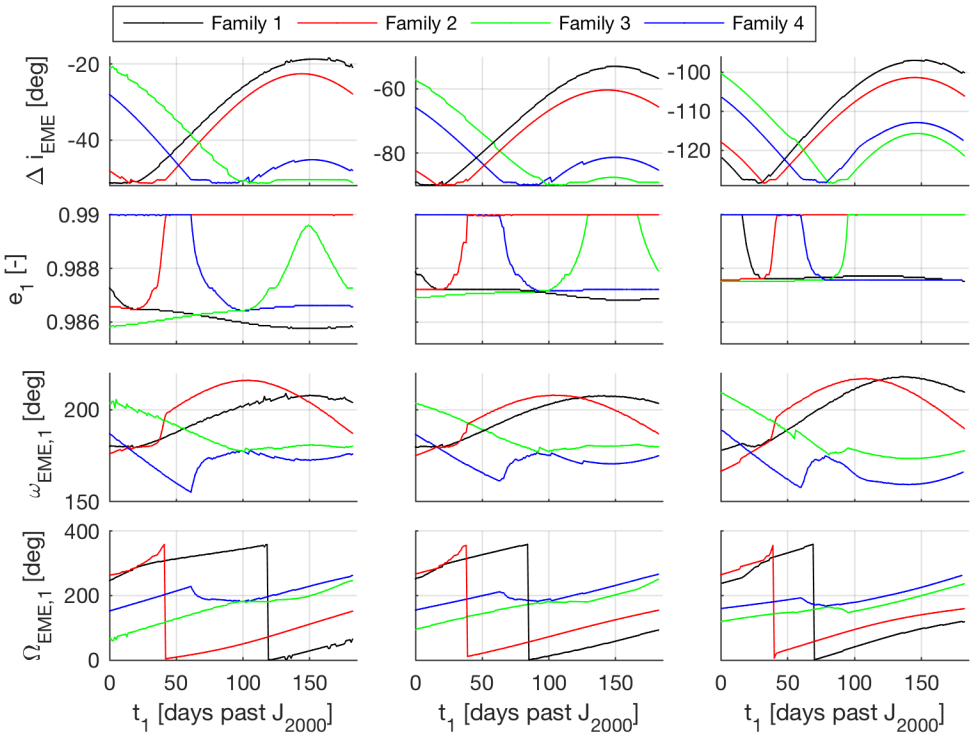

Figure 3.9: Realized inclination change and initial orbital elements in the EME frame for transfers from the four different families (indicated by different colors) with the correct perigee raise, departing from $i_{\mathrm{EME},1} = 51.5°$ (left), 90° (middle) and 128.5° (right).

For different $i_{\mathrm{EME},1}$, very similar structures are observed in the initial orbital elements. A clear shift in e_1 can be observed: for higher initial $i_{\mathrm{EME},1}$, the families start at higher e_1. Therefore, they reach the $e_1 = 0.99$ cut-off sooner, resulting in less feasible trajectories. A trajectory is deemed

feasible when the second perigee condition is within 1° $i_{\mathrm{EME},2}$ and 100 km $r_{p,2}$ of a geostationary orbit. For an initial $i_{\mathrm{EME},1}$ of 51.5°, 90° and 128.5°, respectively 325, 225 and 113 days per year have feasible transfers. The initial orbital elements for the feasible transfers are shown in Fig. 3.10, where the different families of transfers are indicated by different colors. This figure highlights the similarity in the orbital element structure for the different $i_{\mathrm{EME},1}$. At first, $\omega_{\mathrm{EME},1}$ is around 180°, after which it increases, accompanied by a strong increase in e_1. Meanwhile, $\Omega_{\mathrm{EME},1}$ increases linearly with t_1. When the e_1 limit of 0.99 is encountered, the transfers are deemed impossible. After this infeasible t_1-region, a different family of transfers becomes feasible. This family has significantly lower values of $\omega_{\mathrm{EME},1}$ and $\Omega_{\mathrm{EME},1}$. The opposite process occurs, as compared to the transfers prior to the cutoff: $\omega_{\mathrm{EME},1}$ value increases strongly while e_1 drops. When $\omega_{\mathrm{EME},1}$ reaches 180°, it lingers there. To make this possible, e_1 needs to increase again. For the 90 and 128.5° scenario, the 0.99 e_1 cutoff is reached again, indicating another infeasible region.

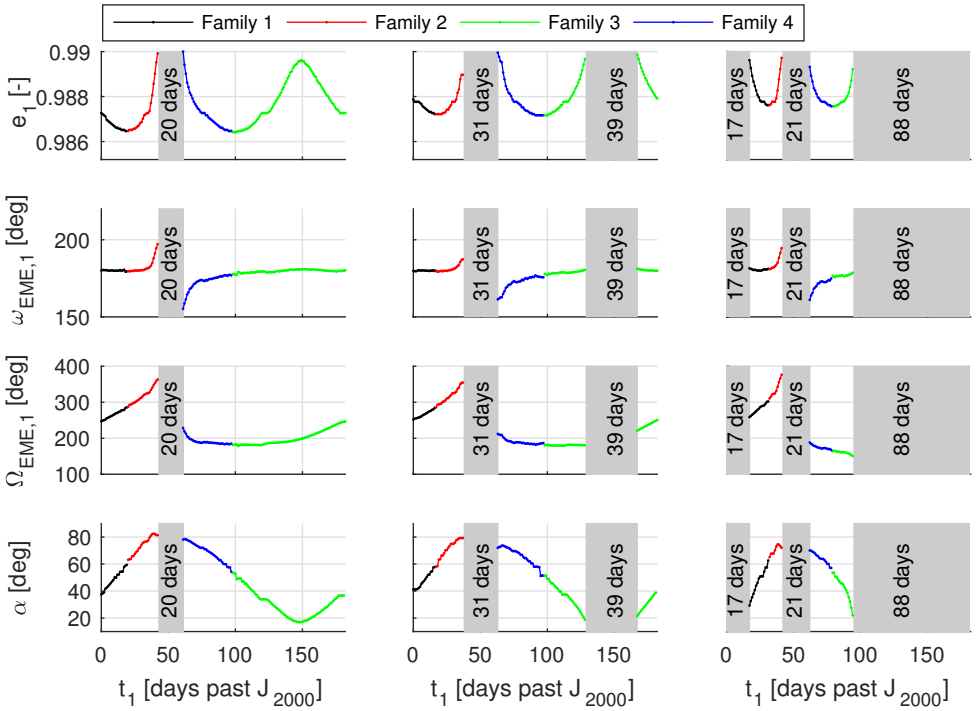

Figure 3.10: Initial orbital elements in the EME frame and apogee angle α for transfers arriving within 1° i_{EME} and 100 km r_p of a geostationary orbit, for different initial equatorial inclinations. From left to right: 51.5°, 90° and 128.5°. The different colors indicate the different families of the transfers.

The bottom row of Fig. 3.10 displays the clockwise angular distance between the positive y axis in the Hill reference frame and the apogee location, α. From theory, it is known that the largest r_p increase occurs near an angle of 45° [8, 60, 76], see Subsection 2.4.3. If α deviates from this location, a larger e_1 is required to realize the same Δr_p. It is observed that there are two i_{EME} reduction regions, that move through the rotating frame in opposite directions. Initially, one of these regions is in the vicinity of $\alpha = 45°$. Thus, a low e_1 suffices. This region travels counter-clockwise, requiring the e_1 to increase to realize the correct $r_{p,2}$. Then, the i_{EME} reduction regions crosses the quadrant boundary near the 50 day mark. Thus, no r_p increase can be realized simultaneously with the i_{EME} reduction; the transfers become infeasible. Meanwhile, the second i_{EME} reduction region undergoes an opposite, clockwise trend. When it crosses into the correct quadrant, the trajectories become feasible again. Throughout its clockwise trajectory through the quadrant, e_1 decreases when α approaches 45°. Then, the e_1 increases again when the region travels towards the positive y-axis. For $i_{\text{EME},1}$ of 90° and 128.5°, the region crosses the quadrant around day 120. Again, the transfers are infeasible until the other i_{EME} reduction region crosses counter-clockwise into the correct quadrant. For $i_{\text{EME},1}$ of 51.5°, this happens instantaneously, explaining why there is no infeasible region.

Figure 3.11 shows the time of flight versus ΔV for the different transfer strategies and for the different values of initial inclination. The total required ΔV for the designed transfers is smaller than the optimal two-burn, as well as the bi-elliptic transfers explained in Subsection 2.1.4. The higher the initial inclination, the larger the ΔV savings are, relative to conventional transfers. For a higher initial inclination, a slightly higher initial eccentricity is required, resulting in a slightly higher ΔV. Thus, the required ΔV only varies slightly with initial inclination, while the two- and three-burn ΔV changes significantly between different initial inclinations. The required ΔV is higher than for the lunar gravity assist transfers. However, the designed transfers only cross the Van Allen belts once, have launch opportunities that are less dependent on the Moon's location and are operationally easier, as they don't have a critical and sensitive lunar flyby.

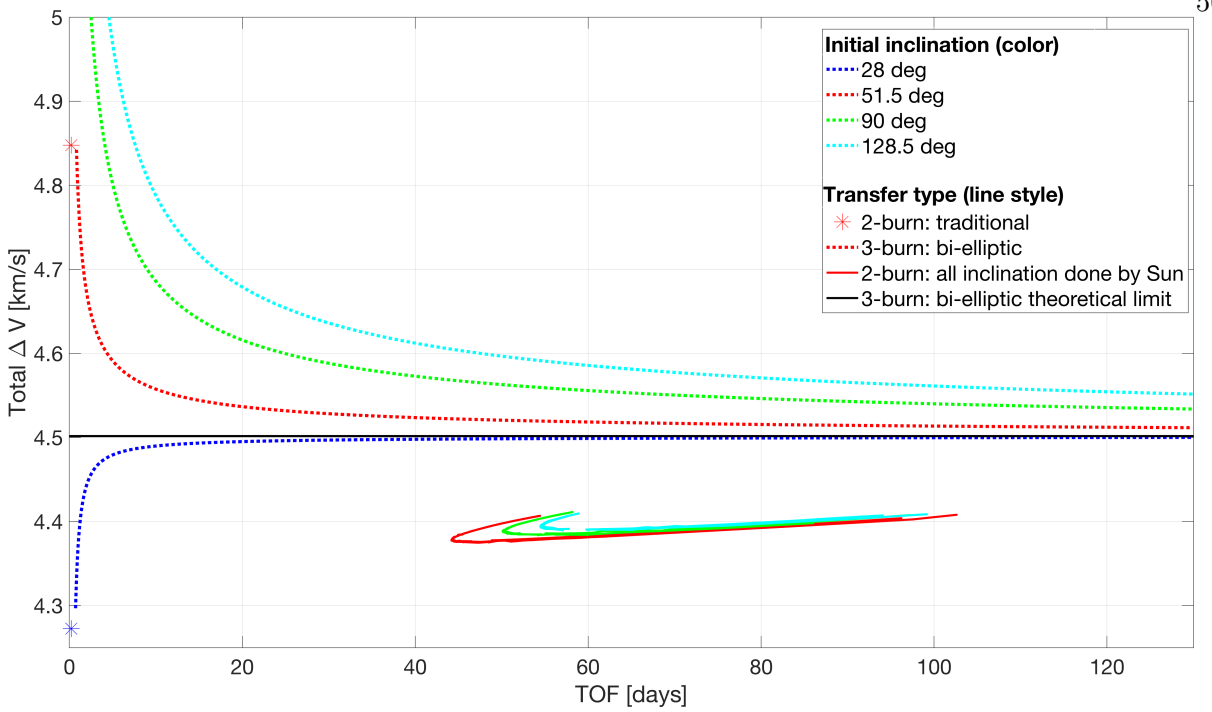

Figure 3.11: ΔV and TOF comparison for different transfer strategies from inclined LEO to GEO.

3.5 Validation

The accuracy of the transfers is verified by integrating the transfers with the gravitational accelerations of the Sun and Earth from the DE405 ephemeris model. Figure 3.12 shows significant deviations from the target orbit, especially near the infeasible region. The observed errors can be mainly attributed to ignoring Earth's heliocentric eccentricity in the used dynamical model. The differences between an eccentric and circular Hill problem are largest for transfers with high e_1. Although the identified transfers have significant errors in the real ephemeris, they are very close to the solutions in the real ephemeris. For a few trajectories, indicated by black asterisks at day 0, 42 and 150, the errors are respectively 3,267 km, 212,003 km, and -5,746 km in $r_{p,2}$, and 0.57°, 12.50° and 1.00° in $i_{\text{EME},2}$. If the initial $(\omega_{\text{EME},1}, \Omega_{\text{EME},1})$ coordinates are changed by respectively (0.30°, -2.00°), (1.50°,1.15°), and (0.00°,1.60°), those errors reduce to respectively 3, 94 and 27 km in $r_{p,2}$, and 0.46°, 1.84°, and 1.05° in $i_{\text{EME},2}$. This suggests a sensitivity in the state space, especially near the infeasible region, which will be studied in more detail in the next section.

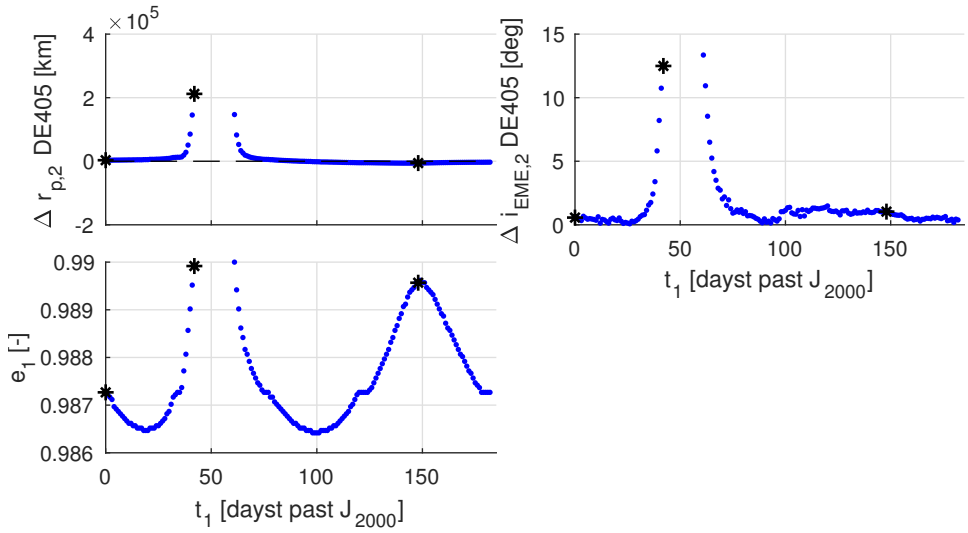

Figure 3.12: Errors in $r_{p,2}$ and $i_{\mathrm{EME},2}$ when modeling the Earth's and the solar gravity based on the DE405 ephemeris, as compared to the circular Hill problem implementation for the $i_{\mathrm{EME},1} = 51.5°$ transfers, and the transfers' e_1.

The lunar gravity is not included in these simulations because this research focuses on the effects of the tidal forces from the Sun. The Moon's effects may be overlaid based on its current geometry, which changes monthly and creates monthly "holes" where the transfers are significantly perturbed by the Moon, and may be infeasible; or they must be modified substantially to accommodate the lunar effects. However, this issue can be avoided by holding off on launches for a few days as the Moon moves through a keep-out zone, or by using the $\omega_{\mathrm{EME}} + 180°$ symmetric transfer; if the nominal transfer travels close to the Moon, the symmetric transfer usually does not. An example has been computed for day 93: when the lunar gravity is included, an error of 18.92° in final $i_{\mathrm{EME},2}$ and 25,433 km in perigee altitude occurs. For the symmetric transfer, this error is 0.11° and 915 km. A slight tweak of the initial conditions of the transfers, or a tiny correction maneuver performed halfway during the transfer can easily clean up this relatively small error.

3.6 Contingency analysis

The nominal transfers are designed under the assumption that the departure conditions and maneuvers are executed with infinite precision. In reality, this is never the case. Therefore, in this section, the designed transfers' robustness is assessed. First, the behavior of the trajectories is investigated when the GEO insertion burn is not executed, followed by the performance of neighboring trajectories as a result of an imperfect first maneuver. For definiteness, only the $i_{\text{EME},1} = 51.5°$ transfers are discussed.

3.6.1 Missed GEO insertion burn

In this subsection, it is assumed that the maneuver at perigee 2 is not executed. The orbit is thus not injected into GEO, but continues along its natural dynamics. Through computation of the next Poincaré maps, the inclination and perigee radius at the next perigees can be computed, displayed in Fig. 3.13. The black dashed line in the r_p plot is the geostationary r_p-value. The impacting trajectories are indicated by a cyan dot. From this figure, one can see that for the third perigee, a large percentage of the trajectories stay under 20° inclination. The region of trajectories in between the two impact regions has a significant inclination change; those 24 days transition to retrograde orbits. The perigee altitude also shows significant variations: the third perigee occurs at altitudes between the Earth's surface and up to 84,000 km above GEO. If both the inclination and perigee altitude stay close to their GEO values, one could recover from the missed maneuver by maneuvering at the third perigee. If one allows an inclination error of 5° and a perigee radius error of 5,000 km, 16 trajectories per year can be injected into a near-GEO orbit on the third perigee. For the next perigees, the inclination and perigee altitude show more variation, and more trajectories impact. For the same tolerances, no trajectories can be injected into a near-GEO orbit on the fourth and fifth perigees.

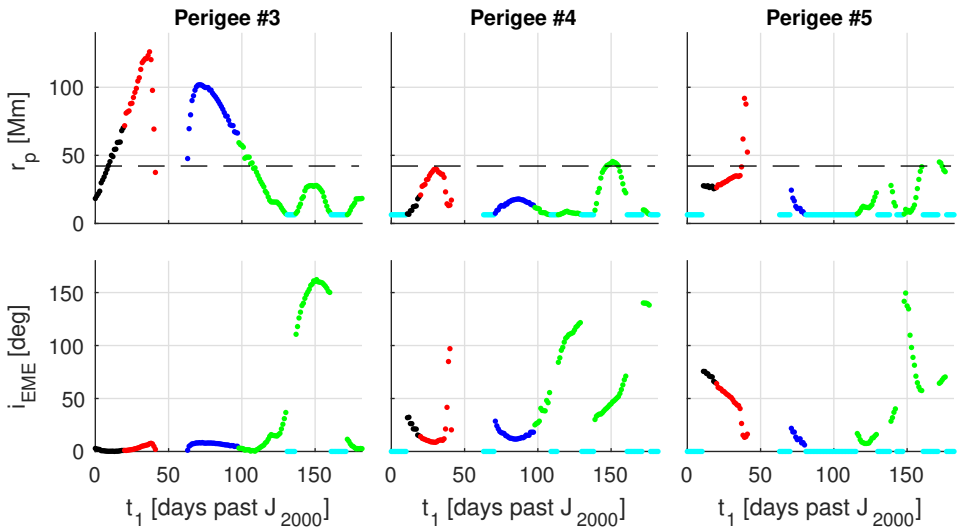

Figure 3.13: Orbital elements at the next perigees when the GEO insertion burn does not occur.

3.6.2 Neighboring trajectory analysis

In this subsection, the stability of neighboring trajectories is assessed. First of all, the rate of exponential divergence from perturbed initial conditions is computed. Then, a Monte Carlo study is performed to determine the effect of launch injection errors on achieved $i_{\text{EME},2}$ and $r_{p,2}$, as well as on impact and escape characteristics. One key driver for the upcoming discussion is the Jacobi constant (J). The non-dimensional formula can be found in Eq. 2.23. In this discussion, the dimensional form is used, defined below:

$$J = \frac{1}{2}v_{\text{Hill}}^2 - \frac{\mu_{\text{Sun}}}{2R^3}(3x_{\text{Hill}}^2 - z_{\text{Hill}}^2) - \frac{\mu_{\text{Earth}}}{r_{\text{Hill}}} \tag{3.8}$$

At a value of -0.3995 km^2/s^2, a spacecraft could reach the L_1 and L_2 point with zero velocity. Thus, the zero-velocity surface at this J-value touches the L_1 and L_2 point. The zero-velocity surface is a surface that a body with a certain J-value cannot cross, since beyond the surface, its velocity would be negative [43]. If J is smaller (more negative) than this value, the spacecraft is contained to a central shape around the Earth. If J is larger than this value, the spacecraft can theoretically escape the Earth system. Examples for both options are shown in Fig. 3.14. Four different transfers for each of the four transfer families are analyzed. Per family, one transfer with J smaller than the theoretical level, and three transfers with increasingly larger J. Those transfers have been indicated with a black asterisk in Fig. 3.15 and visualized in Fig. 3.16.

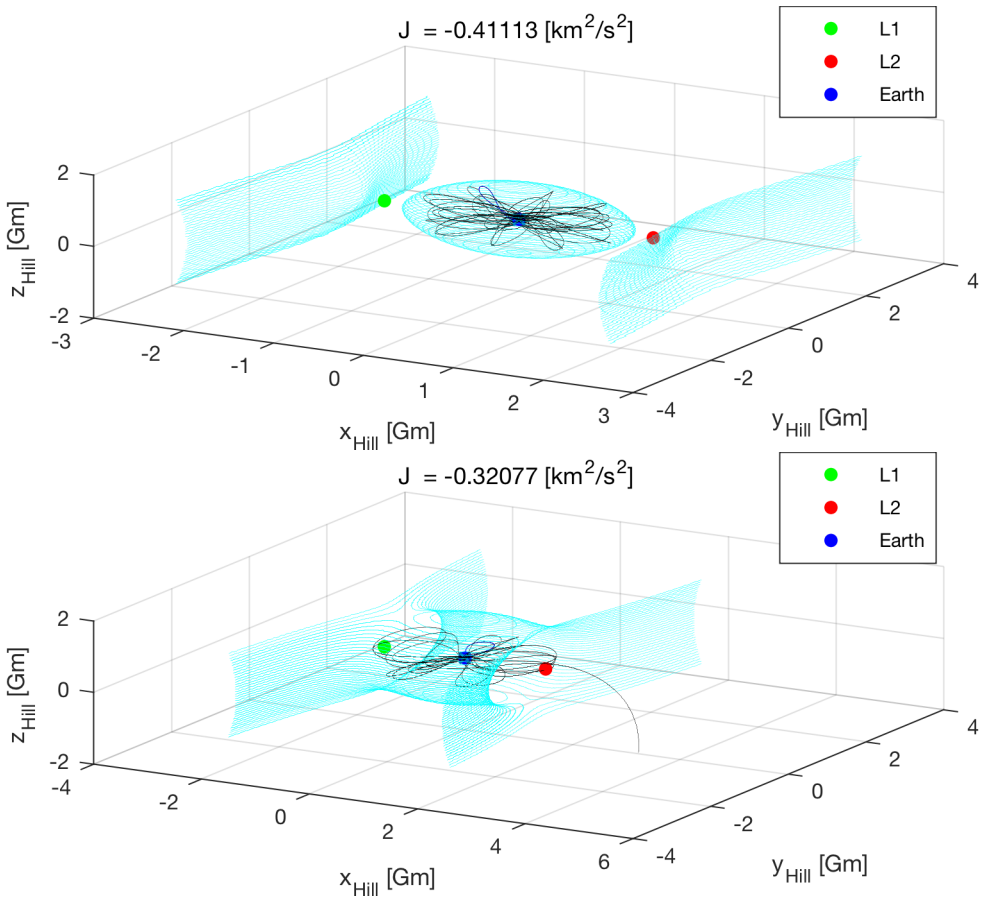

Figure 3.14: Example of a closed (top) and an open (bottom) zero-velocity surface.

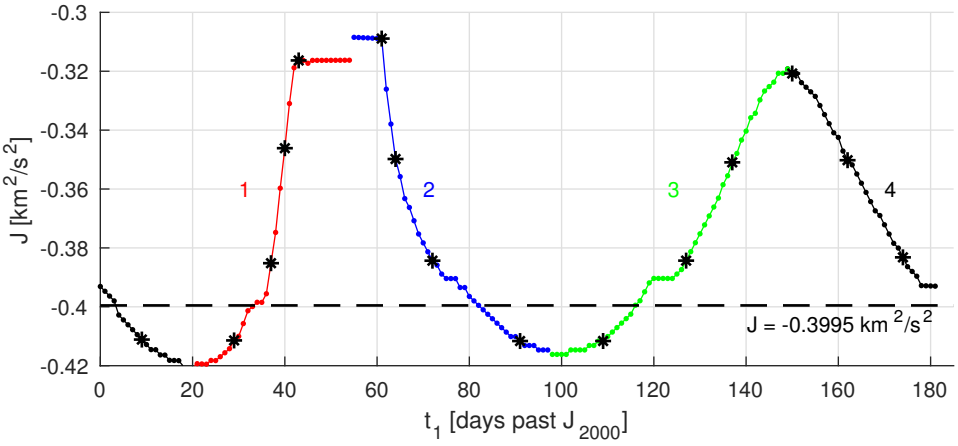

Figure 3.15: Jacobi constant of the transfers, and the selected transfers of the four families. The dashed line shows the limiting case where J = -0.3995 km^2/s^2.

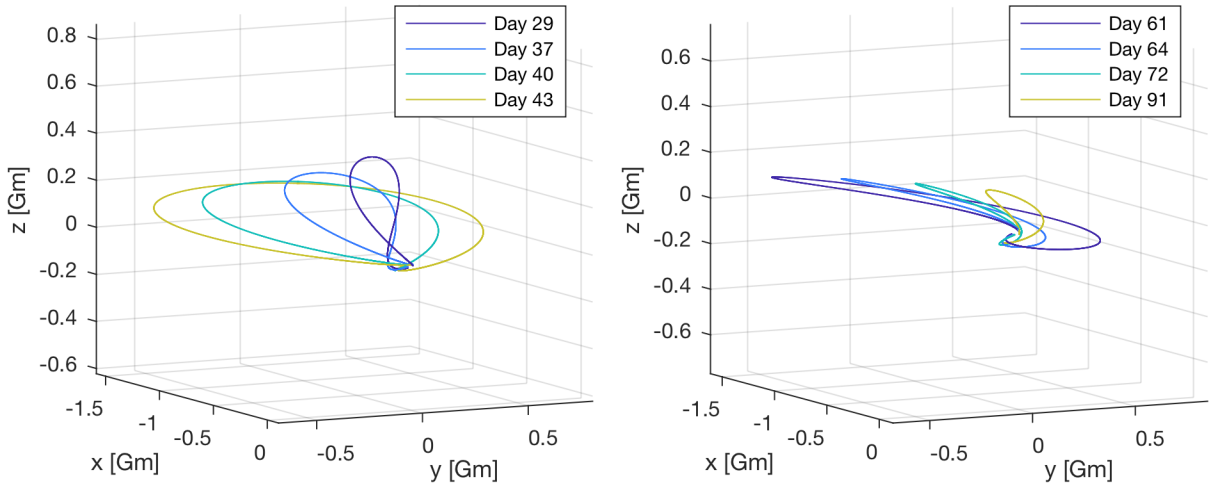

(a) Family 1.

(b) Family 2.

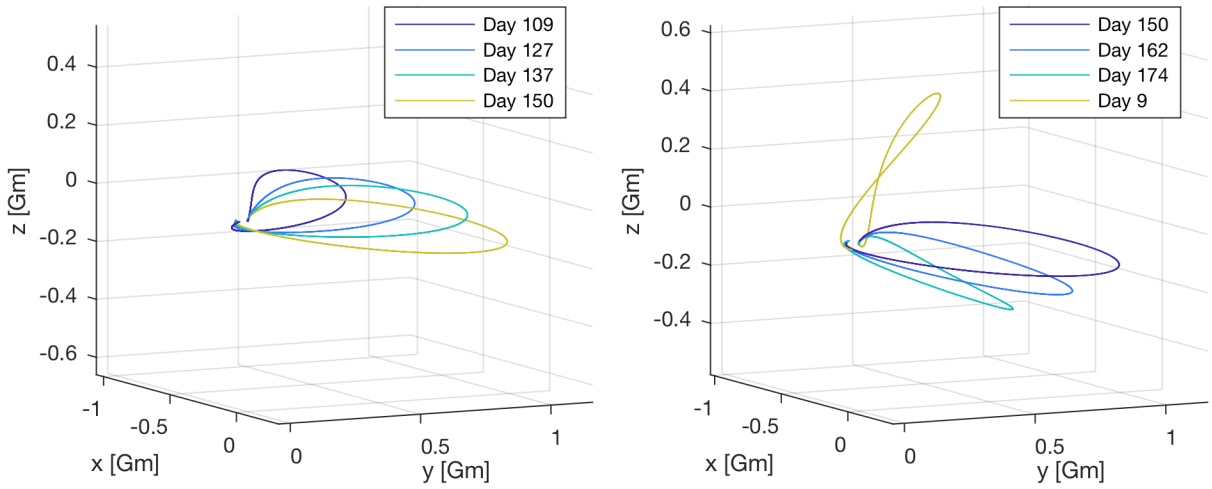

(c) Family 3.

(d) Family 4.

Figure 3.16: Visualization of the selected transfers for each of the four families in Fig. 3.15.

3.6.2.1 Lyapunov characteristic exponents and Lyapunov characteristic time

Lyapunov characteristic exponent (LCE) analysis is a method to determine the rate of exponential divergence from perturbed initial conditions. Therefore, they "are a widely used tool for the estimation of chaoticity in dynamical systems" [77]. The LCE is defined by the following:

$$\chi = \lim_{t\to\infty} \frac{1}{t} \ln\left(\frac{d(t)}{d(t_0)}\right) \tag{3.9}$$

where $d(t)$ is the distance in the phase space between the reference trajectory and a shadow trajectory, which are initially separated by a distance $d(t_0)$ [77]. The shadow trajectory is initialized by multiplying the initial state of the reference trajectory by a factor $(1+\varepsilon)$. The initial distance is hence $(1+\varepsilon)$ times the norm of the initial state. From this equation, it can be seen that the neighboring trajectory only diverges slower than exponentially when χ is zero.

During the computation of the shadow trajectory, a renormalization procedure needs to be applied at given intervals of time τ. This re-normalization maintains the direction of the vector from the reference to the shadow trajectory, but resets the distance to $d(t_0)$ [78]. This is done to "avoid overflow of the lengths of the vectors in the case of a chaotic orbit" [79]. The LCE can then be computed from [77].

$$\chi = \lim_{N\to\infty} \frac{1}{N\tau} \sum_{i=0}^{N} \ln\left(\frac{d(i\tau)}{d(t_0)}\right) \tag{3.10}$$

For this procedure, two tuning parameters exist: first, the ε-parameter that determines the initial distance. Second, the time interval τ to re-normalize. For this research, $\varepsilon = 1e-6$ and τ= 50 days are used. In practice, a trajectory can not be integrated for infinite time. Therefore, the computations have been cut-off when the LCE converges; i.e., when it is clear that the LCE will keep on reducing to zero, or if it levels off and settles on a constant, non-zero value.

An example for the selected transfers in the third family (green) in Fig. 3.15 can be found in Fig. 3.17. One can see that the departure days with the lower J (days 109, 127, and 137) converge onto a non-zero value. However, for the day with the high J, day 150, it can be shown that the LCE should converge to zero for this scenario. The high J value allows the nominal trajectory

to escape from the Earth's system. Hence, at infinite time, it travels at a constant velocity. A small perturbation to this state results in a slightly different, but still constant velocity. Hence, the nominal and shadow trajectory move with two different constant velocities at infinity; as such, they do not diverge exponentially. Therefore, the LCE must be zero.

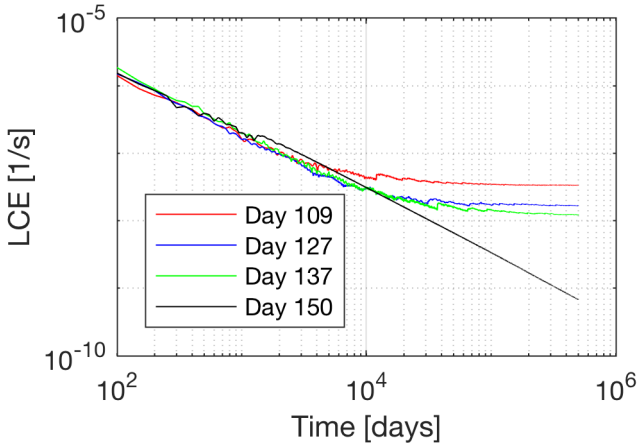

Figure 3.17: LCE trends for the third transfer family indicated in green in Fig. 3.15.

From the LCE computation, one can easily compute its reciprocal; the Lyapunov characteristic time (LCT). The LCT is the time for the separation between the nominal trajectory and a shadow trajectory to increase by a factor e. The LCEs and LCTs have been computed for all transfers. In Fig. 3.18, the LCTs are plotted. The crosses indicate trajectories with an LCE of zero, which have infinite LCT values. The ratio between LCT and transfer TOF is at least seven. Hence, during the nominal TOF, initial perturbations are not expected to increase by a factor e.

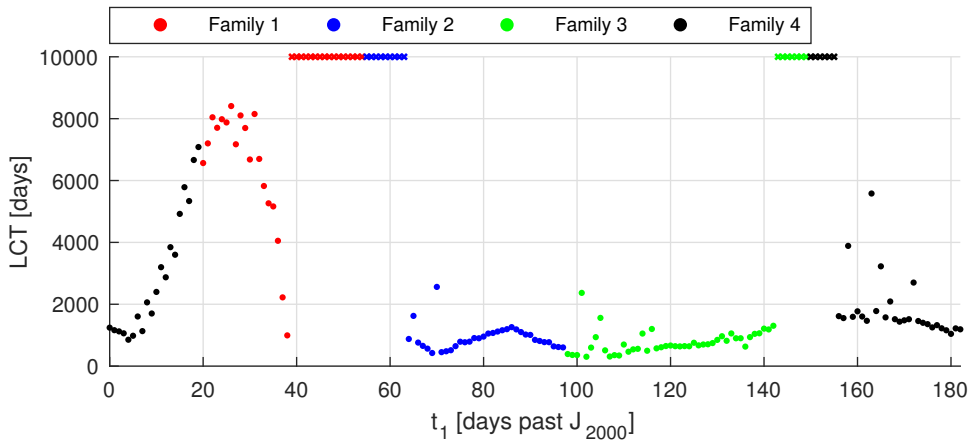

Figure 3.18: Lyapunov characteristic times. The different colors indicate the different families of the transfers in Fig. 3.15.

3.6.2.2 Monte Carlo study on launch dispersion

The amount of information one can infer from non-exponential divergence is limited. It does not provide any information on the sensitivity of the final inclination and perigee altitude to launch injection errors, or on impact and escape characteristics of the transfers. To this end, a 10,000 element Monte Carlo analysis is performed on each of the selected transfers in Fig. 3.15, using the circular Hill dynamical system. The three position and velocity errors are sampled from normal distributions with mean 0 and standard deviations of, respectively, 10 km and 10 m/s. For this study, an orbit is assumed to escape if it does not have a perigee within the first 1500 days. The results of this Monte Carlo study are shown in Fig. 3.19, where the trajectories are grouped by their family (color and number from Fig. 3.15) and ranked from smallest to largest nominal J from top to bottom within each sub-figure. In each subfigure, the nominal J is indicated by a green, dashed line. When an orbit impacts or escapes before performing one perigee-to-perigee transfer, the results are indicated by a red or black dot respectively. If a next perigee-to-perigee transfer exists, the response is indicated by a blue dot. One can clearly see from these figures that the inclination and perigee response is dominated by a single parameter; the Jacobi constant. It can be observed that the Jacobi constant has an almost perfect Gaussian response with a mean at the nominal value, and a standard deviation between 0.14 and 0.145 km^2/s^2. The analysis will be subdivided into two categories based on whether J is smaller or larger than the nominal value.

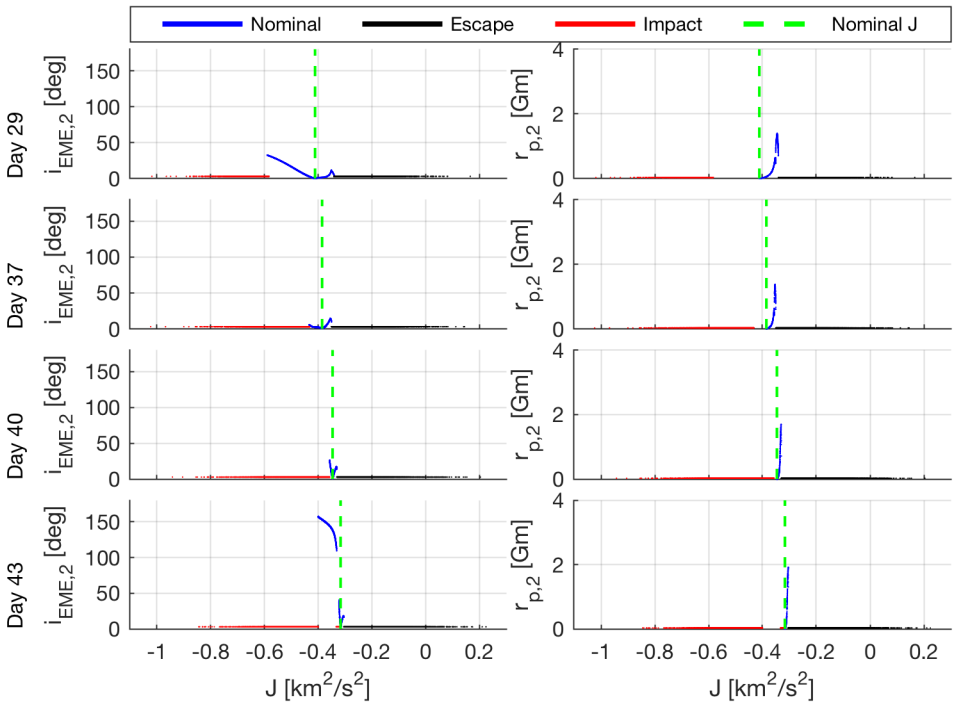

(a) Family 1: depicted in red in Fig. 3.15.

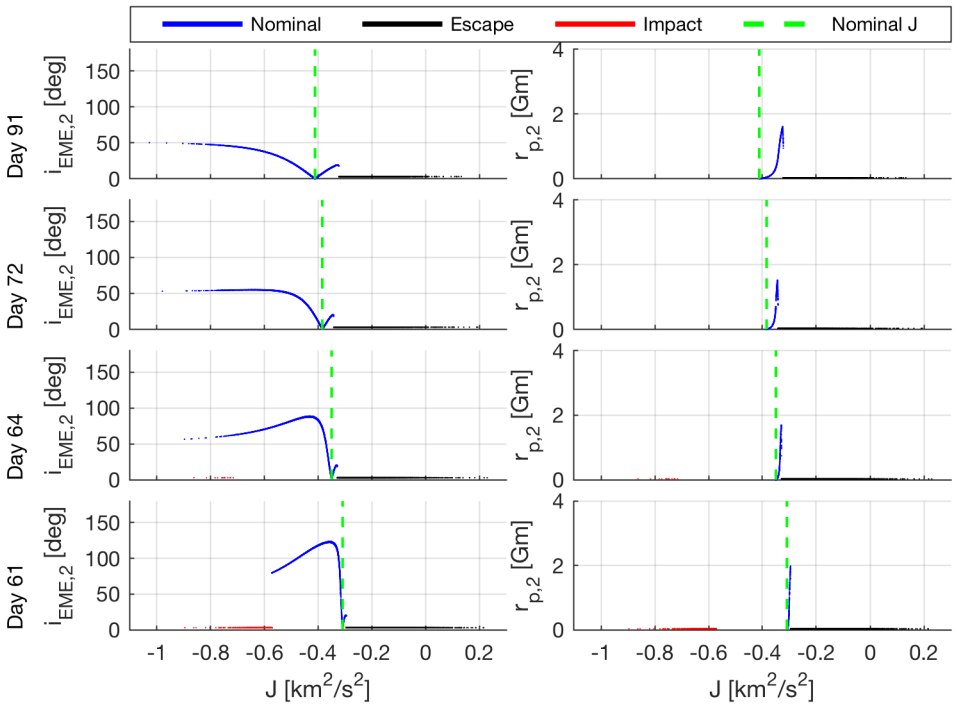

(b) Family 2: depicted in blue in Fig. 3.15.

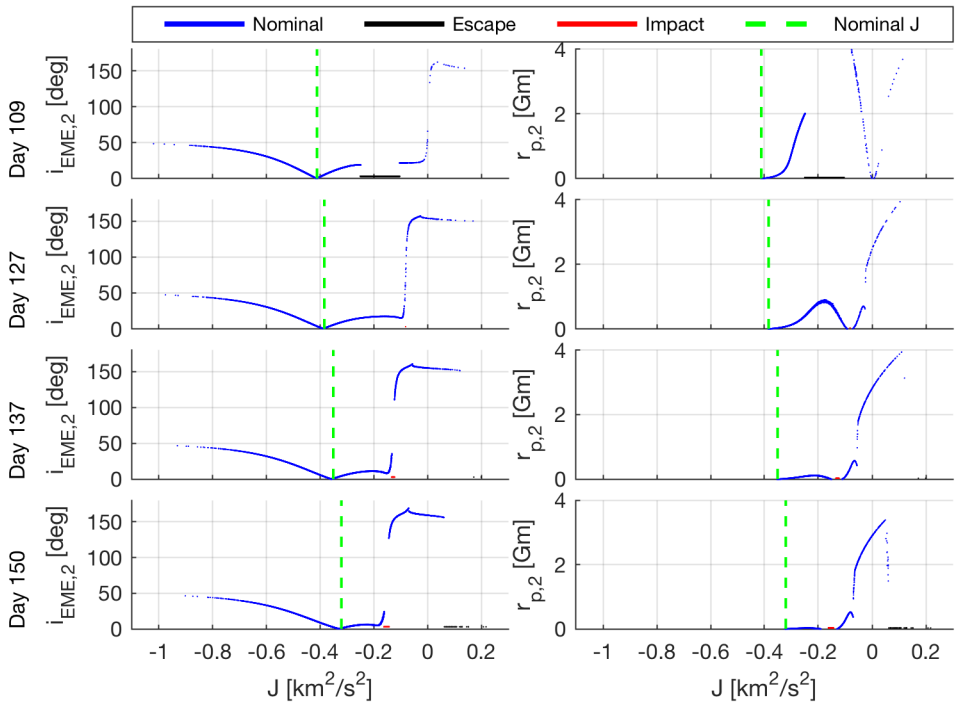

(c) Family 3: depicted in green in Fig. 3.15.

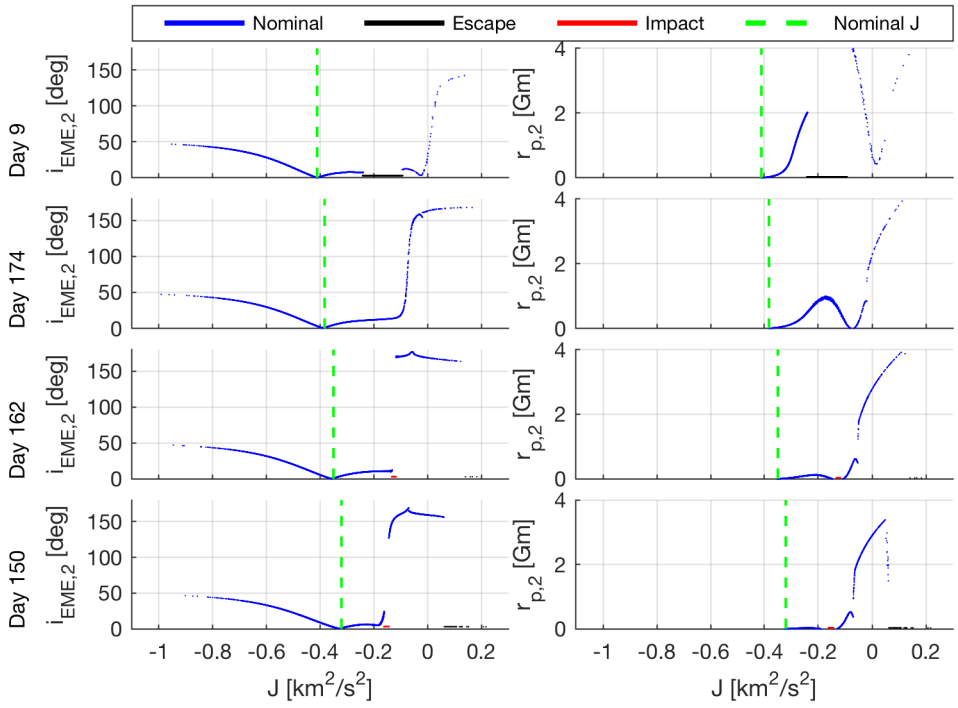

(d) Family 4: depicted in black in Fig. 3.15.

Figure 3.19: Results of the 10,000 element Monte Carlo analysis quantifying the effect of launch injection errors on the four selected transfers for each of the four transfer families, depicted in red, blue, green, and black in Fig. 3.15.

Smaller than nominal levels of J: For most days at smaller levels of J, the trajectory converges on the unperturbed, original orbit. For small levels of J, the original eccentricity is small. Hence, the orbit does not fly far enough from the Earth to be significantly perturbed by the solar gravity. Figure 3.20a depicts a selection of trajectories for day 150 that have a smaller J than the nominal trajectory (displayed in black). The smallest J's are depicted in blue, the largest in red.

For family 1 and 2, at the two days with the largest J, i.e. days 40, 43, 61 and 64, this convergence on the unperturbed orbit is also observed. However, at J's close to the nominal, one can see that the trajectories go retrograde. This can be explained through Fig. 3.20b. One can see that the nominal trajectory, in black, goes from prograde to retrograde, and then back to prograde. Trajectories with a J close to the nominal value go retrograde, but are then not perturbed enough to return to a prograde regime. Hence, they arrive at perigee with an inclination larger than 90°. For day 40, this behavior cannot be seen from the inclination profile, as an impact region masks the retrograde perigee passings.

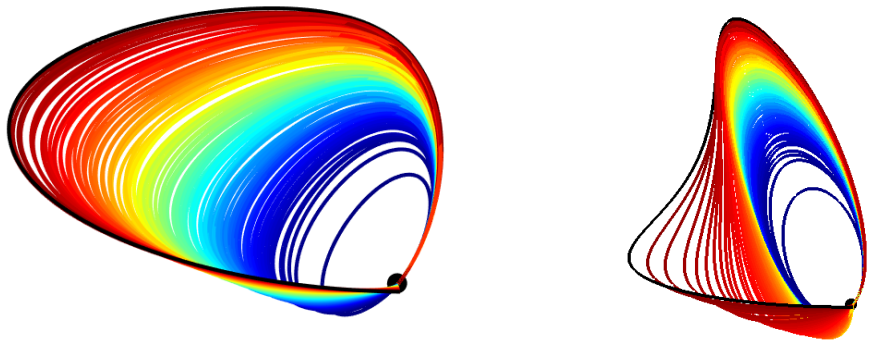

(a) Day 150: J smaller than nominal.

(b) Day 64: J smaller than nominal.

Figure 3.20: Monte Carlo analysis trajectory highlights for smaller than nominal levels of J.

Larger than nominal levels of J: For trajectories with J's larger than the nominal value, two different responses can be observed. For family 1 and 2, the inclination and perigee start increasing, after which they drastically decrease. At a certain J, they escape. This has been visualized in Fig. 3.21a. For family 3 and 4, a distinctly different response can be observed. For the

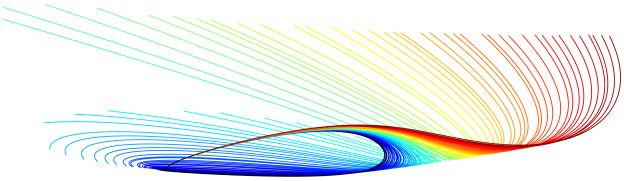

(a) Day 64: J larger than nominal.

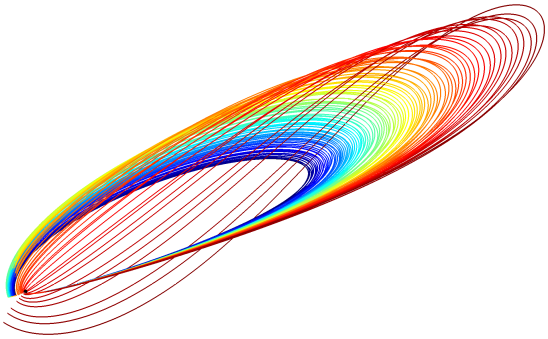

(b) Day 150: J larger than nominal, part 1.

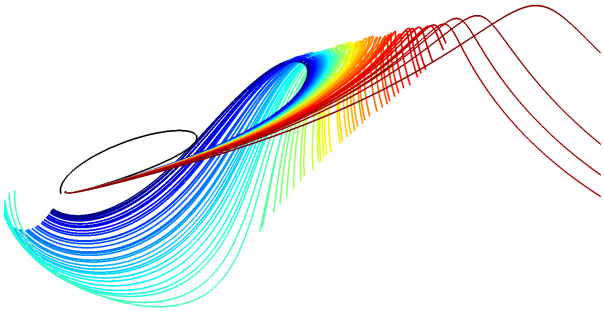

(c) Day 150: J larger than nominal, part 2.

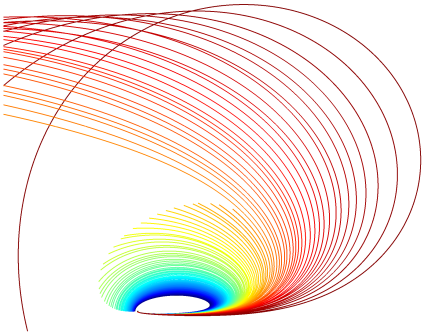

(d) Day 109: J larger than nominal.

Figure 3.21: Monte Carlo analysis trajectory highlights for larger than nominal levels of J.

three largest J trajectories, one can see that the inclination and perigee altitude start increasing. Then, the perigee altitude starts dropping again, after which an impact region occurs. After this impact region, the trajectories go retrograde and perigee starts increasing, until the trajectories escape. This process has been visualized in Fig. 3.21b and 3.21c. Note that this escape region is not observed for day 127 and day 174, as it occurs far from the nominal Jacobi constant where only a few points have been sampled. The days with the smallest J for family 3 and 4 show a very similar response. But, at an intermediate J, there is an additional escape region, visualized in Fig. 3.21d.

Conclusion Monte Carlo analysis: In summary, family 3 and 4 are more robust against perturbed initial conditions. Family 1 and 2 have regions where the trajectories go retrograde, and they have an earlier onset of escape. Finally, family 1 has a significant impact region at small levels of J. This sensitive behavior has also been observed in the validation section: family 1 and 2 have much larger errors when integrated in the DE405 ephemeris.

3.7 Conclusion

This chapter presents how third-body perturbed plane changes can be utilized to transfer from highly inclined low-earth orbits to the geostationary orbit. A method has been developed that can depart from any circular orbit with arbitrary inclination and arrive at any circular, equatorial orbit. Furthermore, the developed method can be easily extended for transfers around other sun-planet and planet-moon systems by a simple rescaling of the dynamics. The developed method has been applied to demonstrate that the geostationary orbit can be achieved for a wide range of initial inclinations, at a lower ΔV cost than traditional transfers. The required ΔV only varies slightly for different inclinations and is approximately 4.38 km/s. This technology could thus facilitate flexibility in launch site selection to launch a spacecraft into GEO. There are disadvantages to using this transfer type. First, the required ΔV is higher than for lunar gravity assist transfers. However, the designed transfers only cross the Van Allen belts once, and can have more than two launch opportunities per month. Second, they have a significantly larger TOF than the two-burn strategies. Third, they lack the bi-elliptic transfers' flexibility of picking any desired TOF; for a specific time of year, only two TOF trajectories (the designed trajectories, and their $\omega + \pi$ symmetric counterpart) are feasible without supplemental maneuvers. Fourth, not all times of year have feasible transfers. The number of days for which such transfers exist depends strongly on the initial inclination. Considering these limitations, when transfer time is subordinate to fuel savings, the newly designed trajectories can be a viable alternative to the classic transfers for high latitude launch sites. The mentioned disadvantages could be countered by relaxing some of the constraints put on the trajectory. It has been observed that a significant eccentricity increase is required for

a marginal reduction in the final inclination. Therefore, small out of plane maneuvers during the transfer should be allowed. This is expected to slightly increase the total ΔV budget, but reduce the time of flight significantly. Furthermore, this is expected to increase the number of days for which a feasible trajectory exists. This research can provide good initial guesses for those trajectories.

For highly eccentric transfers, a significant difference in response is observed between the circular and the eccentric Hill system, despite Earth's moderate heliocentric eccentricity of 0.0167. It has been shown that the true transfers in the eccentric system are very close to the solutions in the circular system, and can be found with a simple predictor-corrector scheme. For Mars' eccentricity of 0.0934, it is expected that these differences are larger. Therefore, for the remainder of the dissertation, the transfers should be designed accounting for Mars' heliocentric eccentricity.

It has been shown that missing the GEO insertion burn has severe effects. Only for a few trajectories does the natural dynamics return the spacecraft close to GEO at a next perigee. Therefore, more thought should be put into mitigating the risk of a missed GEO insertion burn. Through Lyapunov characteristic time analysis, it has been demonstrated that the trajectories do not diverge by a factor e during the nominal transfer time. However, the inclination and perigee changes from the targeted GEO values are large for the performed Monte Carlo analysis. Hence, navigational solutions must be obtained early in the transfer to identify the magnitude of the launch injection errors. A trajectory correction maneuver must then be designed and executed to correct for the error. The timing and ΔV budget that should be allocated should be studied in more detail.

Chapter 4

Deployment dynamics for multiple-spacecraft architectures around Mars

4.1 Motivation

This chapter introduces a new mission concept, enabled by the large control authority of the Sun. Missions such as ESA/JAXA's BepiColombo [37], NASA's Dawn [86] and JAXA's Hayabusa 1 and 2 [87, 88] all use solar electric propulsion (SEP) for their interplanetary transfers. SEP is characterized by high exhaust velocities, and thus a high fuel efficiency. Existing and new launch vehicles such as Delta 4, Atlas 5, Falcon 9, Falcon Heavy, New Glenn, SLS, can accelerate large payload masses to escape velocities, as shown in Table 4.1. When combining these capabilities with fuel-efficient interplanetary SEP transfers, large payloads can be sent to other planets, enabling the simultaneous transfer of multiple satellites. A multiple-satellite mission increases the science return, while cost-intensive phases of the mission are shared, such as launch, and interplanetary cruise operation and navigation. An example of this new mission paradigm is BepiColombo. This

Table 4.1: Performance of current and planned launch vehicles.

Launcher	LEO [tons]	GTO [tons]	Trans-Mars injection injection [tons]	Source
Delta IV Heavy	28.8	14.2	8	[80]
Atlas V	18.9	8.9	?	[81]
Falcon 9	22.8	8.3	4	[82]
New Glenn 2-stage	45	13	?	[83]
Falcon Heavy	64	22.2	13.6	[84]
SLS Block 2	130	?	45	[85]

mission to Mercury has two spacecraft, using a common SEP module for the interplanetary transfer and a common chemical module for Mercury orbital insertion maneuvers [37]. The two spacecraft have a common orbital plane around Mercury but different orbital altitudes. For some missions, the science return is increased when the spacecraft are injected into different orbital planes at different altitudes. This architecture requires an efficient orbital transfer strategy.

Similar to BepiColombo, the envisioned mission architecture has multiple spacecraft with a shared SEP system for the interplanetary transfer. The usage of SEP allows the heliocentric transfers to arrive with a zero relative velocity with respect to Mars. The spacecraft are then deployed one by one. In between the deployment of the spacecraft, a combination of solar perturbations and SEP changes the orbital parameters. Chapter 3 demonstrates that there are two requirements to design solar gravity transfers: high apoapse, and freedom in initial periareion orbital elements.

Traditional, chemical missions arrive at Mars on a hyperbola. A maneuver then reduces the eccentricity below one, such that the satellite is captured around Mars. The multiple spacecraft missions arrive on a parabola. An infinitesimal small maneuver reduces the eccentricity below one. Depending on the size of the maneuver, the apoareion of the capture orbit can be controlled. The larger the maneuver, the lower the apoareion. Thus, any arbitrarily high apoareion can be achieved.

Chemical missions' orbital plane of the incoming hyperbola is constrained by the relative velocity vector, $\mathbf{V}_\infty$, of the interplanetary transfer. This vector depends heavily on the chosen launch window. Transfers arriving on a parabola however, have a much larger degree of freedom in the choice of orbital elements of this parabola. This can be demonstrated by the following analysis: 25,000 different parabolas with a fixed periareion altitude of 500 km are analyzed, with uniformly sampled i, ω and Ω. These parabolas are integrated backwards in time from periareion, to the sphere of influence radius of 576,000 km. There, the heliocentric position and velocity of Mars is added to the state. For simplicity, it is assumed that Mars' orbit is circular, with radius equal to its semi-major axis. Note that the MMO reference frame is used for this system. Further note that Mars is assumed to cross the x-axis at the moment the spacecraft reaches the sphere of influence (SOI). This heliocentric state is converted into orbital elements, which are shown in Fig. 4.1. The

largest changes are 3% for a, 0.033 for e, 0.9° for i, and 0.14° for true longitude λ. ω, Ω, and ν are poorly defined on lowly inclined, near-circular orbits, and are therefore not shown. Since the heliocentric states are so similar, the heliocentric low-thrust trajectories targeting these states are also very similar. To target a certain parabola, it suffices to rendezvous with its corresponding heliocentric trajectory. Note that the patched conics approach and the ignored eccentricity of Mars' orbit introduce errors, but the general trend of this analysis holds.

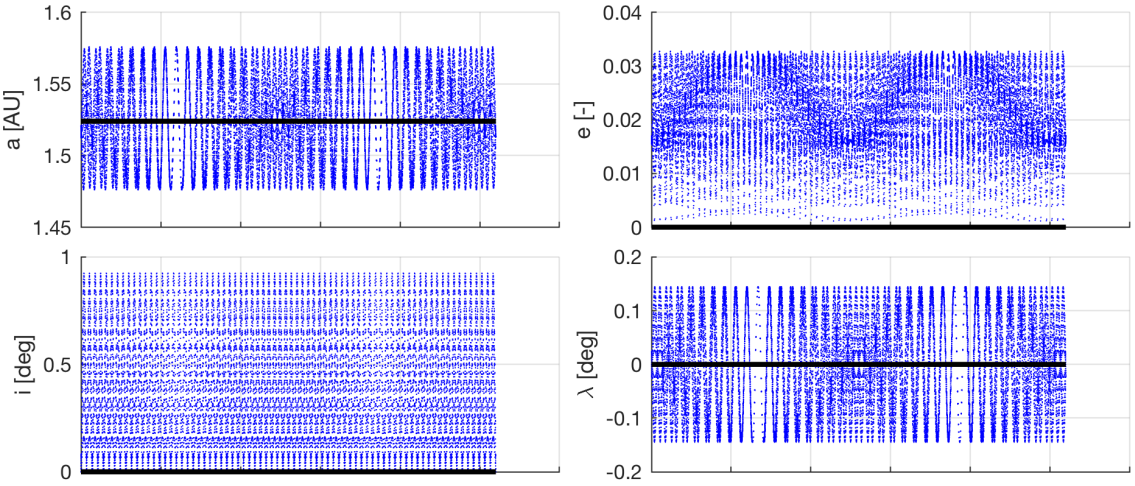

Figure 4.1: Heliocentric orbital elements at the SOI crossing for the 25,000 sampled areocentric parabolas (blue), compared to the assumed heliocentric orbital elements for Mars (black).

In conclusion, SEP transfers that rendezvous with Mars satisfy both requirements to design solar gravity driven transfers: high apoapse and freedom in initial periareion orbital elements. Therefore, solar gravity driven transfers can be used to deploy multiple spacecraft around Mars into different orbital planes at different orbital altitudes. This requires knowledge of possible transfers and an efficient way to identify them; a well-defined and easily accessed database of solutions. This chapter's goal is twofold. First, setting up the framework to create the database of transfers, on a small subset of the phase space, centered around one specific application. The small subset allows the exploration of the basic mechanisms required to construct the database, while limiting the required computational resources. Furthermore, this chapter investigates the effects of varying levels of fidelity of the database: a circular versus an eccentric model of the Martian orbit.

Second, this chapter investigates a specific application to showcase the large control authority of the Sun, warranting the interest in the research and the construction of a more extensive database. An example application is selected that is fuel intensive to execute using traditional transfer strategies. At the first periareion, one spacecraft immediately lands at a high latitude. Then, the second spacecraft follows a highly eccentric orbit that is significantly perturbed by the Sun. At the next periareion, the second spacecraft is deployed in a near-equatorial orbit with the orbital radius of Phobos or Deimos.

The structure of this chapter is as follows. First, the proposed transfer type is explained in greater detail and the assumptions on the orbits of Phobos and Deimos are explained. Second, the control authority of the Sun is determined for a simplified scenario where Mars' eccentricity is ignored. The methodology relies on the time invariance of the circular Hill problem to reduce the required number of integrations. Third, it is investigated how Mars' eccentricity of 0.0934 affects the solutions obtained in the circular Hill system. The time variance of the eccentric Hill system greatly increases the required number of integrations. This prevents from efficiently identifying all potential transfers in the eccentric scenario. Therefore, this section limits itself to computing the necessary conditions; identifying the regions of the phase space where transfers could exist.

4.2 Structure of the proposed transfer type

Figure 4.2 visualizes the transfers of interest. The transfers start at the periareion of the incoming areocentric parabola. The lack of relative velocity with Mars allows a large degree of freedom to select this parabola. At periareion one, a small maneuver reduces the eccentricity below one. For the Phobos and Deimos examples, the initial maneuver sizes are, respectively between $[12, 57]$ m/s, and $[12, 48]$ m/s. Then, the transfer follows a solar perturbed, ballistic trajectory. The transfers are designed to target a specific i_2 and $r_{p,2}$ at the next periareion. A second maneuver then circularizes the spacecraft into its final, circular orbit. In this paper, index 2 reflects the state at the second periareion before the circularization maneuver. For the Phobos and Deimos examples, the second maneuver sizes are, respectively between $[854, 866]$ m/s, and $[512, 532]$ m/s.

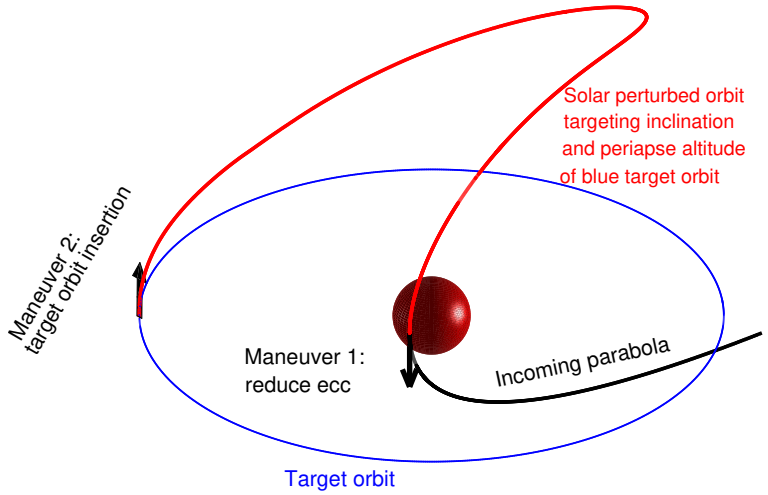

Figure 4.2: Schematic of the solar gravity driven transfer structure around Mars. Not to scale: red solar perturbed orbit has an apoapse radius $\mathcal{O}(10^5$ km), blue target orbit has a radius $\mathcal{O}(10^3$-10^4 km).

For this research, it is assumed that Phobos and Deimos are in equatorial, circular orbits with orbital radii equal to their semi-major axis of 9,376 and 23,460 km respectively. Their true longitudes are ignored. Phobos' and Deimos' orbital periods are much shorter than the time of flight of the transfers. Hence, the transfers, and thus their time of flight, can be slightly altered to achieve the desired true longitude, or an intermediate phasing orbit can be used.

4.3 Designing transfers in the circular Hill problem

In this subsection, a database of solutions is developed for a simplified scenario ignoring Mars' eccentricity. First, the advantages of using the circular Hill system for this application are explained. Second, based on preliminary results and a Pareto front method, bounds are placed on the interesting departure orbital elements space for which the results need to be computed in higher resolution. Finally, the methods to use this database for a practical application are explained.

4.3.1 Advantages of the circular Hill system

The circular Hill system is a time invariant system; every solution in the Hill system is valid for any departure time t_1. Specific departure $i_{\text{Hill},1}$ and $\Omega_{\text{Hill},1}$ will have different Ω_{MMO}, depending

on t_1. This will translate into different initial $i_{\text{MME},1}$ through Eq. 2.38. Therefore, the same Hill trajectory integration can be re-used for different $i_{\text{MME},1}$ and t_1, reducing the computational load. Furthermore, as explained in Subsubsection 2.2.2.4, the Hill problem has three spatial symmetries in the orbital element representation; the entire $(\omega_{\text{Hill}}, \Omega_{\text{Hill}})$ phase space can be represented by the [0°, 180°]×[0°, 180°] region. This reduces the computational load by a factor four.

4.3.2 Creation of the database

First, the region within the first periareion phase space is determined that gets mapped to orbital elements near the application's target elements. The phase space is sampled with a coarse resolution. The periareion Poincaré maps then compute the orbital elements at the second periareion using the circular Hill EOM in Eq. 2.22. Prior to this, some pruning of the phase space is already done:

(1) $i_{\text{Hill},1}$: this chapter's application focuses on near-polar departure orbits. Any $i_{\text{Hill},1} \in [65°, 115°]$ $(90° \pm \varepsilon)$ has one or two Ω_{Hill} / epochs that maps this $i_{\text{Hill},1}$ to $i_{\text{MME},1} = 90°$. This chapter limits its results to this $i_{\text{Hill},1}$ region.

(2) $\omega_{\text{Hill},1}$ and $\Omega_{\text{Hill},1}$: utilizing the Hill symmetries, the design space is reduced to [0°, 180°] × [0°, 180°]. Both parameters are sampled with a step size of 2.5°.

(3) $e_{\text{Hill},1}$: a lower and upper bound of 0.98 and 0.99 have been identified through empirical testing; the lower limit to realize substantial changes in the system and the upper to constrain the time of flight between periareions (TOF) to reasonable values.

(4) $r_{p,1}$: the periareion altitude is kept constant for this chapter's application at 185 km.

The coarse resolution mapping is performed on grids in ($\omega_{\text{Hill},1}$,$\Omega_{\text{Hill},1}$), computed for 11 e_1-values between 0.98 and 0.99 and for 6 $i_{\text{Hill},1}$-values between 65° and 115°. For the studied application, the transfers only target a specific $r_{p,2}$ and i_2. Therefore, a Pareto front in $r_{p,2}$ and $i_{\text{Hill},2}$ is computed for each ($\omega_{\text{Hill},1}$,$\Omega_{\text{Hill},1}$)-grid at different e_1- and $i_{\text{Hill},1}$-values. The Pareto front

bounds the reachable phase space in $r_{p,2}$ and $i_{\text{Hill},2}$, without the need to plot every individual transfer. Creating the Pareto front requires the determination of the minimum and maximum $r_{p,2}$. Then, at 150 equidistant points between the two extrema, the contour lines of transfers arriving at that $r_{p,2}$-value are identified (top left part of Fig. 4.3). Multiple contour lines are found that arrive with the target $r_{p,2}$, and should be plotted in the same color on the $r_{p,2}$-contour plot. To distinguish between the different contours, each received a different color coding, used in the bottom part of Fig. 4.3. For each of the contour lines with the correct $r_{p,2}$, the achievable $i_{\text{Hill},2}$ is determined (top right part of Fig. 4.3). The $i_{\text{Hill},2}$ on the contour lines change smoothly with no discrete jumps. Therefore, every possible $i_{\text{Hill},2}$ between the minimum and maximum observed $i_{\text{Hill},2}$ is achieved for each contour line (bottom left part of Fig. 4.3). Finally, the lack of gaps is verified in reachable

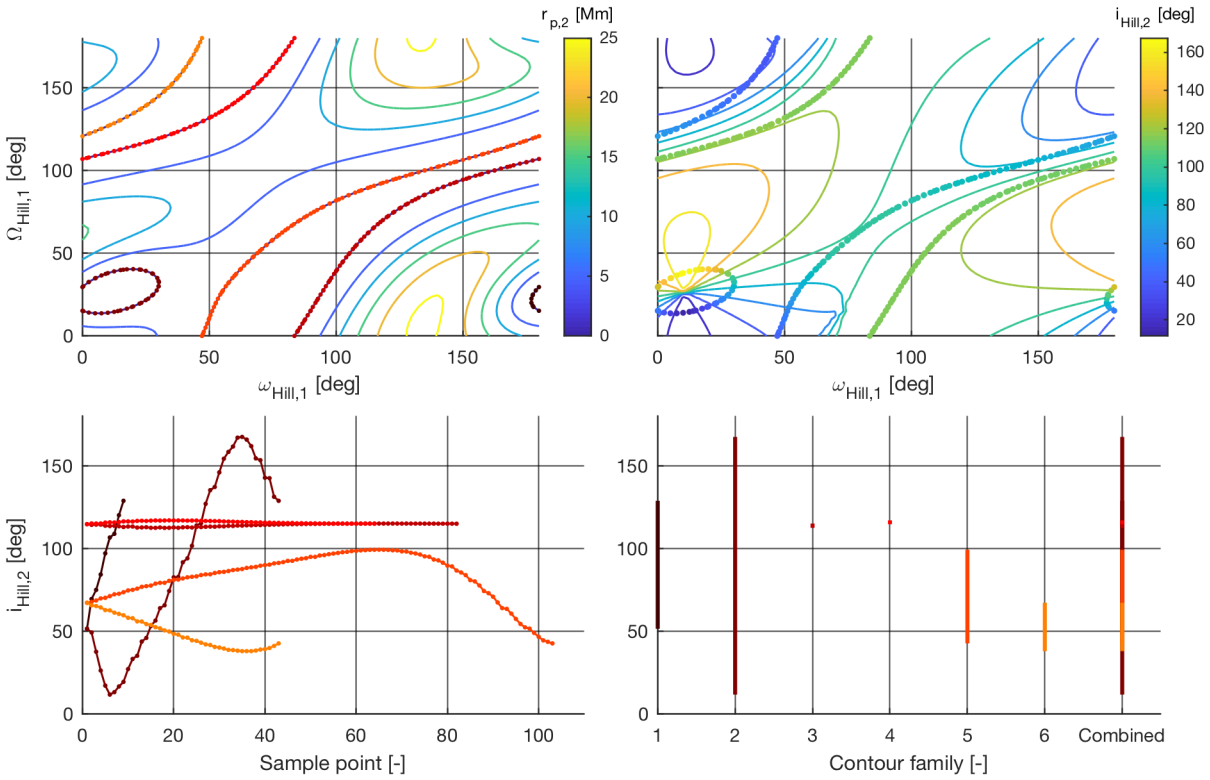

Figure 4.3: Determining the bounds for one sampled $r_{p,2}$-value of 3574.5 km within the Pareto front of $i_{\text{Hill},1}$= 115°, e_1 = 0.99. Top left: determine contours satisfying target $r_{p,2}$, indicated by different shades of red. Top right: determine $i_{\text{Hill},2}$ on the $r_{p,2}$-contours. Bottom: verify all $i_{\text{Hill},2}$ between the $i_{\text{Hill},2}$ extrema on the $r_{p,2}$-contours are achieved.

$i_{\text{Hill},2}$ between the different contour lines (bottom right part of Fig. 4.3). If this is the case, any $i_{\text{Hill},2}$ between the extrema of all contour lines is achieved for the sampled $r_{p,2}$-value. Those two boundaries are the entries of the Pareto front for the sampled $r_{p,2}$-value. This procedure is repeated for the 150 equidistant $r_{p,2}$ values, creating the Pareto front for a specific e_1 and $i_{\text{Hill},1}$ combination. An example is given in Fig. 4.4.

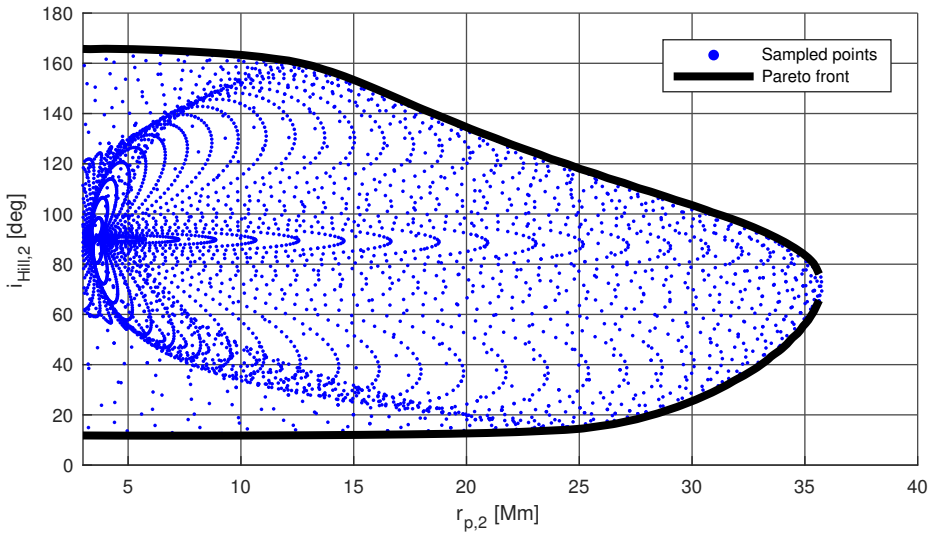

Figure 4.4: Pareto front for arrival orbital elements $r_{p,2} - i_{\text{Hill},2}$ for departure orbital elements $i_{\text{Hill},1} = 90°$, $e_1 = 0.99$ computed through a circular Hill periareion Poincaré mapping. The Pareto front successfully bounds the reachable phase space, without the need to plot every individual transfer.

The Pareto fronts are computed for 6 $i_{\text{Hill},1}$-values between 65° and 115°, for 11 e_1-values between 0.98 and 0.99 (Fig. 4.5). The Pareto fronts are used to determine the interesting region of the phase space for the two considered targets; Phobos and Deimos. The figures have vertical red lines indicating the periapse radii of Phobos and Deimos, and a horizontal black line where $i_{\text{Hill},2} = \varepsilon$. Reaching Phobos's altitude and an equatorial orbit for a specific $i_{\text{Hill},1}$ and e_1 requires the Pareto front to include the crossing between the black i and the red r_p lines of Phobos. For Phobos, the minimum e_1 varies between 0.987 and 0.988 for the $i_{\text{Hill},1} = 65°$ case and between 0.989 and 0.99 for the $i_{\text{Hill},1} = 115°$ case. These detected bounds are then used to compute the database with a more dense grid, with e_1 spacing of 0.0001 and $i_{\text{Hill},1}$ spacing of 1°.

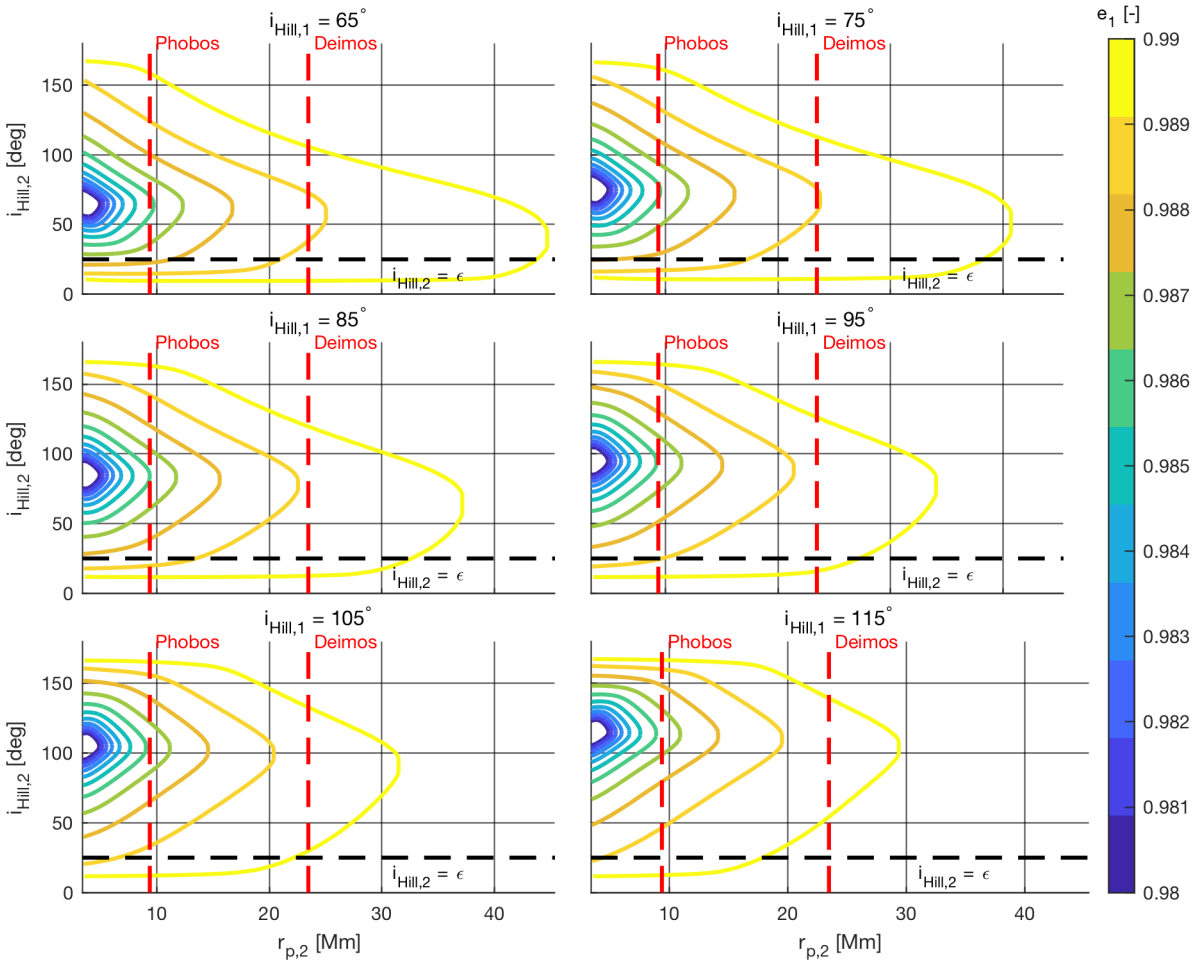

Figure 4.5: Pareto fronts in arrival orbital elements $r_{p,2}$-$i_{\text{Hill},2}$ for departure orbital elements $i_{\text{Hill},1} \in [65°, 115°]$ for $e_1 \in [0.98, 0.99]$ computed through a circular Hill periareion Poincaré mapping.

4.3.3 Usage of the database

The second goal of this section is to showcase the capabilities of solar perturbed transfers on a specific application. The method for using the database is therefore explained; how to find the correct initial time and orbital elements in the equatorial reference frame to target a specific $r_{p,2}$ and $i_{\text{MME},2}$ using the circular Hill dynamical system. This method is applied to determine the initial conditions for an orbit that arrives at the equator. The methodology consists of five steps and is summarized in Algorithm 1.

First, for all $i_{\text{Hill},1}$ and e_1-values in the database, the contour in $(\omega_{\text{Hill},1}, \Omega_{\text{Hill},1})$-space with the target $r_{p,2}$ is determined. Then, using a spline interpolation scheme, the points on this contour with $i_{\text{Hill},2} = \varepsilon$ are identified. Second, these starting conditions are numerically integrated to verify that they arrive at the correct $r_{p,2}$ and $i_{\text{Hill},2}$ to within 500 km and 1° respectively. If these accuracy requirements are satisfied, the initial Hill conditions to target a certain final orbit are known. The $r_{p,2}$ tolerance is fairly loose considering transfers with $r_{p,2}$ $\mathcal{O}(10^4$ km). For a limited resolution database, the more stringent the tolerances, the fewer solutions are found. For the chosen tolerance, all regions of the phase space with feasible transfers are identified. While the transfers do not arrive at the exact $r_{p,2}$-values, exact solutions in between the database's entries can be found. Third, the timing is determined. For the considered application, the transfers arrive at the equator, requiring $i_{\text{Hill},2} = \varepsilon$, and $\Omega_{\text{MMO},2} = 180°$ (Eq. 2.38). A specific value of $\Omega_{\text{Hill},2}$ sweeps through the entire range of $\Omega_{\text{MMO},2}$ throughout a Martian year. The Hill system solution is therefore mapped onto the equator at one specific second periareion time, t_2. The conversion between $\Omega_{\text{MMO},2}$ and $\Omega_{\text{Hill},2}$ is determined by the angular difference between the Hill and MMO frame at t_2. Using Eq. 2.46, t_2 can be found by solving:

$$\Omega_{\text{MMO},2} = \pi = \Omega_{\text{Hill},2} + \Theta_0 + N(t_2 - t_0) \tag{4.1}$$

From t_2 and the TOF obtained from the integration in the Hill system, the time of the first periareion, t_1 is computed.

$$t_1 = t_2 - TOF, \tag{4.2}$$

Fourth, the initial state in the MMO frame is computed:

$$\Omega_{\text{MMO},1} = \Omega_{\text{Hill},1} + \Theta_0 + N(t_1 - t_0) \tag{4.3}$$

$$i_{\text{MMO},1} = i_{\text{Hill},1} \tag{4.4}$$

Fifth and final, these MMO orbital elements are mapped to the initial state in the MME frame using Eq. 2.38.

In conclusion, the equatorial initial orbital elements and timing can be computed to guarantee that a trajectory reaches a target $r_{p,2}$ and $i_{\text{MME},2}$ at the next periareion. For a wide variety of

final states, the same data set can be used. Hence, the data only needs to be computed once. The initial states and times of flight for two example final orbits matching Phobos and Deimos's i_{MME} and r_p can be found in Fig. 4.6. Note that the reference epoch is when Mars is at its perihelion. Transfers with specific characteristics can be selected. For instance, if one wants to go to Phobos's i_{MME} and r_p in 80 days, and depart from a polar orbit, one can pick the transfer indicated by the red asterisk departing at day 282, with $i_{\mathrm{MME},1} = 90°$, $\omega_{\mathrm{MME},1} = 5°$, $\Omega_{\mathrm{MME}} = 196°$ and $e_1 = 0.9895$. Similarly, if one wants to target Deimos' i_{MME} and r_p and depart from the highest possible $i_{\mathrm{MME},1}$, one needs to depart at day 462, with $i_{\mathrm{MME},1} = 85°$, $\omega_{\mathrm{MME},1} = 23°$, $\Omega_{\mathrm{MME},1} = 294°$ and $e_1 = 0.99$. This transfer takes 93 days.

The solution structure depends strongly on the target orbit, but some common phenomena are observed. First, a temporal symmetry exists that can be linked to the Ω_{Hill} symmetry in the circular Hill system. Each solution for Ω_{Hill} has a corresponding solution $\Omega_{\mathrm{Hill}} + 180°$. This symmetry is mapped through Eq. 4.1 and 4.2 to create a temporal symmetry with a period of half a Martian year. Second, for a specific eccentricity and inclination, usually zero or two solutions exist in the $[0°, 180°]\times[0°, 180°]$ ($\omega_{\mathrm{MME},1}$,$\Omega_{\mathrm{MME},1}$) phase space. On a contour with the correct $r_{p,2}$, all $i_{\mathrm{Hill},2}$ are achieved between the minimum and maximum values (Fig. 4.3). If one of the extrema is different from the required $i_{\mathrm{Hill},2}$, a solution exists on both sides of the extrema. The two solutions have different arrival $\Omega_{\mathrm{Hill},2}$ and thus a different t_1. With the used sample spacing, the extrema are rarely exactly equal to the required $i_{\mathrm{Hill},2}$. The departure times where there is only one solution is therefore under sampled. This phenomenon is observed for Phobos in Fig. 4.6 near departure day 320, where both families meet. An exception is found near departure day 100 for Deimos, where for a large enough e_1 for small $i_{\mathrm{Hill},1}$, an extra set of two solutions exists. The origin of this extra family is shown in Fig. 4.7. This figure also demonstrates how, for the aforementioned reasons, there is an even number of extra solutions. The main family of solutions have very similar $\Omega_{\mathrm{Hill},1}$ and arrive with a similar $\Omega_{\mathrm{Hill},2}$. Hence, they are mapped to roughly the same t_1. The extra family exists in a different area of the phase space and is mapped to a different t_1. This region appears to lack much structure. A more systematic structure is expected for a higher resolution sampling.

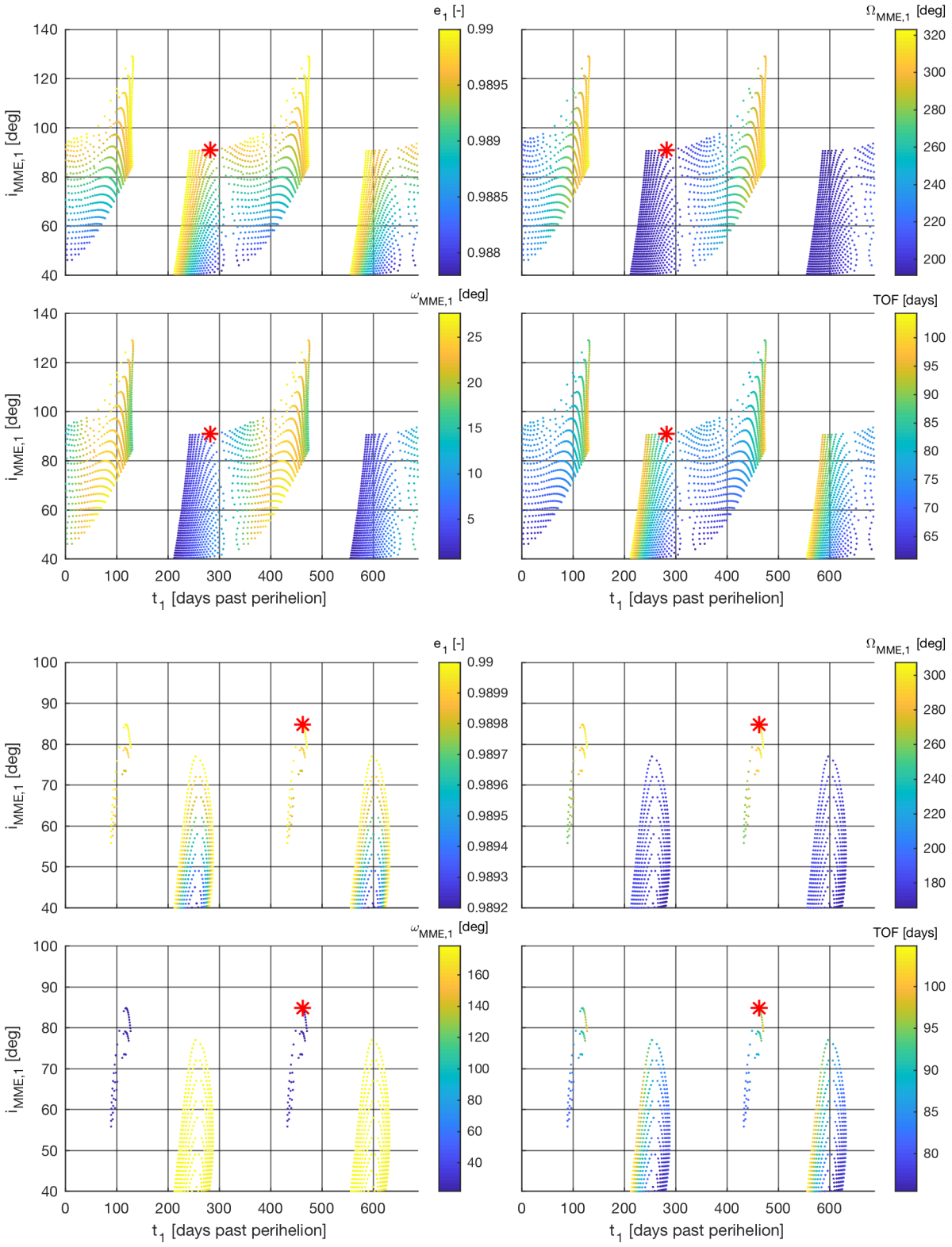

Figure 4.6: Equatorial conditions and timing of periareion one to reach Phobos' (top) and Deimos' (bottom) r_p and i_{MME} at periareion two in the circular Hill dynamical system.

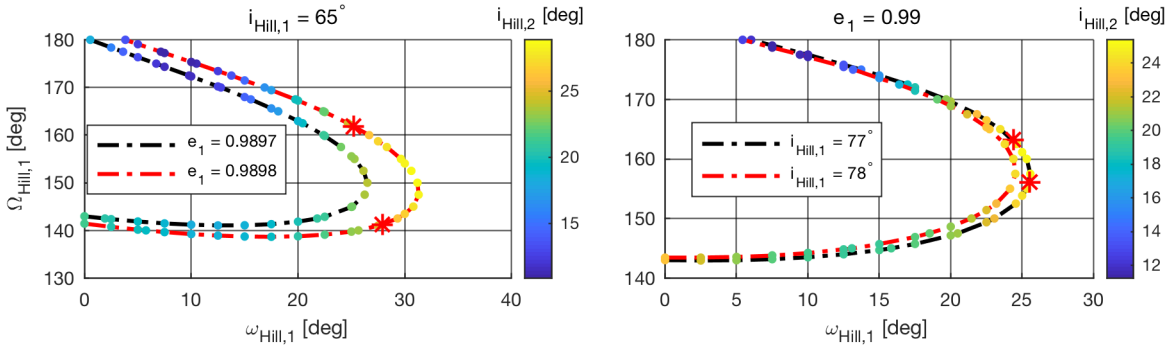

Figure 4.7: Origin of the extra family for Deimos. The $i_{\text{Hill},2}$ are shown on contours of points with $r_{p,2}$ equal to Deimos' orbital radius. Points where $i_{\text{Hill},2} = \varepsilon$ are indicated by a red asterisk. On the left figure, at $i_{\text{Hill},1} = 65°$, at $e_1 = 0.9897$, all $i_{\text{Hill},2} < \varepsilon$ and no transfers exist. At $e_1 = 0.9898$, max $i_{\text{Hill},2} > \varepsilon$ and transfers exist. On the right figure, at $e_1 = 0.99$, at $i_{\text{Hill},1} = 77°$, max $i_{\text{Hill},2} > \varepsilon$ and transfers exist. At $i_{\text{Hill},1} = 78°$, max $i_{\text{Hill},2} < \varepsilon$: no transfers exist.

4.4 Designing transfers in the eccentric Hill problem

From the validation of the LEO-GEO transfers in Section 3.5, it was concluded that Earth's eccentricity of 0.0167 introduces significant errors for transfers with very high apoapse. Mars has a higher orbital eccentricity of 0.0934. Therefore, it must be investigated how this eccentricity affects the solutions observed in the circular Hill system.

4.4.1 Effect of eccentricity on Pareto fronts

The dynamics in Eq. 2.31 are dependent on the heliocentric true anomaly of Mars and are thus time dependent. The varying Mars-Sun distance affects the reachable phase space. As an example, the Pareto fronts for $i_{\text{Hill},1} = 65°$ and $e_1 = 0.99$ are computed for different values of ν_M at periareion one (Fig. 4.8). These fronts are computed using numerically integrated periareion Poincaré maps in the eccentric Hill system. $\nu_{M,1}$ has a large impact on the reachable phase space at periareion two and its effect cannot be ignored. For this example, $\nu_{M,1}$-values of roughly 340° and 160° achieve the largest and smallest phase spaces, respectively. In other words, the transfers that depart when Mars is at perihelion do not have the largest reachable phase space, nor do the transfers that depart when Mars is at aphelion have the smallest phase space. Because the trajectory

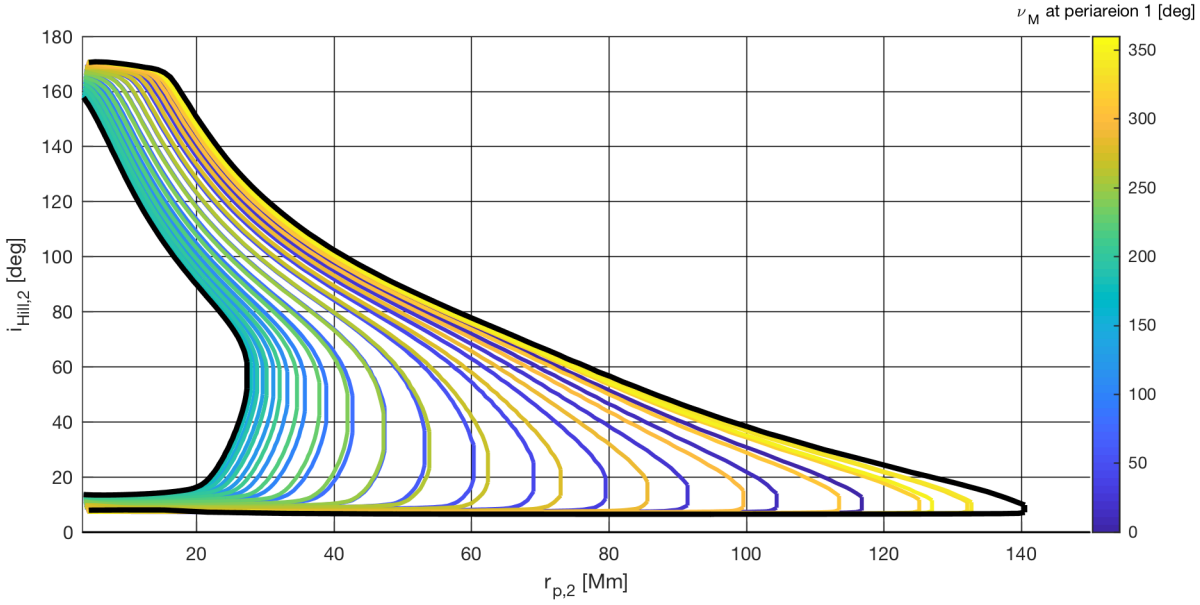

Figure 4.8: Effect of ν_M at the start of the transfer on the reachable phase space for the eccentric Hill dynamical system. Apoareion scaled circular Hill bounds are shown in black.

is perturbed most near its apoareion, it is hypothesized that the largest and smallest phase space are achieved when the spacecraft's apoareion passage coincides with Mars being respectively at perihelion and aphelion. Figure 4.9 confirms this hypothesis. The ν_M at apoareion for which the phase space is largest and smallest are thus constant, in contrast to the transfer dependent extrema of $\nu_{M,1}$. Using the eccentric Hill system to identify the bounds of the phase space is thus impractical. Using different scaled versions of the circular Hill system at Mars' aphelion and at perihelion is more straightforward. The different solar distances affect the scaling for the dynamics of the circular Hill system in Eq. 2.20. Figure 4.9 shows that these circular Hill systems place accurate bounds on the reachable phase space in periapse and inclination (black lines in Figs. 4.8 and 4.9). Furthermore, the circular Hill problems approximate the eccentric arrival $\omega_{\text{Hill},2}$, $\Omega_{\text{Hill},2}$ and TOF reasonably well, as can be seen from Fig. 4.10.

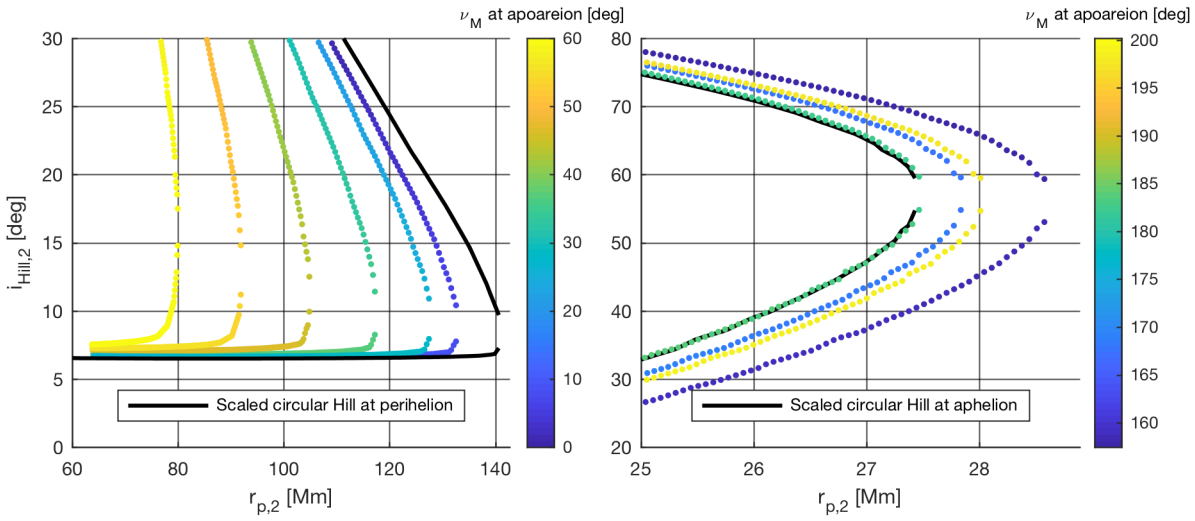

Figure 4.9: Reachable state in function of ν_M when SC is at apoareion with scaled circular Hill bounds shown in black. Left: largest phase space region. Right: smallest phase space region.

4.4.2 Determine the bounds

Two scaled circular Hill problems give a good indication of the minimum and maximum achievable phase space at periareion two. Pareto fronts are computed for six different $i_{\text{Hill},1}$-values for five e_1-values (Fig. 4.11). The Pareto fronts are used to determine the interesting region of the phase space. Unlike the circular problem, this must be done for each departure time. For computational reasons, a finer grid is only computed for departure times when Mars is near aphelion, perihelion or the true anomaly for which the Mars-Sun distance is equal to Mars' semi-major axis. The results of these runs are summarized in Fig. 4.12, which shows the minimum e_1, with a 0.0001 resolution, for which one can achieve a certain $r_{p,2}$ and arrive with $i_{\text{Hill},2} = \varepsilon$. Note that Deimos can not be reached at aphelion. In Fig. 4.11, it appears that at aphelion, with $i_{\text{Hill},1} = 65°$ and $e_1 = 0.99$, the Pareto front touches the crossing of the lines indicating Deimos and $i_{\text{Hill},1} = \epsilon$. In reality, the Pareto front is just to the left and above this line crossing. Further note that the transfers are not guaranteed to arrive at the equator. Unlike the circular Hill system, the found solutions are time dependent. Hence, the arrival time cannot be changed to enforce arriving at an equatorial orbit. The arrival Ω_{Hill} and the arrival time must be such that $\Omega_{\text{MMO},2} = 180°$.

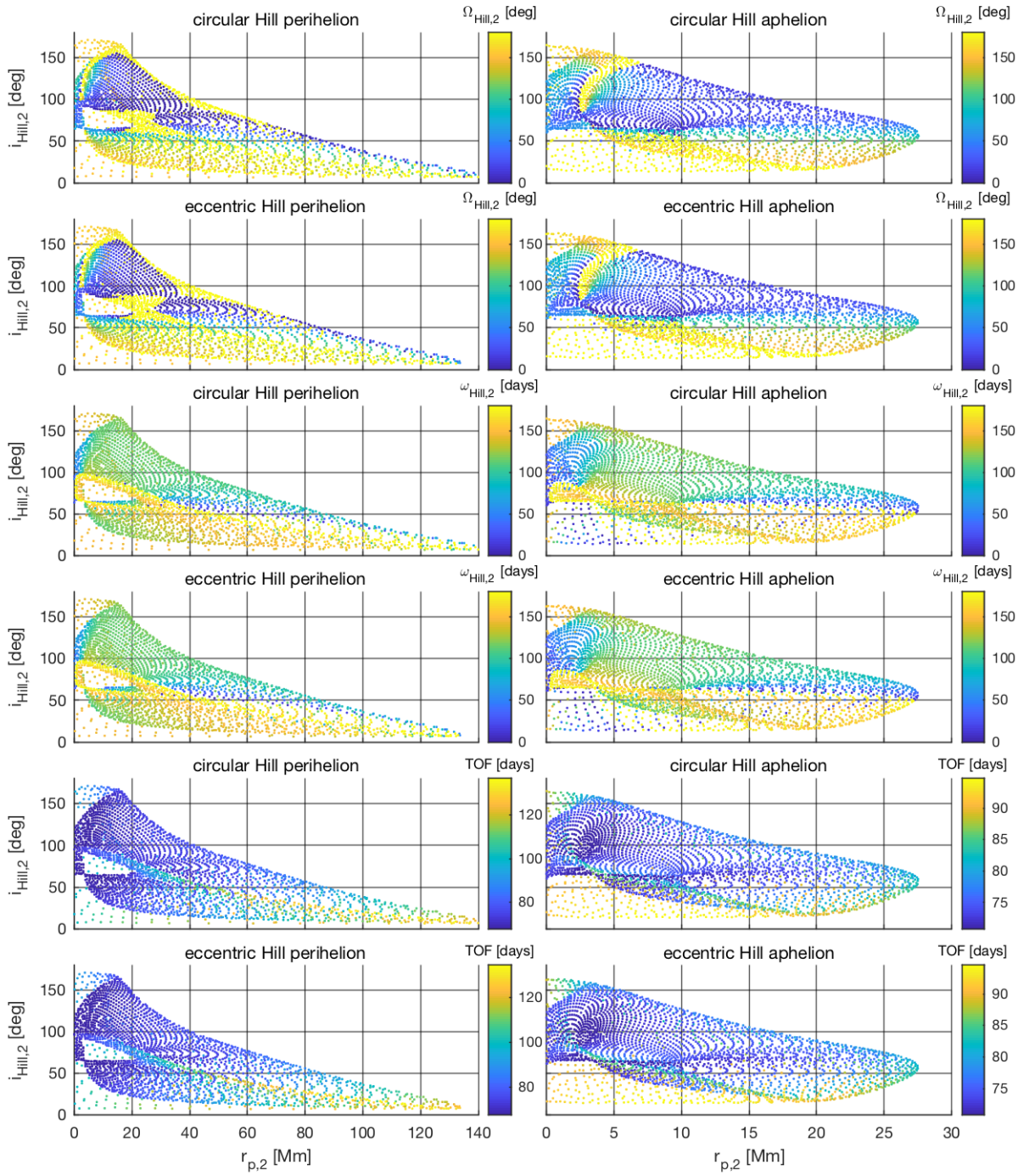

Figure 4.10: Comparison between the response of the second periareion for initial orbital elements $e_1 = 0.99$ and $i_{\text{Hill},1} = 65°$ integrated to the next periareion in the scaled circular Hill approximation and eccentric Hill system: $\Omega_{\text{Hill},2}$ (top), $\omega_{\text{Hill},2}$ (middle) and TOF (bottom) when Mars is at perihelion (left) and aphelion (right).

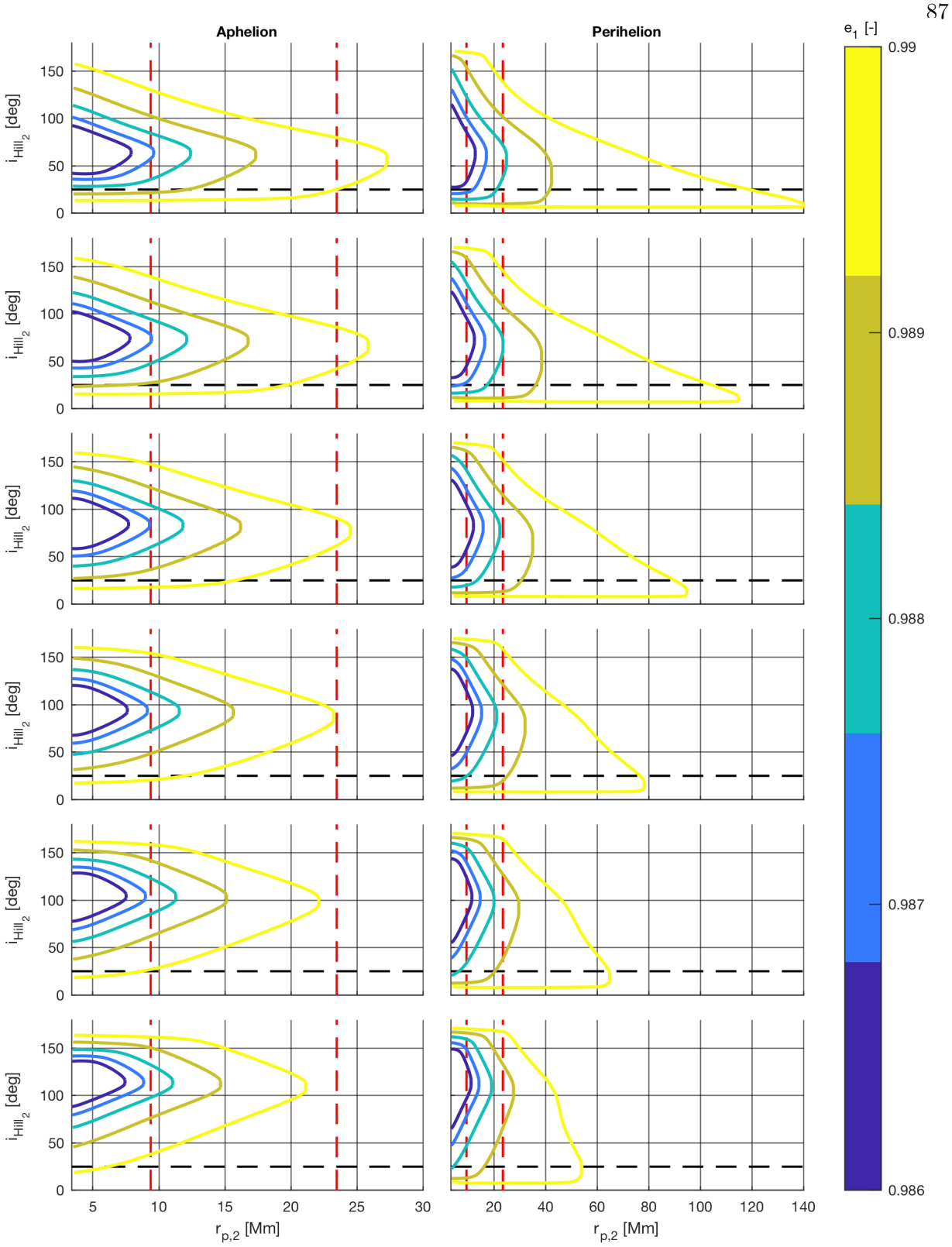

Figure 4.11: Pareto fronts for the scaled circular Hill systems at Mars' aphelion (left) and perihelion (right). Pareto fronts are computed using the response at periareion 2 in $r_{p,2}$ and $i_{\text{Hill},2}$ for initial orbital elements at periareion 1, $i_{\text{Hill},1} \in [65°, 115°]$ for e_1 between 0.986 and 0.99. The red horizontal lines indicate Phobos and Deimos. The black vertical line indicates $i_{\text{Hill},2} = \epsilon$.

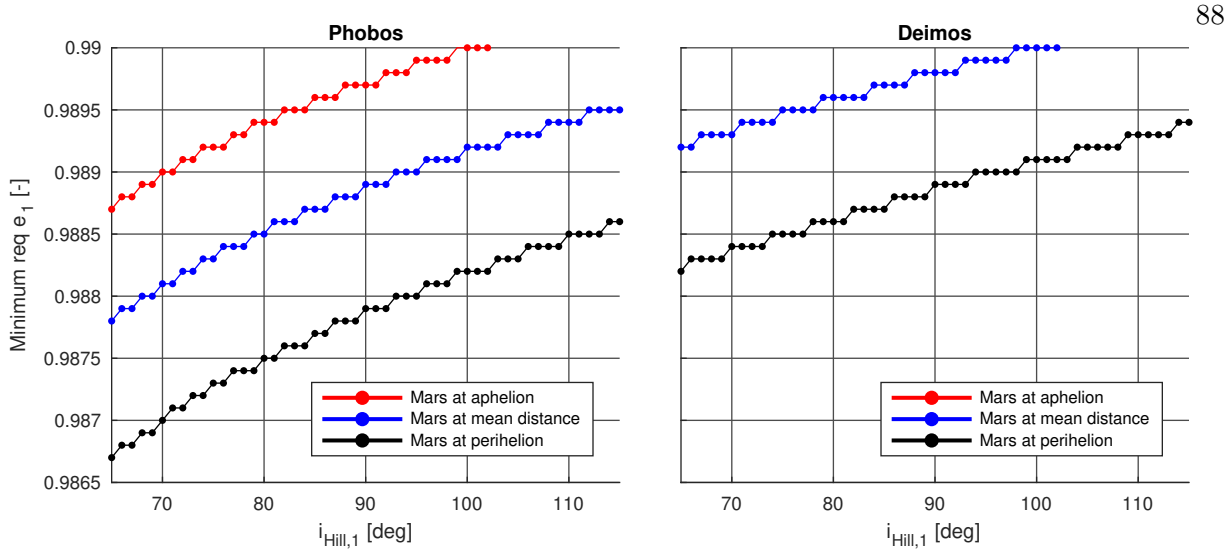

Figure 4.12: Minimum required e_1 to satisfy the necessary condition to reach the equator: $i_{\text{Hill},2} = \varepsilon$ at different target periapse radii $r_{p,2}$: Phobos (left) and Deimos (right), at different initial inclinations $i_{\text{Hill},1}$, and for different heliocentric ν_M when the transfers pass through apoareion.

Therefore, the bounds presented here are necessary conditions. They can be used by a mission designer; for every departure time of interest, the entire phase space, bounded by this analysis, must be computed and analyzed.

4.5 Conclusion

In this chapter, the general mission architecture for the deployment of multiple satellites around Mars is explained. Furthermore, several techniques to develop a database of solutions are discussed. For the circular Hill problem, generating a database in transfers in the Hill reference frame allows the re-use of integrated trajectories for different initial inclinations and different departure times. For the eccentric Hill problem, the time variance of the dynamics prevents from re-using transfers. This drastically increases the required number of integrations to create the database. This chapter therefore limits itself to the development of a method to compute the necessary conditions. The next chapter investigates methods to mitigate the computational costs associated with the high required number of integrations in the eccentric system.

Chapter 5

Artificial neural networks

5.1 Motivation

In the previous chapter, it is demonstrated that the time variance in the eccentric Hill system increases the required number of integrations. This prevents from creating the entire database to identify the transfers of interest around Mars. In this chapter, it is demonstrated how artificial neural networks can be used to reduce the required number of integrations, while maintaining sufficient accuracy for preliminary studies.

First, an artificial neural network architecture is developed for the small area of the phase space considered in Chapter 4. Second, it will be shown how this architecture can be expanded to encompass a large area of the phase space. This will be done for forward and backwards Poincaré maps predicting the next and previous periareions respectively. Finally, an example is given on the usage of artificial neural networks for a different application; finding heteroclinic connections in the CRTBP.

5.2 Feasibility study for small section of phase space

This section explains a second method to create the database; machine learning techniques. Many machine learning approaches are available, including artificial neural networks, random forests, and support vector machines. This field of astrodynamics has not developed a lot of experience using one or another, but it is clear that this astrodynamics application yield nonlinear state spaces, wrapped angular units, and other bifurcation challenges. This dissertation uses ANN. The main reasons are: ease of implementation, good generalization performance on problems with non-linear relationships [89], ability to work on problems with locally very non-linear areas, such as bifurcations [90], and the ability to handle any form of input distributions [91] and level of correlation between input parameters [89]. ANN's biggest disadvantage is the sensitivity to hyper-parameters, such as number of neurons and number of hidden layers [92]. A balance must be found between ANN with insufficient neurons that miss trends, and ANN with too many nodes that suffer from over-fitting [93]. The author does not claim other machine learning methods do not work on this specific application, nor does the author make claims on ANN outperforming those other methods. This dissertation demonstrates the application of a machine learning technique, ANN, to a difficult problem in mission design. Given the demonstrated ability to carry out this analysis using a machine learning technique can motivate future studies of what the most efficient application of these methods would be.

First, ANN are developed for the scenario where Mars' eccentricity is ignored. This development functions as a testbed to establish the main ANN design choices. Second, the lessons learned from the circular case are used to develop ANN for the eccentric scenario. Third, example transfers are identified in the eccentric system. Finally, those transfers are validated in higher fidelity force models.

5.2.1 Artificial neural network for the circular approximation

In Subsection 4.3, the circular Hill problem database is entirely constructed using numerical integration of a large set of initial conditions. In the next paragraphs, the methodology is explained to construct the same database, using a much smaller set of integrated trajectories to train ANN. The goal of the ANN is to predict the mapping from the orbital elements at periareion 1 to the orbital elements at periareion 2 with sufficient accuracy. This allows the construction of a finely gridded database relating the specified first periareion inputs to conditions at the second periareion. Then, this populated dataset is post-processed to identify the input conditions at periareion 1 that result in desired output conditions at periareion 2. First, the required input and output parameters are listed. Second, the required training data is explained; i.e., the data created by numerical integration of the Hill trajectories. Third, the utilized data pre-processing is described. This allows faster training of the ANN and a larger accuracy. Fourth, the design of the ANN is explained in more detail. Fifth, the ANN's accuracy is validated using a Monte Carlo analysis. Finally, it is shown how the designed neural networks can be used to reconstruct the database of solutions developed in Subsection 4.3.

5.2.1.1 Structure of the inputs and outputs

The input should fully determine the initial periapse state. The $r_{p,1}$ parameter is kept constant since all orbits are assumed to depart from the same altitude of 185 km. The input parameters are thus limited to $r_{a,1}$, $i_{\text{Hill},1}$, $\omega_{\text{Hill},1}$ and $\Omega_{\text{Hill},1}$. For the application of interest, Algorithm 1 requires knowledge of $i_{\text{Hill},2}$, $\Omega_{\text{Hill},2}$, $r_{p,2}$ and TOF. Note that $r_{a,1}$ is used as an input parameter, and not e_1. For a uniform sampling in $r_{a,1}$, the $r_{p,2}$ and TOF output parameters change more linearly than with a uniform sampling in e_1, facilitating learning.

5.2.1.2 Training data creation and pre-processing

The database in Subsection 4.3 was sampled with grids in $(\omega_{\text{Hill},1} \times \Omega_{\text{Hill},1}) \in ([0°, 180°] \times [0°, 180°])$ with 2.5° resolution for $i_{\text{Hill},1} \in [65°, 115°]$ with a 1° resolution and for $e_1 \in [0.987, 0.99]$

with a 0.0001 resolution. In total, 8,425,149 numerical integrations were performed. The ANN method functions with only a fraction of that data: grids in $(\omega_{\text{Hill},1} \times \Omega_{\text{Hill},1}) \in ([0°, 180°] \times [0°, 180°])$ with 5° resolution for $i_{\text{Hill},1} \in [65°, 115°]$ with a 10° resolution and for $r_{a,1} \in [560000, 720000]$ with a 20,000 km resolution. In total, 73,926 numerical integrations are required; less than one percent of the data requirement of the first approach.

The training of a neural network is a minimization problem. Thus, several pre-processing techniques for optimization can be used. First, all input and output parameters are scaled to $[-1, 1]$ using a feature scaling method:

$$x_{\text{scaled}} = 2\frac{x - \min(x)}{\max(x) - \min(x)} - 1 \tag{5.1}$$

Second, an artificial bifurcation in $\Omega_{\text{Hill},2}$ is observed at the $360° - 0°$ boundary. The ANN incorrectly identifies a large error when the predicted and true value are on opposites sides of this boundary. Furthermore, when $\Omega_{\text{Hill},2}$ changes from 360 to 0°, the ANN must capture a very strong bifurcation. An example can be seen in Fig. 5.1. For a constant $r_{p,1}$, $r_{a,1}$, and i_1, $\Omega_{\text{Hill},2}$ is shown in function of $\omega_{\text{Hill},1}$ and $\Omega_{\text{Hill},1}$. In the two red regions, $\Omega_{\text{Hill},2}$ changes from the fourth to the first quadrant and strong gradients exist. These strong changes are difficult to capture using ANN. This bifurcation is

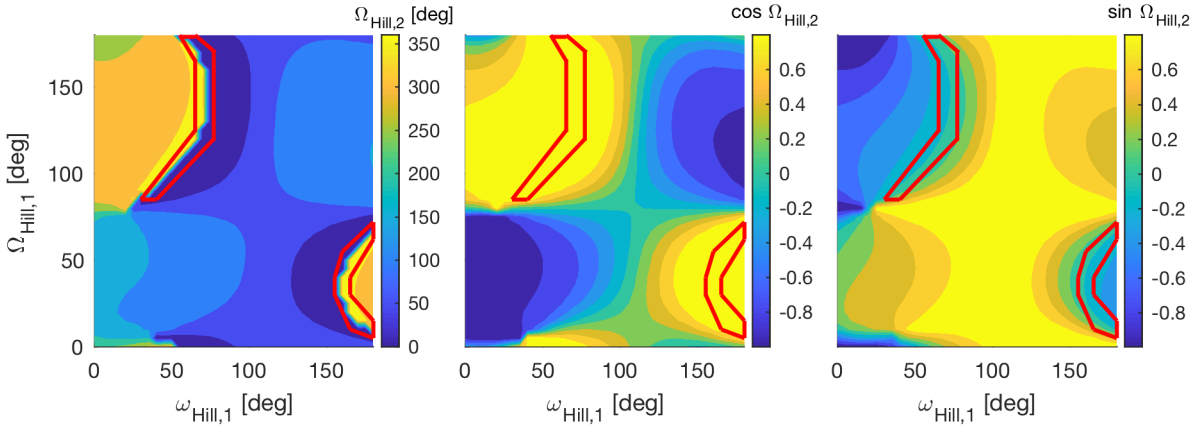

Figure 5.1: Example of how an artificial angular bifurcation can be resolved by splitting the angle in its cosine and sine components. In the regions indicated in red, the angle passes through the 360° - 0° region, introducing strong gradients on the contours. Those are not present in the cosine and sine components.

removed by splitting up $\Omega_{\text{Hill},2}$ into two output parameters: $\cos\Omega_{\text{Hill},2}$ and $\sin\Omega_{\text{Hill},2}$. The predicted sine and cosine terms are then used to compute the $\Omega_{\text{Hill},2}$ value using an arctangent operator. This extra output parameter increases training time. An attempt to avoid this extra parameter merges $i_{\text{Hill},2}$ and $\Omega_{\text{Hill},2}$ into the h and k modified equinoctial elements [94]:

$$h = \tan\frac{i}{2}\cos\Omega \qquad\qquad k = \tan\frac{i}{2}\sin\Omega \tag{5.2}$$

However, the extraction of the individual, classical orbital elements from the predicted modified equinoctial elements proves difficult. It is useful to track the errors produced using the ANN predictions of the h and k modified equinoctial elements. These errors are non-linearly propagated to the errors in $i_{\text{Hill},2}$ and $\Omega_{\text{Hill},2}$. For the studied example, the transfers arrive at the second periareion with $i_{\text{Hill},2} \in [15°, 150°]$ and $\Omega_{\text{Hill},2} \in [0°, 360°]$. These values translate in h and $k \in [-2.8, 2.8]$ (Fig. 5.2). For a 1% accuracy in predicted h and k, these errors in h and k propagate to maximum errors in $i_{\text{Hill},2}$ and $\Omega_{\text{Hill},2}$ of 9.0° and 36.98°, respectively. Typical errors are less, but these worst-case errors must be understood. Therefore, the increased accuracy that comes with the extra parameter is decided to outweigh the additional training costs.

5.2.1.3 ANN design

A multi-layer ANN can capture any data perfectly, given it has enough layers and neurons [95]. In practice, the accuracy of the model is traded-off against the required data to train the model, and the computational time required for training. More hidden layers and more neurons usually translate into higher required training times. In this subsection, the design choices for the ANN architecture are explained. The author does not claim that the choices made are necessarily the best for this system in terms of obtained accuracy and computational performance. They do however provide sufficient levels of accuracy and acceptable training times.

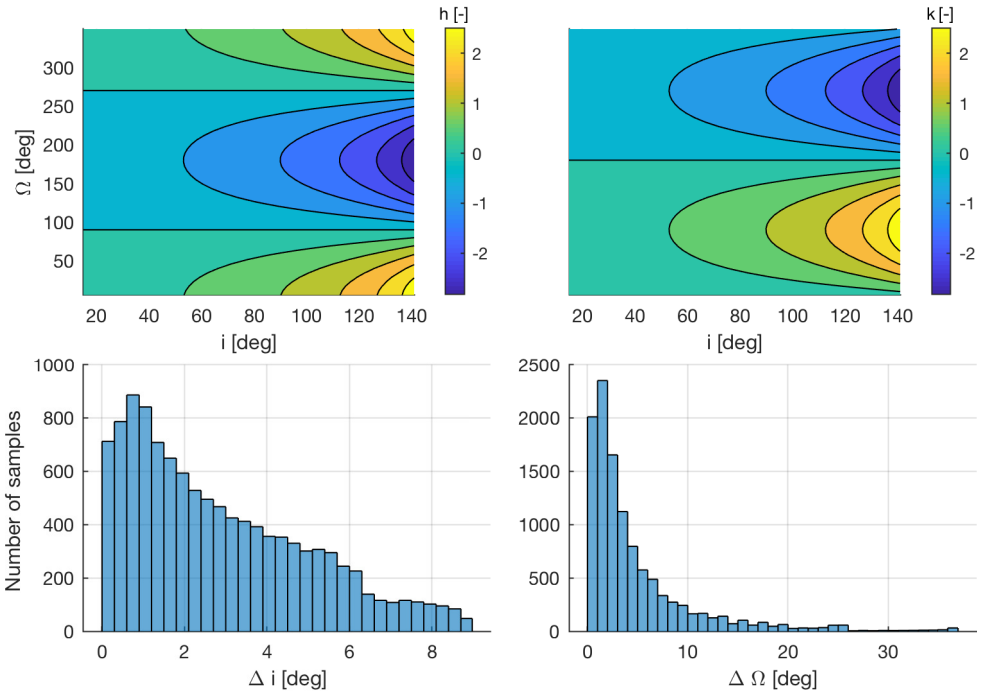

Figure 5.2: Visualization of the h and k modified equinoctial elements, in function of i and Ω. For each (i, Ω) combination, an error in h and k of 1% is added. These erroneous h and k parameters are converted back to i and Ω. The histograms show the resulting errors for i and Ω.

From Fig. 3.2, it is known that the input parameters map to the outputs via a non-linear function. Hence, a two-layer input-output ANN does not work for this application. At least one hidden layer is required. For regression problems, in- and output layers have the identity function as the activation function; i.e., the output of the input- and output layer neurons are identical to their input. For the hidden layer, some examples of commonly used activation functions are a standard logistic function and a hyperbolic tangent function [70]. For this research, the hyperbolic tangent function is selected as it is centered around the mean at the origin, and its output $\in [-1, 1]$. This mapping guarantees that the input for the next layer is also bounded by $[-1, 1]$ [70]. Furthermore, the hyperbolic tangent provides stronger gradients than the standard logistic function. Hence, the training with hyperbolic tangent functions often converge faster [70, 96].

Second, a choice is made on the cost function and the back propagation algorithm used for training. This problem can be categorized as a small-to-medium sized machine learning problem.

For such problems, the Levenberg-Marquardt algorithm [97, 98] with a mean squared error (MSE) cost function [70] is commonly used, as it is fast and accurate [99]. This back propagation method relies on approximating the Hessian to provide second order derivatives. The use of the Hessian improves the convergence rate, but its computational complexity grows with $\mathcal{O}(W^3)$ [70], with W the total number of weights. This cubic growth explains why Levenberg-Marquardt is only used for small-to-medium sized problems.

Third, the training data is subdivided into training, validation and testing sets. The data is randomly assigned to these sets to avoid clustering. The optimal training, validation and test ratios are problem specific, and depend on the size of the total data set. For this specific research, decent generalization performance is achieved for 70, 15 and 15% for the training, validation and testing sets, respectively.

Fourth, the number of neural networks that need to be trained is determined. Two different architectures exist: an architecture where all output parameters are predicted in a single ANN, and an architecture where each output parameter has its own dedicated ANN. The former is commonly known as multi-task learning [100]. Within multi-task learning, the back-propagation procedure updates the weights and biases to enable the identification of common traits, improving generalization performance for "related tasks" [100]. A comparison between both architectures is conducted on a small dataset. For this analysis, $r_{a,2}$, $\cos\omega_{\text{Hill},2}$, and $\sin\omega_{\text{Hill},2}$ are added to the list of outputs. While these outputs may not be of interest for the goals of this investigation, they are required later in the dissertation, and may be important during training. Their addition might allow the ANN to learn the underlying relationships between the inputs and outputs better, and thus potentially make more accurate predictions. This analysis has been performed using the MATLAB Statistics and Machine Learning Toolbox 11.2 [101] on an Intel i7-4870HQ @ 2.50GHz CPU. The results of this analysis are shown in Table 5.1. The shown MSE accuracies are the non-dimensional values for the independent test set. For the multiple ANN architecture, different numbers of neurons per hidden layer are used for different output parameters, indicated by the footnote symbols. The multi-task ANN architecture has only one ANN. Hence, the number of

Table 5.1: Comparison between the training time and accuracy performance for a multi-task architecture versus a multiple ANN architecture.

Output parameter	Multiple ANN MSE	Multi-task MSE*	Multi-task MSE†	Multi-task MSE‡
$r_{p,2}$	*6.7e-6	7.3e-4	1.4e-4	4.6e-5
$r_{a,2}$	*1.8e-7	6.6e-5	1.5e-5	4.4e-6
TOF	*4.2e-7	3.9e-4	1.4e-6	9.6e-5
$i_{\text{Hill},2}$	†3.4e-5	1.3e-3	3.1e-4	1.3e-4
$\cos\Omega_{\text{Hill},2}$	†5.0e-5	1.5e-3	3.4e-4	1.6e-4
$\sin\Omega_{\text{Hill},2}$	†5.2e-5	8.1e-4	3.2e-4	1.6e-4
$\cos\omega_{\text{Hill},2}$	†5.4e-5	1.1e-3	2.6e-4	1.1e-4
$\sin\omega_{\text{Hill},2}$	†5.2e-5	1.2e-3	4.2e-4	1.5e-4
Training [min]	67.5	41.3	116.5	602.3

*2 hidden layers, 15 neurons per layer.
†2 hidden layers, 25 neurons per layer.
‡2 hidden layers, 35 neurons per layer.

neurons per hidden layer for all predicted parameters within this ANN are equal, indicated by the footnote symbols. The multiple ANN architecture clearly outperforms the multi-task architecture for this application, both in accuracy and in training time. Even with ninefold training time, the accuracy of the multi-task architecture is worse than the multiple ANN architecture. It is observed that the angular outputs have a more non-linear response near bifurcations than the other three parameters. Therefore, they require more neurons to capture these effects. This incompatibility between the different tasks explains the better performance of the multiple ANN architecture for this problem. While these results do not necessarily carry over to a scenario with more data, it was decided to implement the multiple ANN architecture throughout this dissertation, unless otherwise noted.

Finally, the number of hidden layers and the number of neurons in each hidden layer is determined. A trade-off between accuracy (cost function) and required training time is performed. As a threshold, the 99 percentile prediction errors on an independent validation set should be order of magnitude 1%. Figure 5.3 shows an example of the trade-off for the $r_{p,2}$ output ANN. This analysis has been performed using the MATLAB Statistics and Machine Learning Toolbox 11.2

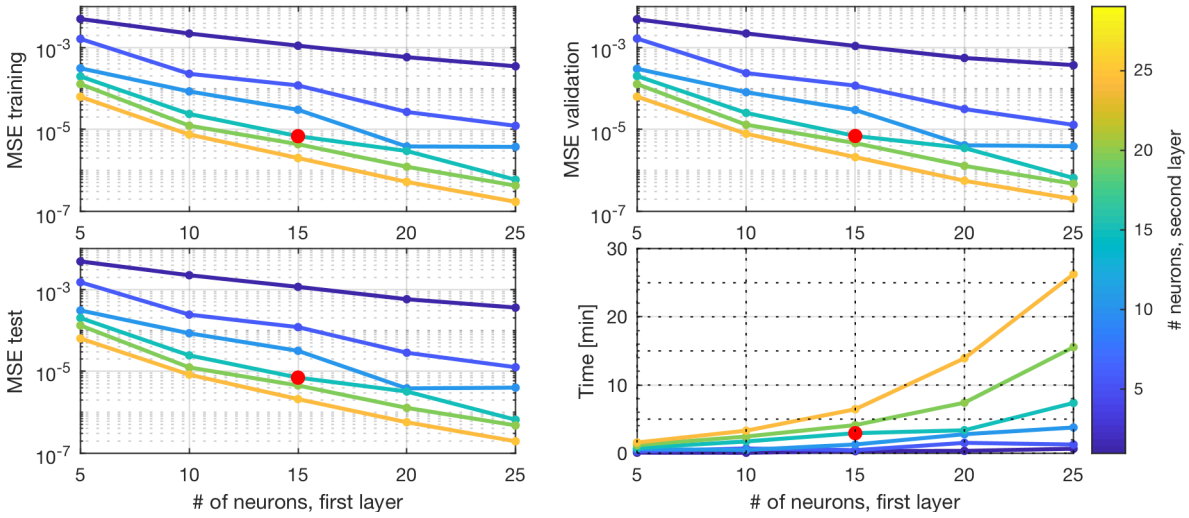

Figure 5.3: Hidden layers and neurons architecture trade-off for $r_{p,2}$. The MSE for the training, validation and test set are shown, along with the training time for different number of neurons and different number of layers.

[101] on an Intel i7-4870HQ @ 2.50GHz CPU. Note that the depicted mean squared errors are non-dimensionalized. The darkest blue line represents a single hidden layer architecture, the other lines a two-hidden layer architecture. The single hidden layer's accuracy tapers off. Therefore, a second hidden layer is required. The selected architecture is a 15 by 15 neuron, two hidden layer architecture, indicated by the red dot. This architecture provides a good balance between achieved accuracy and required training time. The almost identical accuracies between the training, validation and test data sets demonstrate that over fitting is most likely not occurring in this ANN. The ANN should therefore work well on data outside of the training data. For the TOF ANN, this architecture provides satisfactory results. However, the ANN for $i_{\text{Hill},2}$, $\cos\Omega_{\text{Hill},2}$ and $\sin\Omega_{\text{Hill},2}$ provide insufficient accuracy. When investigating these outputs, they display strong bifurcations in the phase space. Those are difficult to capture and require more neurons. A similar neuron size and hidden layers trade-off is performed for the $i_{\text{Hill},2}$ ANN, depicted in Fig. 5.4. From this analysis, a two-hidden layer, 25 by 25 neuron neural network is selected. This 25 by 25 architecture also provides satisfactory results for $\cos\Omega_{\text{Hill},2}$ and $\sin\Omega_{\text{Hill},2}$.

In conclusion, a schematic representation of the $i_{\text{Hill},2}$ ANN architecture is shown in Fig. 5.5. Note that not all neurons in the hidden layers are displayed, for figure clarity reasons.

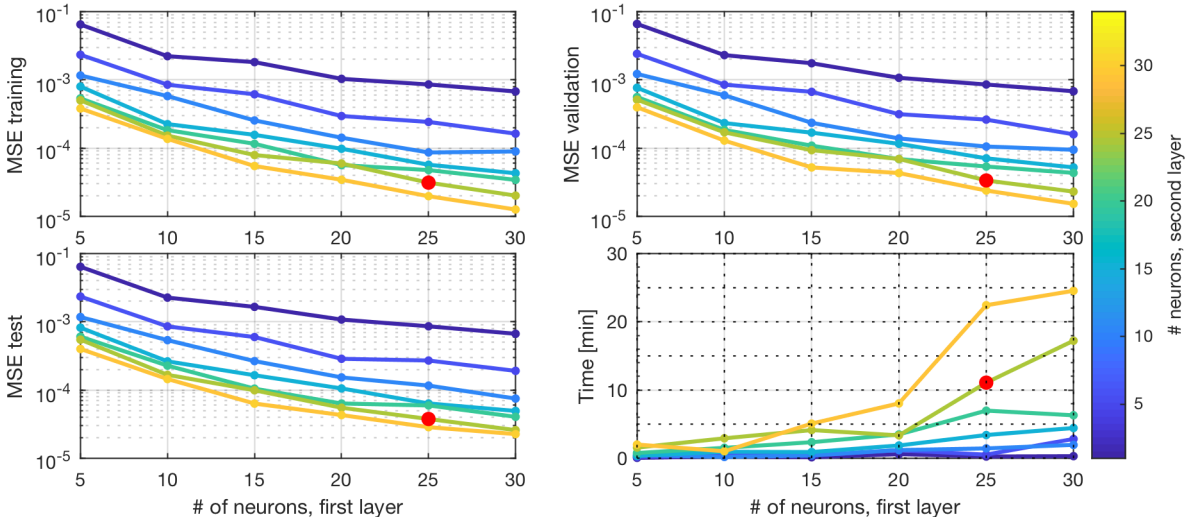

Figure 5.4: Hidden layers and neurons architecture trade-off for $i_{\text{Hill},2}$. The MSE for the training, validation and test set are shown, along with the training time for different number of neurons and different number of layers.

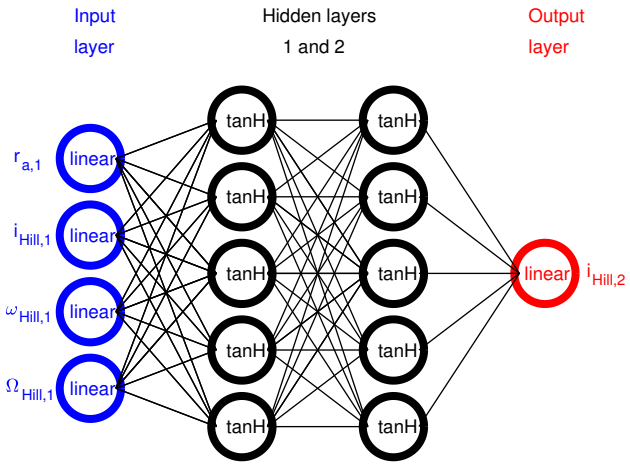

Figure 5.5: Example of the designed neural network architecture, mapping the Hill orbital elements at the first periareion to the Hill inclination at the second periareion. Note that not all neurons in the hidden layers are displayed.

5.2.1.4 ANN training results and validation

Table 5.2 shows the training results for the different neural networks. Both the non dimensionalized MSE values and the dimensional standard deviation 1σ are listed. All ANN have similar performance over the training, testing and validation data, indicating over fitting is not occurring. The ANN predictions outside of the training data should be accurate. The accuracy is tested

Table 5.2: ANN training results for the circular Hill system.

Output parameter	Hidden layer neuron sizes	Non-dimensional MSE , dimensional 1σ Training	Validation	Test	Units	Training time [min]
$r_{p,2}$	15x15	6.1e-6 , 122	6.3e-6 , 123	6.7e-6 , 128	[-,km]	3.0
TOF	15x15	4.0e-7 , 0.912	4.3e-7 , 0.936	4.2e-7 , 0.912	[-,hrs]	3.1
$i_{\text{Hill},2}$	25x25	2.4e-5 , 0.77	2.4e-5 , 0.78	3.4e-5 , 0.92	[-,deg]	17.3
$\cos\Omega_{\text{Hill},2}$	25x25	2.4e-5 , 0.010	4.8e-5 , 0.013	5.0e-5 , 0.014	[-,-]	12.6
$\sin\Omega_{\text{Hill},2}$	25x25	3.7e-5 , 0.012	4.6e-5 , 0.014	5.2e-5 , 0.014	[-,-]	10.2

and quantified through a Monte Carlo simulation. 100,000 random initial conditions are sampled uniformly in the considered phase space of the first periareion, listed in the "Data selection" paragraph. The orbital elements at the next periareion are predicted using the ANN, and compared to the orbital elements obtained from numerical integration. Figure 5.6 shows the distribution of the error in the predicted orbital elements. The best fitting Gaussian distribution is plotted in red. While the errors are not Gaussian, the Gaussian can be used as a conservative bound on the error distribution. The 1σ values from the Monte Carlo simulation are very similar to the ones tabulated in Table 5.2. In 99% of the cases, the errors in predicted $r_{p,2}$, $i_{\text{Hill},2}$, $\omega_{\text{Hill},2}$ and TOF are below 293 km, 2.58°, 2.16° and 0.085 days. The integrated $r_{p,2}$ varies between 3,389 km (Martian

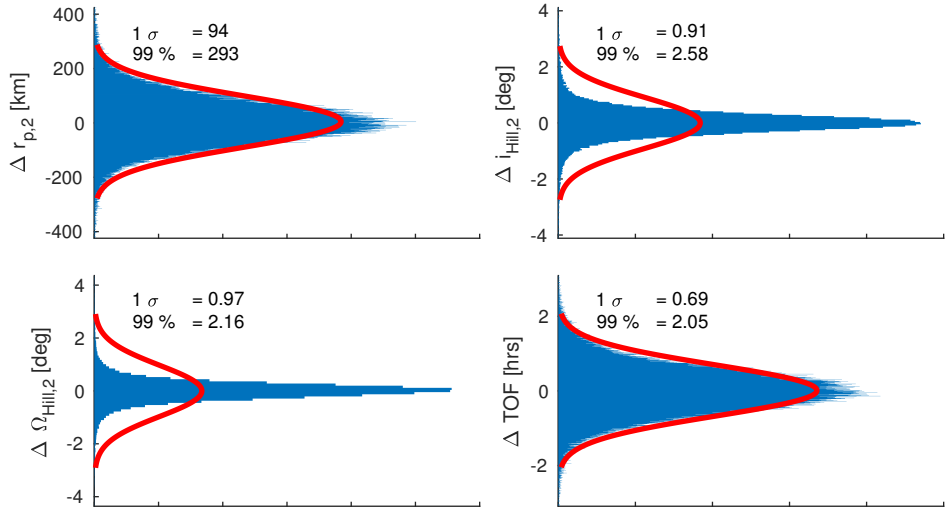

Figure 5.6: Distribution of the errors between the predicted and integrated orbital elements at periareion two for the 100,000 samples in the Monte Carlo analysis for the circular Hill system. The x-axis shows the number of samples for each y-axis bin.

surface) and 50,000 km (Fig. 4.5), $i_{\text{Hill},2}$ between 10 and 170°, $\omega_{\text{Hill},2}$ and $\Omega_{\text{Hill},2}$ between 0 and 360° and TOF between 50 and 106 days. The errors indeed satisfy the accuracy threshold with an order of magnitude 1%. If better accuracy is needed, this process can be repeated with more neurons, and/or more layers. Simply adding more layers/neurons may not improve the accuracy. For these larger networks, more training data is generally required for good generalization ability [96, 102, 103].

The correlations between the different orbital element errors are shown in Table 5.3. Some minor correlation exists between $\Delta r_{p,2}$ and ΔTOF. Both parameters are related to the magnitude of the angular momentum vector, h. Both ANN have similar errors in regions of the phase space where h varies quickly. A larger correlation exists between $\Delta i_{\text{Hill},2}$ and $\Delta\Omega_{\text{Hill},2}$. Figure 5.7 shows the orbital elements at periareion one, and $\Delta i_{\text{Hill},2}$ and $\Delta\Omega_{\text{Hill},2}$, when either error is larger than 5°. A band structure in $\omega_{\text{Hill},1} - \Omega_{\text{Hill},1}$ is observed. A grid is computed in the neighborhood of a selected point; for $i_{\text{Hill},1} = 108.54°$, $r_{a,1} = 617,551$ km, $\omega_{\text{Hill},1} = 23.12°$, and $\Omega_{\text{Hill},1} = 18.42°$, the errors are $\Delta i_{\text{Hill},2} = 40.58°$ and $\Delta\Omega_{\text{Hill},2} = -59.75°$. Figure 5.8 shows the integrated and predicted response in the neighborhood of this point, for constant $i_{\text{Hill},1}$ and $r_{a,1}$. A bifurcation in $i_{\text{Hill},2}$ and $\Omega_{\text{Hill},2}$ is observed. The ANN capture the global trend of the bifurcation, but the identified boundaries deviate from the truth. Near those bifurcation boundaries, locally, large errors exist. The $\omega_{\text{Hill},1} - \Omega_{\text{Hill},1}$ location of this bifurcation is dependent on $i_{\text{Hill},1}$ and $r_{a,1}$, and traces out the band structure observed in Fig. 5.7. Further analysis reveals the origin of this bifurcation; all points within this band structure have $r_{p,2}$ well below the Martian surface. For any practical application, these regions will be avoided and the largest errors in predicted $i_{\text{Hill},2}$ and $\Omega_{\text{Hill},2}$ are irrelevant.

Table 5.3: Correlation between the circular Hill ANN prediction errors for the 100,000 sampled points in the Monte Carlo analysis.

	$\Delta r_{p,2}$	ΔTOF	$\Delta i_{\text{Hill},2}$	$\Delta\Omega_{\text{Hill},2}$
$\Delta r_{p,2}$	1	0.087	0.010	0.011
ΔTOF	0.087	1	−0.012	−0.001
$\Delta i_{\text{Hill},2}$	0.010	−0.012	1	−0.191
$\Delta\Omega_{\text{Hill},2}$	0.011	−0.001	−0.191	1

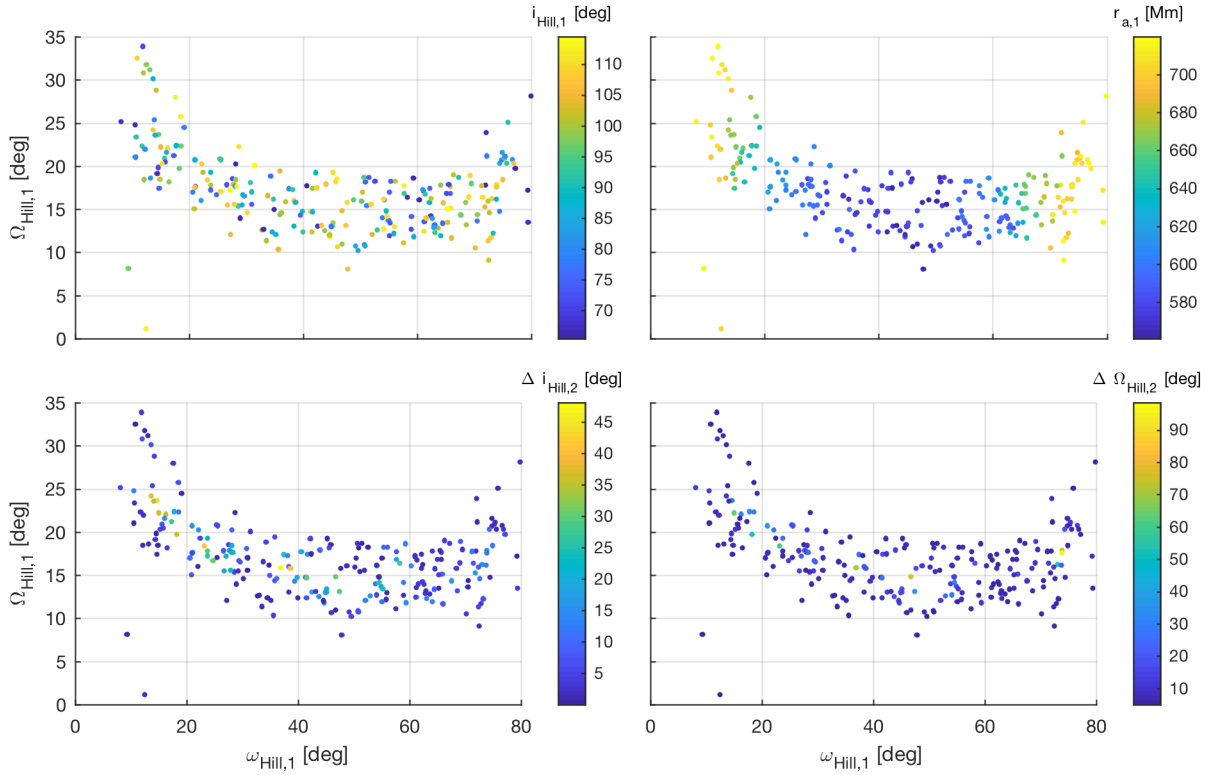

Figure 5.7: Region in initial orbital elements-space where the errors in $i_{\text{Hill},2}$ or $\Omega_{\text{Hill},2}$ are larger than 5° for the 100,000 samples in the Monte Carlo analysis for the circular Hill system.

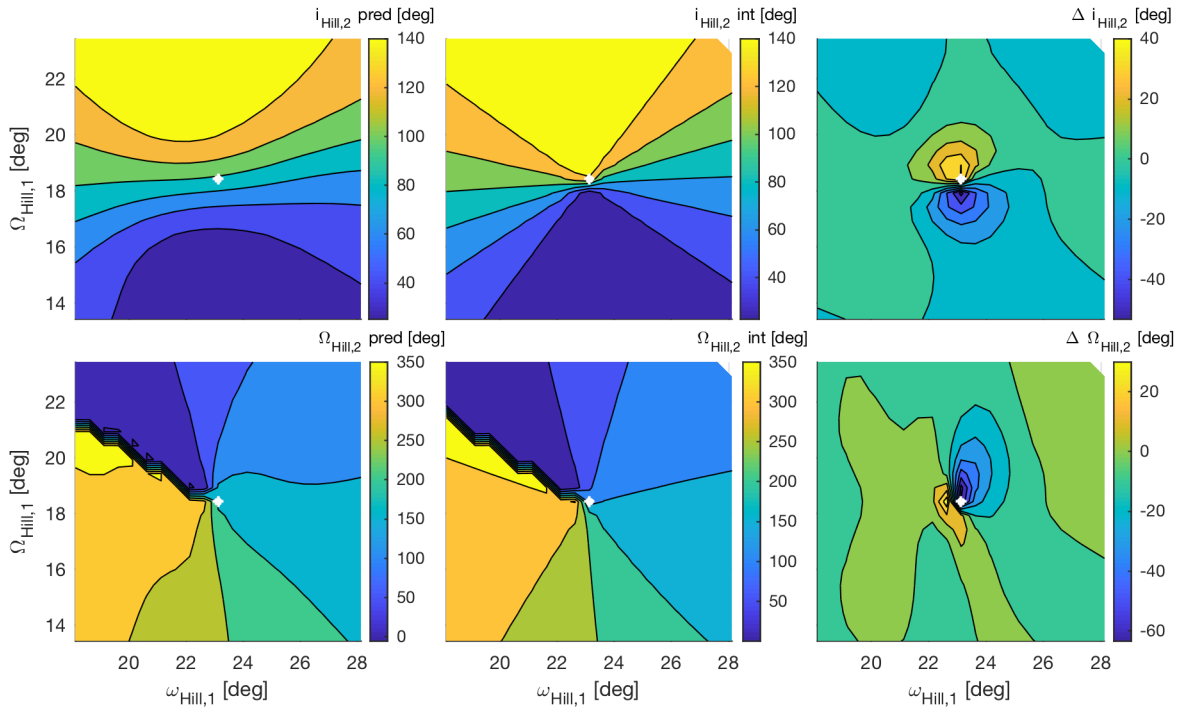

Figure 5.8: Comparison between the predicted and integrated response in the neighborhood of a point from the Monte Carlo analysis with a large error in $i_{\text{Hill},2}$ and $\Omega_{\text{Hill},2}$ (white asterisk).

5.2.1.5 ANN prediction of initial conditions to target final state

The ANN are used to re-create the results from Fig. 4.6. The same methodology described in Algorithm 1 is used to find trajectories that target Phobos' or Deimos' r_p and i_{MME}. Instead of the integrated orbital elements at periareion two, the ANN predicted elements are used. The results are shown in Fig. 5.9. While small differences occur with Fig. 4.6, the ANN provide sufficient accuracy to predict the region within the phase space where the initial conditions target the desired $r_{p,2}$ and $i_{\text{MME},2}$.

5.2.2 Artificial neural network for the eccentric problem

The previous subsection demonstrates that ANN can be used to improve on computational requirements, while being able to predict the periareion Poincaré maps for the circular Hill problem to within a specified tolerance. In this subsection, it is demonstrated how this can be extended to predict results when taking into account Mars' eccentricity. Classically, this is modeled as an eccentric Hill problem. Section 4.4 demonstrated that the eccentricity of Mars increases the computational burden to compute a database. This section also showed how the eccentric Hill problem can be approximated by differently scaled circular Hill problems, based on the heliocentric true anomaly of Mars when the transfers pass through apoareion. This subsection combines this knowledge to set up the method to predict the periareion Poincaré maps in the scaled circular Hill problem. First, an implementation choice is explained concerning the apoaerion scaled circular Hill approximations with ANN. Second, the training data creation, training and validation procedures of the ANN are explained. Third, the ANN are used to predict the initial orbital elements and timing to target Phobos and Deimos. Finally, those transfers are integrated in a higher fidelity model as a final test.

5.2.2.1 Approximation by an apoareion scaled circular Hill problem

The response in the eccentric Hill system can be approximated by the response in an apoareion scaled circular Hill system. The apoareion scaled circular Hill dynamical system has the same

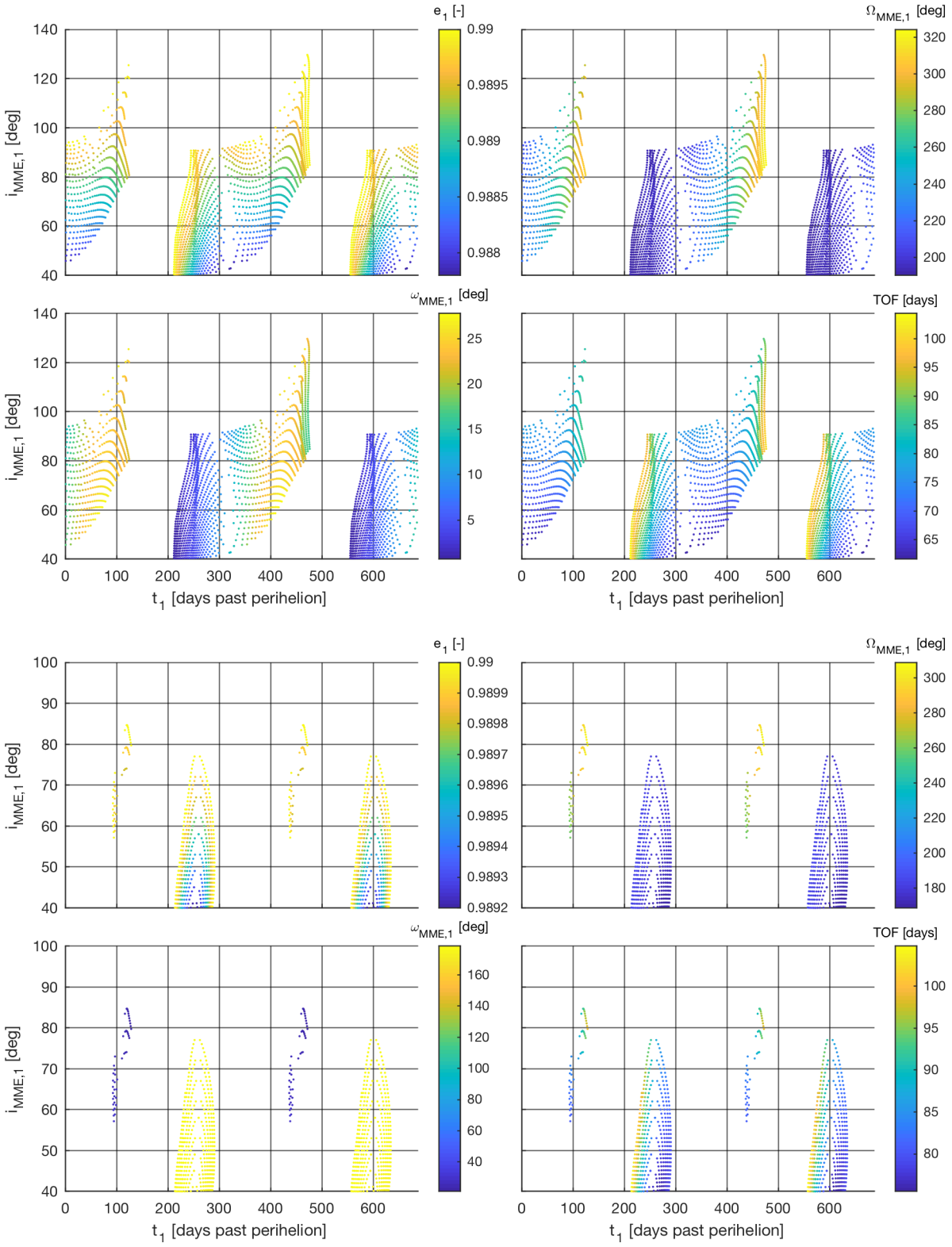

Figure 5.9: ANN predicted equatorial conditions and timing of periareion one to reach Phobos' (top) or Deimos' (bottom) r_p and i_{MME} at periareion two in the circular Hill dynamical system.

assumptions as the eccentric Hill system, with one major difference: Mars orbits around the Sun in a circular orbit, with radius $d_{\text{M, apoareion}}$; the instantaneous Sun-Mars distance when the transfers pass through their apoareion. This form of the circular Hill system is again implemented in a non-dimensional version using the definition of the length scale l and time scale τ from Eq. 2.20.

$$l = \left(\frac{\mu_{\text{M}}}{\mu_{\text{S}}}\right)^{\frac{1}{3}} d_{\text{M, apoareion}} \qquad \tau = \sqrt{\frac{d^3_{\text{M, apoareion}}}{\mu_{\text{S}}}}$$

The dimensional position and velocity vectors $\mathbf{R}$ and $\mathbf{V}$ are scaled to the non-dimensional position vector $\mathbf{r}$ and velocity $\mathbf{v}$:

$$\mathbf{r} = \frac{\mathbf{R}}{l} \qquad \mathbf{v} = \frac{\tau}{l}\mathbf{V} \tag{5.3}$$

This scaling can be incorporated in two different ways.

(1) Nominal initial state, scaled dynamics: the difference in solar distance can be translated into different values of length and time scales.

(2) Scaled initial state, nominal dynamics: scale $r_{p,1}$ and $r_{a,1}$, integrate the dynamics using mean length and time scales. Scale $r_{p,2}$, $r_{a,2}$ and TOF.

The first option requires adding the different length and time scales to the inputs of the ANN, which is equivalent to adding $\nu_{\text{M, apoareion}}$ to the inputs of the ANN. This parameter drastically affects the response of the periareion Poincaré map (Fig. 4.8). A relatively large number of different values of $\nu_{\text{M, apoareion}}$ would need to be sampled to capture its effect.

For the second option, the non-dimensional equations of motion allow for the use of a constant length and time scale l_{mean} and τ_{mean}

$$l_{\text{mean}} = \left(\frac{\mu_{\text{M}}}{\mu_{\text{S}}}\right)^{\frac{1}{3}} a_{\text{M}} \qquad \tau_{\text{mean}} = \sqrt{\frac{a^3_{\text{M}}}{\mu_{\text{S}}}}$$

by creating a scaled version of the dimensional position and velocity vectors.

$$\mathbf{r} = \frac{1}{l}\mathbf{R} = \frac{1}{l_{\text{mean}}}\frac{l_{\text{mean}}}{l}\mathbf{R} \tag{5.4}$$

$$
\begin{aligned}
&= \frac{1}{l_{\text{mean}}}\mathbf{R}_{\text{scaled}} \\
\mathbf{v} = \frac{\tau}{l}\mathbf{V} &= \frac{\tau_{\text{mean}}}{l_{\text{mean}}}\frac{l_{\text{mean}}}{l}\frac{\tau}{\tau_{\text{mean}}}\mathbf{V} \\
&= \frac{\tau_{\text{mean}}}{l_{\text{mean}}}\mathbf{V}_{\text{scaled}}
\end{aligned}
\tag{5.5}
$$

This scaling translates into the orbital elements domain by scaling r_a and r_p. For instance, near Mars' perihelion, the scaling increases $r_{a,1}$, mimicking the stronger solar perturbations. The second option requires adding $r_{p,1}$ to the inputs of the ANN. A study on the effect of $r_{p,1}$ shows that the outputs of the periareion Poincaré map only differ slightly for small differences in $r_{p,1}$. It is thus expected that only a relatively small number of $r_{p,1}$-values must be sampled. The large changes observed in Fig. 4.8 can be mostly attributed to the differences in scaled $r_{a,1}$. The effect of $r_{a,1}$ is already part of the ANN. Hence, this option capitalizes on this knowledge. The scaling increases the range of $r_{a,1}$ values, increasing the computational load compared to the circular case. Despite this, the reduced sampling requirements on $r_{p,1}$ compared to $\nu_{\text{M, apo}}$ renders option two more efficient.

5.2.2.2 Development of the ANN

The next few paragraphs explain how the training data is created, and how the ANN are trained and validated.

Training data creation To start training the more extensive neural networks, the new scaled training data range must first be computed. The nominal $r_{p,1}$ of 3389.5 km is mapped to [3100,3738] km. The bounds on $r_{a,1} \in [560000, 720000]$ km (Fig. 4.12) are mapped to [512000,794000] km. The training data range and sampling frequency is summarized in Table 5.4. The total number of integrations is 492,840; seven times the required training data for the circular Hill case. In comparison, if all trajectories are integrated with the same resolution as the circular case, and a 1° resolution in $\nu_{M,1}$, 3.04 billion integrations are required; an increase by a factor 6,000.

ANN design The ANN architecture for the circular scenario is re-used, be it with two major differences. First, an extra input parameter is required; $r_{p,1}$. Second, as will be demonstrated later, an extra output parameter is required; the time of flight from periareion to apoareion, TOF_{apo}.

Table 5.4: Training data range for the apoareion scaled Hill ANN

Input parameter	Sampling range	Sampling frequency	Unit
$r_{p,1}$	3100 - 3700	200	km
$r_{a,1}$	520,000-800,000	20,000	km
$i_{\text{Hill},1}$	65-115	10	deg
$\omega_{\text{Hill},1}$	0 - 180	5	deg
$\Omega_{\text{Hill},1}$	0 - 180	5	deg

ANN training results and validation The training results for the different ANN is shown in Table 5.5. Both the non-dimensionalized MSE, and the dimensional 1σ values are shown. The performance is again consistent over the training, testing and validation sets indicating that the ANN predictions on new data should be accurate. This accuracy is quantified through a Monte Carlo analysis. 100,000 random initial conditions uniformly sampled within the bounds in Table 5.4 are numerically integrated to the next periareion. The difference between predicted and integrated response is shown in Fig. 5.10. While the MSE results are very similar to the circular results, the dimensional 1σ and 99 percentiles of $r_{p,2}$ and TOF are significantly higher. The larger RMS values can be attributed to the scaling: the maximum $r_{p,2}$ is roughly five times higher for the eccentric case. Thus, for the same non-dimensionalized MSE accuracy, the dimensional 99 percentile is higher. The obtained accuracy is still deemed good enough for preliminary transfer design; the errors of the ANN and the errors introduced by the scaled Hill approximation of the eccentric Hill problem, have similar order of magnitude, and can be corrected with a predictor-corrector scheme. This will be demonstrated in the next subsections.

Table 5.5: ANN training results for the apoareion scaled circular Hill system.

Output parameter	Hidden layer neuron sizes	Non-dimensional MSE , dimensional 1σ			Units	Training time [min]
		Training data	Validation data	Test data		
$r_{p,2}$	15x15	2.8e-6 , 431	3.1e-6 , 450	3.2e-6 , 458	[-,km]	20.8
TOF_{apo}	15x15	7.7e-7 , 1.344	7.8e-7 , 1.344	7.9e-7 , 1.368	[-,hrs]	21.0
TOF	15x15	1.3e-6 , 3.696	1.3e-6 , 3.696	1.3e-6 , 3.744	[-,hrs]	22.5
$i_{\text{Hill},2}$	25x25	4.4e-5 , 1.10	4.4e-5 , 1.11	4.6e-5 , 1.14	[-,deg]	186.5
$\cos\Omega_{\text{Hill},2}$	25x25	3.6e-5 , 0.012	3.9e-5 , 0.012	4.4e-5 , 0.013	[-,-]	177.0
$\sin\Omega_{\text{Hill},2}$	25x25	4.7e-5 , 0.014	4.7e-5 , 0.014	5.0e-5 , 0.014	[-,-]	62.8

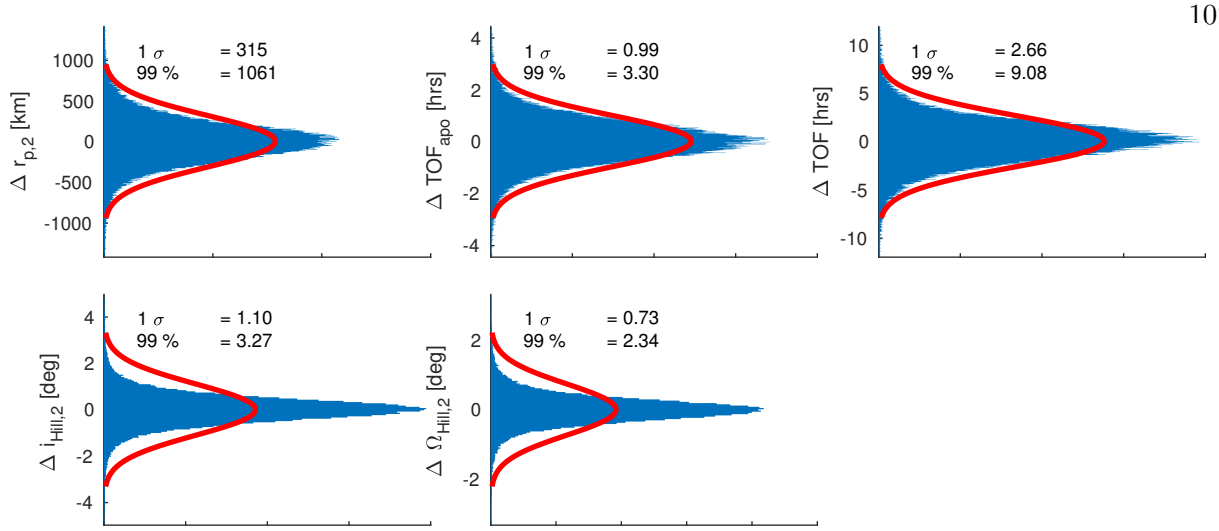

Figure 5.10: Distribution of the errors between the predicted and integrated orbital elements at periareion two for the 100,000 samples in the Monte Carlo analysis for the apoareion scaled Hill system. The x-axis shows the number of samples for each y-axis bin.

The correlations between the orbital element errors are shown in Table 5.6. Again, some minor correlation exists between $\Delta r_{p,2}$ and ΔTOF. The newly introduced ΔTOF_{apo} also has minor correlation with $\Delta r_{p,2}$, and some correlation with ΔTOF. The same parameters that affect the TOF_{apo} intuitively affect TOF in a similar manner. The correlation between $\Delta i_{\text{Hill},2}$ and $\Delta\Omega_{\text{Hill},2}$ is significantly lower, compared to the circular case. Nonetheless, the same band structure in $\omega_{\text{Hill},1}$ and $\Omega_{\text{Hill},1}$ is observed where the largest $\Delta i_{\text{Hill},2}$ and $\Delta\Omega_{\text{Hill},2}$ occur (Fig. 5.11). Again, these large errors occur in an impact region.

Table 5.6: Correlation between the apoareion scaled circular Hill ANN prediction errors for the 100,000 sampled points in the Monte Carlo analysis.

	$\Delta r_{p,2}$	ΔTOF	ΔTOF_{apo}	$\Delta i_{\text{Hill},2}$	$\Delta\Omega_{\text{Hill},2}$
$\Delta r_{p,2}$	1	−0.044	−0.055	−0.016	0.003
ΔTOF	−0.044	1	0.200	−0.005	−0.017
ΔTOF_{apo}	−0.055	0.200	1	−0.014	−0.0192
$\Delta i_{\text{Hill},2}$	−0.016	−0.005	−0.014	1	0.037
$\Delta\Omega_{\text{Hill},2}$	0.003	−0.017	−0.0192	0.037	1

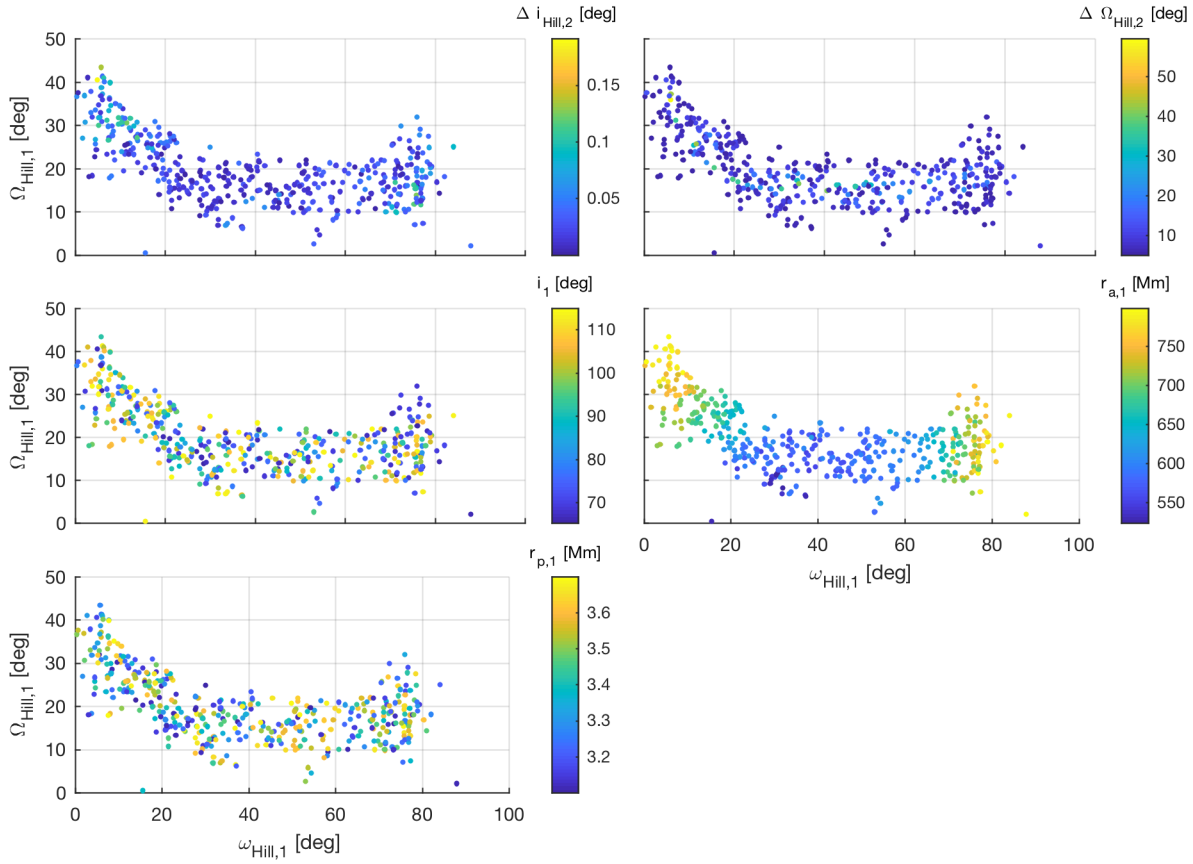

Figure 5.11: Region in initial orbital elements-space where the errors in $i_{\text{Hill},2}$ or $\Omega_{\text{Hill},2}$ are larger than 5° for the 100,000 samples in the Monte Carlo analysis for the apoareion scaled circular Hill system.

5.2.2.3 ANN prediction of initial conditions to target final state

The scaled circular Hill results are predicted with a uniform sampling in e_1, $\nu_{M,a}$, and $i_{\text{Hill},1}$ with steps of respectively 0.0001, 1°, and 1°. For each realization of e_1, $\nu_{M,a}$ and $i_{\text{Hill},1}$, $\omega_{\text{Hill},1}$ and $\Omega_{\text{Hill},1}$ are predicted that satisfy the necessary conditions to arrive at Phobos or Deimos. This prediction requires proper scaling of $r_{p,1}$ and $r_{a,1}$ using e_1 and $\nu_{M,a}$. Next, the departure and arrival times are predicted. This process requires the time at apoareion, known from $\nu_{M,a}$, and the predicted TOF_{apo} and TOF. The timing allows the conversion of the initial and final states between the Hill and equatorial systems. Some of the arrival points that satisfy the necessary conditions are mapped to the equator. The used algorithm is summarized in Algorithm 2. Figure 5.12 shows

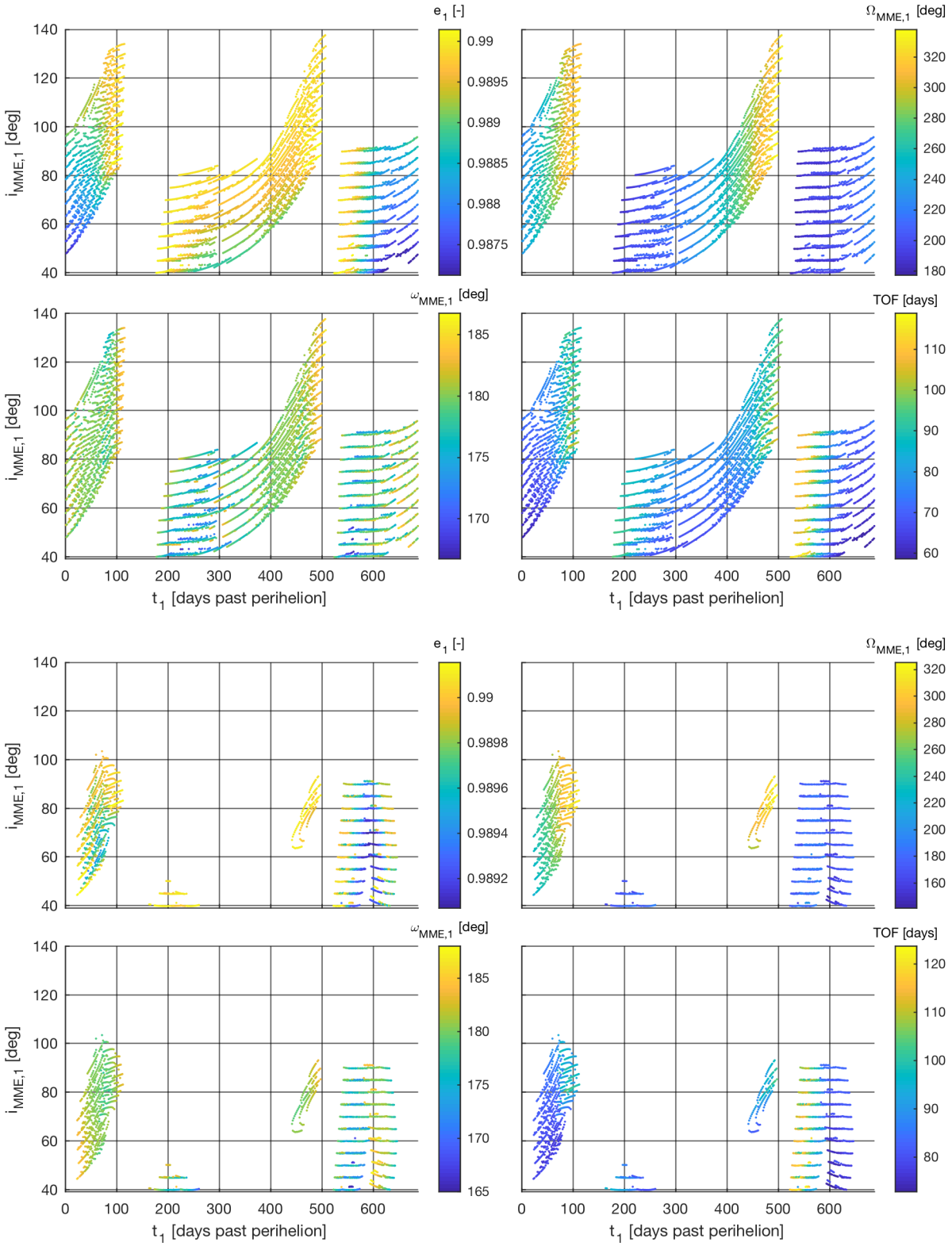

Figure 5.12: ANN predicted equatorial conditions and timing of periareion one to reach Phobos' (top) or Deimos' (bottom) r_p and i_{MME} at periareion two in the apoareion scaled circular Hill system.

the solutions with $i_{\mathrm{MME},2} < 3°$ that arrive at Phobos' or Deimos' r_p-values. This inclination value is chosen in accordance with the expected 99 percentile accuracy of the ANN (Fig. 5.10). Further note that only solutions with a 5° spacing in $i_{\mathrm{Hill},1}$ are shown to avoid cluttering the figure.

5.2.2.4 Validation of the predicted transfers

The results in Fig. 5.12 leveraged several assumptions and approximations, each introducing errors. The main assumptions are the approximation of real dynamics using the eccentric Hill model, which are then approximated by scaled circular Hill models, which in turn are predicted using neural networks. The accuracy of the identified initial conditions is assessed in this paragraph. The solutions with predicted $i_{\mathrm{MME},2} < 1°$ are integrated in a full Mars-Sun ephemeris model in the General Mission Analysis Tool (GMAT) developed at NASA Goddard Space Flight Center [104]. Some of the inclination and periapse errors are significant. A breakdown of the errors is shown in Fig. 5.13. The trajectories are predicted to arrive at Phobos or Deimos in the scaled Hill model. When integrated in the scaled circular Hill model, the observed errors of approximately 1000 km in periapse radius and a few degrees in inclination are in line with the results of the Monte Carlo analysis (Fig. 5.10). The scaled circular Hill system is an approximation of the eccentric Hill dynamics. This simplification introduces periapse errors of approximately 3000 - 6000 km, along with inclination errors between -3° and 6°. The next row of figures shows the errors observed for integrations in full Mars-Sun ephemeris using GMAT. Little difference exists between these solutions and the eccentric Hill integrations. The two main error sources are the neural network predictions and the difference between the scaled circular Hill and the eccentric Hill system. Adding more neurons, layers, and training data could improve the former. The latter is a more structural error source; the same departure day regions display similar error structures.

For further analysis, three predicted points are selected that target Phobos' $r_{p,2}$ and $i_{\mathrm{MME},2}$ in the apoareion scaled Hill system. When integrated in the eccentric Hill system, point 1 overshoots the required $r_{p,2}$ by about 2500 km, point 2 is about 3000 km too low and point 3 has a 6° error in $i_{\mathrm{Hill},2}$. Those errors can be corrected using a simple predictor-corrector scheme. For each of the

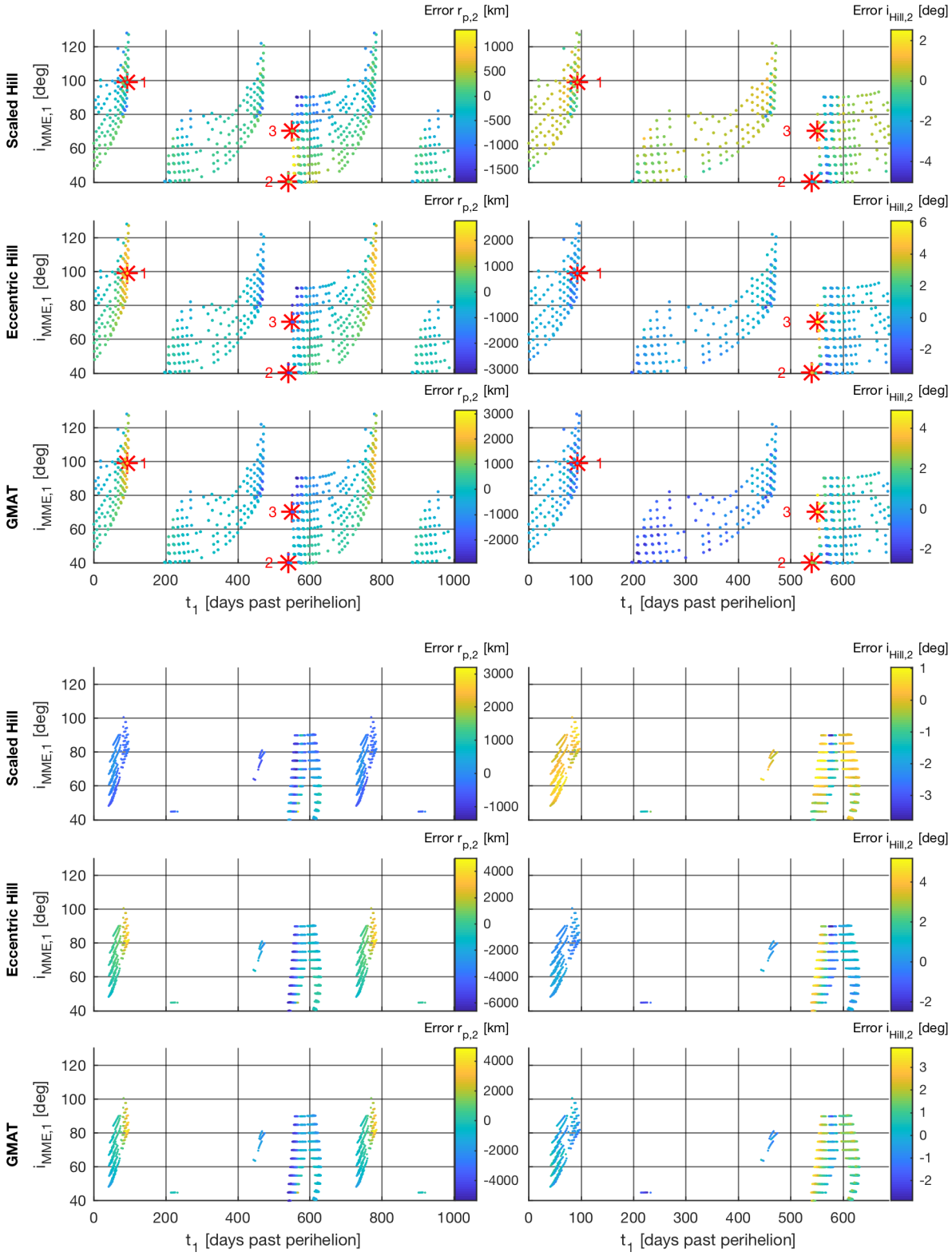

Figure 5.13: Error breakdown of the transfers predicted to arrive at Phobos' (top) and Deimos' (bottom) r_p and i_{MME} at periareion two in the apoareion scaled circular Hill dynamical systems. Top: error in arrival conditions when integrating the predicted initial states in the apoareion scaled Hill system. Middle: errors integrated in the eccentric Hill system. Bottom: errors integrated in the DE405 ephemeris in GMAT.

three points, a grid in $\omega_{\text{Hill},1}$ and $\Omega_{\text{Hill},1}$ is computed, while constraining $i_{\text{Hill},1}$, departure time and e_1 to be constant. Figure 5.14 shows the results of this process. The initial conditions on this grid are numerically integrated in the eccentric Hill system to the next periareion. For point 1 and 2, the errors are mainly in $r_{p,2}$, and for point 3, the error is mainly in $i_{\text{Hill},2}$. Therefore, the left side of Fig. 5.14 shows the deviation from Phobos' $r_{p,2}$ in the neighborhood of point 1 and 2; $\delta r_{p,2}$, and the deviation from Phobos' $i_{\text{Hill},2}$ in the neighborhood of point 3; $\delta i_{\text{Hill},2}$. The points are predicted to satisfy the necessary conditions in the scaled Hill system. Because of the inaccuracies in the ANN, and the difference between the scaled and eccentric system, these points deviate from the locations satisfying the necessary conditions in the eccentric Hill system. For point 1 and 2, the true necessary conditions are located on the intersection between the blue line indicating $\delta r_{p,2} = 0$ km, and the black line where $i_{\text{Hill},2} = \varepsilon$. For point 3, the necessary condition is located on the intersection between the blue line indicating $\delta i_{\text{Hill},2} = 0°$, and the black line where $r_{p,2} = 9376$ km, Phobos' orbital radius. From this figure, one can see that the points have strong gradients in either $r_{p,2}$ and/or $i_{\text{Hill},2}$. Due to these strong gradients, the predicted locations of the necessary conditions are a few degrees off in $\omega_{\text{Hill},1}$ and $\Omega_{\text{Hill},1}$. On the right hand side of Fig. 5.13, the $i_{\text{MME},2}$ integrated in the eccentric Hill system is shown. The minimum $i_{\text{MME},2}$ contour closely follows the lines where $i_{\text{Hill},2} = \varepsilon$. On these lines, the arrival times and $\Omega_{\text{Hill},2}$ vary, resulting in different final $i_{\text{MME},2}$. This difference explains the small features observed in $i_{\text{MME},2}$. For all three scenarios, the corrected solution has $i_{\text{MME},2}$ of maximum three degrees. A simple predictor-corrector scheme in the eccentric Hill dynamical system with more design variables could correct for these errors. Besides changes in $\omega_{\text{Hill},1}$ and $\Omega_{\text{Hill},1}$, small changes in sampled e_1, $i_{\text{Hill},1}$ and apoapse times should be allowed. The obtained results provide very close initial guesses for the actual initial conditions. For the predictor-corrector scheme shown in Fig. 5.14 where only $\omega_{\text{Hill},1}$ and $\Omega_{\text{Hill},1}$ are allowed to vary, the predicted and corrected solutions have identical e_1. Hence, the size of the first maneuver is identical. For the three transfers, the corrected TOF vary between 100 and 108 days and the magnitudes of the second maneuver, ΔV_2, between 878 and 898 m/s. The predicted TOF and ΔV_2 differ by a maximum of 3 days and 33 m/s; roughly a three percent difference.

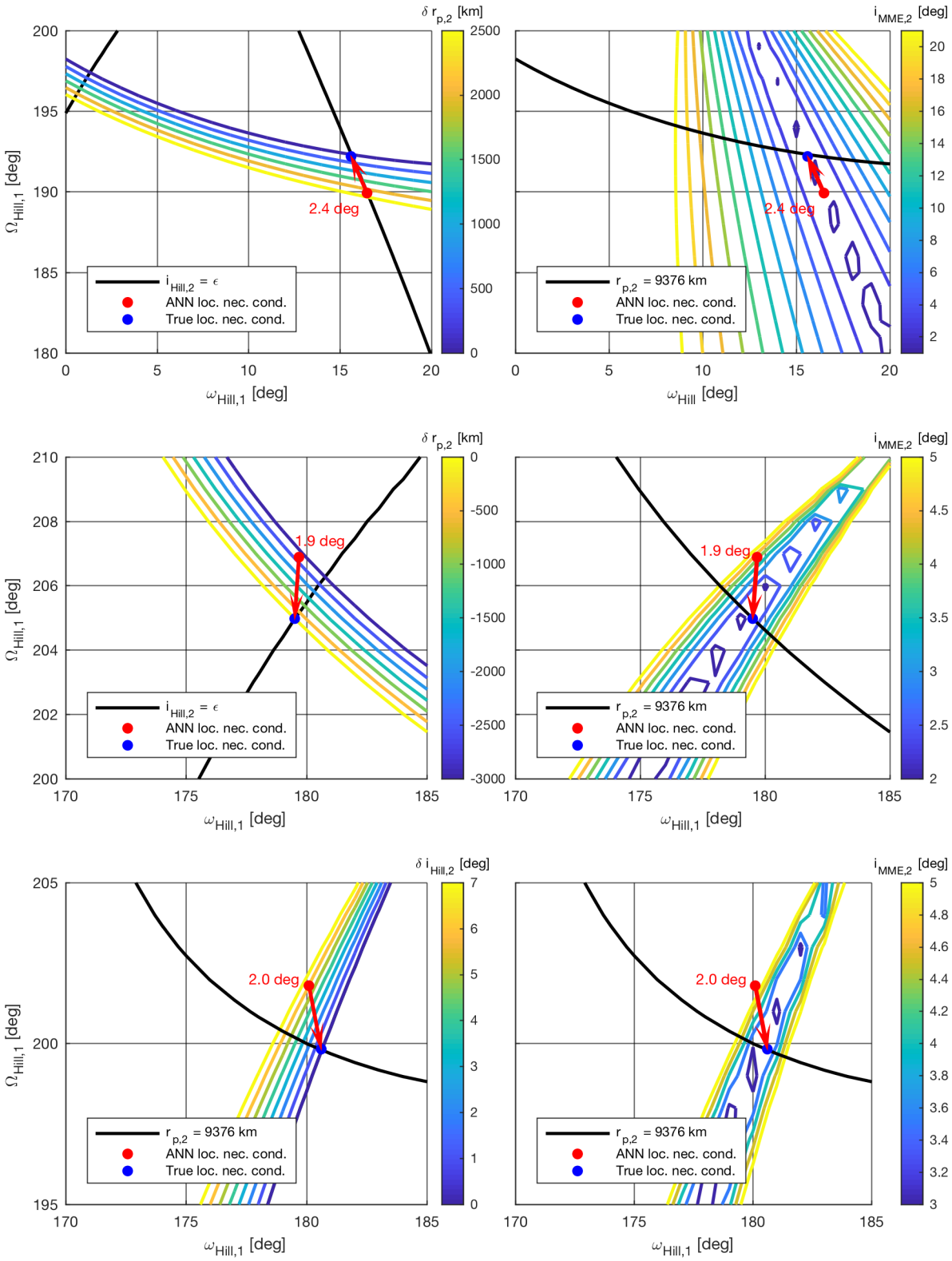

Figure 5.14: Visualization of the deviations from the locations of the necessary conditions predicted using the scaled Hill ANN, and their true location and the effect on $i_{\mathrm{MME},2}$ when integrated in the eccentric Hill system, for transfers 1 (top), 2 (middle), and 3 (bottom).

5.2.3 Discussion

In this subsection, the results of the feasibility study are discussed. The discussion is split up according to the two original goals set up in Chapter 4; showcasing the large control authority of the Sun on an example application, and developing the framework to create a database of transfers.

5.2.3.1 Showcasing large control authority of the Sun

As an example of the large control authority of the Sun, transfers were analyzed between near-polar orbits at 185 km altitude and near-equatorial orbits at Phobos' or Deimos' orbital radius. The transfers to both Phobos and Deimos have a similar structure and occur in the same times within the Martian year (Fig. 5.12). However, the lower required periapse increase to reach Phobos is easier to achieve than the high periapse increase to reach Deimos. Hence, for an initial polar inclination with respect to the Martian equator, Phobos can be reached for 319 days vs 116 days per Martian year for Deimos. Furthermore, one can see that the eccentricity and thus required time of flight is higher for the Deimos case. Phobos can be reached in 60 to 115 days, Deimos in 75 to 120 days. For both targets, the argument of periapse fluctuates around 180°. The Hill system has a symmetry in ω. Thus, an equivalent solution exists with $\omega_{\text{Hill},1} \approx 0°$. The longitude of ascending node shows similar trends and structure throughout the year for both applications. Note that the symmetry in the Hill system in Ω is not present in the equatorial system.

Fewer transfers appear to exist for initial $i_{\text{MME},1} < 90°$. The ANN captures all possible transfers departing from an initial polar orbit with respect to the equator with a periareion altitude of 185 km. For all other initial inclinations, the database is not complete. The shown results are for $i_{\text{Hill},1} \in [65°, 115°]$. In the top of Fig. 5.12, in the [0,100] day region, the lowest line is made up of points with $i_{\text{Hill},1} = 65°$. If lower $i_{\text{Hill},1}$ are included in the database, the lower right triangle in the [0,100] day region will most likely become feasible. Similarly, the [200,480] day lower right triangle is expected to be feasible. These transfers can be identified through a straightforward expansion of the training data to include lower $i_{\text{Hill},1}$.

5.2.3.2 Database framework development

In Chapter 4 and this subsection, two different methods were developed to create a database, on a small subset of the phase space, centered around one specific application. For method one developed in Chapter 4, all database entries are created using numerical integration. Method two developed in this subsection computes some database entries using numerical integration, and machine learning techniques to predict the other database entries. Both methods were developed for a circular and eccentric model of the Martian orbit around the Sun. In the next paragraphs, both methods are compared in terms of computational requirements and accuracy.

For the circular model, the usage of ANN reduced the required number of integrated transfers from 8.4 million to 74,000 for the small subset of the phase space of the first periareion. The integration of the training data, training and the prediction of the 8.4 million transfers required 50 minutes on a 2.5GHz Intel Core i7 processor. On the same computational set-up, the numerical integration of 8.4 million transfers required 10 days. The developed ANN for the circular scenario were able to identify the transfers of interest to within a few 100 km and a few degrees. Only marginal differences were found between the solutions identified by the ANN and the numerically integrated database.

For the eccentric model, the ANN reduced the number of integrated transfers from 3.04 billion to 492,000. The creation of the training data, training and the prediction of the 3.04 billion transfers required roughly one day. The numerical integration of the 3.04 billion transfers would require 3570 days. The entries in the numerical database would exactly map the states at periareion one to the states at periareion two in the eccentric Hill system. However, the large number of database entries prevented the computation of the numerical database. For the ANN created database, the states were mapped in the scaled Hill system. While the responses in the scaled and eccentric Hill systems are qualitatively very similar (Fig. 4.10), the approximation is not exact. In fact, the scaled Hill approximation of the eccentric Hill system, and the ANN produced similar errors with Δr_p $\mathcal{O}(1000$ km) and Δi $\mathcal{O}(1^\circ)$ (Fig. 5.13). Despite these errors, the initial conditions of the transfers identified

in the scaled Hill system are near the solutions in the eccentric Hill system and can be corrected using a simple predictor-corrector scheme.

5.2.4 Conclusion and recommendations

This section demonstrates that ANN can be used to create a database of solutions, at a more tangible computational cost than when created solely through numerical integration. Furthermore, the usage of an apoareion scaled circular Hill system, where the initial states are scaled and integrated in nominal dynamics, proved critical to reduce the required number of integrations. This system captures the majority of the time variance of the eccentric Hill system through a simple expansion of the considered $r_{p,1}$-$r_{a,1}$ domain. The trained ANN predict the behavior of a solar perturbed transfer over one revolution, throughout the Martian year. The obtained accuracy allows to identify the initial orbital elements and timing to target specific final orbits. The predicted transfers are found to be near the real solutions in the eccentric Hill system.

This predictor-corrector step could be made obsolete through two improvements. First, the accuracy of the developed ANN could be improved. The most significant error for the scaled Hill ANN occurs for the $r_{p,2}$ parameter. While the non-dimensional MSE value is similar to its circular ANN value, the dimensional 1σ value is almost four times higher. For the apoareion scaled Hill system, some transfers have $r_{p,2}$-values as high as 250,000 km. These transfers are not very interesting for most practical applications, and make up the bulk of the 1σ error value. Therefore, they should not be included in the ANN, allowing the ANN to focus on improving the accuracy of the transfers in the region of interest. Similarly, the strongest gradients for $i_{\text{Hill},2}$ and $\Omega_{\text{Hill},2}$ occur for impacting transfers. These transfers should be excluded from the training data. Second, the difference between the apoareion scaled circular, and eccentric Hill system is observed to be systematic. Therefore, the difference in response between both systems could be approximated by separate ANN. Those ANN could provide a correction to the predicted scaled response, allowing the prediction of the mapping in the eccentric Hill system. These suggested improvements are implemented in the next section, for a significant expansion of the phase space of periareion one.

5.3 ANN architecture for forward Poincaré maps on large section phase space

This section's goal is the design of an ANN architecture that can predict the next periareion for transfers starting within a certain specified range of periareion and apoareion radii ranges, for every possible initial orbital orientation and time, with multiple solar perturbed revolutions around Mars. This requires a significant expansion of the phase space, as compared to the previous section. Furthermore, the previous section's recommendations to make the ANN more accurate are implemented; filtering out impact regions, as well as transfers with very high $r_{p,2}$, from the training data, and approximating the systematic error between the apoareion scaled circular Hill and the eccentric Hill system. First, the enlarged phase space is discussed. Second, the considered ANN architecture and the methodology to design the ANN architecture are treated. Third, the accuracy of the architecture for one revolution is computed. Fourth, the accuracy for multiple revolutions is determined. Finally, some concluding remarks on the developed architecture are listed.

5.3.1 Considered phase space

Table 5.7 shows the region of the considered phase space. One can see that the entire phase space for i_1, ω_1, Ω_1, and t_1 is considered, using the symmetries present in the eccentric Hill system. For $r_{p,1}$ and $r_{a,1}$, this is impossible as the phase space is unbounded. Therefore, only a section of the phase space is considered, be it a large section. The lower bound of $r_{p,1}$ is at the surface of Mars, while the upper bound is imposed to solely include the region where practical applications exist. The lower bound for $r_{a,1}$ has been imposed to ensure that significant changes between subsequent periareions can occur. The upper limit on $r_{a,1}$ has been set to limit the transfer duration to reasonable values. These orbits go near or beyond the Laplace sphere of influence at 574,000 km.

From the shown bounds, it should be evident that numerically integrating this phase space with a fine resolution is highly impractical. Sampling this phase space with a relatively sparse resolution of 1,000 km in $r_{p,1}$, 10,000 km in $r_{a,1}$, 5° in i_1, ω_1 and Ω_1, and 10 days in t_1 results in

Table 5.7: Bounds on the considered phase space.

Parameter	Lower bound	Upper bound	Unit
$r_{p,1}$	3,390	45,000	km
$r_{a,1}$	440,000	720,000	km
$i_{\text{Hill},1}$	0	180	deg
$\omega_{\text{Hill},1}$	0	180	deg
$\Omega_{\text{Hill},1}$	0	180	deg
t_1	0	1	Martian year

approximately 4.6 billion numerical integrations. Therefore, artificial neural networks are designed to predict the changes in orbital elements between subsequent periareions, requiring only a fraction of the numerical integrations.

Using the phase space reduction technique described in Subsubsection 5.2.2.1, the phase space in Table 5.7 can be reduced to the bounds listed in Table 5.8. Using the same resolution as earlier, only 98.4 million integrations are required compared to 4.6 billion. The approximation of the eccentric Hill system with an apoareion scaled circular Hill system is not exact, but the introduced errors are systematic, and can be predicted using an ANN, as will be shown in Subsubsection 5.3.2.3. A visualization of the bounds on the phase space in the non-dimensional circular Hill system are shown in Fig. 5.15.

Table 5.8: Difference between the real and the scaled bounds of the considered phase space.

Parameter	Real bounds	Scaled bounds	Unit
$r_{p,1}$	3,390-45,000	3100-49,200	km
$r_{a,1}$	440,000-720,000	399,000-787,000	km
$i_{\text{Hill},1}$	0-180	0-180	deg
$\omega_{\text{Hill},1}$	0-180	0-180	deg
$\Omega_{\text{Hill},1}$	0-180	0-180	deg
t_1	0-1	N.A.	Martian year

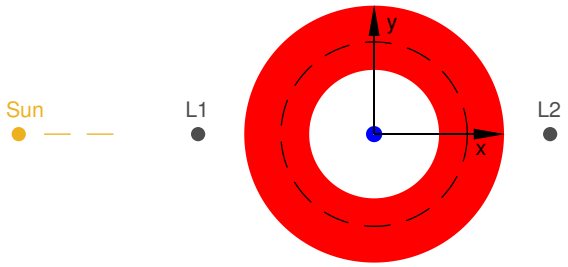

Figure 5.15: Visualization of the scaled bounds of the first periareion in the circular Hill system. Blue and red are the considered regions for, respectively, $r_{p,1}$ and $r_{a,1}$. The black dotted line is the Laplace sphere of influence.

5.3.2 Methodology

In this subsection, the envisioned architecture is developed. First, an overview is given on the neural network architecture, with three groups of ANN. Then, each of the three identified groups is treated in more detail, where the training data creation, training and validation procedures of the neural networks are explained.

5.3.2.1 General architecture

An overview of the architecture is given in Fig. 5.16. First, an initial state at periareion is selected, and a specific time when the transfer passes through its apoareion. The timing is used to scale the initial state using Eqs. 5.4 and 5.5. Second, using classification neural networks, anomalies such as impacting and escaping transfers are identified. For the anomaly-free initial states, the response in the scaled Hill system is predicted. Furthermore, a correction term is predicted. This correction term predicts the difference between the response at the next periareion when integrated in the apoareion scaled Hill system and the eccentric Hill system. Those two terms are combined into a predicted response in the eccentric Hill system. There are thus three different groups of ANN: a group of regression ANN to predict the response in the apoareion scaled Hill system, a group of regression ANN to predict the difference between the apoareion scaled Hill and the eccentric Hill system, and a group of classification ANN to predict escape or impact. Each of those groups are explained in further detail in the next paragraphs.

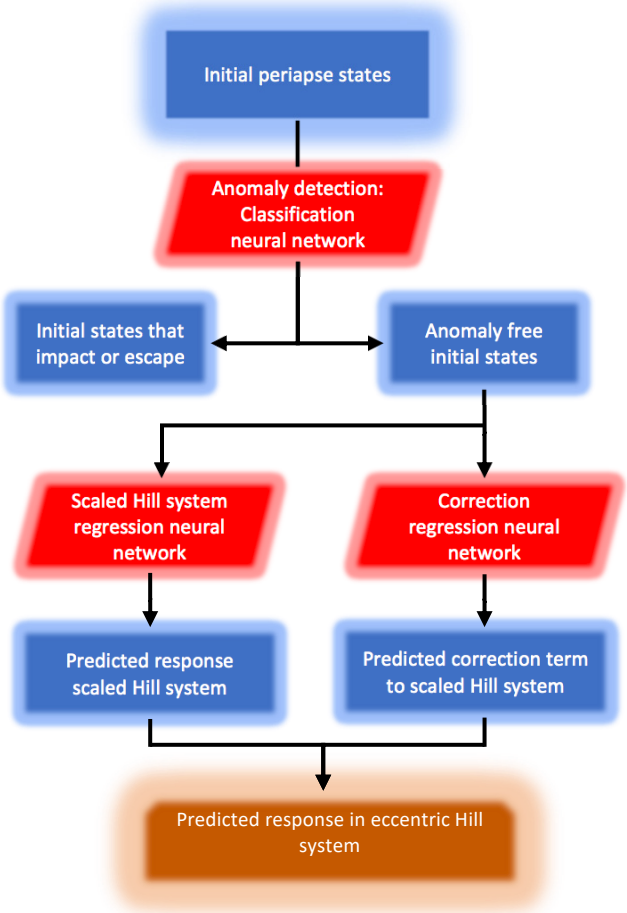

Figure 5.16: Overview of the three-group ANN architecture where the relationships are shown between states (blue) and neural network groups (red) to predict the Poincaré map response in the eccentric Hill system.

5.3.2.2 Apoareion scaled circular Hill neural networks

The apoareion scaled Hill system has continuous output, and is captured in a regression feedforward neural network. Before looking into the design of the neural network, the data is created and analyzed.

Data creation The five parameters at periareion 1 with scaled bounds listed in Table 5.8 are sampled to create the training data. Prior analysis shows that at low values of $r_{p,1}$, small variations in $r_{p,1}$ have larger effects on the control authority than at high values. Therefore, a non-uniform sampling in $r_{p,1}$ is used. The other four parameters are sampled uniformly. The sampled

values are listed in Table 5.9. Note that $i_{\text{Hill},1}$ is sampled between 5° and 175° and not between 0° and 180°. At those extreme inclinations, the initial state's position is on the ecliptic plane, and its velocity is entirely in the ecliptic plane. As such, no inclination changes are possible [14]. These regions are therefore not included in the training data. The scaled Poincaré map is computed for every permutation. In total, 6,209,784 numerical integrations are performed. If the periareion-to-apoareion segment, or apoareion-to-periareion segment of the trajectory is longer than 250 days, the integration is terminated and the trajectory is considered to escape.

Table 5.9: Sampling density of the orbital elements at the first periareion used as training data for the scaled Hill and classification neural networks.

	Region 1			Region 2			Sampled points
	Lower bound	Spacing	Upper bound	Lower bound	Spacing	Upper bound	
$r_{p,1}$ (km)	3,100	3,000	12,100	17,100	5,000	52,100	12
$r_{a,1}$ (km)	400,000	20,000	800,000	-	-	-	21
$i_{\text{Hill},1}$ (deg)	5	10	175	-	-	-	18
$\omega_{\text{Hill},1}$ (deg)	0	5	180	-	-	-	37
$\Omega_{\text{Hill},1}$ (deg)	0	5	180	-	-	-	37
							Total: 6,209,784

Data processing Prior to training, the raw integration data is processed. First, the escaping trajectories are filtered out and indexed for later use in an escape classification neural network. Second, some data is pruned out. In Fig. 5.17, the state at the next periareion is shown. Based on the recommendation in the previous section, the trajectories that dip below the Martian surface are filtered out. A lower limit of 1,000 km is imposed on $r_{p,2}$. Those trajectories are indexed, and are later used to train an impact classification neural network. This lower limit has not been set equal to the Martian radius, to have a buffer against large errors in predicted orbital elements near this boundary, as will be shown in the Validation paragraph. In Fig. 5.17, those transfers are depicted in red. One can see that this impact detection also removes some outliers in $r_{a,2}$. Furthermore, $r_{p,2}$ can grow very large. For any practical application around Mars, the periareion is expected to remain below 50,000 km. By limiting the upper $r_{p,2}$, the scaling of the $r_{p,2}$-parameter

during the training procedure is lower. Thus, for the same non-dimensional training accuracy, the dimensional error is smaller. An upper limit of 70,000 km is imposed, again, to introduce a buffer area. These transfers exhibit similar characteristics as the escaping trajectories. Their indices are thus added to the index list of escaping trajectories. These transfers are depicted in green and are also the longest. Lengthy transfers remain present in Fig. 5.17. A limit of 120 days is then imposed. The classification limit is set slightly higher at 150 days to create a buffer. The transfers that are longer than 150 days are added to the list of escape trajectories and are depicted in black. In total, 5,556,519 transfers survive the data pruning. Their response is indicated in blue. Third, there is an artificial bifurcation in $\omega_{\text{Hill},2}$ and $\Omega_{\text{Hill},2}$. Similarly to the discussion accompanying Fig. 5.1, the response for both parameters are split up in their cosine and sine components.

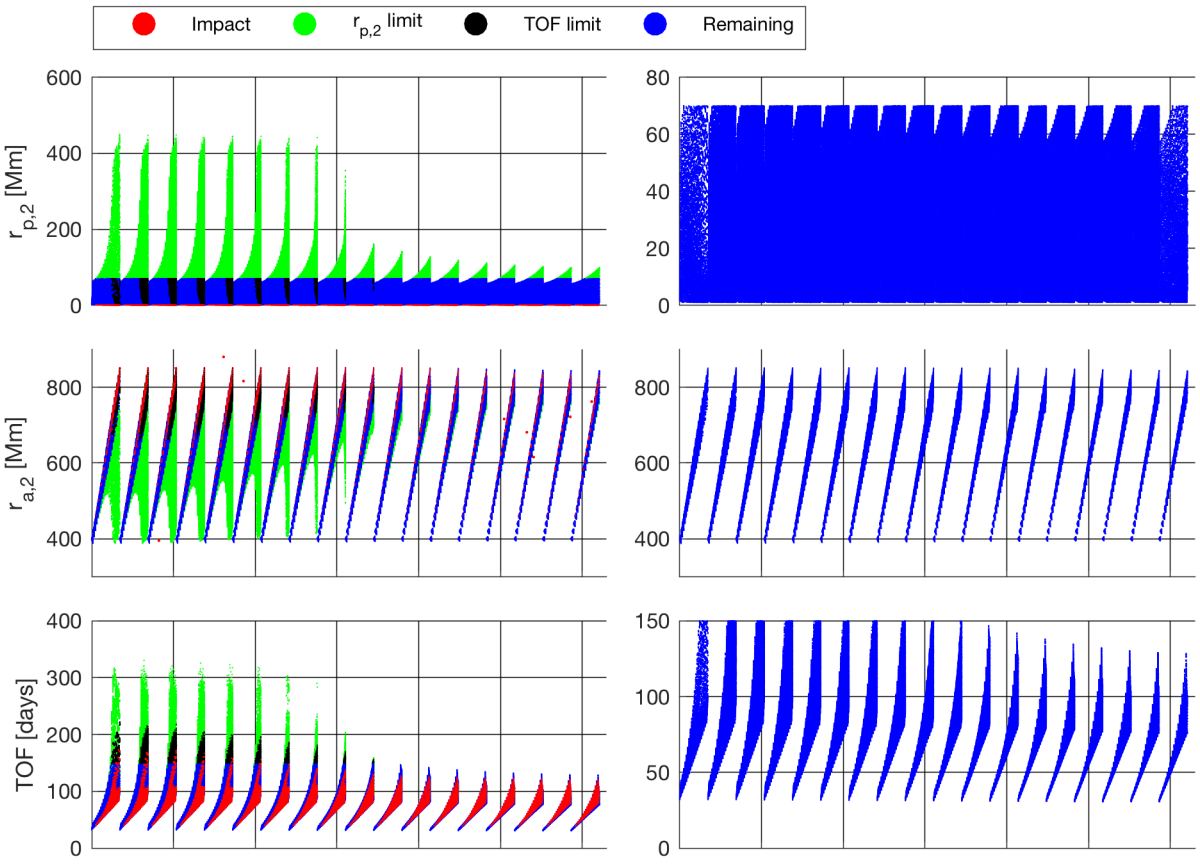

Figure 5.17: Pruning of the training data for the apoareion scaled Hill neural networks. Left: original data. Right: remaining data after data pruning.

Overview of input and output parameters From the discussion in Subsubsection 5.2.2.1, there are five input parameters: $r_{p,1}$, $r_{a,1}$, $i_{\text{Hill},1}$, $\omega_{\text{Hill},1}$, $\Omega_{\text{Hill},1}$. The input parameters are scaled based on the time of apoareion. In order to predict the response over several revolutions, all orbital elements at each next periareion must be predicted. Therefore, the nine output parameters at the next periareion are $r_{p,2}$, $r_{a,2}$, $i_{\text{Hill},2}$, $\cos\omega_{\text{Hill},2}$, $\sin\omega_{\text{Hill},2}$, $\cos\Omega_{\text{Hill},2}$, $\sin\Omega_{\text{Hill},2}$, time of flight TOF, and the time of flight between periareion and apoareion, TOF_{apo}. The latter is required to map the time at apoareion to the initial periareion time, which in its turn can be used to compute the next periareion time.

Training Several ANN design choices need to be made that affect the training. The same design choices are made as in Section 5.2, except for the numbers of neurons in each layer. The $r_{p,2}$, $r_{a,2}$, TOF and TOF_{apo} ANN have 30 neurons in each layer. The $i_{\text{Hill},2}$, $\cos\omega_{\text{Hill},2}$, $\sin\omega_{\text{Hill},2}$, $\cos\Omega_{\text{Hill},2}$, and $\sin\Omega_{\text{Hill},2}$ output parameters exhibit more non-linear responses. Therefore, their ANN have 40 neurons in each layer. Furthermore, because of the larger size of the ANN, a different computational set-up is used. The neural networks are trained using the MATLAB Statistics and Machine Learning Toolbox 11.2 [101] for a maximum of 23 hours on 12 cores. Each core has 1 Intel Xeon E5-2680 v3 @ 2.50GHz CPU.

Note, for each of the 9 output parameters, three separate ANN are trained for three different $i_{\text{Hill},1}$-regions; one ANN for $i_{\text{Hill},1} \in [5°, 65°]$, one for $i_{\text{Hill},1} \in [65°, 115°]$, and one for $i_{\text{Hill},1} \in [115°, 175°]$. All regions could have been trained in a single network per output parameter. The training of this larger ANN would be more efficient; the same trends for varying $i_{\text{Hill},1}$ on each output parameter only need to be learned once, in stead of three times. However, the training time per iteration, which increases linearly with provided number of data points, is roughly triple. This larger required training time surpassed the 24-hour cut-off for each task on the used computational set-up.

Validation As an independent test of the networks, a Monte Carlo analysis is performed. 100,000 points are uniformly sampled from the region within the bounds listed in Table 5.9. Using the scaled Poincaré maps, those initial conditions are mapped to the next periareion, and compared

to the ANN predicted response. The resulting error distributions are shown in Fig. 5.18 and the 1σ value and the 99 percentiles are displayed. The best fitting Gaussian distribution through this histogram is plotted in red. One can see that while the errors are not Gaussian, the Gaussian can be used as a conservative bound on the error distribution.

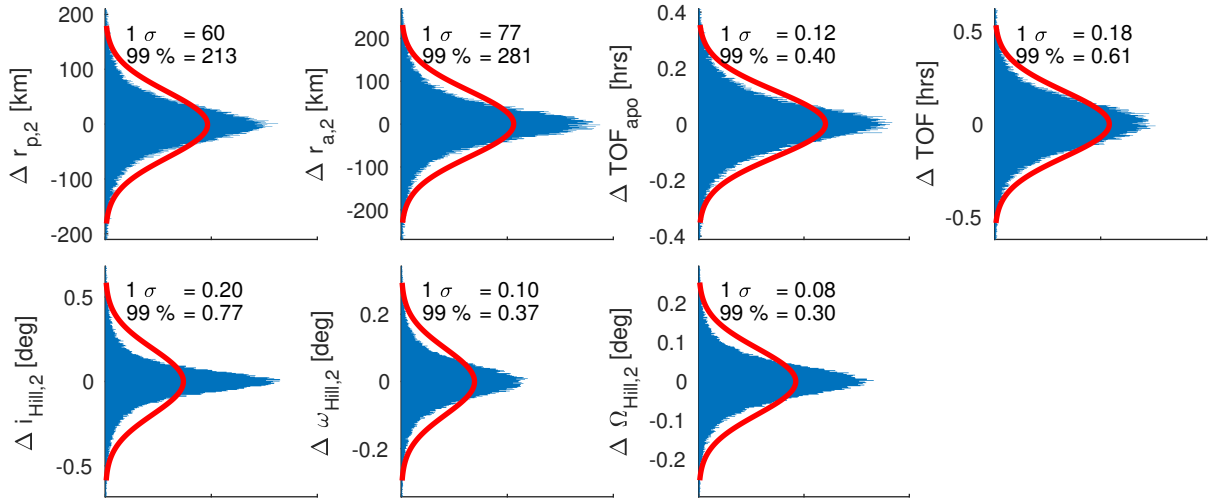

Figure 5.18: Distribution of the errors between the predicted and integrated apoareion scaled circular Hill Poincaré map for the 100,000 sampled points in the Monte Carlo simulation. The x-axis shows the number of samples for each y-axis bin.

Each output is predicted with a separate ANN and the errors are therefore expected to be independent. In Table 5.10, the correlations between the errors are shown. The most correlation exists between $r_{p,2}$, $r_{a,2}$, TOF and TOF_{apo}. Those parameters are all related to the magnitude of the angular momentum vector. As such, in regions of the phase space where this parameter changes quickly, and the ANNs struggle to capture this, all four parameters have larger errors.

Table 5.10: Correlation between the apoareion scaled Hill ANN prediction errors for the 100,000 sampled points in the Monte Carlo analysis.

	$\Delta r_{p,2}$	$\Delta r_{a,2}$	ΔTOF_{apo}	ΔTOF	$\Delta i_{\text{Hill},2}$	$\Delta\omega_{\text{Hill},2}$	$\Delta\Omega_{\text{Hill},2}$
$\Delta r_{p,2}$	1.00	−0.27	0.06	0.06	−0.02	0.01	0.01
$\Delta r_{a,2}$	−0.27	1.00	−0.02	−0.07	0.01	−0.03	0.05
ΔTOF_{apo}	0.06	−0.02	1.00	0.16	−0.00	0.01	−0.03
ΔTOF	0.06	−0.07	0.16	1.00	0.01	0.03	−0.04
$\Delta i_{\text{Hill},2}$	−0.02	0.01	−0.00	0.01	1.00	0.01	−0.04
$\Delta\omega_{\text{Hill},2}$	0.01	−0.03	0.01	0.03	0.01	1.00	−0.10
$\Delta\Omega_{\text{Hill},2}$	0.01	0.05	−0.03	−0.04	−0.04	−0.10	1.00

To determine if the ANN produces systematic errors, the $(\omega_{\text{Hill},1}, \Omega_{\text{Hill},1})$ locations are determined where errors occur that are larger than the 99 percentile for the apoareion scaled Hill ANN. There are systematic error regions that are similar to the band structures observed in Fig. 5.11. Those band structures were identified to be in impact regions. During the training of the apoareion scaled Hill ANN, those impact, and escape regions, are filtered out the training data. This creates local holes in the training phase space, and the ANN only have information of the gradients on one side of this boundary. Therefore, it is expected that the large error regions are near the impact and escape boundaries. Figure 5.19 verifies this hypothesis. This figure shows the points with errors larger than the 99 percentile, plotted in function of their response at the next periareion. For $r_{p,2}$, $r_{a,2}$, TOF, and TOF_{apo}, the errors are mainly near the escape boundary. This makes intuitive sense, since those parameters are largest in this region. The three angular

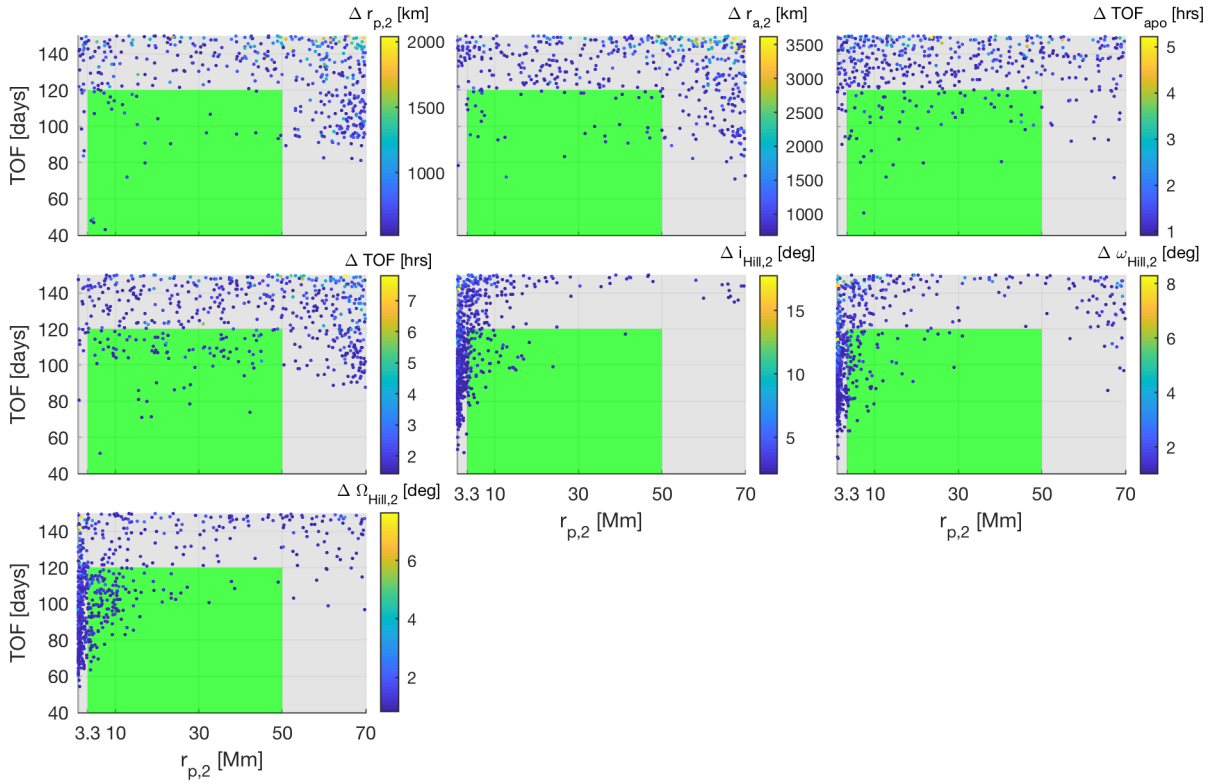

Figure 5.19: Locations in $r_{p,2} - TOF$ arrival phase space where errors larger than the 99 percentile for the apoareion scaled Hill ANN occur.

orbital elements have the largest errors near the impact boundary. In Fig. 5.8, it was shown that for low $r_{p,2}$-values, the $i_{\text{Hill},2}$-values vary very quickly in the $(\omega_{\text{Hill},1}, \Omega_{\text{Hill},1})$ phase space. Near this impact zone, the angular orbital elements still have strong gradients. Those gradients are difficult to capture, especially considering the lack of information on the behavior on the other side of the boundary.

This boundary issue is resolved through buffer zones introduced in the "Data processing" paragraph. While the true impact occurs at the Martian radius, only transfers below 1,000 km are filtered out. This introduces a buffer region, indicated in grey in Fig. 5.19. Within this region, the ANN have limited information of the surrounding points, in the direction of the boundary. At the true boundary of the impact, the ANN have more information in the direction of the 1,000 km boundary and can more accurately capture the gradients. The grey escape buffer region between 120 and 150 days TOF and between 50,000 and 70,000 km in $r_{p,2}$ functions similarly. Figure 5.20 re-creates Fig. 5.18, but excludes the errors of the points predicted to be the grey buffer region. This improves the accuracy of all parameters by 13-27%.

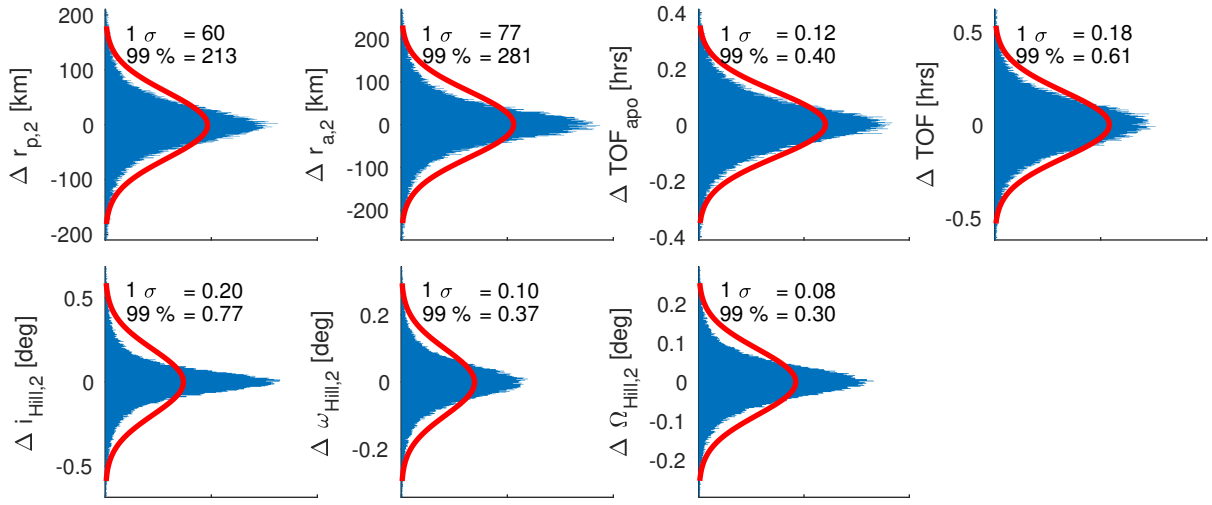

Figure 5.20: Distribution of the errors between the predicted and integrated apoareion scaled circular Hill Poincaré map for the 100,000 sampled points in the Monte Carlo simulation, excluding the grey buffer regions. The x-axis shows the number of samples for each y-axis bin.

5.3.2.3 Correction neural networks

The correction term between the apoareion scaled Hill system and the eccentric Hill system has continuous output, and is captured in a regression feedforward neural network. Before looking into the design of the neural network, the data is created and processed.

Data creation The difference in response for the scaled and eccentric Poincaré maps is quantified in a Monte Carlo analysis. The initial conditions, comprised of $r_{p,1}$, $r_{a,1}$, $i_{\text{Hill},1}$, $\omega_{\text{Hill},1}$, $\Omega_{\text{Hill},1}$ and initial time t_1 are uniformly sampled from the unscaled bounds in Table 5.8. The eccentric Poincaré map is numerically integrated, from which $\nu_{\text{M,apoareion}}$ can be extracted. This parameter is then used to scale the initial conditions prior to the scaled Poincaré map computation. Finally, the difference in response between the two dynamical systems is computed.

Data processing Prior to training, the raw integrated data is processed and some data is pruned out. The rationale is described in this paragraph. Figure 5.21 shows trends between the difference in $r_{a,2}$ for the eccentric and scaled Hill systems, and several states associated with the scaled Poincaré map. For instance, the differences in $r_{a,2}$ are very large for trajectories that have large $r_{p,2}$-response in the scaled Hill system. The scaled Hill networks filter out trajectories with $r_{p,2} > 70{,}000$ km. For these transfers, there is no need to predict the difference between the dynamical systems. For the correction networks, a limit of 50,000 km is therefore introduced (top left of Fig. 5.21). Second, large differences in $r_{a,2}$ occur for high TOFs and $r_{a,2}$-values in the scaled Hill system. A limit of 120 days on TOF (top right of Fig. 5.21) and a limit of 850,000 on $r_{a,2}$ (bottom left of Fig. 5.21) is imposed. Those transfers are lengthy and are deemed non-interesting as they are close to escape. By pruning out this data, the extrema in the $r_{a,2}$ differences are decreased by an order of magnitude, improving the expected training accuracy. A similar reduction is observed for the other output parameters.

No new classification networks are required to detect the $r_{p,2}$ and TOF limits. The $r_{p,2}$ and TOF limits are already captured at 70,000 km and 150 day respectively. As will be shown in the next subsection, buffer regions exists for the classification network in which erroneous classifications

might occur. The 50,000 km and 120 day limits bound this buffer region and the trajectories are most likely correctly classified. As shown in the previous subsubsection, the scaled Hill ANN include this buffer region. Therefore, the scaled Hill ANN should be accurate enough to detect if the real boundaries of 50,000 km $r_{p,2}$ and 120 day TOF are exceeded. The $r_{a,2}$ limit is a new limit and needs to be added to the criteria for the escape classification neural network. As a buffer, a 900,000 km limit is used for the classification, while an 850,000 km value is used for the data pruning for the correction networks. In the bottom right of Fig. 5.21, a trend between the difference in $r_{a,2}$, $i_{\text{Hill},1}$ and $\nu_{\text{M,apoareion}}$ is observed. The trends for the other parameters are shown in Fig. 5.22. The ANN are expected to be able to identify these trends.

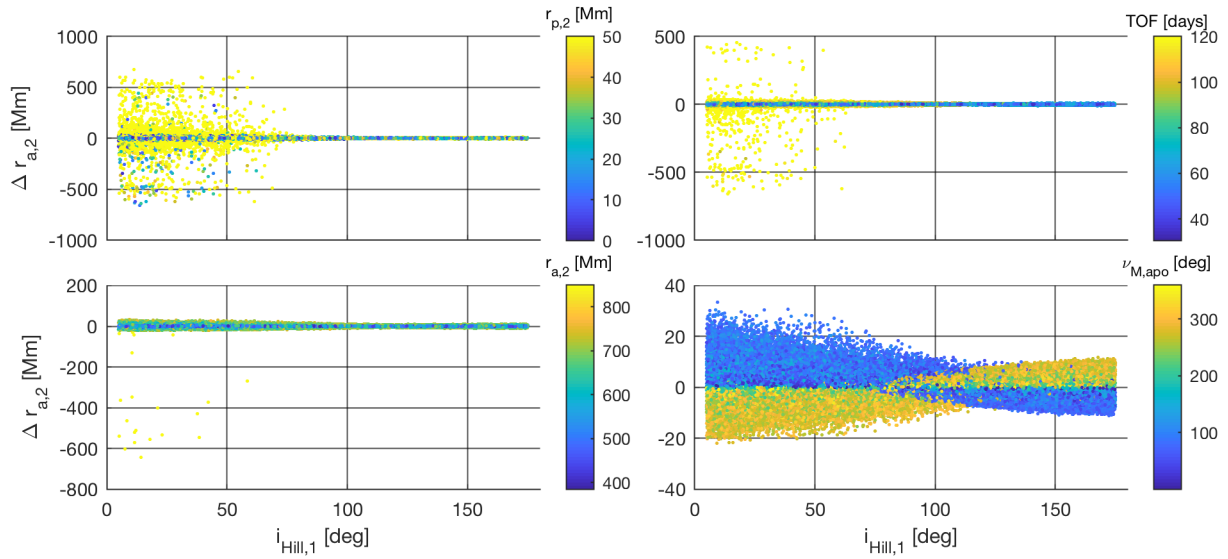

Figure 5.21: Example of the pruning procedure on the training data for the correction ANN. Example for the $r_{a,2}$ parameter.

Overview of input and output parameters

For the correction neural networks, the inputs are the unscaled $r_{p,1}$, $r_{a,1}$, $i_{\text{Hill},1}$, $\omega_{\text{Hill},1}$, $\Omega_{\text{Hill},1}$ and $\nu_{\text{M,apoareion}}$. The outputs are the unscaled errors in $r_{p,2}$, $r_{a,2}$, $i_{\text{Hill},2}$, $\omega_{\text{Hill},2}$, $\Omega_{\text{Hill},2}$, TOF and TOF_{apo}.

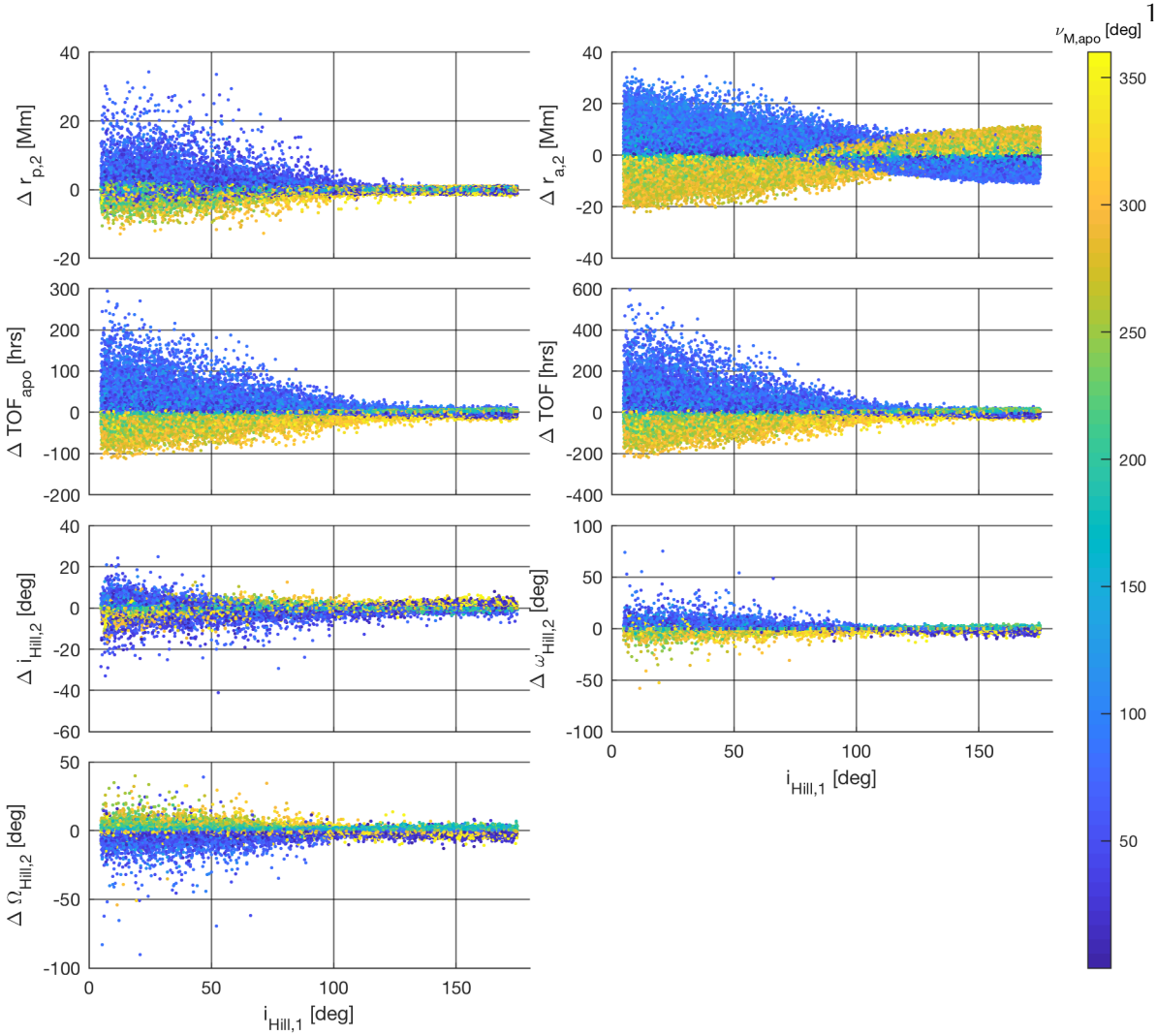

Figure 5.22: Visualization of the systematic differences between the integrated response in the apoareion scaled circular, and eccentric Hill systems.

Training Similar design choices as for the scaled Hill neural networks are made with a separate ANN for each output parameter, and a two hidden layer architecture with 30 by 30 neurons and a hyperbolic tangent activation function. The same cost function and training algorithms are used. The same training time constraints and computational set-up are used. However, the maximum training time is never encountered.

Validation The training is performed with 1e5, 2e5 and 1e6 points. As an independent accuracy test, another 100,000 sample points are created from a uniform distribution in input parameters. Table 5.11 lists the distribution statistics for the errors between the predicted and

integrated difference between the eccentric and scaled Poincaré map. The observed accuracy improvement is not linear with the number of training points. The majority of the difference between the eccentric and scaled Poincaré map is captured with 1e5 or 2e5 points, but the achieved accuracy is worse than the accuracies of the scaled Hill ANN. Despite the decreasing accuracy improvement per computed sample point, 1e6 points (Fig. 5.23) are required to provide similar accuracies as the scaled Hill ANN (Fig. 5.18). For problems with a large evaluation cost for the more complex dynamical model, this high number of evaluations is not always possible.

Table 5.11: Distribution statistics for the errors between the predicted and integrated difference between the eccentric and apoareion scaled circular Hill Poincaré maps for the 100,000 sampled points of the Monte Carlo simulation.

	Before training		100,000 training points		200,000 training points		1,000,000 training points		Units
	σ	99 perc.	σ	99 perc.	σ	99 perc.	σ	99 perc.	
$r_{p,2}$	697	2,419	178	507	133	400	77	281	km
$r_{a,2}$	2,677	10,001	168	505	149	483	101	371	km
TOF_{apo}	0.32	1.29	0.62	1.81	0.26	0.80	0.13	0.42	hrs
TOF	0.62	2.56	0.91	2.48	0.63	1.79	0.33	1.11	hrs
$i_{\text{Hill},2}$	0.55	2.08	0.33	1.19	0.28	0.91	0.21	0.71	deg
$\omega_{\text{Hill},2}$	0.63	1.95	0.35	0.85	0.31	0.73	0.21	0.59	deg
$\Omega_{\text{Hill},2}$	1.31	3.91	0.44	1.25	0.38	1.01	0.26	0.76	deg

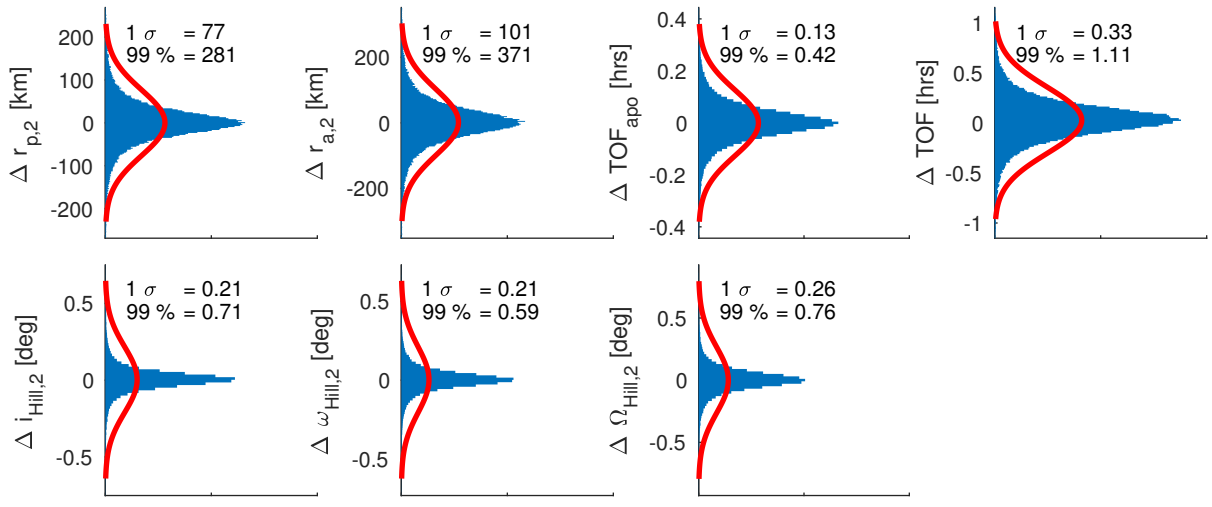

Figure 5.23: Distribution of the errors between the predicted and integrated difference between the eccentric and apoareion scaled circular Hill Poincaré maps for the 100,000 sampled points of the Monte Carlo simulation. The x-axis shows the number of samples for each y-axis bin.

The correlations between the errors are shown in Table 5.12. Similar conclusions can be drawn as for the scaled Hill error correlation terms. Again, it is verified if certain areas in initial phase space exist for which the correction ANN produce large errors. No systematic trend could be identified. It appears that the magnitude of the errors is random. Figure 5.24 demonstrates that the initial orbital elements that result in errors larger than the 99 percentile for the correction ANN are more or less uniformly distributed. In combination with the decreasing accuracy improvement per computed sampled point, observed in Table 5.11, this seems to suggest that the correction ANN capture all major systematic input-output couplings in the phase space. Hence, no specific zones within the phase space exist for which the correction ANN errors are systematically larger.

Table 5.12: Correlation between the correction ANN prediction errors for the 100,000 sampled points in the Monte Carlo analysis.

	$\Delta r_{p,2}$	$\Delta r_{a,2}$	ΔTOF_{apo}	ΔTOF	$\Delta i_{\text{Hill},2}$	$\Delta\omega_{\text{Hill},2}$	$\Delta\Omega_{\text{Hill},2}$
$\Delta r_{p,2}$	1.00	−0.24	0.02	0.09	0.04	0.02	−0.03
$\Delta r_{a,2}$	−0.24	1.00	0.06	−0.03	−0.03	−0.01	−0.01
ΔTOF_{apo}	0.02	0.06	1.00	0.36	−0.01	0.03	−0.07
ΔTOF	0.09	−0.03	0.36	1.00	0.03	0.05	−0.05
$\Delta i_{\text{Hill},2}$	0.04	−0.03	−0.01	0.03	1.00	0.05	−0.05
$\Delta\omega_{\text{Hill},2}$	0.02	−0.01	0.03	0.05	0.05	1.00	−0.24
$\Delta\Omega_{\text{Hill},2}$	−0.03	−0.01	−0.07	−0.05	−0.05	−0.24	1.00

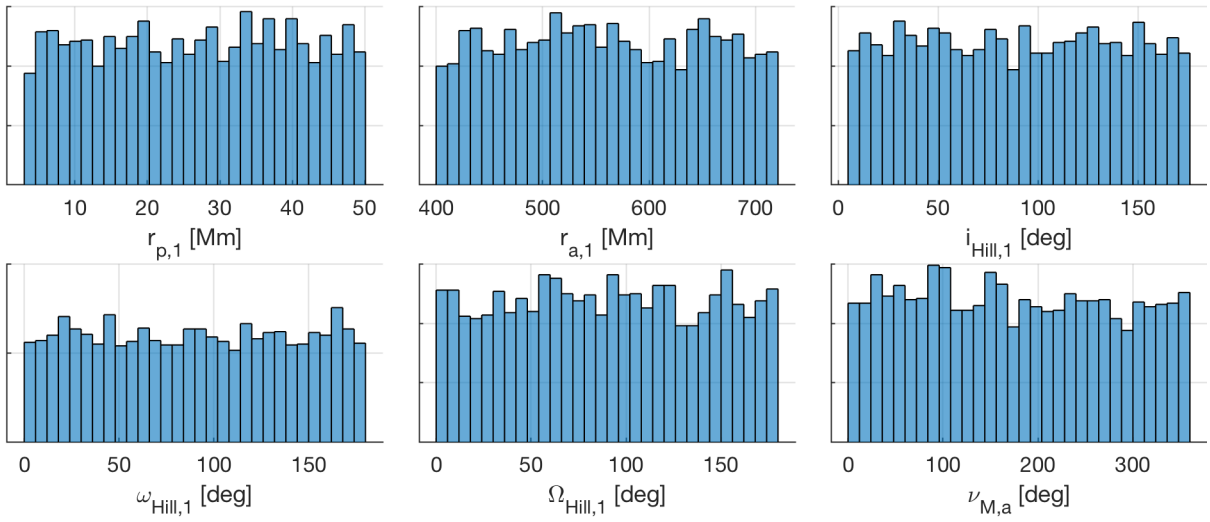

Figure 5.24: Distributions of all input states for which any of the predicted correction terms has an error larger than its 99 percentile value shown in Fig. 5.23. The y-axis shows the number of samples for each x-axis bin.

5.3.2.4 Escape and impact classification neural networks

Escape and impact are discrete events; therefore, a classification neural network is used to predict which initial conditions lead to escape or impact.

Data creation The integrated trajectories to train the scaled Hill ANN are re-used, with the same bounds and resolution listed in Table 5.9. From those integrations, the data for the classification neural networks is constructed. Some trajectories are immediately indicated as escape trajectories, if the periareion-to-apoareion segment, or apoareion-to-periareion segment of the trajectory is longer than 250 days. Furthermore, transfers with a TOF $>$ 150 days, $r_{p,2}$ >70,000 km, or $r_{a,2} >$ 900,000 km, are marked as escaping trajectories. Similarly, trajectories with $r_{p,2} <$ 1,000 km are marked as impacting transfers. Note that these numbers are the boundaries of the buffer regions and not the actual boundaries of the anomalies.

Overview of input and output parameters There are five scaled input parameters: $r_{p,1}$, $r_{a,1}$, $i_{\text{Hill},1}$, $\omega_{\text{Hill},1}$, $\Omega_{\text{Hill},1}$, scaled according to the time at apoareion. The outputs of a classification network indicate the chance that a specific input results in a specific output category. For the considered classification networks, there are only two possible classes: anomaly or no anomaly. Therefore, there are two outputs. For the training data, the corresponding class is known deterministically. Therefore, for a trajectory without anomaly, the first output is 0, and the second output 1. For a trajectory with anomaly, the first output is 1, and the second output 0. When evaluating a classification neural network on new data, the output can take intermediate values. The class associated with the output neuron with the largest output is the most likely. The sample is thus classified as that class.

Training A separate ANN is created to detect the escape and impact conditions. Each of those networks has two outputs, and a two-hidden layer architecture with 30 neurons each. The outputs of a classification neural network describes a probability. Therefore, each output must be positive, and the sum of all outputs must be equal to one. For a linear activation function, this is not guaranteed. Therefore, a softmax activation layer is applied to the output layer [105]. First, as

for any neuron in a neural network, the weighed input of the two output neurons are computed, z_1 and z_2. After activation, the outputs of neuron 1 and neuron 2 are:

$$\phi(z_1) = \frac{e^{z_1}}{e^{z_1} + e^{z_2}} \qquad \phi(z_2) = \frac{e^{z_2}}{e^{z_1} + e^{z_2}} \tag{5.6}$$

For a classification neural network with a softmax layer, a cross-entropy cost function usually finds a better local optimum than the mean squared error cost function [106]. The cross-entropy cost function is incompatible with the Levenberg-Marquardt back-propagation algorithm. Therefore, the scaled conjugate gradient algorithm is used. The training is done on a NVIDEA Tesla K80 GPU unit and does not exceed 15 minutes.

Validation As an independent test of the networks, a Monte Carlo analysis is performed. The 100,000 element data set created for the validation of the scaled Hill ANN is re-used, and the predicted and true classifications are compared. The left part of Fig. 5.25 shows the confusion matrix for the escape classification network. The green and red entries display the correct and incorrect classifications, respectively. The last column displays the percentages of the samples predicted to escape or not escape that are correctly (green) and incorrectly (red) classified. The bottom row shows the percentages of the samples that truly escape or not escape that are correctly (green) and incorrectly (red) classified. The bottom right element shows the high overall accuracy. There are some false positives, and some false negatives. The integrated results for those points are shown in the leftmost part of Fig. 5.26. All false positives (blue) are in the buffer region (grey). Even though they do not escape according to the 70,000 km and 150 day standard (red region), they escape under the more strict 50,000 km and 120 day standard (green region) and are thus correctly classified. For the false negatives (black), the escape is not detected. The scaled Hill networks' training data includes the buffer region and the false negatives fall just outside this region. It is expected that the scaled Hill networks provide sufficient accuracy to verify that these points are indeed outside the 50,000 km and 120 day region. This is shown in the right part of Fig. 5.26. The predicted responses for the false negatives are plotted and indeed fall outside the 50,000 km and 120 day region. Thus, the predicted responses can be used to detect escape of

the false negatives. By using the buffer region, the incorrect classification of the false positives and false negatives is entirely resolved. A similar procedure is followed for the validation of the impact classification network. Again, the buffer region resolves the incorrect classification of the false positives and negatives.

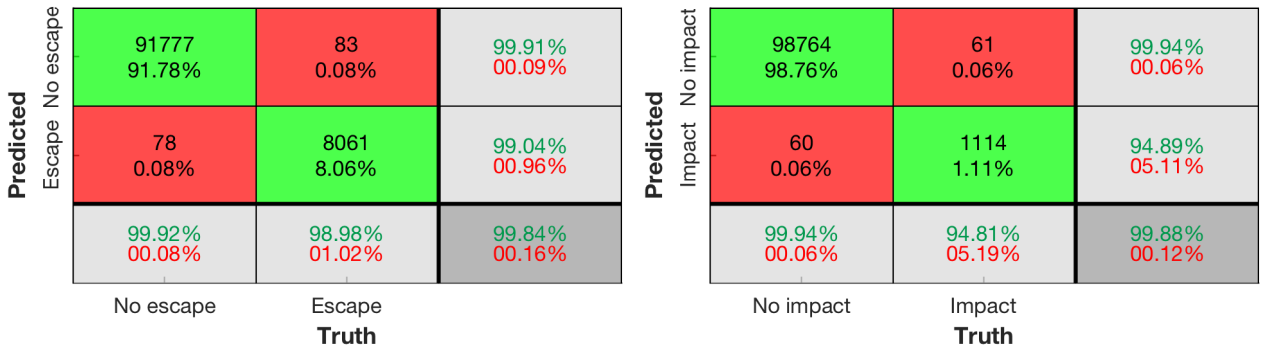

Figure 5.25: Confusion matrices for the escape (left) and impact (right) classification ANN.

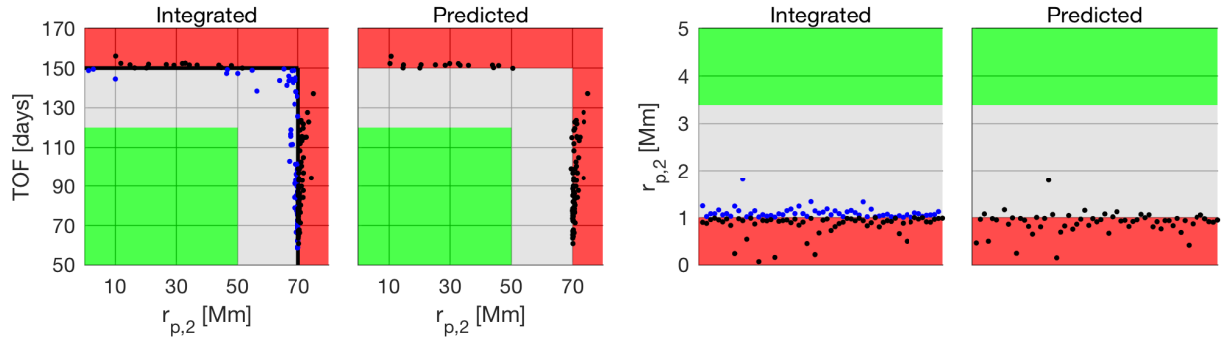

Figure 5.26: Comparison of the integrated versus predicted results for erroneously classified transfers: false positives (blue), false negatives (black), for escape (left) and impact (right) classification.

5.3.3 Architecture accuracy

In this subsection, the overall accuracy of the architecture is evaluated when the three groups of ANN co-operate to predict the response of the periareion Poincaré map in the eccentric Hill system. A 100,000 point Monte Carlo analysis is performed where the unscaled phase space in Table 5.7 is uniformly sampled. Note that the departure time is sampled, and not the time when the transfers pass apoareion. Those samples are numerically integrated using the eccentric Hill

system. The flow chart in Fig. 5.16 is followed to predict the response in the eccentric Hill system, with a small difference. All the ANN families use $\nu_{\mathrm{M,apoareion}}$ either as an input parameter, or a parameter to scale the input parameters. However, this parameter is not readily known from the initial time. Therefore, an iterative procedure is followed where the $\nu_{\mathrm{M,apoareion}}$ is predicted. The $\nu_{\mathrm{M,apoareion}}$ is initialized to $\nu_{\mathrm{M},1}$. Then, using the scaled Hill and correction ANN, the TOF_{apo} is predicted. From this, the new $\nu_{\mathrm{M,apoareion}}$ is computed and used to adjust the scaling of the initial periareion. This procedure is repeated until convergence, i.e., when $\nu_{\mathrm{M,apoareion}}$ does not change by more than 1e-6 rad. Using the final value for $\nu_{\mathrm{M,apoareion}}$, the initial states are scaled. Those scaled states are then used to predict which states do not impact nor escape. For those scaled states, the response in the scaled Hill system is computed. The predicted points that arrive in the buffer region are filtered out: $r_{p,2}$ above 50,000 km, $r_{a,2}$ above 850,000 km and TOF above 120 days, i.e. the points outside the green region. For the remaining states, the response is scaled back to the real phase space and the correction terms are computed and added to the response of the scaled Hill system.

For 16,256 points, the integrated and predicted transfers are both outside the green region. For 172 points, or 0.172% of the points, there is a conflict between the integrated and predicted green region classifications. For those points, the predicted and integrated $r_{p,2}$ and TOF are plotted in Fig. 5.27. The difference in classifications are due to small oscillations near the escape and impact criteria, depicted as black dashed lines. Those oscillations are a result of the inaccuracies in the scaled Hill and correction ANN and cannot be avoided. The oscillations can potentially be reduced in size by improving the scaled Hill and correction ANN by increasing the amount of data, the number of hidden layers, the number of neurons, etc.

83,560 out of the 100,000 points are correctly predicted to be in the green region and the difference between the predicted and integrated response can be quantified. The error statistics for those points are displayed in Fig. 5.28. As a summary, the 1σ and 99 percentiles are shown in Table 5.13, along with the accuracies of the different ANN families. From this table, one can see that the combined σ-value is smaller than the root squared value of the scaled Hill and correction ANN

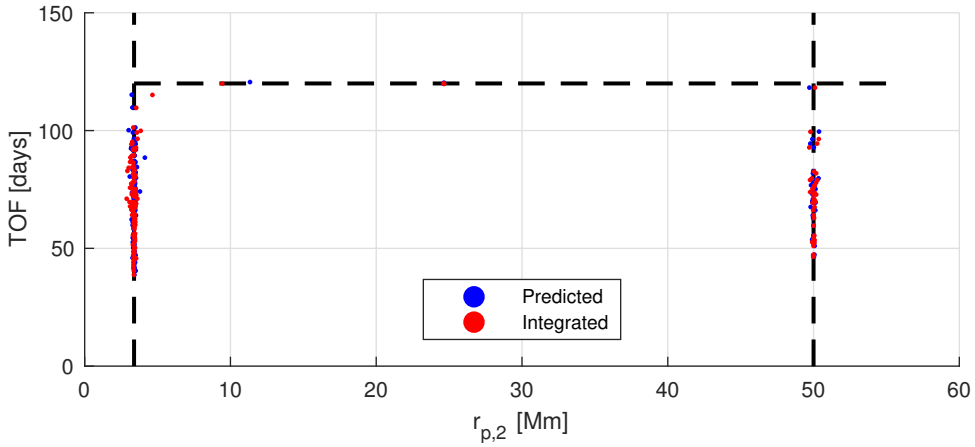

Figure 5.27: Integrated versus predicted $r_{p,2}$ and TOF response at 172 incorrectly classified samples for the single-loop validation.

σ-values. While the distributions are not Gaussian, the sum of the two Gaussian approximations, whose σ is equal to the RSS of the individual σ's, can be used as a conservative error distribution. This sum of the Gaussians is plotted in black. Table 5.14 displays the correlation between the errors. Again, there is some correlation, mostly between $r_{p,2}$, $r_{a,2}$, TOF and TOF_{apo}.

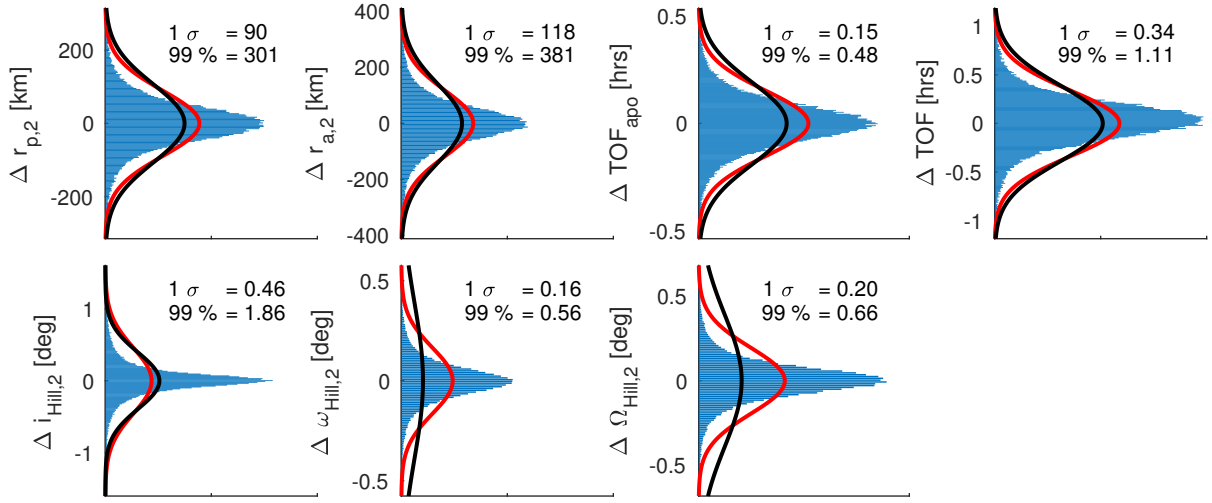

Figure 5.28: Distribution of the errors of the predicted orbital elements at periareion two using the entire architecture, compared to the orbital elements integrated in the eccentric Hill system for the 100,000 sample points in the Monte Carlo simulation of the entire architecture. The x-axis shows the number of samples for each y-axis bin.

To understand if the entire architecture produces systematic errors, Fig. 5.29 shows where in the phase space at the second periareion the errors occur that are larger than the 99 percentile for

Table 5.13: Distribution statistics for the errors of the predicted response, compared to the integrated response, for different elements of the ANN architecture.

Parameter	Scaled Hill		Correction		Entire architecture		RSS scaled Hill and correction		Unit
	σ	99 perc.	σ	99 perc.	σ	99 perc.	σ	99 perc.	
$r_{p,2}$	74	263	77	281	90	301	106	387	km
$r_{a,2}$	96	345	101	371	118	381	141	508	km
TOF_{apo}	0.14	0.46	0.13	0.42	0.15	0.49	0.19	0.62	hrs
TOF	0.21	0.71	0.33	1.11	0.34	1.17	0.39	1.32	hrs
$i_{\text{Hill},2}$	0.26	1.06	0.21	0.48	0.46	1.87	0.34	1.28	deg
$\omega_{\text{Hill},2}$	0.14	0.50	0.21	0.59	0.17	0.56	0.25	0.77	deg
$\Omega_{\text{Hill},2}$	0.11	0.41	0.26	0.76	0.20	0.66	0.28	0.86	deg

Table 5.14: Correlation between the prediction errors of the entire architecture.

	$\Delta r_{p,2}$	$\Delta r_{a,2}$	ΔTOF_{apo}	ΔTOF	$\Delta i_{\text{Hill},2}$	$\Delta\omega_{\text{Hill},2}$	$\Delta\Omega_{\text{Hill},2}$
$\Delta r_{p,2}$	1.00	−0.28	−0.10	−0.12	0.04	−0.00	−0.01
$\Delta r_{a,2}$	−0.28	1.00	0.02	0.08	−0.04	0.02	0.02
ΔTOF_{apo}	−0.10	0.02	1.00	0.34	0.01	−0.02	0.06
ΔTOF	−0.12	0.08	0.34	1.00	0.00	−0.04	0.07
$\Delta i_{\text{Hill},2}$	0.04	−0.04	0.01	0.00	1.00	−0.00	−0.02
$\Delta\omega_{\text{Hill},2}$	−0.00	0.02	−0.02	−0.04	−0.00	1.00	−0.20
$\Delta\Omega_{\text{Hill},2}$	−0.01	0.02	0.06	0.07	−0.02	−0.20	1.00

the entire architecture. Again, the largest errors are found near the impact and escape boundaries. The errors are combinations of errors in the apoareion scaled Hill ANN and errors in the correction term ANN. The former has a clear structure (Fig. 5.19), while the latter appears random (Fig. 5.24). The structure is therefore dominated by the error regions of the apoareion scaled Hill ANN.

5.3.4 Architecture accuracy multiple loops

The framework developed in the previous sections can be used to chain multiple orbits; i.e, the predicted orbital elements at periareion two can be used as the initial condition for a next prediction procedure. In this section, the architecture for this procedure is developed, and its accuracy is determined, based on a 10,000 point Monte Carlo analysis. For the first loop, the exact same architecture is used. For the subsequent loops, a very similar architecture is used. Again,

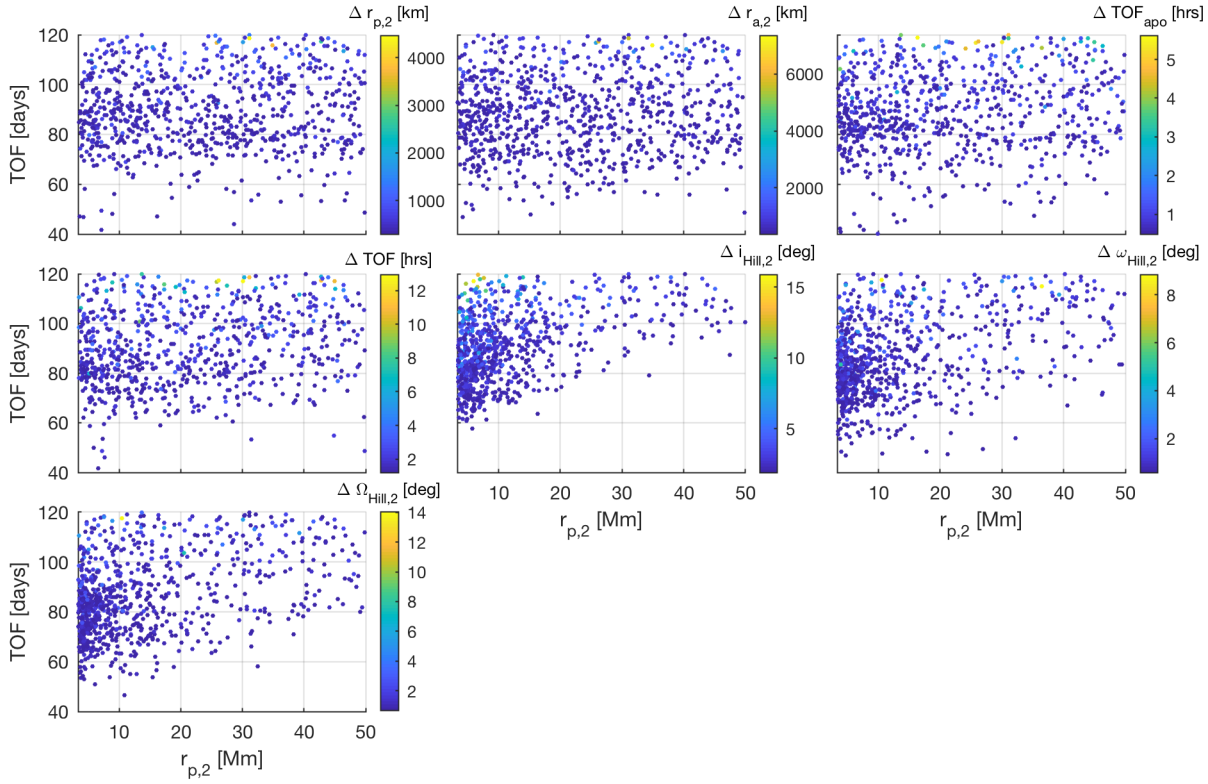

Figure 5.29: Locations in $r_{p,2} - TOF$ arrival phase space where errors larger than the 99 percentile for the entire architecture occur.

the $\nu_{\mathrm{M,apoareion}}$ is computed using an iterative procedure. Using the final value for $\nu_{\mathrm{M,apoareion}}$, the initial states are scaled. An extra filtering step is required: some of the scaled initial states are outside the scaled bounds in Table 5.9 for which the ANN are trained. An example are transfers that return after the first loop with $r_{a,2}$ larger than 720,000 km. If they return when Mars is near its perihelion, the scaled value is above 800,000 km and must be filtered out. Furthermore, some transfers return with $i_{\mathrm{Hill},2}$ smaller than 5° or larger than 175°. After this extra step, the exact same architecture is used.

A more complex classification problem occurs: trajectories that are incorrectly classified in the first loop are carried over to the next loop. Table 5.15 gives an overview of the classification performance. There are five entries. "Points at start of loop" lists how many transfers still exist at the start of the loop. "Both green" lists the points for which both the integrated and predicted

response are in the green region. For this category, the error can be quantified, shown in Table 5.16. "Both outside green" lists the transfers for which the integrated and predicted transfers are both outside the green region. For the "conflict" category, the integrated and predicted transfer conflict on the classification. Similar to Fig. 5.27, Fig. 5.30 is created. Again, these conflicts are caused by small oscillations near the escape and impact criteria. Finally, for the "outside ANN training" category, the scaled state is outside the training region and can no longer be predicted.

Table 5.15: Statistics of the classification errors for the multiple loop architecture.

Loop	1	2	3	4
Points at start of loop	10,000	8,388	6,981	5,932
Both green	8,388	6,981	5,932	5,218
Both outside green	1,598	1,327	1,002	680
Conflict	14	28	26	21
Outside ANN training	0	52	21	14

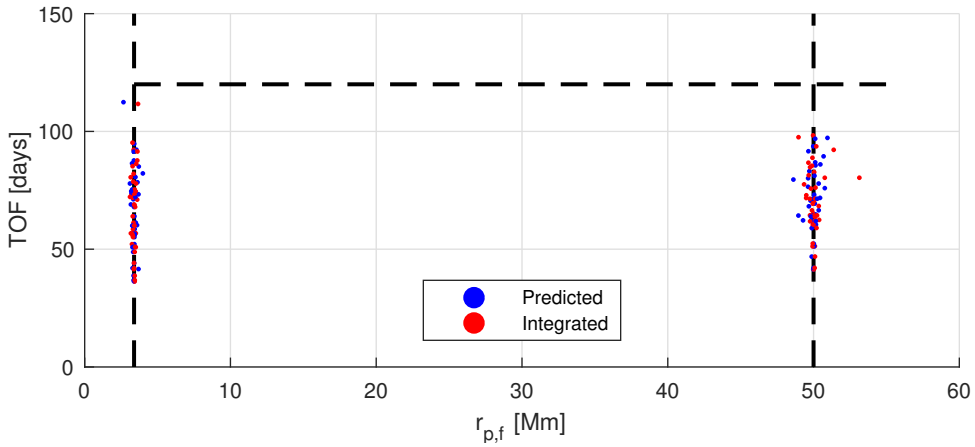

Figure 5.30: Integrated versus predicted $r_{p,f}$ and TOF response at 89 incorrectly classified samples for the multiple-loop validation.

The errors for the points in the "Both green" category can be quantified. The 1 σ and 99 percentiles are listed in Table 5.16, and the histograms for loop 2, 3 and 4 are shown in Fig. 5.31. The errors do not grow linearly. Between loop 1 and loop 2, the errors increase strongly. This increase levels of for subsequent loops. An exception is the continuous increase in errors in TOF_{apo} and TOF. These parameters are used for the iterative refinement of $\nu_{\text{M,apoareion}}$. As this procedure

Table 5.16: Statistics of the prediction errors of the multiple loop architecture.

Parameter	Loop 1		Loop 2		Loop 3		Loop 4		Unit
	σ	99 perc.	σ	99 perc.	σ	99 perc.	σ	99 perc.	
r_p	90	297	247	797	311	1222	334	1274	km
r_a	118	384	253	874	325	1270	360	1399	km
TOF_{apo}	0.15	0.48	1.34	4.88	2.97	11.88	4.60	19.41	hrs
TOF	0.34	1.11	2.71	10.02	4.08	17.13	5.74	22.74	hrs
i_{Hill}	0.46	1.86	0.59	2.39	0.66	2.62	0.66	2.63	deg
ω_{Hill}	0.16	0.56	0.30	0.98	0.40	1.28	0.41	1.46	deg
Ω_{Hill}	0.20	0.66	0.30	1.04	0.40	1.35	0.45	1.62	deg

uses the identified timing from the previous loop, small errors in the previous loops amplify the errors. While the time is roughly off by a day after four loops, this only results in a small angular difference in predicted $\nu_{\text{M,apoareion}}$. Therefore, the scaling of the Hill system, and as such the other predicted orbital elements, are only marginally affected. Another concern arises from Table 5.16. For multiple loops, the 99 percentile r_p error grows above 1000 km, which is a significant error for low periareions. Therefore, in Fig. 5.32, the error distribution is given for different regions of $r_{p,5}$, the periareion after loop 4. At small $r_{p,5}$ levels, the $r_{p,5}$ errors are smaller, alleviating the concern.

5.3.5 Conclusion and discussion

This section demonstrates how a combination of artificial neural networks can be used to capture the response of a periareion Poincaré map for a large phase space in the eccentric Hill system. Several common issues to construct a database with Poincaré maps are alleviated through the use of ANN. First, the required number of integrations can be significantly lowered because of the excellent capabilities of ANN to interpolate in between provided data. Furthermore, the number of integrations can be decreased using a simplified dynamical model allowing a dimensionality reduction. Despite this simplified dynamical model, little to no accuracy is lost by using a combination of two ANN families: one to predict the response in the simplified model, and one to predict the difference in response between the simplified and more accurate dynamical model. Second, large databases with a lot of numerically integrated data require a large storage space.

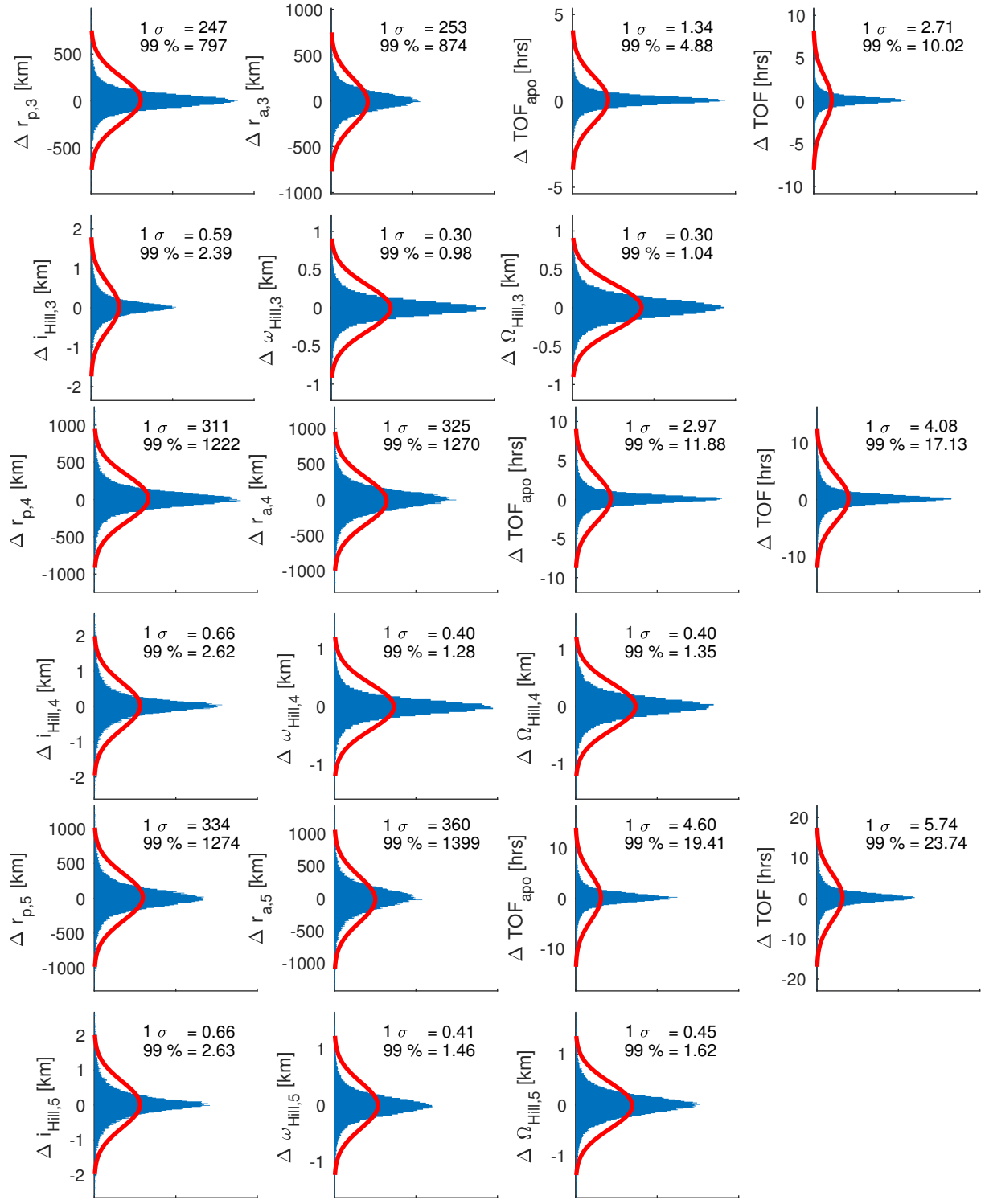

Figure 5.31: Distribution of the errors of the predicted orbital elements at periareions three, four, and five, using the entire architecture, compared to the orbital elements integrated in the eccentric Hill system for the 10,000 sample points in the Monte Carlo simulation of the entire architecture. The x-axis shows the number of samples for each y-axis bin.

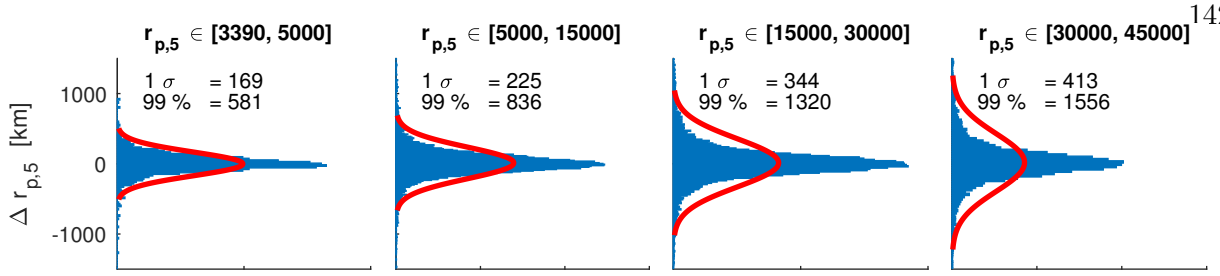

Figure 5.32: Distribution statistics of the errors of the predicted orbital elements at the fifth periareion using the ANN architecture for multiple loops, compared to the orbital elements integrated in the eccentric Hill system for different orbital regimes of $r_{p,5}$. The x-axis shows the number of samples for each y-axis bin.

Once the ANN are trained, their fast evaluation allows for the data to be recomputed on the fly. Thus, the database does not require to be stored. For this research, all the ANN combined require a megabyte of storage space. The ANN thus essentially function as compression agents on the data. Third, anomalies can occur for Poincaré maps. Those have been monitored through the usage of classification neural networks. For this, buffer regions were found to be of utmost importance. These regions resolve the incorrect classification of false positives and false negatives. Furthermore, they improve the accuracy of the scaled Hill ANN near the boundaries of the anomaly.

5.4 ANN architecture for backward Poincaré maps

In Subsubsection 5.2.2.3, Algorithm 2 was developed to find the initial conditions to target a specific final state. This has been done by creating grids in initial conditions, predicting the next periareions, and filtering out the transfers arriving near Phobos or Deimos. Thus, a large number of the predictions are done in vain. For this application, it is more efficient to create a grid in the arrival conditions at Phobos or Deimos, and predicting the initial conditions. That way, it is guaranteed that every prediction results in a transfer that arrives at the desired arrival orbit. This requires the prediction of backwards periareion Poincaré maps; i.e., predict a periareion backwards in time to its previous periareion. In analog with the previous section, this section designs a backwards ANN architecture that allows the evaluation of transfers departing at different periapse radii and that allows to predict transfers for multiple revolutions around Mars. In this section, the ANN will be trained on backwards integrated periareion Poincaré maps. The arrival periareion is indexed with subscript f, subsequent previous periareion with $f-1$, $f-2$, ... This section's structure is identical to the structure of the previous section.

5.4.1 Considered phase space

The region of the phase space that is considered for the backwards ANN architecture is identical to the region of the forward ANN architecture. The bounds on the phase space can be seen in Table 5.17.

Table 5.17: Bounds on the considered backwards phase space.

Parameter	Lower bound	Upper bound	Unit
$r_{p,f}$	3,390	45,000	km
$r_{a,f}$	440,000	720,000	km
$i_{\text{Hill},f}$	0	180	deg
$\omega_{\text{Hill},f}$	0	180	deg
$\Omega_{\text{Hill},f}$	0	180	deg
t_f	0	1	Martian year

5.4.2 Methodology

In this section, the different neural networks are developed. First, an overview is given on the envisioned architecture, with three groups of artificial neural networks. Then, each of the three identified groups is treated in more detail, where the training data creation, training and validation of the neural networks are explained.

5.4.2.1 General architecture

The same design philosophy as for the forward architecture is used where three different groups of neural networks co-operate. The first group uses regression neural networks that predict the response in the scaled Hill system. The second group uses regression neural networks to predict the error between the scaled Hill and the eccentric Hill system. The third group uses classification neural networks to predict when transfers escape or impact. The terms escape and impact are still used throughout this section to emphasize the analog with the forward architecture. In reality, they represent different anomalies. Therefore, a note must be made on the terminology escape and impact. The term escape made intuitive sense for forward integration. Transfers that at a previous periareion have a very large r_p, r_a, or time of flight are not technically escaping trajectories. In fact, they are transfers that are gravitationally captured around Mars due to an eccentricity reduction caused by the solar perturbations. While these transfers can be used for specific applications, they are filtered out in this research. Similarly, trajectories that are below the Martian surface at the previous periareion are in reality not impacting transfers, but transfers originating from below the surface of Mars.

5.4.2.2 Scaled Hill neural networks

The scaled Hill system has continuous output, and is captured in a regression feedforward neural network. The same five steps are followed to design, train and validate these ANN.

Data creation The used training range and resolution is tabulated in Table 5.18.

Table 5.18: Sampling density of the orbital elements at the final periareion used as training data for the backwards scaled Hill and classification neural networks.

	Region 1			Region 2			Sampled points
	Lower bound	Spacing	Upper bound	Lower bound	Spacing	Upper bound	
$r_{p,f}$ (km)	3,100	3,000	12,100	17,100	5,000	52,100	12
$r_{a,f}$ (km)	400,000	20,000	800,000	-	-	-	21
$i_{\text{Hill},f}$ (deg)	5	10	175	-	-	-	18
$\omega_{\text{Hill},f}$ (deg)	0	5	180	-	-	-	37
$\Omega_{\text{Hill},f}$ (deg)	0	5	180	-	-	-	37
							Total: 6,209,784

Data processing Prior to training, the raw integration data is processed. First, the trajectories that escape are filtered out and indexed for the escape classification neural network. Second, some data is pruned out. In analogy with the forward networks' limits on $r_{p,2}$, TOF, and $r_{a,2}$, upper and lower limits on $r_{p,f-1}$ are imposed, with buffer regions against wrongful classification. A lower limit of 1000 km is imposed on $r_{p,f-1}$. In Fig. 5.33, those transfers are depicted in red. Furthermore, an upper limit of 70,000 km is imposed. These transfers are again added to the index list of escaping trajectories. These transfers are depicted in green and are also the longest. Further, a limit of -150 days TOF has been imposed. These indexes are also added to the list of escape trajectories. These transfers are depicted in black. Furthermore, an $r_{a,f-1}$ upper limit of 900,000 km has been imposed. In total, 5,556,519 transfers survived the data pruning. Their response is indicated in blue.

Overview of input and output parameters Similar to the forward scenario, there are five input and nine output parameters. The input parameters are $r_{p,f}$, $r_{a,f}$, $i_{\text{Hill},f}$, $\omega_{\text{Hill},f}$, and $\Omega_{\text{Hill},f}$. The output parameters are $r_{p,f-1}$, $r_{a,f-1}$, $i_{\text{Hill},f-1}$, $\cos\omega_{\text{Hill},f-1}$, $\sin\omega_{\text{Hill},f-1}$, $\cos\Omega_{\text{Hill},f-1}$, $\sin\Omega_{\text{Hill},f-1}$, time of flight TOF, and the time of flight between periareion f and the apoareion between periareion f and $f-1$, TOF_{apo}.

Training The same ANN architecture and training framework is used as for the forward neural networks. Unlike the forward neural networks, 6 different ANN per output parameter are trained. Again, three regions based on the inclination. Furthermore, each of those three regions is

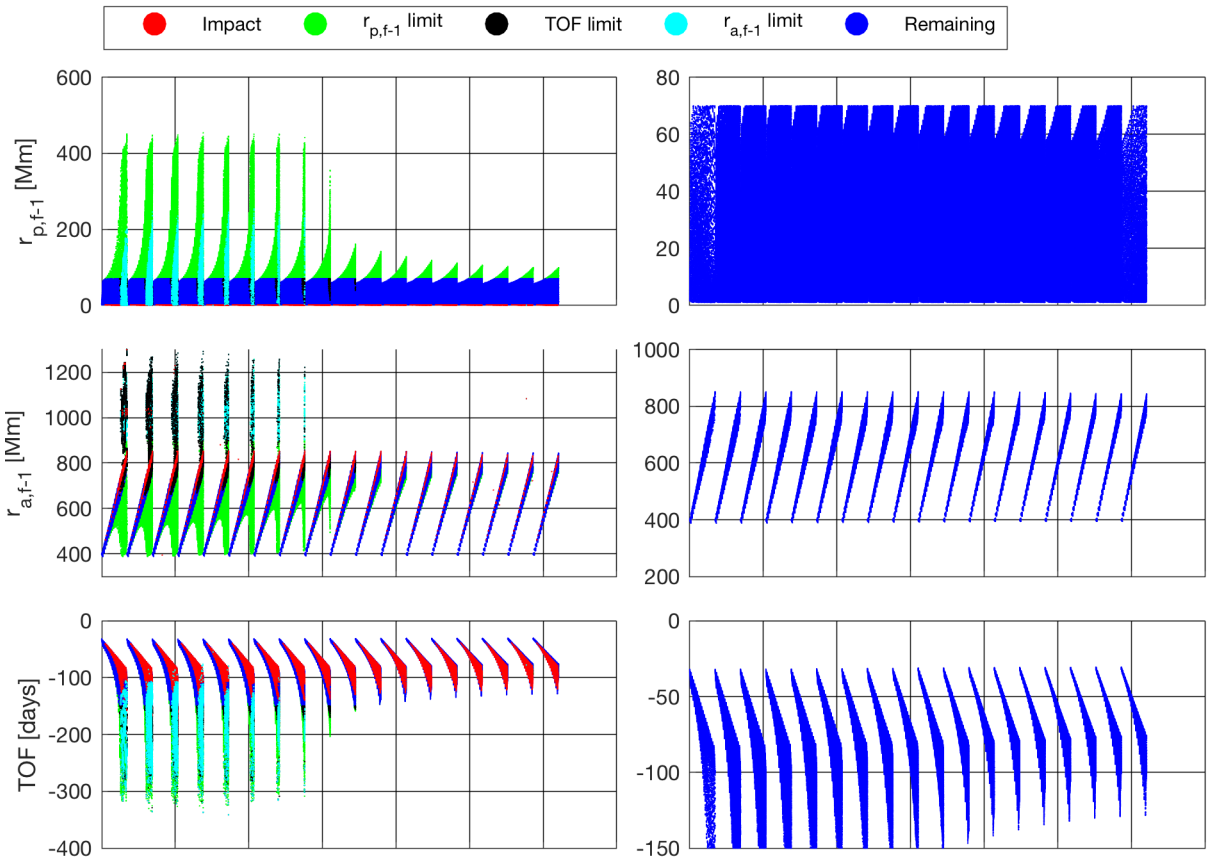

Figure 5.33: Pruning of the training data for the backwards apoareion scaled Hill neural networks. Left: original data. Right: remaining data after data pruning.

split up in two regions based on apoareion radius. The training of 6 regions was not required to obtain a good overall accuracy, but was done as a result of a smaller phase space that was originally considered. The original training range was $r_{a,f} \in [520\text{e}3, 800\text{e}3]$. Later, it was decided to add the $r_{a,f} \in [400\text{e}3, 520\text{e}3]$ region. The ANN for the $r_{a,f} \in [520\text{e}3, 800\text{e}3]$ was already trained at that time, with good levels of accuracy. Therefore, it was decided to train the $r_{a,f} \in [400\text{e}3, 520\text{e}3]$ region in a separate network, avoiding the computational resources required to re-train the $r_{a,f} \in [520\text{e}3, 800\text{e}3]$ region, as part of a single ANN for the entire $r_{a,f} \in [400\text{e}3, 800\text{e}3]$ region.

Validation As an independent test of the networks, a Monte Carlo analysis is performed. 100,000 points are uniformly sampled from the region within the bounds of Table 5.18. Using the scaled Poincaré maps, those initial conditions are mapped to the previous periareion, and compared to the ANN predicted response. The resulting error distributions are shown in Fig. 5.34 and the 1σ

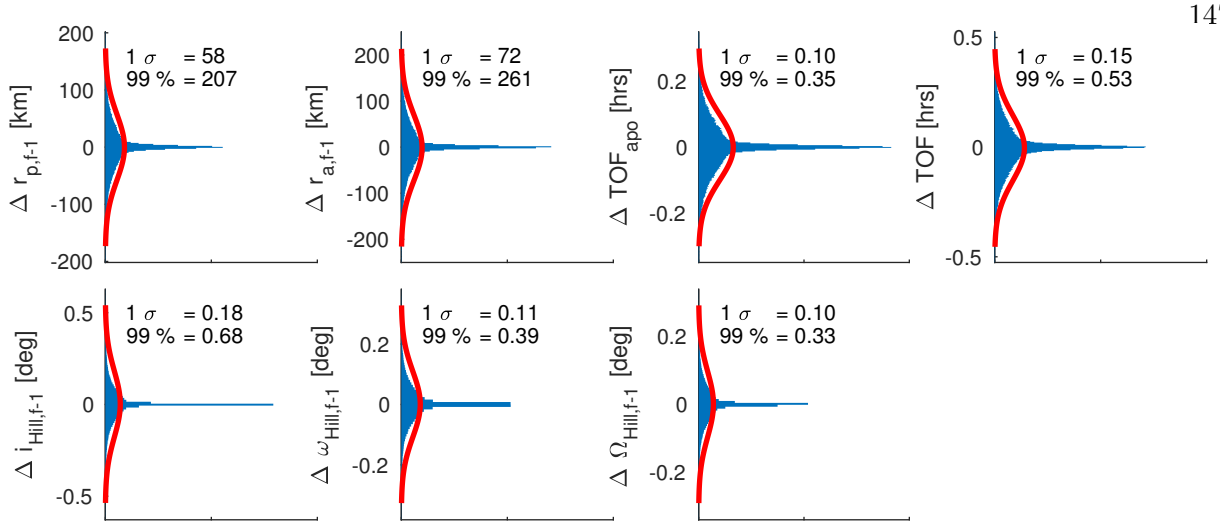

Figure 5.34: Distribution of the errors between the predicted and integrated backwards apoareion scaled circular Hill Poincaré map for the 100,000 sampled points in the Monte Carlo simulation. The x-axis shows the number of samples for each y-axis bin.

value, along with the 99 percentiles are displayed. The best fitting Gaussian distribution through this histogram is plotted in red. One can see that while the errors are not Gaussian, the Gaussian can be used as a conservative bound on the error distribution. A spike is observed near zero. Unlike the forward neural networks, 6 different regions are used for which the ANN are trained. The responses for the ANN for the $r_{a,f} \in [400e3, 520e3]$ have slower, and smaller changes. Hence, the errors are also smaller. This causes the peak observed near the zero error region.

The correlation between the different errors is tabulated in Table 5.19. The most correlation exists between $r_{p,f-1}$, $r_{a,f-1}$, TOF and TOF_{apo}. Analog to Fig. 5.19, Fig. 5.35 show the locations in $r_{p,f-1} - TOF$ phase space where errors occur that are larger than the 99 percentile for the backwards apoareion scaled Hill ANN. Again, it can be concluded that the largest errors occur in the grey buffer region due to a lack of information in the direction of the anomaly boundaries. Figure 5.36 shows the distribution of errors, excluding the errors in the grey buffer region. This improves the accuracy of all parameters by 10-28%.

5.4.2.3 Correction neural networks

The correction term between the scaled Hill and the eccentric Hill system has continuous output, and is captured in a regression feedforward neural network.

Table 5.19: Correlation between the backwards scaled Hill ANN prediction errors for the 100,000 points sampled in the Monte Carlo simulation.

	$\Delta r_{p,f-1}$	$\Delta r_{a,f-1}$	ΔTOF_{apo}	ΔTOF	$\Delta i_{\text{Hill},f-1}$	$\Delta\omega_{\text{Hill},f-1}$	$\Delta\Omega_{\text{Hill},f-1}$
$\Delta r_{p,f-1}$	1.00	−0.21	0.03	−0.08	0.02	−0.01	0.01
$\Delta r_{a,f-1}$	−0.21	1.00	−0.04	0.09	−0.02	0.01	0.02
ΔTOF_{apo}	0.03	−0.04	1.00	0.04	0.04	0.00	0.01
ΔTOF	−0.08	0.09	0.04	1.00	0.01	0.02	0.00
$\Delta i_{\text{Hill},f-1}$	0.02	−0.02	0.04	0.01	1.00	0.03	0.00
$\Delta\omega_{\text{Hill},f-1}$	−0.01	0.01	0.00	0.02	0.03	1.00	−0.10
$\Delta\Omega_{\text{Hill},f-1}$	0.01	0.02	0.01	0.00	0.00	−0.10	1.00

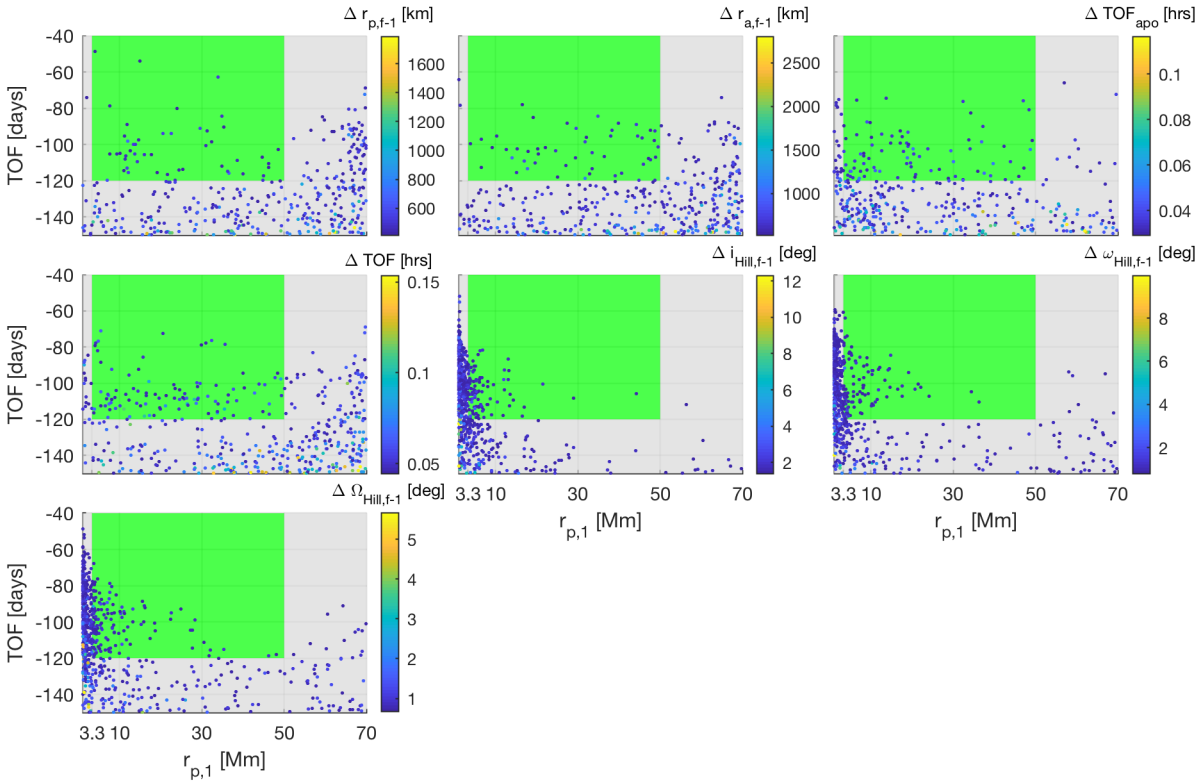

Figure 5.35: Locations in $r_{p,1} - TOF$ phase space where errors larger than the 99 percentile for the backwards apoareion scaled Hill ANN occur.

Data creation Similar to the forward architecture, a Monte Carlo analysis is performed, uniformly sampled from the bounds in Table 5.17. The difference in response between the eccentric and scaled Hill system is computed.

Data processing Prior to training, the raw integrated data is processed and some data is pruned out. Similar to the forward architecture, limits are imposed on $r_{p,f-1}$, $r_{a,f-1}$ and TOF.

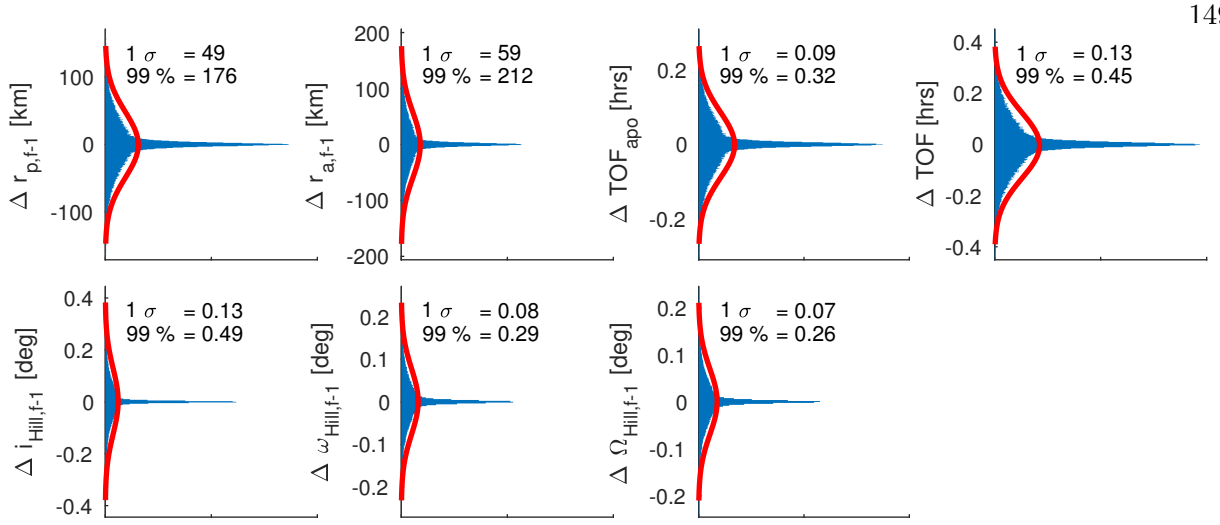

Figure 5.36: Distribution of the errors between the predicted and integrated backwards apoareion scaled circular Hill Poincaré map for the 100,000 sampled points in the Monte Carlo simulation, excluding the grey buffer regions. The x-axis shows the number of samples for each y-axis bin.

Again, those limits are set at 50,000 km, 850,000 km and 120 days. No new classification networks are required to detect the r_p and TOF events. The $r_{p,f-1}$, $r_{a,f-1}$ and TOF limits are already captured at 70,000 km, 900,000 km and 150 day respectively. An example of this pruning procedure for the $r_{a,f-1}$ output parameter is shown in Fig. 5.37. In the bottom right of Fig. 5.37, a trend between the difference in $r_{a,f}$, $i_{\text{Hill},f}$ and $\nu_{\text{M,apoareion}}$ is observed. The trends for the other parameters are shown in Fig. 5.38. The ANN are expected to be able to identify these trends.

Overview of input and output parameters For the correction neural networks, the inputs are the unscaled $r_{p,f}$, $r_{a,f}$, $i_{\text{Hill},f}$, $\omega_{\text{Hill},f}$, $\Omega_{\text{Hill},f}$ and $\nu_{\text{M,apoareion}}$. The outputs are the unscaled errors in $r_{p,f-1}$, $r_{a,f-1}$, $i_{\text{Hill},f-1}$, $\omega_{\text{Hill},f-1}$, $\Omega_{\text{Hill},f-1}$, TOF and TOF_{apo}.

Training The same training framework is used as for the forward neural networks.

Validation The training is performed with 1e6 points. As an independent accuracy test, another 100,000 sample points are created from a uniform distribution in input parameters. Figure 5.39 shows the distribution of the errors between the predicted and integrated difference between the backward eccentric and scaled Poincaré map. Again, the correlations between the errors are computed and shown in Table 5.20. Similar conclusions can be drawn as for the backwards, scaled Hill error covariance terms. Again, it is verified if certain areas in the phase space exist for which

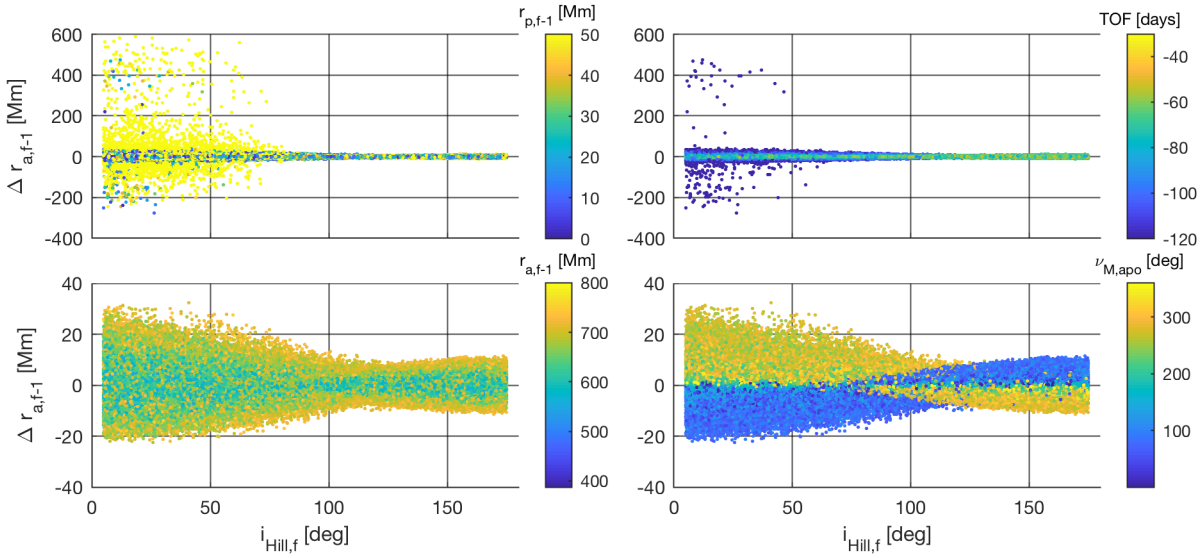

Figure 5.37: Example of the pruning procedure on the training data for the backward correction ANN. Example for the $r_{a,f-1}$ parameter.

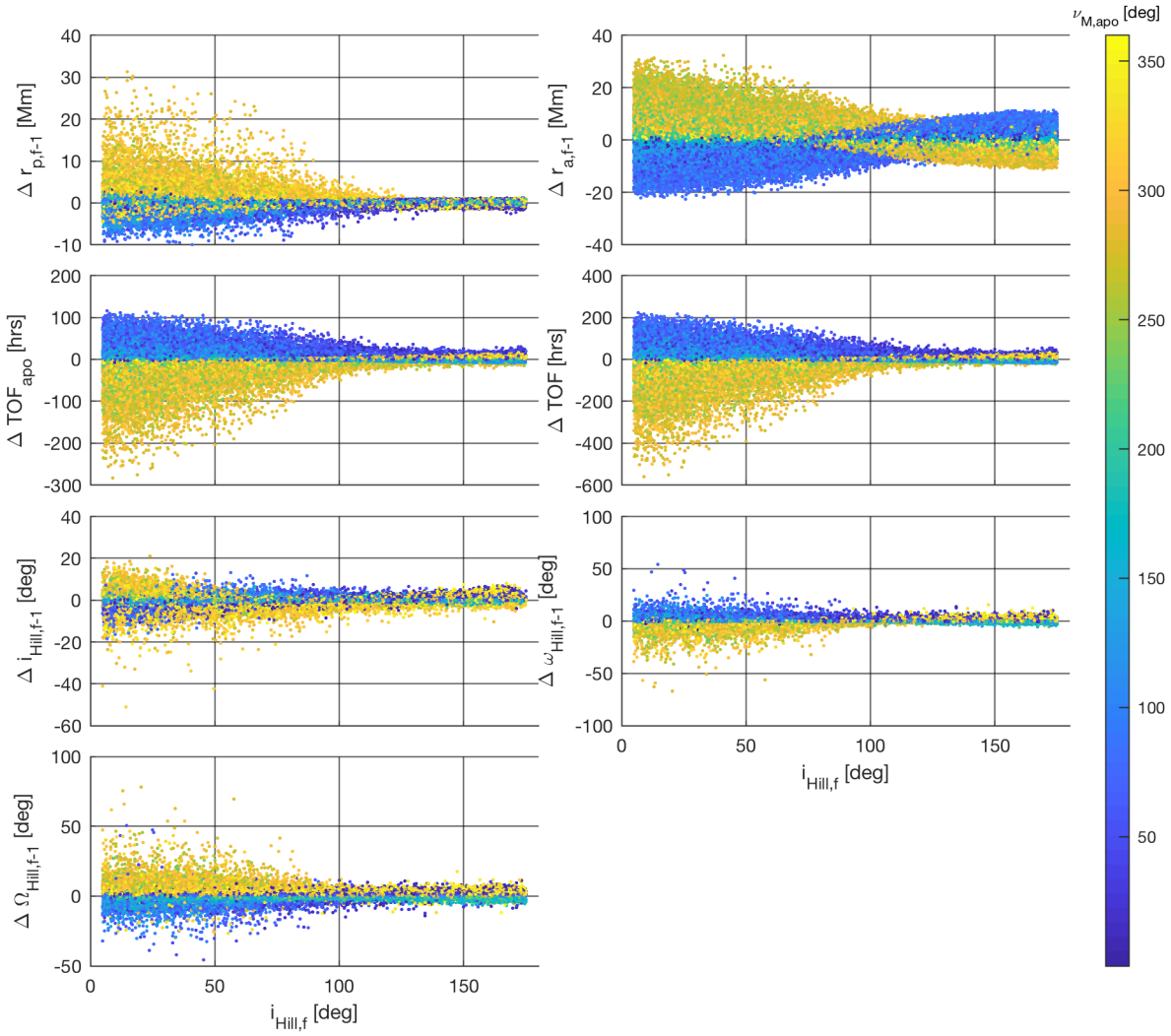

Figure 5.38: Visualization of the systematic differences between the integrated response in the backwards apoareion scaled circular, and eccentric Hill systems.

the correction ANN produce large errors. No systematic trends could be identified. Figure 5.24 shows that the final orbital elements that result in errors larger than the 99 percentile are more or less uniformly distributed. Thus, no specific zones within the phase space exist with systematically larger errors.

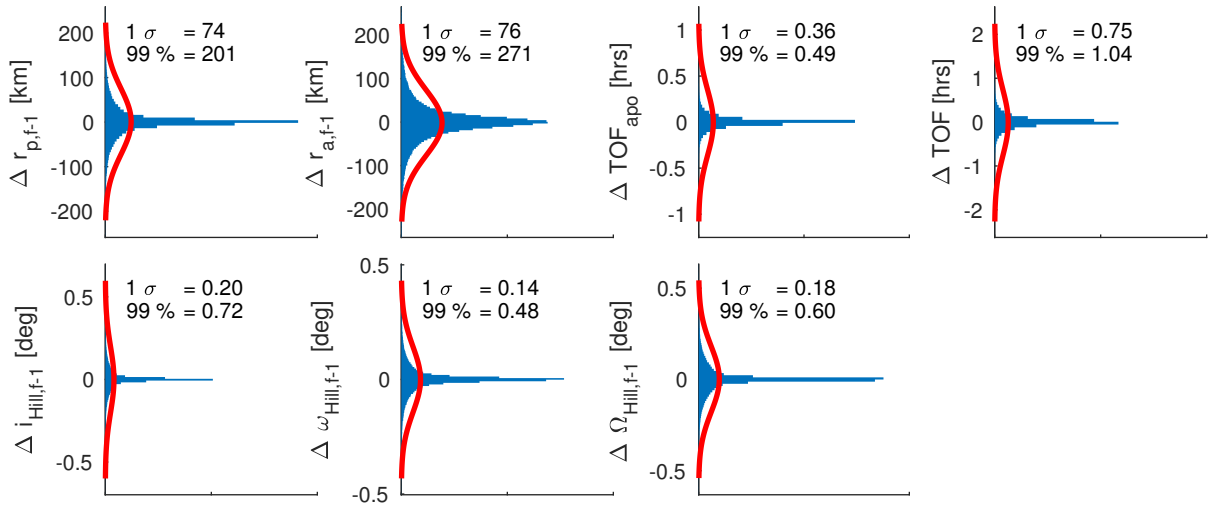

Figure 5.39: Distribution of the errors between the predicted and integrated difference between the backwards eccentric and apoareion scaled circular Hill Poincaré maps for the 100,000 sampled points of the Monte Carlo simulation. The x-axis shows the number of samples for each y-axis bin.

Table 5.20: Correlation between the backwards correction ANN prediction errors for the 100,000 samples in the Monte Carlo analysis.

	$\Delta r_{p,f-1}$	$\Delta r_{a,f-1}$	ΔTOF_{apo}	ΔTOF	$\Delta i_{\text{Hill},f-1}$	$\Delta\omega_{\text{Hill},f-1}$	$\Delta\Omega_{\text{Hill},1}$
$\Delta r_{p,f-1}$	1.00	−0.30	−0.57	−0.61	0.00	−0.00	0.00
$\Delta r_{a,f-1}$	−0.30	1.00	0.05	0.07	−0.00	0.00	−0.00
ΔTOF_{apo}	−0.57	0.05	1.00	0.93	−0.00	−0.00	−0.00
ΔTOF	−0.62	0.07	0.93	1.00	−0.00	−0.00	−0.00
$\Delta i_{\text{Hill},f-1}$	0.00	−0.00	−0.00	−0.00	1.00	−0.05	0.03
$\Delta\omega_{\text{Hill},f-1}$	0.00	0.00	−0.00	−0.00	−0.05	1.00	−0.16
$\Delta\Omega_{\text{Hill},f-1}$	−0.00	−0.00	−0.00	−0.00	0.03	−0.16	1.00

5.4.2.4 Escape and impact classification neural networks

The escape and impact classification are discrete events; therefore, a classification neural network is used to predict which initial conditions lead to escape or impact.

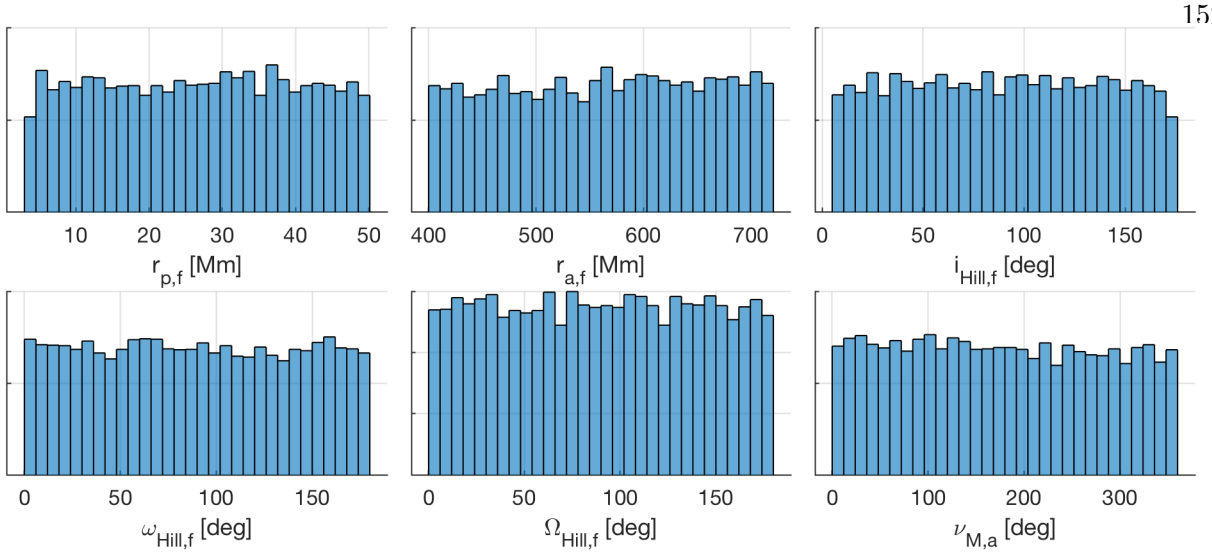

Figure 5.40: Distributions of all input states for which any of the predicted backwards correction terms has an error larger than its 99 percentile value shown in Fig. 5.39. The y-axis shows the number of samples for each x-axis bin.

Data creation The same backwards integrated trajectories computed for the scaled Hill neural networks have been used, with the same bounds and resolution listed in Table 5.18.

From the integrations of the scaled Hill neural networks, the data for the classification neural networks can be constructed. During those integrations, some trajectories have been immediately indicated as escape trajectories, if no next periareion could be found. Furthermore, transfers with a TOF < -150 days, $r_{p,f-1}$ >70,000 km, or $r_{a,f-1}$ > 900,000 km, are marked as escaping trajectories. Similarly, trajectories with $r_{p,f-1}$ < 1,000 km are marked as impacting transfers. Note that these numbers are the boundaries of the buffer regions and not the actual boundaries of the anomalies.

Overview of input and output parameters There are five scaled input parameters: $r_{p,f}$, $r_{a,f}$, $i_{\text{Hill,f}}$, $\omega_{\text{Hill,f}}$, $\Omega_{\text{Hill,f}}$, scaled according to the time of apoareion. There are again two outputs, indicating the chance an anomaly occurs or does not occur.

Training The same training framework is used as for the forward classification networks.

Validation As an independent test of the networks, a Monte Carlo analysis is performed. The 100,000 element data set used for the validation of the backwards scaled Hill networks data is re-used. Figure 5.41 shows the confusion matrix for the escape and impact classification network. Again, it can be shown that the incorrect classification of the false positives and false negatives can be resolved through the buffer regions. This is verified in the right part of Fig. 5.42.

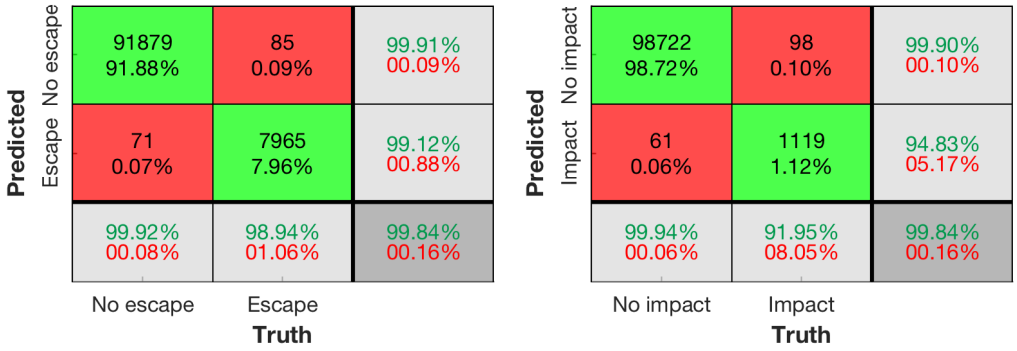

Figure 5.41: Confusion matrices for the backwards escape (left) and impact (right) classification ANN.

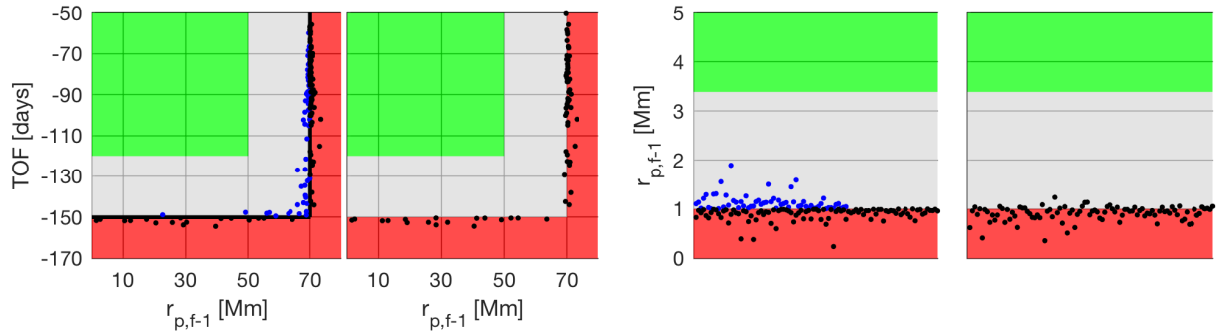

Figure 5.42: Comparison of the integrated versus predicted results for erroneously classified backward transfers: false positives (blue), false negatives (black), for escape (left) and impact (right) classification.

5.4.3 Architecture accuracy

In this subsection, the overall accuracy of the backwards architecture is evaluated, using the same method as used in Subsection 5.3.3, with a 100,000 point Monte Carlo analysis.

For 16,252 points, the integrated and predicted transfers are both outside the green region. For 123 points, or 0.123% of the points, there is a conflict between the integrated and predicted green region classifications. For those points, the predicted and integrated $r_{p,f-1}$ and TOF are plotted in Fig. 5.43. Again, the difference in classifications are due to small oscillations near the escape and impact criteria due to the errors in the scaled Hill and correction ANN.

83,613 out of the 100,000 points are integrated and predicted to be in the green region and the error can be quantified. The error statistics for those points are displayed in Fig. 5.44. As

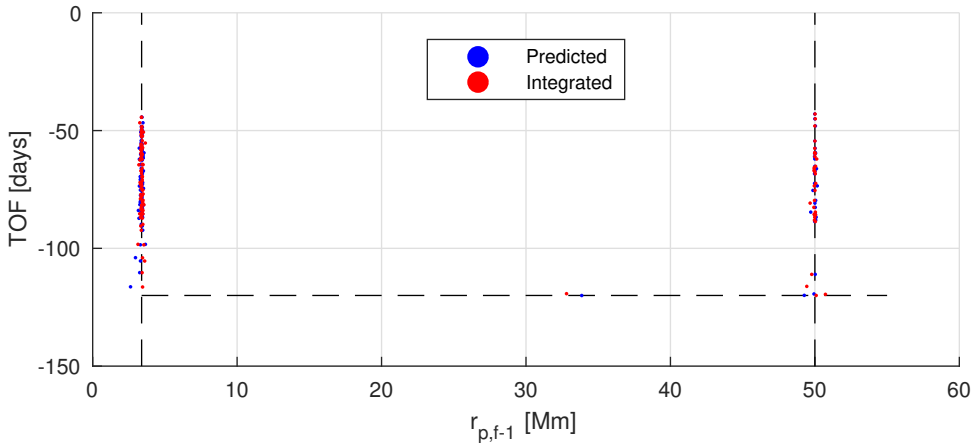

Figure 5.43: Integrated versus predicted $r_{p,f-1}$ and TOF response at 123 incorrectly classified samples for the single-loop validation.

a summary, the 1σ and 99 percentiles are shown in Table 5.21, along with the accuracies of the different ANN families. Similar conclusions can be drawn as in Subsection 5.3.3.

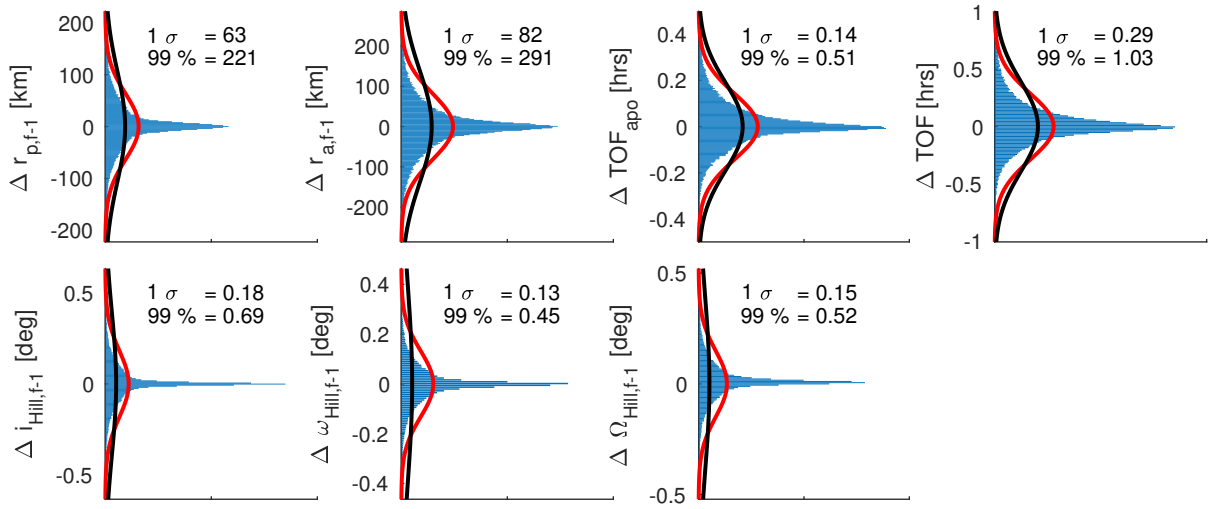

Figure 5.44: Distribution of the errors of the predicted orbital elements at periareion $f-1$ using the entire architecture, compared to the orbital elements integrated in the eccentric Hill system for the 100,000 sample points in the Monte Carlo simulation of the entire architecture. The x-axis shows the number of samples for each y-axis bin.

Table 5.22 displays the non-dimensionalized covariance errors. Again, there is some correlation, mostly between $r_{p,f-1}$, $r_{a,f-1}$, TOF and TOF_{apo}. To understand if the entire architecture produces systematic errors, Fig. 5.45 shows the location in the phase space of the previous periareion for errors that are larger than the 99 percentile for the entire backwards architecture. The

Table 5.21: Distribution statistics for the errors of the predicted response, compared to the integrated response, for different elements of the backwards ANN architecture.

Parameter	Scaled Hill		Correction		Entire architecture		RSS scaled Hill and correction		Unit
	σ	99 perc.	σ	99 perc.	σ	99 perc.	σ	99 perc.	
$r_{p,f-1}$	58	207	74	201	63	221	94	288	km
$r_{a,f-1}$	72	261	76	271	82	291	104	376	km
TOF_{apo}	0.1	0.35	0.36	0.49	0.14	0.51	0.37	0.60	hrs
TOF	0.15	0.53	0.75	1.04	0.29	1.03	0.76	1.17	hrs
$i_{\text{Hill},f-1}$	0.18	0.68	0.20	0.72	0.18	0.69	0.27	0.99	deg
$\omega_{\text{Hill},f-1}$	0.11	0.39	0.14	0.48	0.13	0.45	0.18	0.62	deg
$\Omega_{\text{Hill},f-1}$	0.10	0.33	0.18	0.60	0.15	0.52	0.21	0.68	deg

largest errors are found near the impact and escape boundaries. The errors are combinations of errors in the apoareion scaled Hill ANN and errors in the correction term ANN. The former has a clear structure (Fig. 5.35), while the latter appears random(Fig. 5.40). The structure is therefore dominated by the error regions of the apoareion scaled Hill ANN.

Table 5.22: Correlation between the prediction errors of the entire backwards architecture.

	$\Delta r_{p,f-1}$	$\Delta r_{a,f-1}$	ΔTOF_{apo}	ΔTOF	$\Delta i_{\text{Hill},f-1}$	$\Delta\omega_{\text{Hill},f-1}$	$\Delta\Omega_{\text{Hill},f-1}$
$\Delta r_{p,f-1}$	1.00	−0.20	0.06	0.08	0.01	0.02	0.01
$\Delta r_{a,f-1}$	−0.20	1.00	−0.01	−0.04	−0.03	0.01	−0.03
ΔTOF_{apo}	0.06	−0.01	1.00	0.42	−0.03	−0.05	0.06
ΔTOF	0.08	−0.04	0.42	1.00	0.01	−0.11	0.09
$\Delta i_{\text{Hill},f-1}$	0.01	−0.03	−0.03	0.01	1.00	0.03	0.04
$\Delta\omega_{\text{Hill},f-1}$	0.02	0.01	−0.05	−0.11	0.03	1.00	−0.12
$\Delta\Omega_{\text{Hill},f-1}$	0.01	−0.03	0.06	0.09	0.04	−0.12	1.00

5.4.4 Architecture accuracy multiple loops

Similar to Subsection 5.3.4, the framework can be used to chain multiple orbits. The accuracy is determined for a 10,000 point Monte Carlo analysis. Again, the multiple loops lead to a more complex classification problem. Table 5.23 gives an overview on the classification. For the "conflict" category, the integrated and predicted transfer conflict on the classification. Similar to Fig. 5.43, Fig. 5.46 is created. Again, these conflicts are caused by small oscillations near the escape and

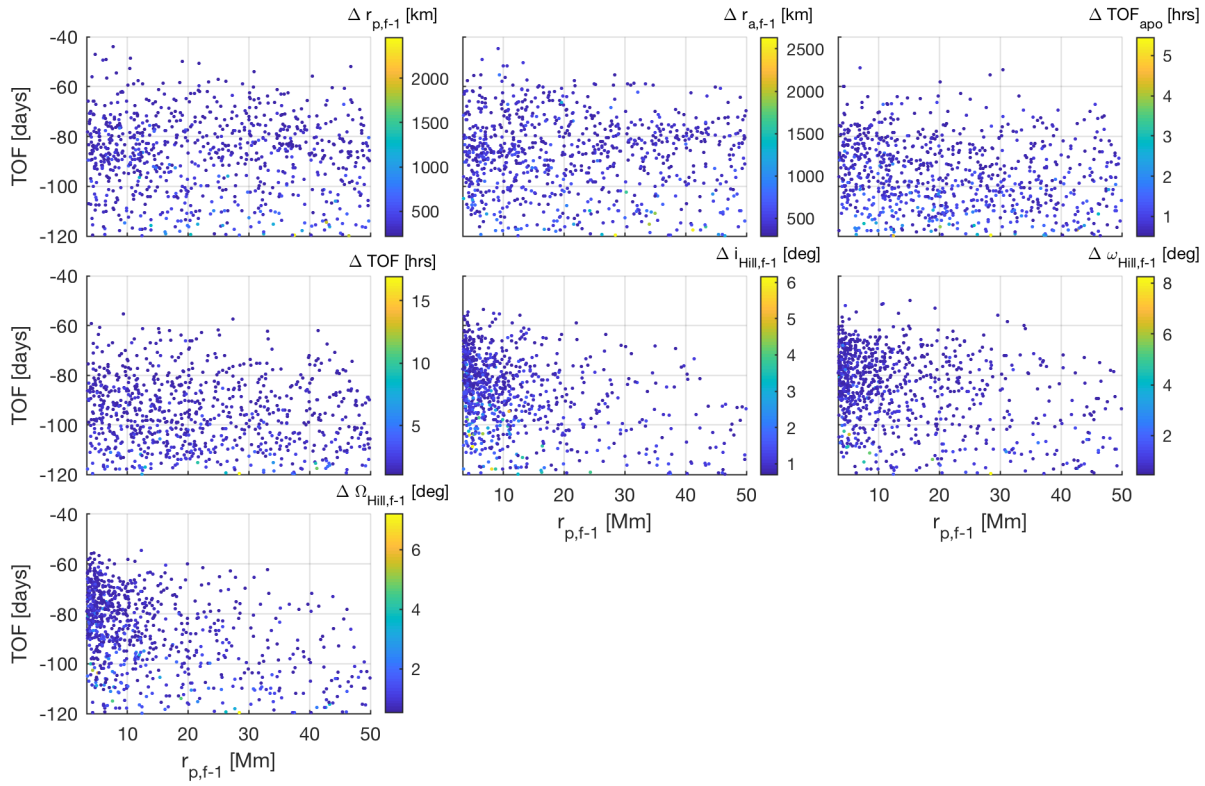

Figure 5.45: Locations in $r_{p,f-1} - TOF$ phase space where errors larger than the 99 percentile for the entire architecture occur.

impact criteria. The errors for the points in the "Both green" category can be quantified. The 1σ and 99 percentiles are listed in Table 5.24, and the histograms for loop 2, 3, and 4 are shown in Fig. 5.47. Similar trends as for the forward neural networks can be observed. One can see that the errors do not linearly grow. Furthermore, a strong increase in errors in TOF_{apo} and TOF can be observed. These parameters are used for the iterative search for $\nu_{\text{M,apoareion}}$. As this procedure uses the identified timing from the previous loop, small errors in the previous loops amplify the errors.

Another concern arises from Table 5.24. For multiple loops, the 99 percentile r_p error grows to 700 km, which is a significant error for low periapses. Therefore, in Fig. 5.48, the error distribution is given for different regions of $r_{p,f-4}$ after four backwards loops. One can see that at small $r_{p,f-4}$ levels, the $r_{p,f-4}$ errors are smaller, alleviating the concern.

Table 5.23: Statistics of the classification errors for the backwards, multiple loop architecture.

Loop	1	2	3	4
Points at start of loop	10,000	8,202	6,849	5853
Both green	8,202	6,849	5,853	5,155
Both outside green	1,786	1,308	964	682
Conflict	12	22	17	10
Outside ANN training	0	23	15	6

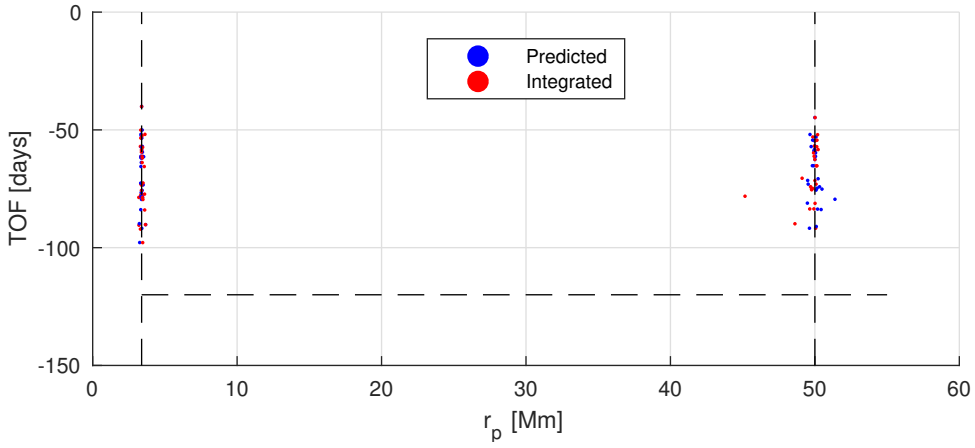

Figure 5.46: Integrated versus predicted r_p and TOF response at 89 incorrectly classified samples for the backwards multiple-loop validation.

Table 5.24: Statistics of the prediction errors of the backwards, multiple loop architecture.

Parameter	Loop 1		Loop 2		Loop 3		Loop 4		
	σ	99 perc.	σ	99 perc.	σ	99 perc.	σ	99 perc.	
r_p	60	210	135	440	161	585	186	710	km
r_a	78	293	141	506	171	594	198	730	km
TOF_{apo}	0.15	0.52	0.55	2.35	1.24	4.84	1.84	7.36	hrs
TOF	0.30	0.94	1.09	4.41	1.67	7.05	2.28	9.51	hrs
i_{Hill}	0.18	0.67	0.21	0.84	0.27	0.98	0.27	1.07	deg
ω_{Hill}	0.14	0.48	0.20	0.66	0.22	0.77	0.23	0.84	deg
Ω_{Hill}	0.13	0.50	0.19	0.73	0.24	0.90	0.26	0.96	deg

5.4.5 Conclusion

The artificial neural network architecture developed for forward Poincaré maps is successfully applied to backwards Poincaré maps. This allows the prediction of previous periareions, for transfers arriving between the Martian surface and 45,000 km, and for transfers consisting of multiple revolutions around Mars.

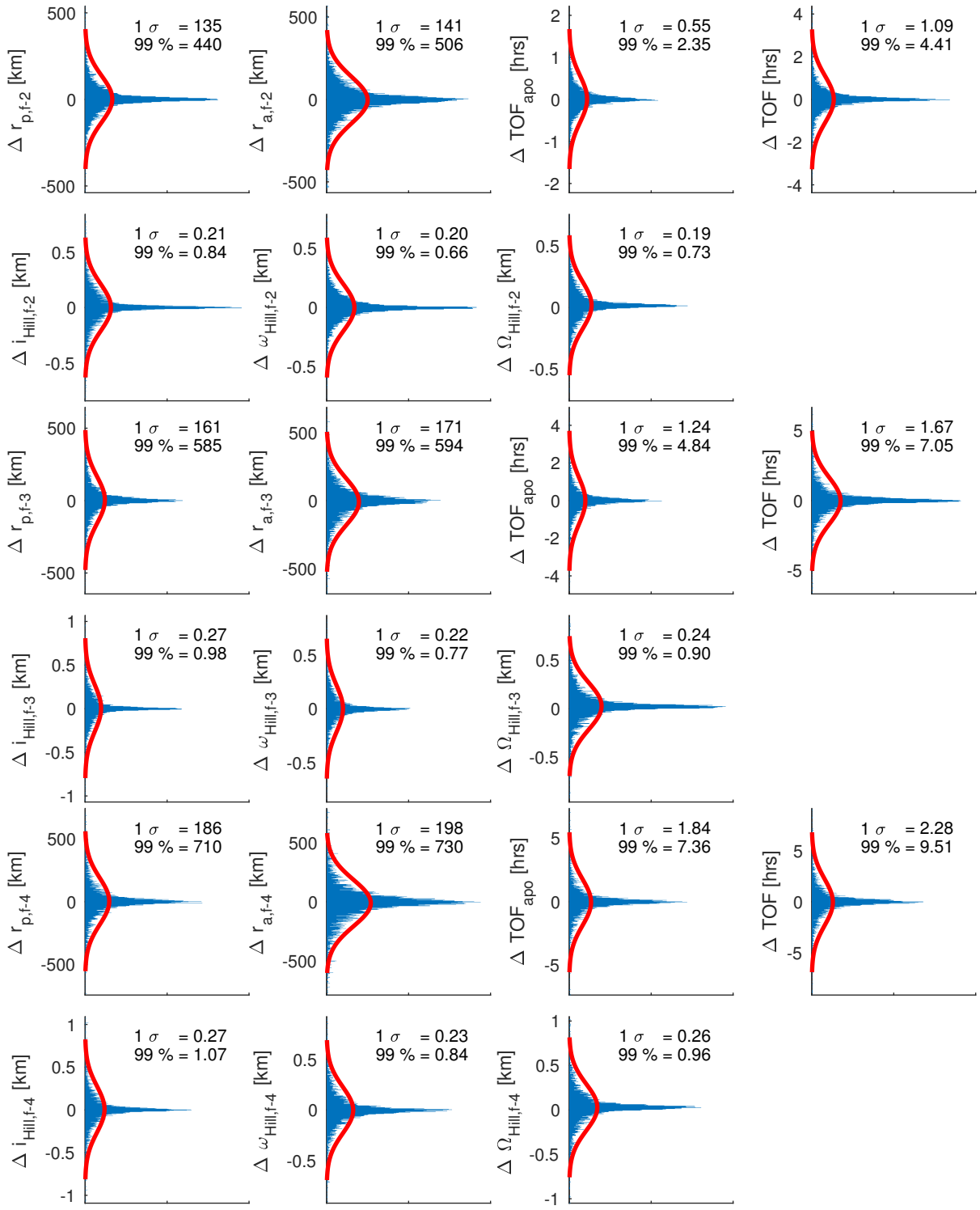

Figure 5.47: Distribution of the errors of the predicted orbital elements at periareions $f-2$, $f-3$, and $f-4$, using the entire backwards architecture, compared to the orbital elements integrated in the eccentric Hill system for the 10,000 sample points in the Monte Carlo simulation. The x-axis shows the number of samples for each y-axis bin.

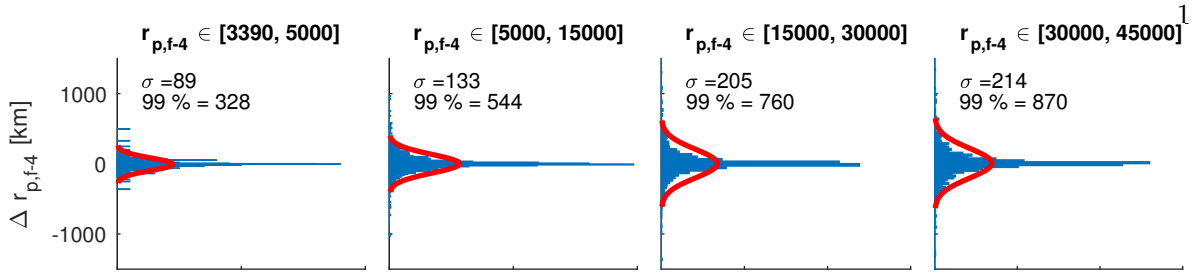

Figure 5.48: Distribution statistics of the errors of the predicted orbital elements at the periareion after four backwards loops, compared to the integrated orbital elements in the eccentric Hill system for different orbital regimes of $r_{p,f-4}$. The x-axis shows the number of samples for each y-axis bin.

5.5 Designing heteroclinic connections using ANN

In this section, the motivation to look at this problem is explained. Then, the training data is created and processed. Then, analog to Section 5.3, a combination of classification and regression feedforward neural networks are trained. Finally, some conclusions are drawn.

5.5.1 Motivation

Heteroclinic connections can be used to freely transfer between different libration point orbits (LPO). They are found by computing the unstable manifolds of the departure LPO, and the stable manifolds of the arrival LPO, and finding the intersections of these manifolds on a Poincaré map [3]. Due to the non-linearity of the manifolds, usually a dense sampling of the phase space is required. Different authors have tried different approaches to reduce this computational burden. The approximation of invariant manifolds using cubic convolution interpolation is introduced by Topputo and Zang [107], and refined by Beeson et al. [108]. Shah and Beeson [27] explored the use of recurrent neural networks and random forests to predict the time history of the state on manifolds. They found that the neural networks were ill suited for this task. However, for identifying heteroclinic connections, one does not need the entire state time history, but only the states at the Poincaré surface of section. Therefore, this section demonstrates how ANN can be employed to reduce the required number of integrated manifolds, while allowing accurate predictions of the Poincaré map for a wide variety of Jacobi values for all possible departure and arrival points on the considered LPO. ANN are designed to predict the Poincaré mapping for the unstable manifold

of the Earth-Moon L_1 point and for the stable manifold of the Earth-Moon L_2 point or Jacobi constants between 3.07 and 3.17, and for different departure locations along the orbits.

5.5.2 Data creation and processing

The manifolds of the L_1 and L_2 Lyapunov orbits are computed in the Earth-Moon CRTBP system, explained in Subsection 2.2.1. First, using the method described in Subsection 2.4.2, the L_1 and L_2 planar Lyapunov orbits are computed. After finding an initial periodic orbit, a continuation method, where the initial x-coordinate is slightly perturbed, is employed to find the orbits with $J \in [3.07, 3.17]$. These orbits are visualized in Fig. 5.49.

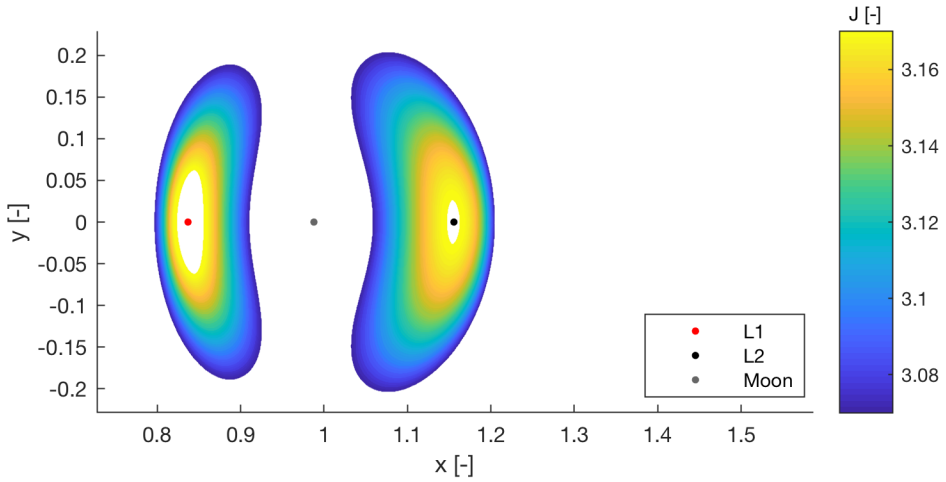

Figure 5.49: Continuation of planar Lyapunov orbits around L_1 and L_2 in the Earth-Moon CRTBP, for different values of the Jacobi constant J.

Any point on a heteroclinic connection must have identical J. Thus, a heteroclinic connection between two orbits requires equal Jacobi constant for both orbits. Therefore, by specifying J, the dimensionality of the problem can be reduced. Similarly, the dimensionality can be reduced by defining a Poincaré map. If one knows four out of the six states, the state is fully defined through a combination of J and the Poincaré surface condition. Commonly, a Poincaré surface at y=0 is used to identify heteroclinic connections between Lyapunov orbits. Such a planar Poincaré surface can encounter transversality issues. Those are resolved by using a periapse surface, defined in Eq.

2.48. L_1 and L_2 Lyapunov orbits, and their manifolds, are planar in the $z = 0$ plane. Therefore, the z and $\dot{z}$ states can be ignored. In combination with a fixed J and the periapse surface section of the Poincaré map, the Poincaré surface can be represented solely through the x and y coordinate.

The stable and unstable manifolds are computed using the method described in Subsection 2.4.2. Note that for this research, an ϵ for the positional deviations of 10 m has been used, while no velocity deviations are applied. The manifolds are computed for every LPO with J between 3.07 and 3.17 with resolution 0.001. The manifolds are computed at different locations along the LPO. To this end, the τ parameter is introduced, where analogous to an angle, 360 equidistant points are selected along the LPO. Not all this data is used for training. A J- and τ-resolution of 0.005 and 10° are used for the training, i.e., a 50th of the created data. The rest of the computed data allows for the validation of the networks. Note, this large set of validation data is not absolutely necessary. However, it facilitates the visualization of the structure in the errors of the ANN.

An example of the unstable manifold computation of L_1 at a J-value of 3.15 is shown in Fig. 5.50. This figure immediately highlights an issue; the manifold stays relatively close to the LPO for a few revolutions. Hence, a few periapses are detected that could be considered to be still on the LPO. Therefore, an x constraint is imposed: the first periapse with an x-coordinate 0.01 larger than the maximum x-coordinate of the LPO is considered to be the first "true" periapse. Then, another Poincaré mapping is performed up to the second periapse. This boundary is arbitrary and orbit dependent, and therefore, it introduces a new problem. For $\tau = 200°$ and $\tau = 220°$, the first and second identified periapses do not belong to the same group. This artificial bifurcation can be overcome by a re-indexing of the periapses, i.e., for $\tau = 200°$, the last periapse before the 0.01 x-condition is satisfied is stored as the first periapse, and the first periapse passed the 0.01 x-condition is stored as the second periapse.

Another issue is shown in Fig. 5.51. At $\tau = 200°$, one can see the nominal behavior: the first periapse is in the region between the periapse boundary and the Moon. However, at $\tau = 190°$, no periapse exists in this region, and the first identified periapse truly belongs to the second group of periapses. A simple re-indexing of the second periapse group solves this issue, along with storing

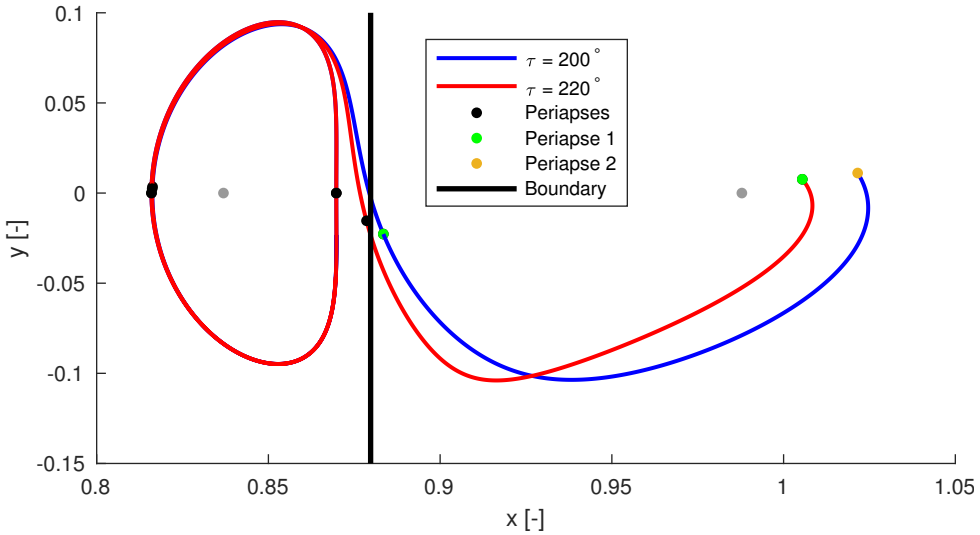

Figure 5.50: Identified periapses on the unstable manifold of the planar Lyapunov orbit around L_1 with $J = 3.15$.

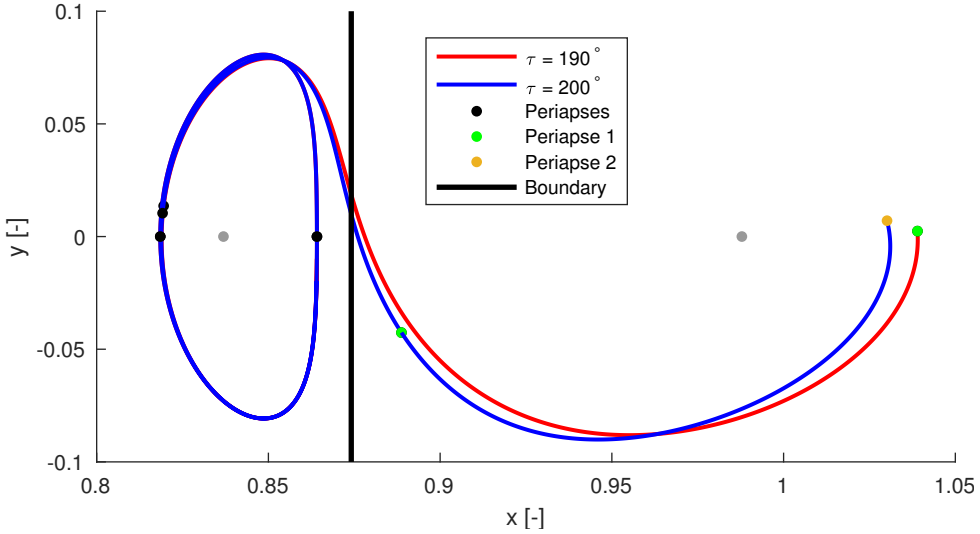

Figure 5.51: Identified periapses on the unstable manifold of the planar Lyapunov orbit around L_1 with $J = 3.16$.

the information that no periapse exists in group 1 for this $J-\tau$ combination. Similarly, information is stored when no periapse exists in group 2, for instance when the manifold escapes. Using these simple re-indexing techniques, the location on the Poincaré section of the first and second periapse group for the unstable manifolds of L_1 are computed and visualized in Fig. 5.52. The classification information on periapse existence is displayed in Fig. 5.53. Note that these figures only show the training data. Similarly, the stable manifolds of L_2 are computed and visualized in Fig. 5.54 and its classification in Fig. 5.55.

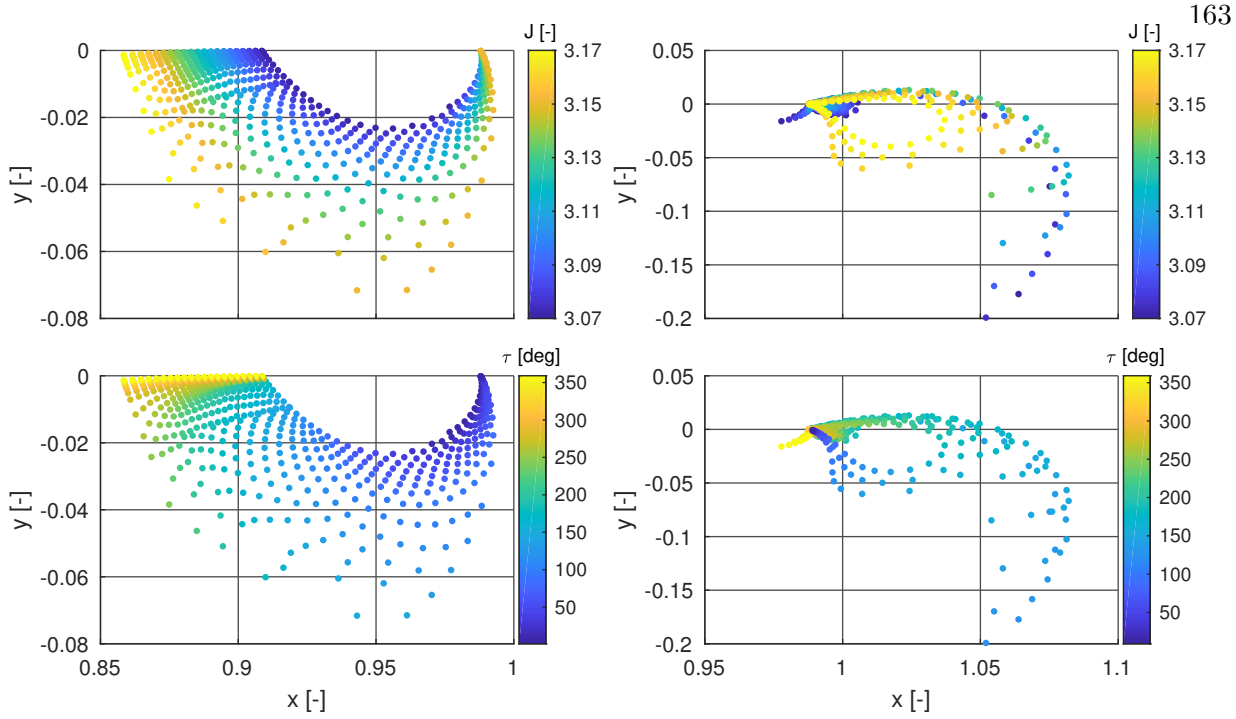

Figure 5.52: Periapse group identification on the unstable manifolds of L_1: group 1 (left) and 2 (right).

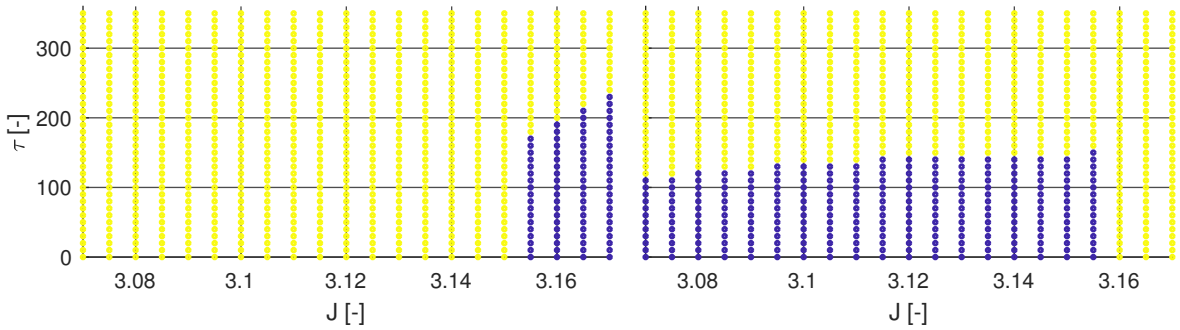

Figure 5.53: Classification whether or not a periapse on the unstable manifolds of L_1 exists for group 1 (left) and 2 (right): periapse exists (yellow) or periapse does not exist (blue).

5.5.3 Classification ANN

Classification ANN are created to identify whether or not a periapse exists for a $J - \tau$ combination. A two-hidden layer architecture with 10 neurons per hidden layer is used and hyperbolic tangent activation for the hidden layers. A softmax activation function is used on the output layer, with a cross entropy cost function and using the scaled conjugate gradient back propagation algo-

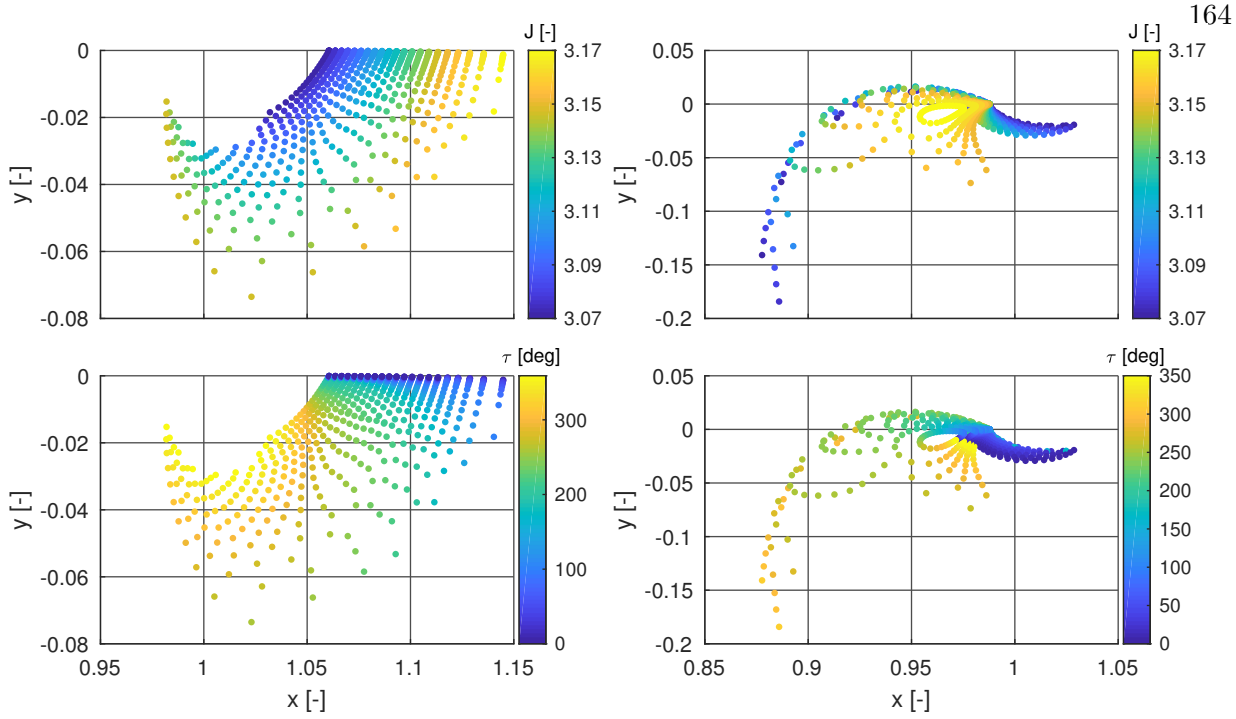

Figure 5.54: Periapse group identification on the stable manifolds of L_2: group 1 (left) and 2 (right).

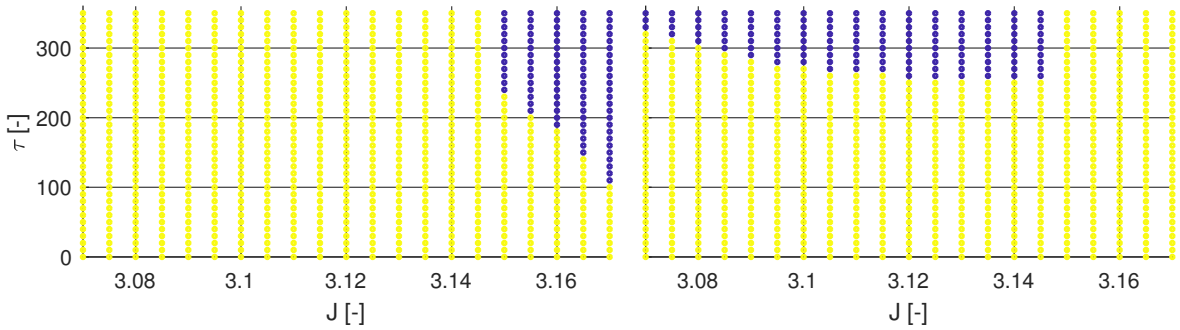

Figure 5.55: Classification whether or not a periapse on the stable manifolds of L_2 exists for group 1 (left) and 2 (right): periapse exists (yellow) or periapse does not exist (blue).

rithm. In total, four classification ANN are created: one for each periapse groups for both the L_1 unstable and L_2 stable manifolds. The combined training time is 3.32 seconds on a single core of a 2.5GHz Intel Core i7 processor. The accuracy of the classification ANN is depicted in Fig. 5.56. One can see that overall, the classification ANN accurately capture the phase space. There are some boundary issues due to the different sampling resolutions of the training and validation data.

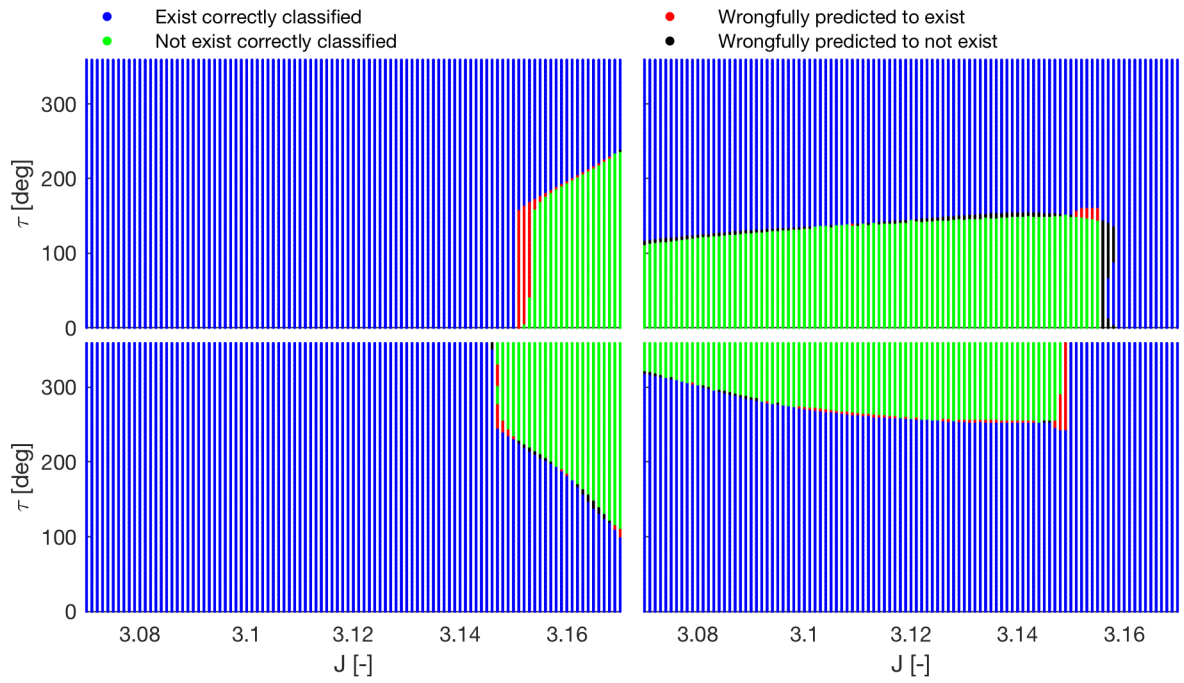

Figure 5.56: Classification results for periapse group 1 (left) and 2 (right) on the unstable manifolds L_1 (top) and stable manifolds L_2 (bottom), in function of the original phase space.

5.5.4 Regression ANN

The periapse Poincaré map for the planar manifolds of interest can be completely represented by the x and y coordinates. The $\dot{x}$ and $\dot{y}$ coordinates can be found from the Jacobi constant and the periapse condition. In total, eight regression ANN are created to predict the x and y coordinates for each periapse group for both the L_1 unstable and L_2 stable manifolds. A two-hidden layer architecture with 15 neurons per hidden layer is used. The hidden layers have hyperbolic tangent activation functions, while the input and output layers have linear activation functions. The mean squared error is used as the cost function with the Levenberg-Marquardt back propagation algorithm. The combined training time for the eight networks is 12 seconds. The accuracy of the regression ANN of the first and second periapse group are shown in Fig. 5.57 and Fig. 5.58. The resulting error distributions show the 1σ value, along with the 99 percentiles. The best fitting Gaussian distribution through the histograms are plotted in red. While the errors are not Gaussian,

the Gaussian places a conservative bound on the errors. Note that for the first periapse group, the neck regions have orders of magnitude higher errors. Those are not shown here for contrast. For periapse group 1, the highest 99 percentile is 0.000675, or 260 km. The results for periapse group 2 are considerably worse. The highest 99 percentile is 0.004666, which corresponds to 1738 km. The networks for group 2 are less accurate because the response of the Poincaré map rapidly varies in several regions, such as the "sickle" features right and left of the Moon for L_1 and L_2 respectively. Another example are the "whip" features left and right of the Moon for L_1 and L_2 respectively, that only exist for low J-values.

Similar to the Hill system regression networks, the large errors occur near the classification boundaries. Previously, this issue was resolved by adding a buffer region between the used boundary and the real boundary. This was possible since the events were defined with respect to a continuous parameter. Unfortunately, for this specific problem, no such continuous parameter exists; a transfer either exists in a group or it does not.

5.5.5 Conclusion

A combination of classification and regression ANN can predict the existence, and xy-location of the periapses for a wide variety of initial J and τ-values for the unstable manifold of L_1 and the stable manifold of L_2. The grouping of periapses with similar characteristics is crucial for the generalization accuracy. The classification boundaries are discrete events and the xy-location of the periapses near this boundary vary rapidly. Therefore, the regression neural networks struggle to accurately capture the response near these buffer regions. Furthermore, the discrete nature of the classification prevents the use of a buffer region to improve the accuracy near the classification boundaries.

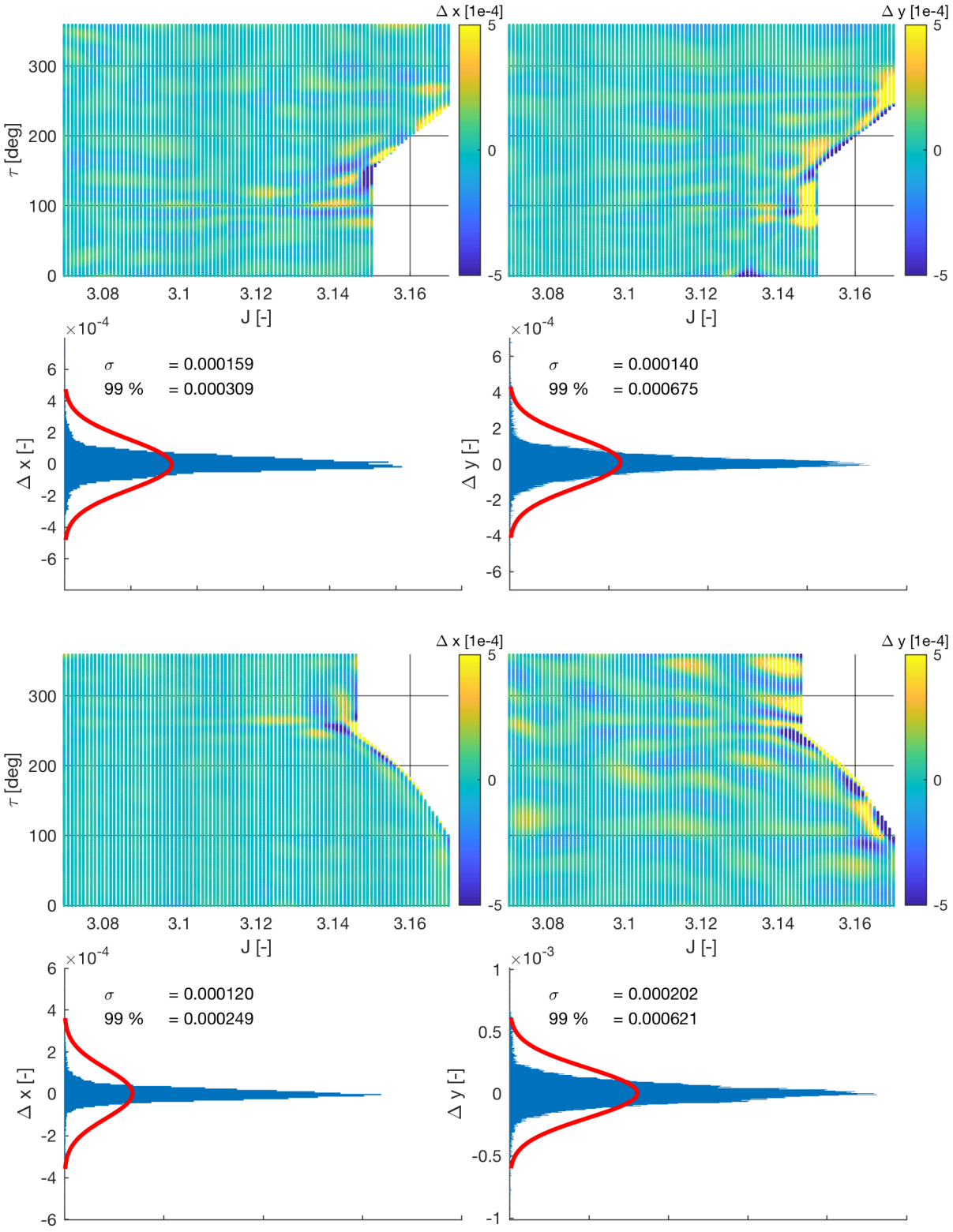

Figure 5.57: Accuracy of the regression ANN for periapse group 1 on the unstable manifolds of L_1 (top) and stable manifolds of L_2 (bottom). The x-axis of the histograms shows the number of samples for each y-axis bin.

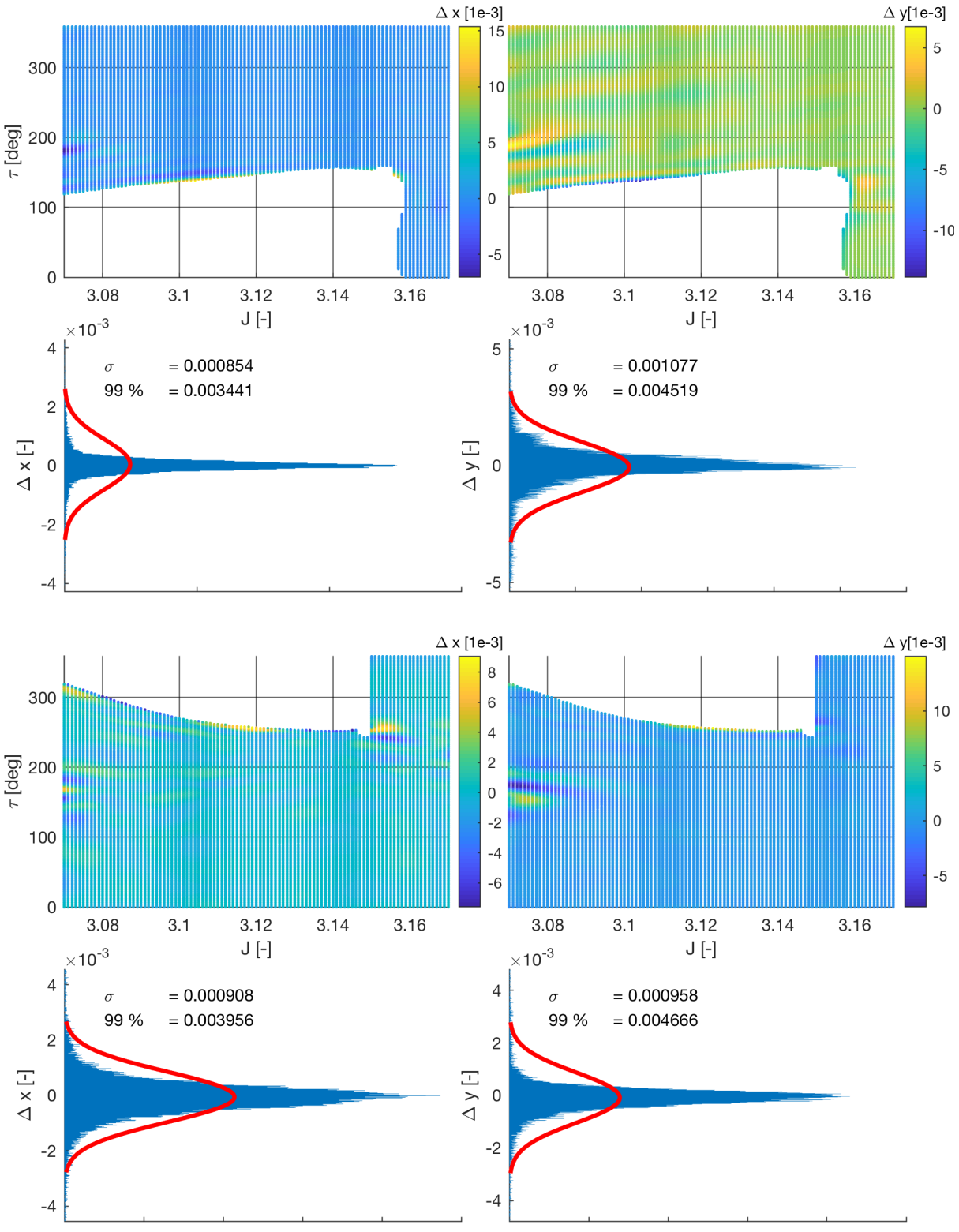

Figure 5.58: Accuracy of the regression ANN for periapse group 2 on the unstable manifolds of L_1 (top) and stable manifolds of L_2 (bottom). The x-axis of the histograms shows the number of samples for each y-axis bin.

Chapter 6

Applications

In this chapter, the designed ANN are used on a variety of applications. First, the initial conditions are determined for transfers to Phobos or Deimos, or transfers that target both Martian moons at subsequent periareions. Second, it is shown how the ANN allow to perform a Monte Carlo analysis on the effect of injection burn errors. Third, it is shown how the ANN can capture the effect of a missed injection burn at the final periareion. Fourth, a trade space study is performed to determine the possible connections between initial and final $(r_p - i_{\text{MME}})$ combinations for a wide variety of arrival conditions. Fifth, it is demonstrated how the ANN can be used to determine the impact and escape stabilities of the phase space for multiple revolutions. Finally, it is shown how the CRTBP ANN enables identifying heteroclinic connections between planar Lyapunov orbits.

6.1 Initial conditions targeting Phobos and/or Deimos

In this section, the initial conditions are determined for transfers that target the Martian moons Phobos or Deimos. In this section, "targeting" means that the transfers arrive at the final periareion with Phobos' or Deimos' $r_{p,f}$ and $i_{\text{MME},f}$. Furthermore, the initial conditions for transfers that target both Martian moons at different periareions are identified. In this section, both ballistic transfers are considered, as well as transfers that allow one in-plane maneuver at one of the intermediate periareions. The initial conditions indicate the full state and time after the first maneuver, occurring at periareion of the incoming parabola, and are indicated with index 1. The arrival conditions occur at the last periareion of the transfer, and are indicated with index f.

6.1.1 Ballistic transfers

In this section, the initial conditions are determined for ballistic transfers. The term ballistic is used for transfers with no maneuvers at intermediate periareions, but with two eccentricity reduction burns: one at periareion 1, and one at periareion f.

6.1.1.1 Methodology

Target one moon Specific transfers have unique arrival states at Phobos or Deimos. For this application, three parameters are free: $r_{a,f}$, $\omega_{\text{Hill},f}$, and t_f. The other parameters are constant variables, or can be computed from other parameters. The orbits of Phobos and Deimos are assumed circular, with radius equal to their semi-major axis, resulting in a known $r_{p,f}$. Furthermore, the orbits are assumed to be equatorial. Hence, $i_{\text{Hill},f}$ must be equal to Mars' obliquity of the ecliptic. Furthermore, $\Omega_{\text{Hill},f}$ can be computed from t_f and the necessary condition $\Omega_{\text{MMO},f} = 180^\circ$ (Eq. 2.38). Using the backwards ANN architecture developed in Section 5.4, the Hill orbital elements at periareion f are mapped to the Hill orbital elements at the previous periareion, $f-1$. Those orbital elements are the predicted initial conditions that target Phobos or Deimos in one revolution. To determine initial conditions for more than one revolution, the process can be repeated by mapping the periareion state $f-1$ back to periareions $f-2$, $f-3$, ..., 1.

The predicted phase space consists of initial time t_1, and predicted initial orbital elements $r_{p,1}$, $r_{a,1}$, $i_{\text{MME},1}$, $\omega_{\text{MME},1}$, and $\Omega_{\text{MME},1}$. This multi-dimensional phase space is impossible to visualize in its entirety. This research is mainly interested in the timing, $r_{p,1}$, and $i_{\text{MME},1}$. Therefore, this research limits itself to visualize the reachable areas of the phase space, projected on the $r_{p,1}-i_{\text{MME},1}$ plane. To include the time component, the projection on this plane is computed for discrete values of arrival days with a 10 day spacing. Due to non-linearities in the dynamical system, a uniform grid in arrival conditions does not translate into a uniform grid in departure conditions on these planes. To reduce the required number of neural network evaluations, a refinement method is developed. For a fixed t_f, for a sparse initial resolution in $\omega_{\text{Hill},f}$, and $r_{a,f} \in [440, 720]$ Mm, the

initial conditions are predicted and projected on the plane of interest. This plane is divided into segments, and the number of points that are projected on each segment is computed. The segments that are under-sampled are detected, and are indicated in red in the top part of Fig. 6.1. Near the arrival conditions within a red rectangle, a grid in $r_{a,f}$, and $\omega_{\text{Hill},f}$ with halve the step size is constructed, as visualized in Fig. 6.2. The point of interest is shown as a black dot. Its closest neighbors in the grid are shown as blue dots. The eight new arrival conditions around the point of

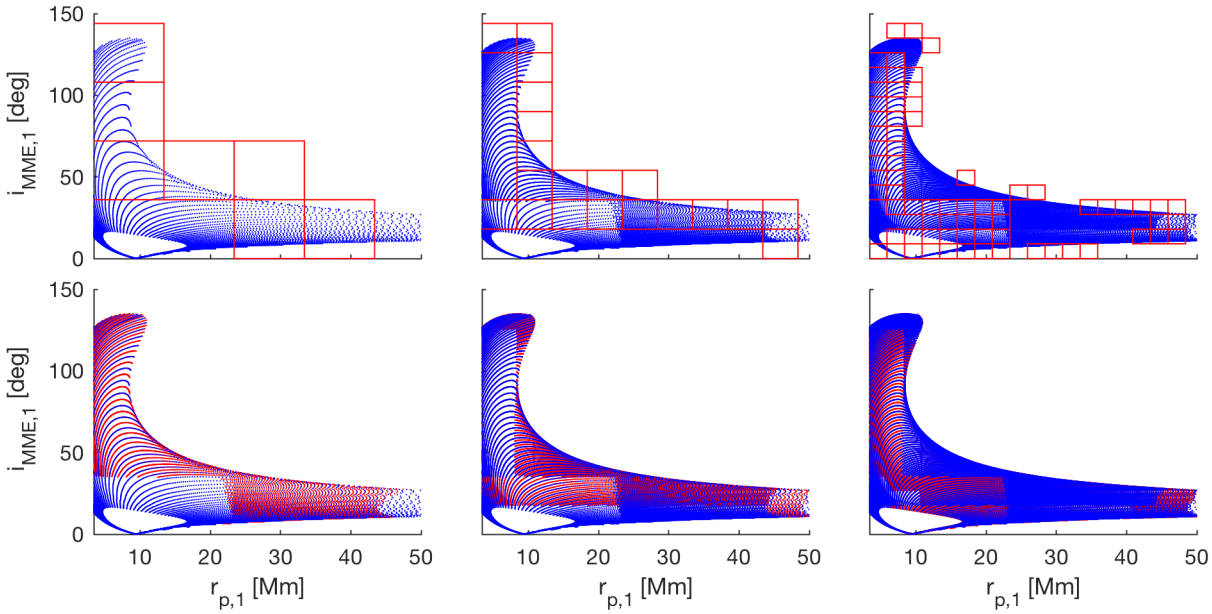

Figure 6.1: Visualization of the refinement procedure for under-sampled regions on the plane of interest: $r_{p,1} - i_{\text{MME},1}$. Top: detection of under-sampled regions. Bottom: new points computed in the under-sampled regions.

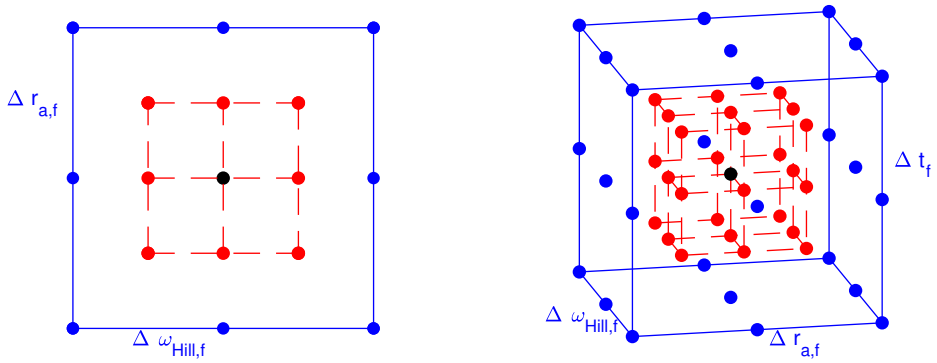

Figure 6.2: Visualization of the grid refinement, for a two-dimensional input grid (left) and a three-dimensional input grid (right). Black: input state for point of interest. Blue: nearest input states in previous resolution. Red: new input states.

interest are indicated in red. Those new arrival conditions are predicted backwards and projected on the plane of interest. After reducing the dimensions of the rectangular segments on the plane of interest by halve, the process is repeated. In the bottom part of Fig. 6.1, the earlier computed transfers are shown in blue, the newly computed transfers in red. The sparse regions on the plane of interest are systematically filled up. The pseudo-code can be found in Algorithm 3.

Target both moons on one transfer A similar method is developed to find transfers that chain the Martian moons; i.e., transfers that flyby one moon and arrive at the other moon. The intermediate flyby conditions significantly reduce the initial phase space. This allows the sampling of the entire Martian year within one grid, rendering the discrete arrival time computations obsolete. A grid is created in $r_{a,f}$, $\omega_{\text{Hill},f}$, and t_f. Then, the ANN architecture is used to predict how the orbital elements loop back N_2 revolutions from the final states at the second moon, to the flyby states at the first moon. The trajectories that pass close to the first moon are detected. Tolerances of 500 km in $r_{p,f-N_2}$ and 2° in $i_{\text{MME},f-N_2}$ are used. Those trajectories are then mapped back N_1 times to determine the initial conditions. The trajectories that pass close to the first moon are fairly rare. Therefore, a three-dimensional refinement method on the plane of interest is employed. A state is composed of $[r_{a,f}, \omega_{\text{Hill},f}, t_f]$. For every state in a sparse area, 26 new states are created using a grid with half the step size compared to the grid of the previous iteration, as visualized on the right-hand side of Fig. 6.2. The algorithm is summarized in Algorithm 4.

6.1.1.2 Results

Target one moon The described methodology is applied on scenarios with up to four loops, for $t_f \in [0, 680]$ days past perihelion, with step size ten days for transfers targeting Phobos or Deimos. For all arrival times and number of loops, the total area on the $r_{p,1} - i_{\text{MME},1}$ plane is computed. This allows the computation of the contribution of additional loops to the total area. An example of this procedure is shown in Fig. 6.3. Starting at the top left part of the figure, the common area for loop 1 and 2 is shown in blue. The area unique to loop 1 is shown in red and the area unique to loop 2 is shown in black. Loop 2, 3 and 4 respectively add 212, 150 and 487

[Mm×deg]. An unexpected feature can be found in the top left part near $r_{p,1} = 9,000$ km and $i_{\mathrm{MME},1} = 0°$. This region should be accessible with one loop, since this is the arrival phase space region at the next periareion. Hence, marginal orbital changes are required. However, for this method, a minimum value of $r_{a,f}$ of 440,000 km is used. For this value, some orbital changes still occur, especially near perihelion, leaving this area empty. It can be easily imagined that for lower values of $r_{a,f}$, these regions would contain transfers. The size of this empty area depends on the Mars-Sun distance, and varies for different t_f-values.

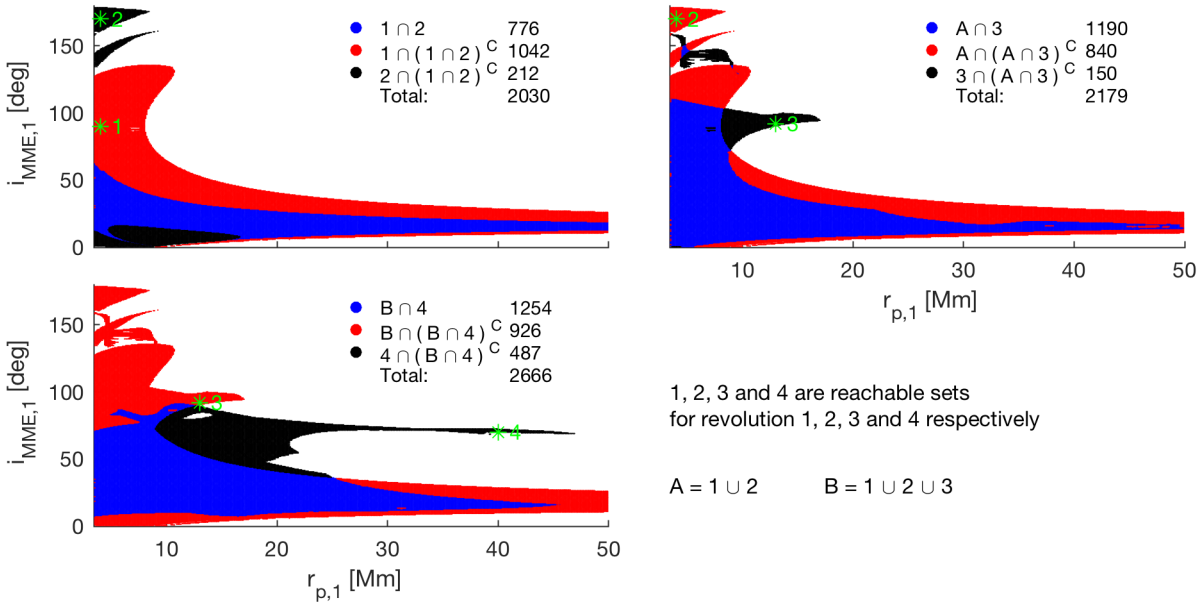

Figure 6.3: Visualization of the effect of additional loops on the $r_{p,1} - i_{\mathrm{MME},1}$ plane for ballistic transfers arriving at Phobos at day 0. Loop 2, 3, and 4, add 212, 150 and 487 [Mm×deg], respectively. One transfer per loop (green) is selected to be discussed in more detail.

As an example, four points are selected on Fig. 6.3 and are plotted in Fig 6.4. The first point is realizable in 1 loop, and departs from $r_{p,1} = 4,000$km and $i_{\mathrm{MME},1} = 90°$. An extra loop allows to depart from the same $r_{p,1}$, but at a retrograde orbit with $i_{\mathrm{MME},1} = 170°$. The one loop, nor the two loop configuration has solutions with initial polar i, and $r_{p,1}$ beyond Phobos. However, a three-loop transfer exists that departs from $r_{p,1} = 13,000$km and $i_{\mathrm{MME},1} = 92°$. No transfers exist with up to three loops that have $i_{\mathrm{MME},1} > 50°$, with very high initial $r_{p,1}$. The addition of a fourth loop enables such transfers, departing from $r_{p,1} = 40,000$km and $i_{\mathrm{MME},1} = 70°$.

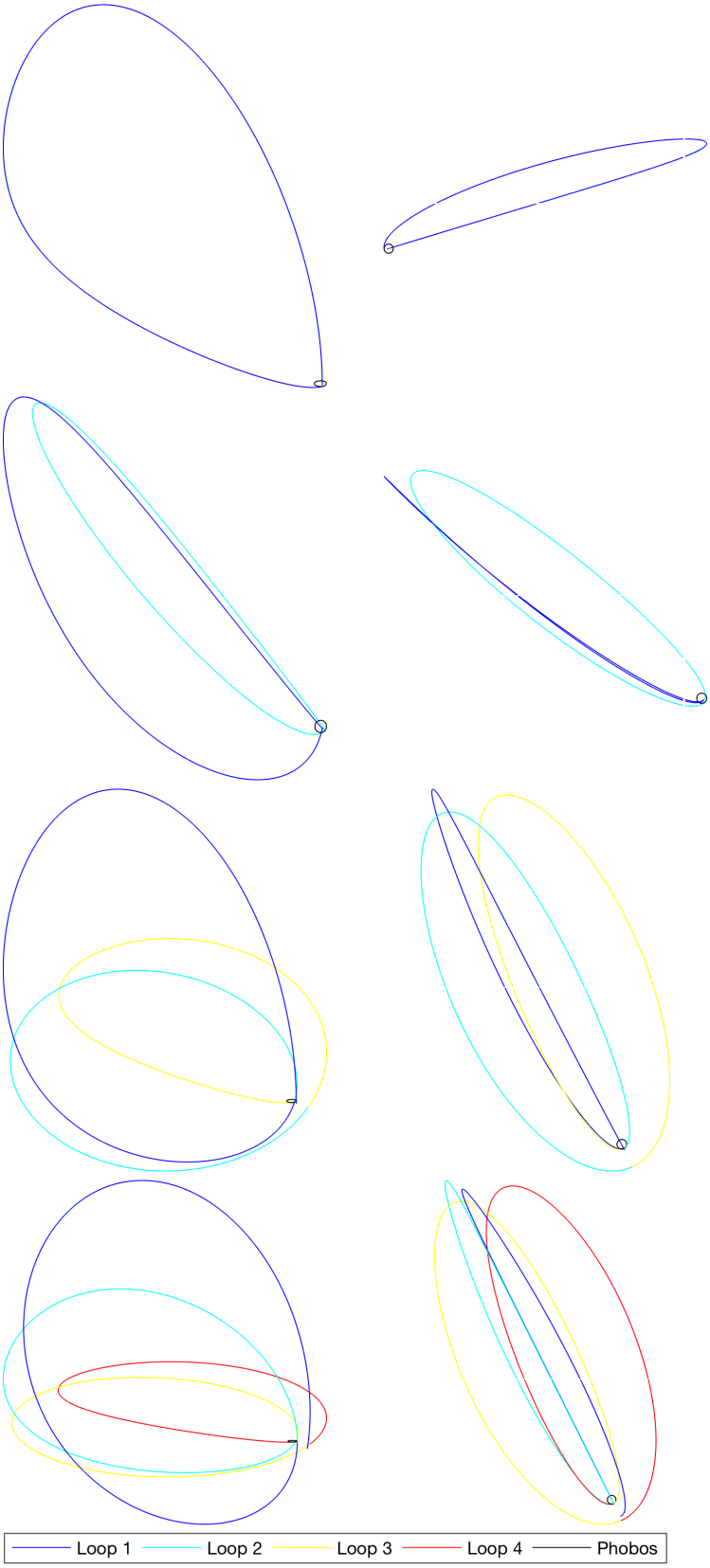

Figure 6.4: Example ballistic transfers arriving at Phobos (black) at day 0 for scenarios with, from top to bottom, 1, 2, 3 and 4 revolutions around Mars. 3-D view (left) and projection on the xy-plane (right), plotted in the MME frame.

The computation of the additional area on the $r_{p,1} - i_{\mathrm{MME},1}$ plane is repeated for all sampled arrival days. Figure 6.5 summarizes the results. Almost identical trends occur for one loop transfers to Phobos or Deimos, which can be attributed to their identical $i_{\mathrm{Hill},f}$, t_f and thus $\Omega_{\mathrm{Hill},f}$. Through the non-linear dynamics, the correlation in the response decreases with each incremental loop. In general, the area on the $r_{p,1} - i_{\mathrm{MME},1}$ plane to target Phobos is larger than to target Deimos.

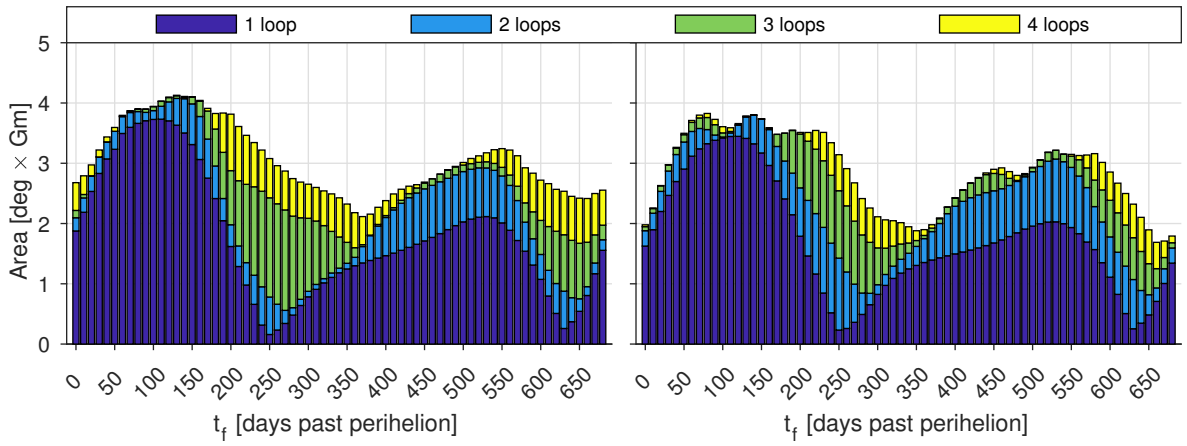

Figure 6.5: Effect of additional loops on the departable phase space projected on the $r_{p,1} - i_{\mathrm{MME},1}$ plane. Ballistic transfers arriving at Phobos (left) or Deimos (right) at day 0 through 680.

For regions in the $r_{p,1} - i_{\mathrm{MME},1}$ plane with overlap between different loops, the minimum TOF transfer can be determined. The $r_{p,1}$ region is divided into 100 equally spaced bins, as are the $i_{\mathrm{MME},1}$ regions. For each of the 10,000 sections, the transfer with the smallest TOF is shown in Fig. 6.6. Not surprisingly, the smallest loop number results in the smallest TOF. Finally, the frequency is computed departing from a certain region in the $r_{p,1} - i_{\mathrm{MME},1}$ plane, for a maximum of 1, 2, 3, and 4 loops (Fig. 6.7). Note that these results show the percentage for a maximum number of loops; i.e., the second figure from the left shows the percentage of year for which transfers exist with one or two loops. Some general conclusions can be drawn. Not a single point can be accessed all year round, with only one revolution. Again, it is noted that the region around Phobos or Deimos should be accessible year-round, for transfers with smaller $r_{a,f}$. The addition of a second and third revolution renders some departure regions accessible year-round. For Phobos, these regions occur at small $r_{p,1}$, all the way down to the surface. For Deimos, they occur at slightly higher altitudes. Another conclusion is that the largest inclination changes occur for lower initial periareion.

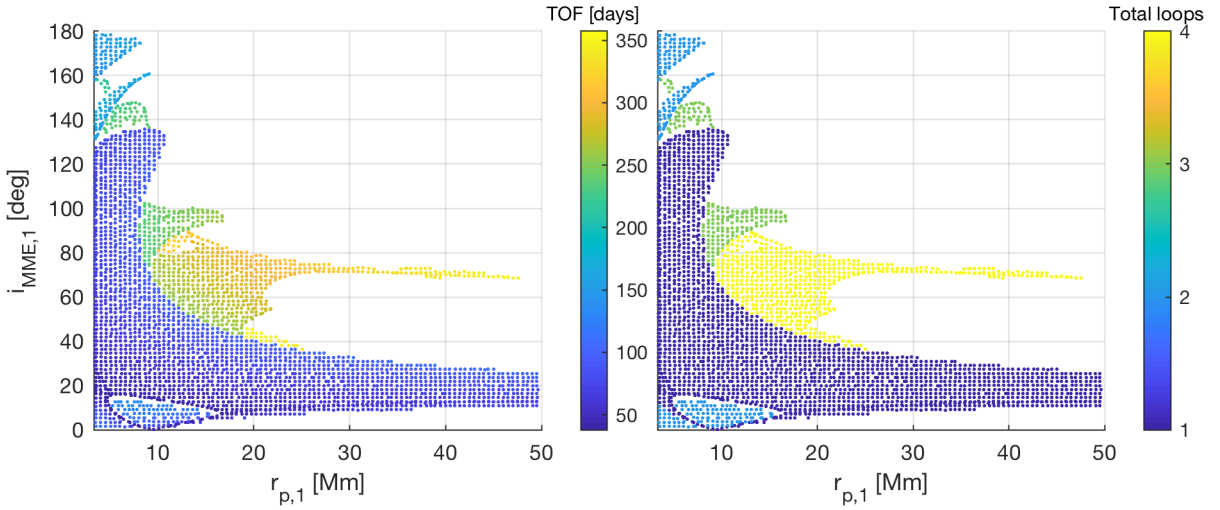

Figure 6.6: TOF and number of loops for minimum TOF transfers targeting Phobos at day 0.

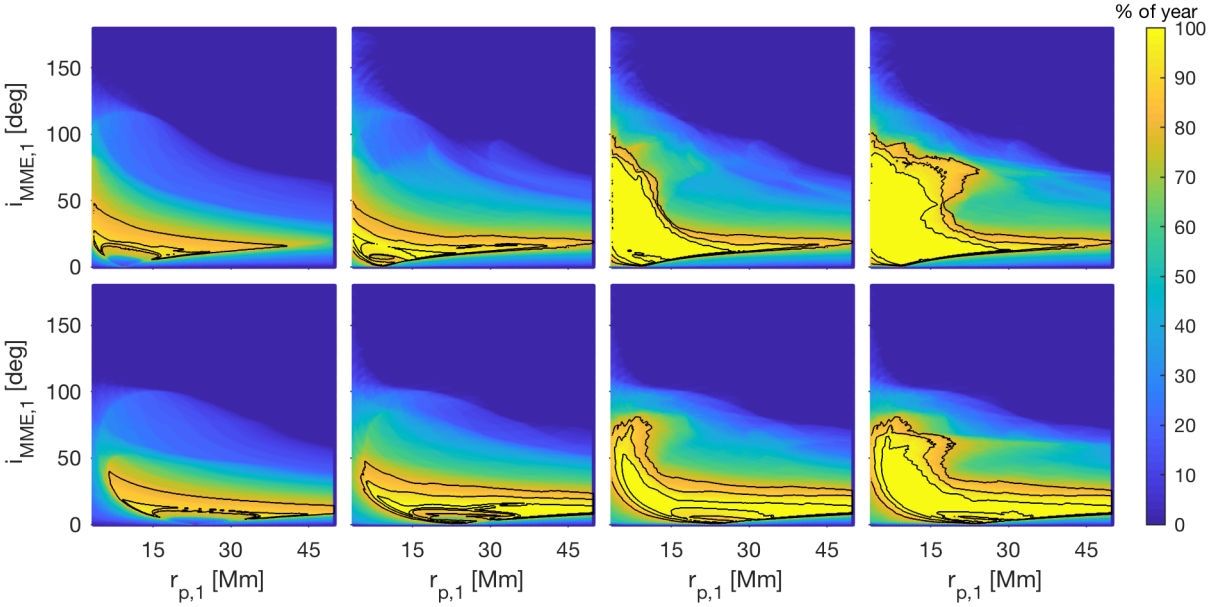

Figure 6.7: Percentage of the year one can arrive at Phobos (top) or Deimos (bottom) within 1, 2, 3 and 4 revolutions (left to right), for different departure regions in the $r_{p,1} - i_{\mathrm{MME},1}$ plane.

The developed methodology can be applied to zoom in on a specific area of the phase space. In analog with Section 5.2, the results with $r_{p,1}$ near 185 km altitude (100 km tolerance) are shown for up to four loop-transfers around Mars in Fig. 6.8 through 6.11. ΔV_1 is the maneuver at periareion one, ΔV_f is the maneuver to circularize the transfers at Phobos. In Subsection 5.2.3, it was argued that certain empty regions in Fig. 5.12 would be filled up if a larger $i_{\mathrm{Hill},1}$-region was considered. Fig. 6.8 shows this is indeed the case.

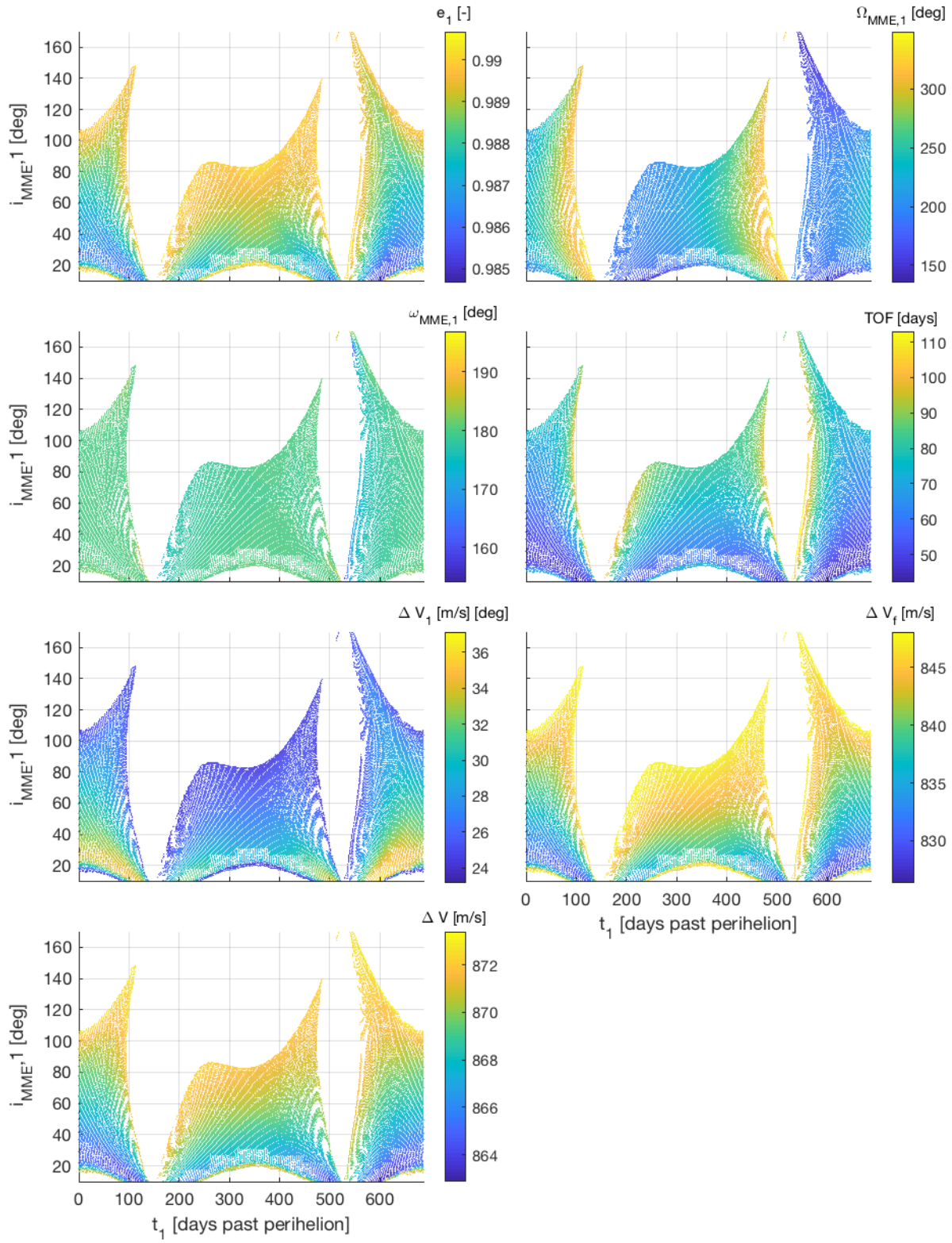

Figure 6.8: Departure time and initial orbital elements, TOF and fuel budget for one-loop transfers targeting Phobos departing at $r_{p,1} = 185 \pm 100$ km altitude.

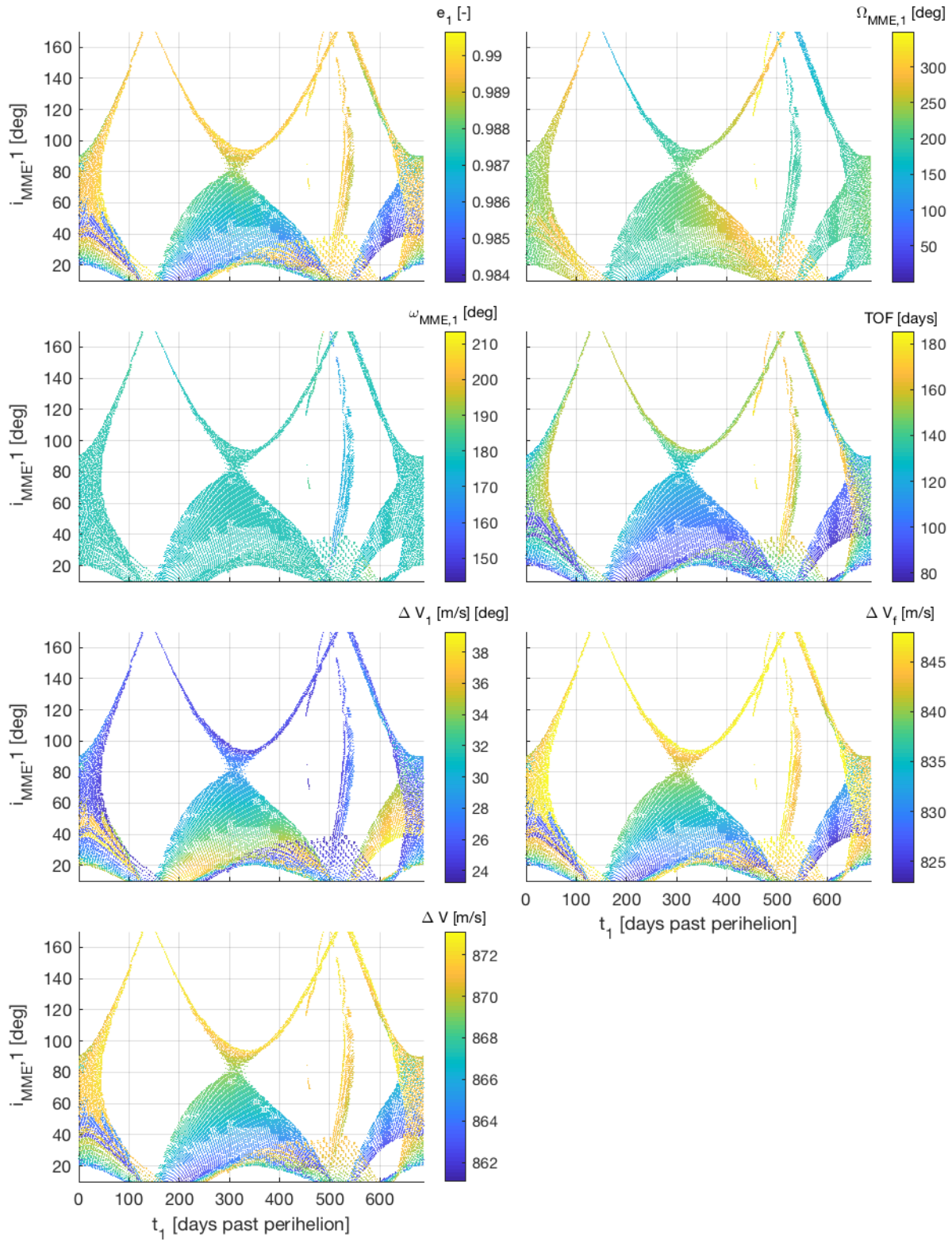

Figure 6.9: Departure time and initial orbital elements, TOF and fuel budget for two-loop transfers targeting Phobos departing at $r_{p,1} = 185 \pm 100$ km altitude.

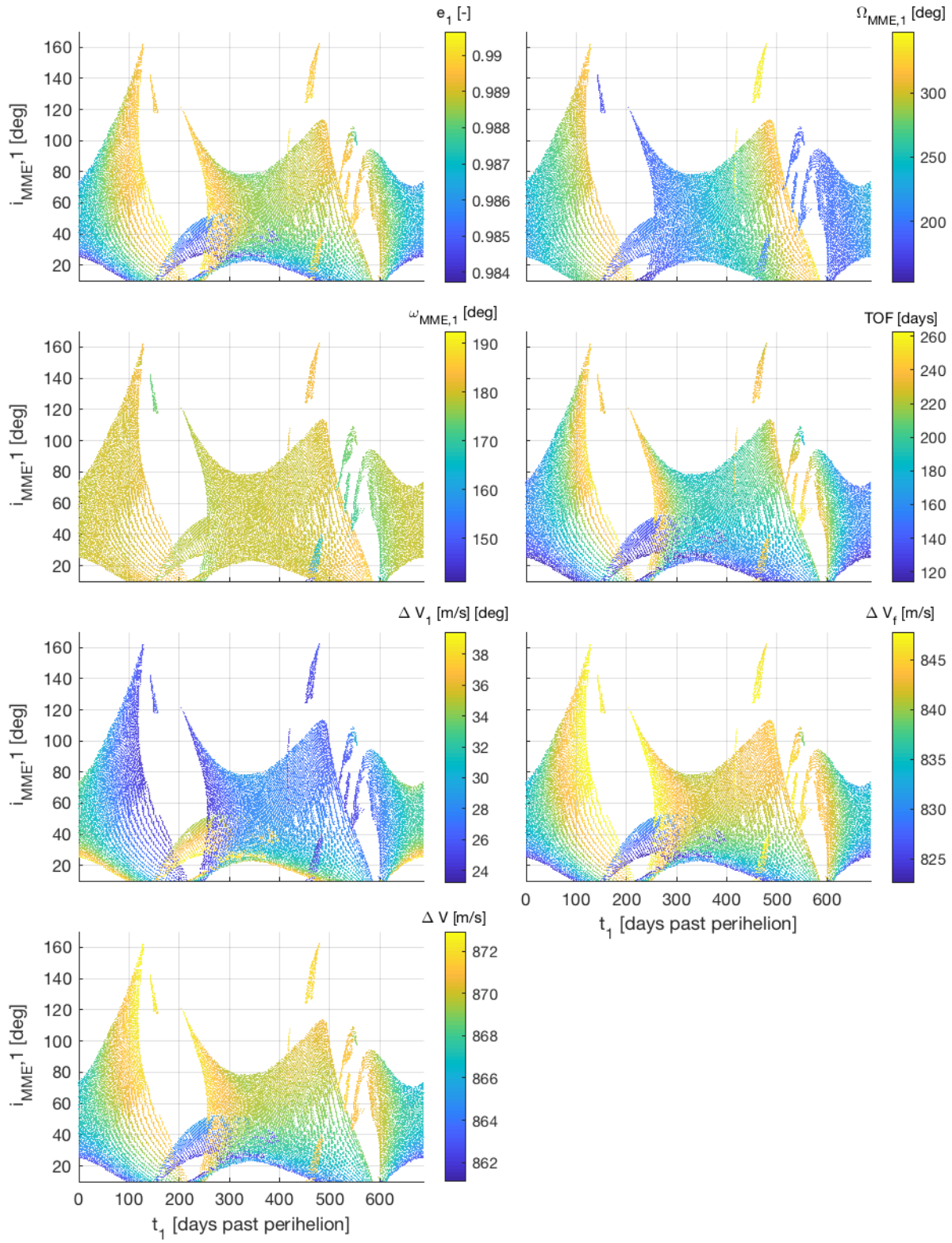

Figure 6.10: Departure time and initial orbital elements, TOF and fuel budget for three-loop transfers targeting Phobos departing at $r_{p,1} = 185 \pm 100$ km altitude.

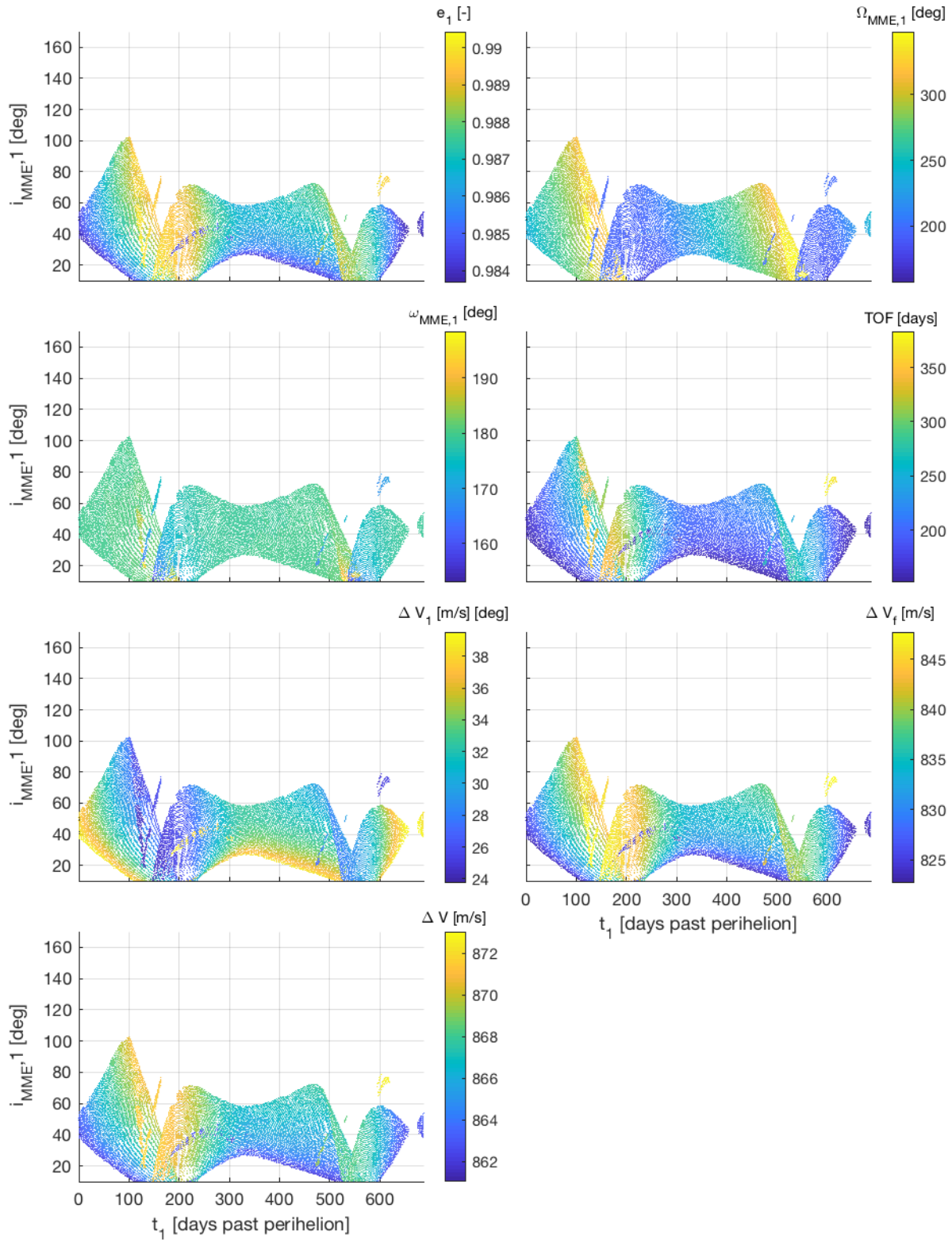

Figure 6.11: Departure time and initial orbital elements, TOF and fuel budget for four-loop transfers targeting Phobos departing at $r_{p,1} = 185 \pm 100$ km altitude.

Furthermore, one can trade-off the time of flight with total fuel cost for transfers departing from a specific region of the phase space. Zooming in on a single point on the $r_{p,1} - i_{\text{MME},1}$ phase space for transfers departing with an initial r_p near 185 km altitude (100 km tolerance) from a polar orbit (0.5° tolerance), Fig. 6.12 is created, showing the results for transfers with up to four loops around Mars. Clear regions exist for different loop numbers and the fuel savings from additional loops are marginal. Within each loop number, different structures exist on top of each other, based on the different departure time regions for which solutions exist. For traditional transfers, usually, longer transfers require less fuel. However, for these solar-perturbed transfers, this is not the case. Transfers arriving at the same $r_{p,f}$ with a high $r_{a,f}$ have a higher semi-major axis at arrival, and thus a larger TOF. At the same time, circularizing the high $r_{a,f}$ transfers requires more fuel. Thus, longer transfers, counter-intuitively, require more fuel.

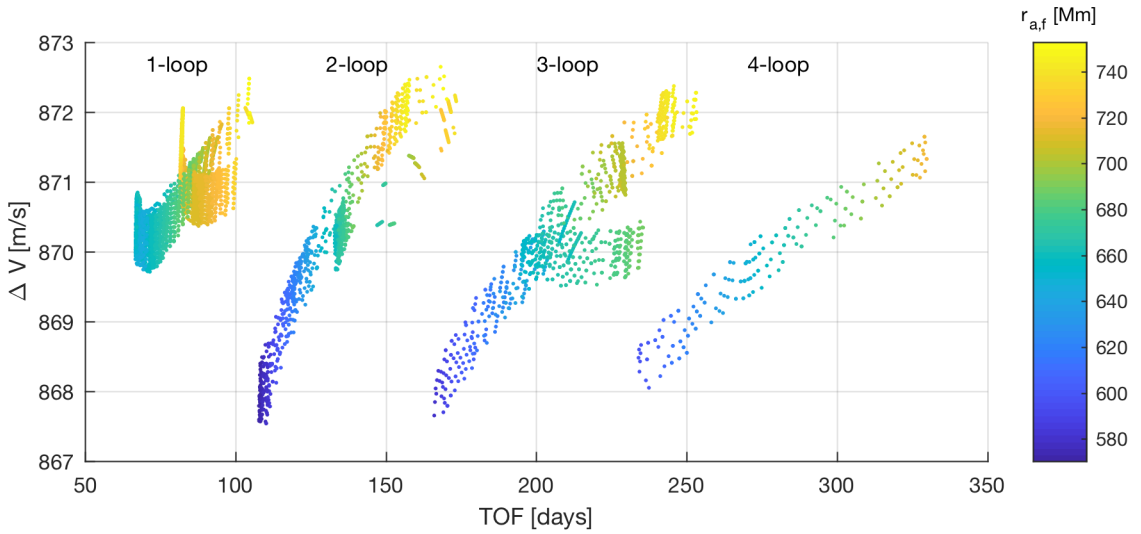

Figure 6.12: TOF and ΔV trade-off for a single point on the $r_{p,1} - i_{\text{MME},1}$ phase space: $r_{p,1} = 185 \pm 100$ km altitude, $i_{\text{MME},1} = 90 \pm 0.5°$. Note that the shown $r_{a,f}$-values are in the MME system, thus, they can be larger than the 720,000 km limit for the transfers in the Hill system.

Target both moons on one transfer The previous results can be trimmed by introducing the intermediate flyby of the other moon. For all permutations of N_1 and N_2, with $N = N_1 + N_2 \leq 4$, transfers are computed that pass within 500 km and 2° of Phobos for injection-Phobos-Deimos transfers, or Deimos for injection-Deimos-Phobos transfers. The results are summarized in Fig. 6.13 where the transfer type numbering is N_1 - N_2. The regions on the $r_{p,1} - i_{\text{MME},1}$ plane are much smaller and only exist for certain periods throughout the Martian year. Again, for areas on the $r_{p,1} - i_{\text{MME},1}$ plane with overlap between the different loop number permutations, the minimum TOF transfer is determined, shown in Fig. 6.14. Finally, similar to Fig. 6.7, Fig. 6.15 is created. Note that the latter groups the loop number permutations with the same total loop number N.

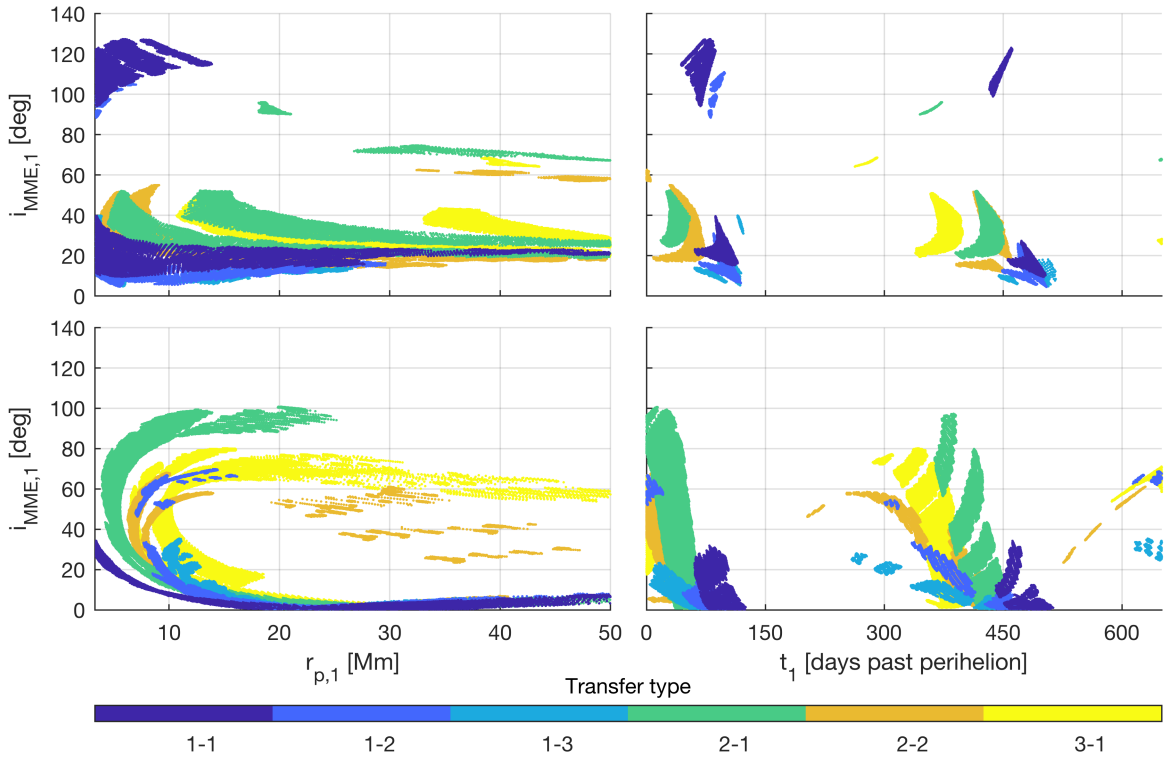

Figure 6.13: Initial conditions for injection-Phobos-Deimos transfers (top) and injection-Deimos-Phobos transfers (bottom).

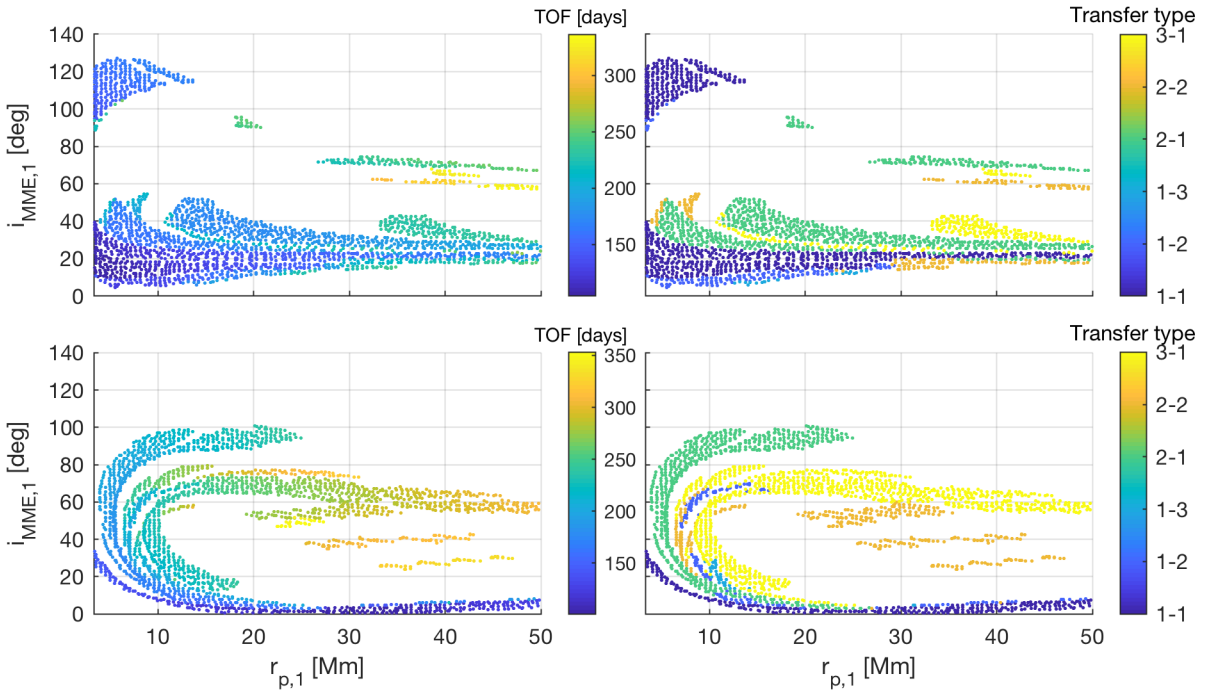

Figure 6.14: *TOF* and transfer structure for minimum TOF transfers: injection-Phobos-Deimos (top) and injection-Deimos-Phobos (bottom).

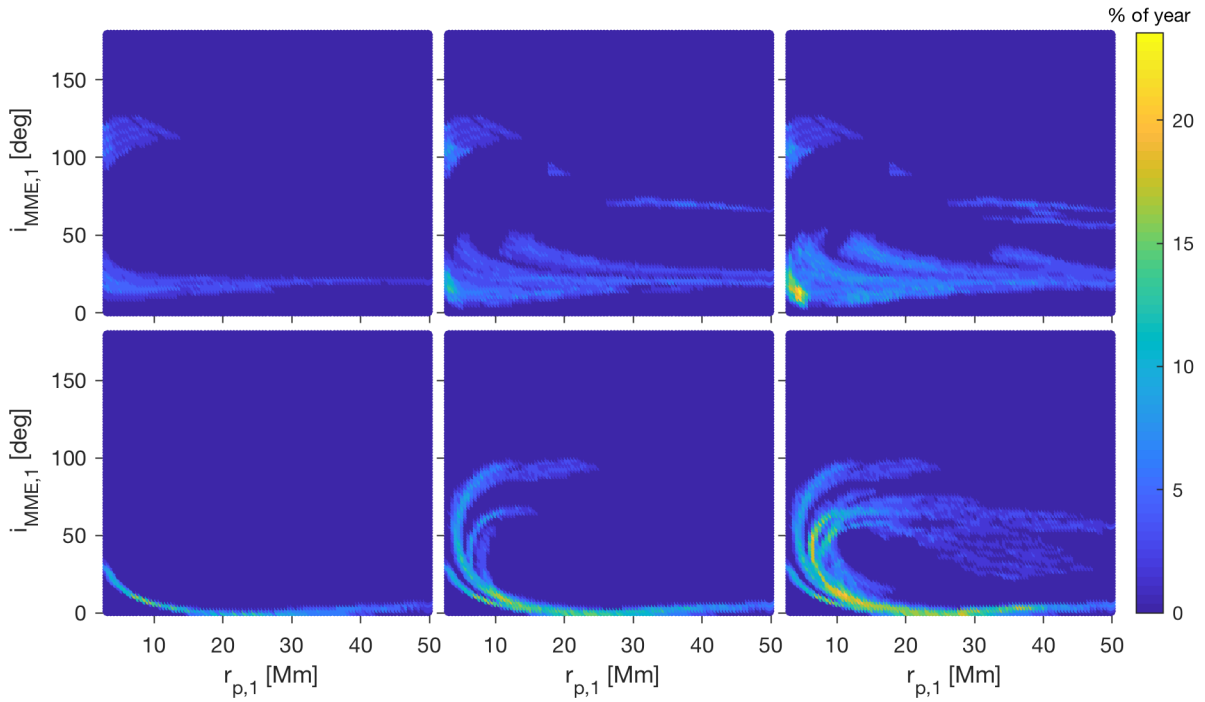

Figure 6.15: Percentage of the year one can arrive at Deimos for injection-Phobos-Deimos transfers (top), or arrive at Phobos for injection-Deimos-Phobos (bottom) transfers, for different departure regions in the $r_{p,1} - i_{\mathrm{MME},1}$ plane. Left to right: transfers with total loop numbers 2, 3 and 4.

6.1.1.3 Validation and correction

Target one moon The transfers are validated by integrating the predicted arrival states backwards in the eccentric Hill system. This allows to quantify the errors in the predicted initial state. As an example, the minimum TOF transfers arriving at Phobos at day 0 are validated in Fig. 6.16. The achieved accuracies are worse than what can be expected from the validation of the entire phase space in Table 5.24. That validation was performed with randomly chosen periareion states, limiting the number of similar transfers. For this application, transfers target the same $r_{p,f}$, $i_{\text{Hill},f}$ and $\Omega_{\text{Hill},f}$. Those transfers exhibit similar features, with highly correlated errors. If one of the selected transfer regions has a higher than nominal error, the entire error distribution is larger. Furthermore, the initial $\omega_{\text{MME},1}$ and $\Omega_{\text{MME},1}$ are poorly predicted for transfers departing at very low and high $i_{\text{MME},1}$. Near 0° and 180°, the node crossing is poorly defined. Small changes in predicted orbital elements in the Hill reference frame are translated into significant errors in

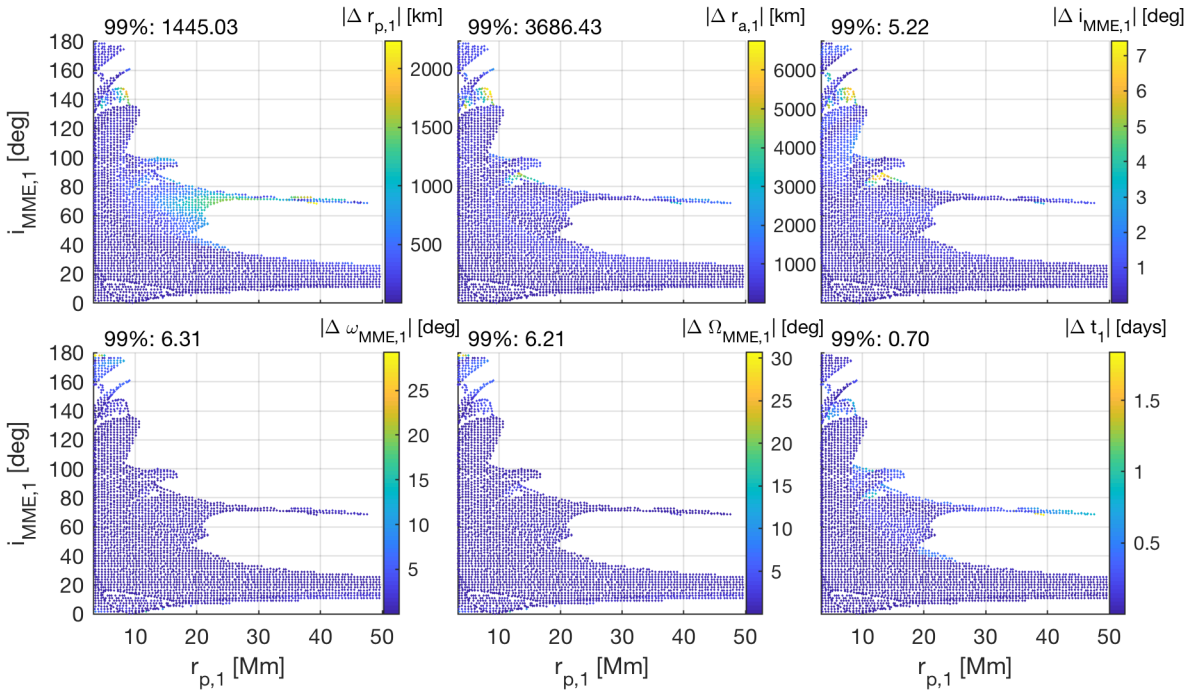

Figure 6.16: Validation of minimum TOF transfers that arrive at Phobos at day 0. Deviations between predicted and true initial orbital elements and timing.

the MME frame. In the validation of the entire architecture, the response in the Hill system was computed for $i_{\text{Hill},1} \in [5°, 175°]$. Hence, this phenomenon did not occur.

A systematic error occurs in some regions. Figure 6.17 demonstrates how this systematic error affects the true location on the $r_{p,1} - i_{\text{MME},1}$ plane. Overall, the predicted transfers give a good representation of the plane of interest. However, for some regions, the systematic error causes gaps in the true locations on the plane. For instance, the entire section near $i_{\text{MME},1} = 70°$ has a similar $r_{p,1}$ error. The true location is slightly to the right, causing a gap. Looking at Fig. 6.6, those transfers are all four loop solutions. The four loop solutions exist on the left of the minimum TOF interface between loop 3 and 4 (Fig. 6.3 and Fig. 6.6). Hence, the predicted four loop-solutions slightly to the left of this minimum TOF interface, with similar r_p errors, are mapped into the gap.

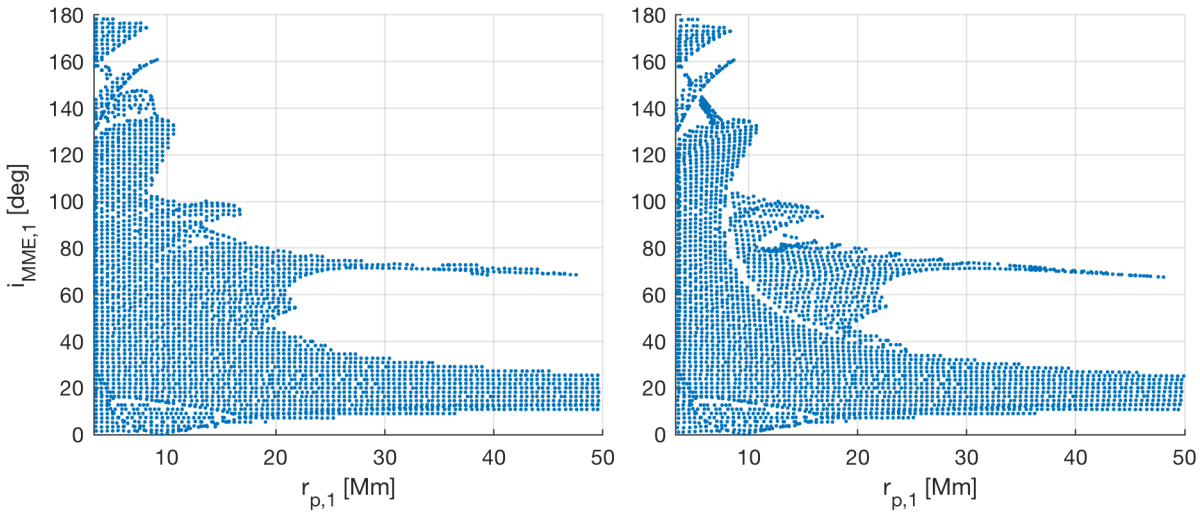

Figure 6.17: Validation of minimum TOF transfers that arrive at Phobos at day 0. Left: predicted location on plane of interest. Right: true location on plane of interest.

Target both moons on one transfer Similarly, the injection-Phobos-Deimos transfers with minimum TOF in the top-part of Fig. 6.14 are validated. The results can be seen in Fig. 6.18. The errors near Phobos are larger than at Deimos. This is expected, since the transfers are predicted to exactly arrive at Deimos, while they are expected to flyby Phobos within 2° and 500 km. A clear structure in inclination error can be observed. Only in the center of the windows do true ballistic connections between Phobos and Deimos exist. Furthermore, the errors in $\omega_{\text{MME},1}$

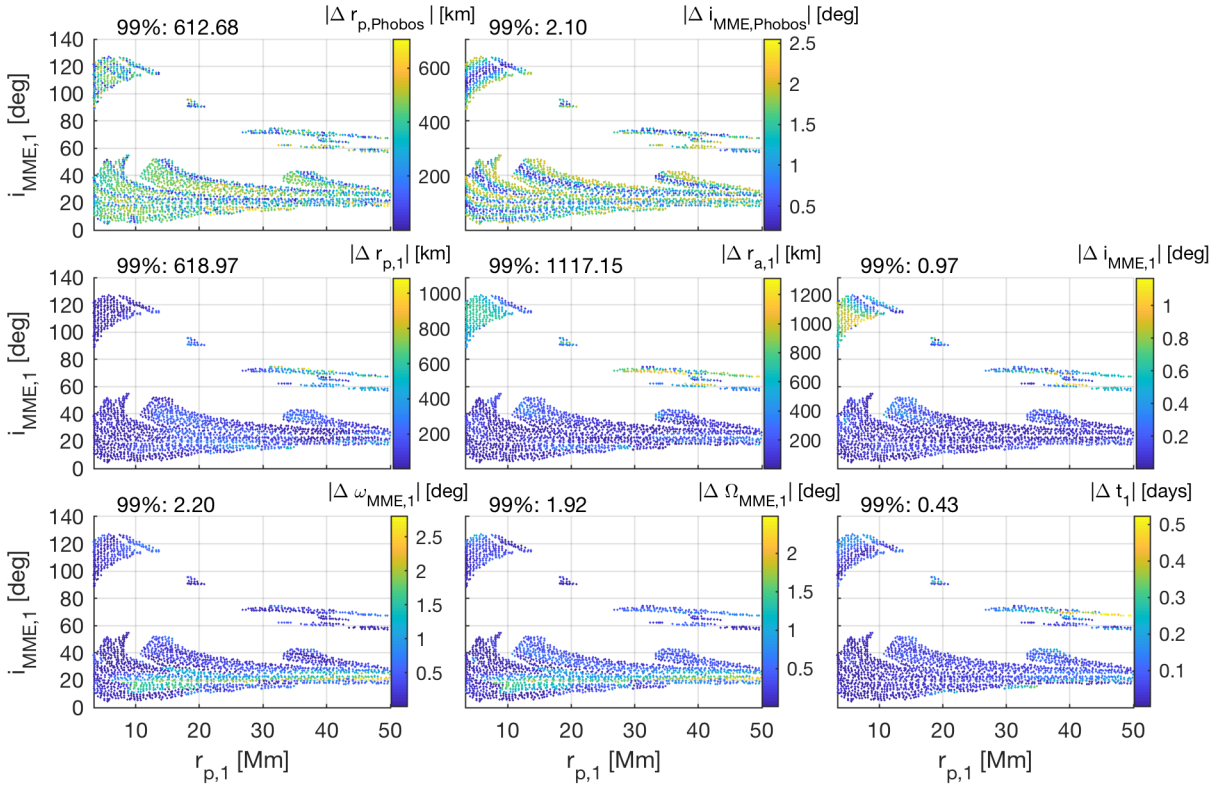

Figure 6.18: Validation of ballistic minimum TOF injection-Phobos-Deimos transfers. Top: errors in flyby state. Bottom: error between predicted and true initial orbital elements and timing.

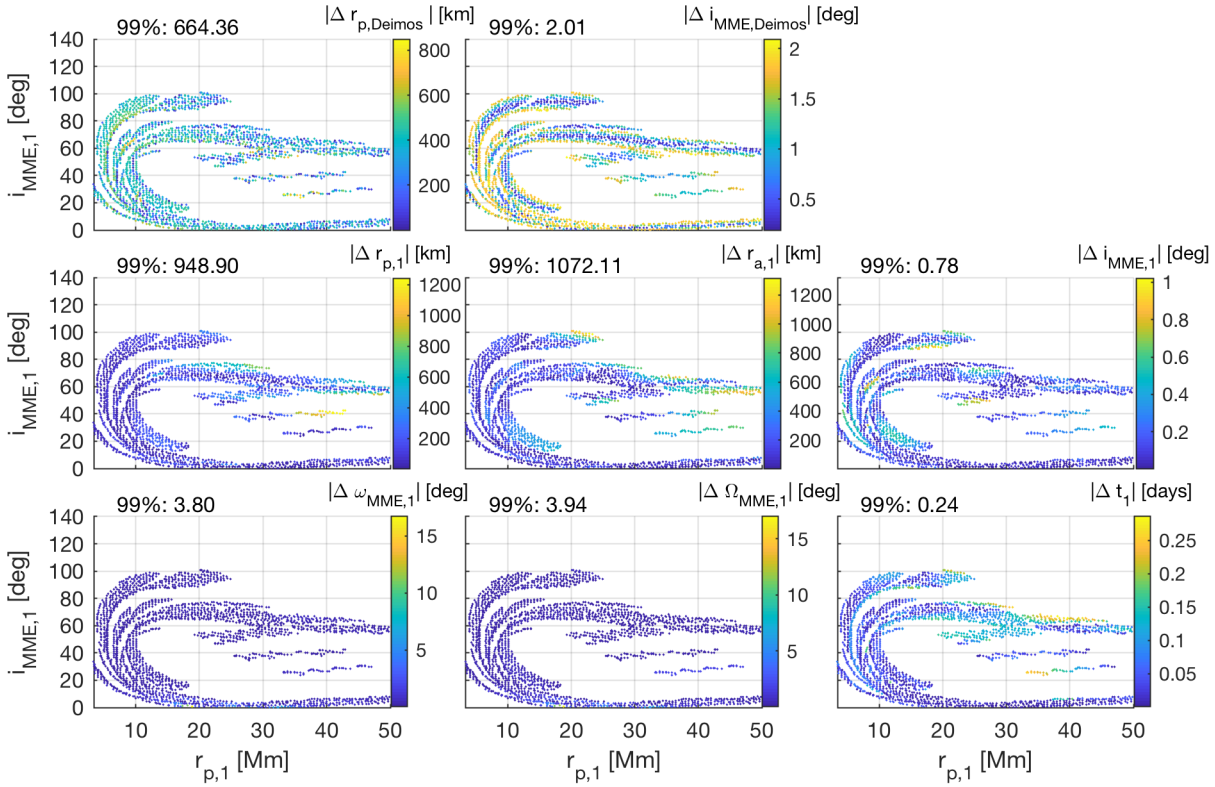

Figure 6.19: Validation of ballistic minimum TOF injection-Deimos-Phobos transfers. Top: errors in flyby state. Bottom: error between predicted and true initial orbital elements and timing.

and $\Omega_{\text{MME},1}$ are much smaller, due to the lack of solutions near 0° and 180° $i_{\text{MME},1}$. The injection-Deimos-Phobos transfers with minimum TOF in the bottom-part of Fig. 6.14 are validated. The results can be seen in Fig. 6.19. Again, a clear structure in inclination error can be observed and the large errors exist in $\omega_{\text{MME},1}$ and $\Omega_{\text{MME},1}$ near $i_{\text{MME},1} = 0°$.

The identified transfers do not perfectly pass by the first moon, nor do they depart exactly from the predicted initial conditions. A predictor-corrector scheme is set-up to determine how much the initial conditions need to vary to nullify the errors and find truly ballistic transfers between the two moons. The predictor-corrector scheme is allowed to change the arrival conditions at the second moon: $r_{a,f}$, $\omega_{\text{Hill},f}$, and t_f. Those final conditions are integrated backwards in the eccentric Hill system. The errors at the first moon are computed and are minimized. This has been done for all six permutations of transfer loops. The difference between the predicted and converged transfers are shown in Table 6.1 for injection-Phobos-Deimos transfers and in Table 6.2 for injection-Deimos-Phobos transfers. The converged injection-Phobos-Deimos, and injection-Deimos-Phobos transfers are visualized in, respectively, Fig. 6.20 and 6.21. The identified transfers provide very good initial guesses for truly ballistic transfers. Within a group in $r_{p,1} - i_{\text{MME},1}$ space, all predicted transfers tend to converge onto the same converged point. This phenomenon can also be seen in Fig. 6.18 and 6.19; clear bands exist where the errors at the flyby moon are smallest. Thus, there is only one truly ballistic solution per group. The other points in the neighborhood are points that satisfy the tolerances, but require some maneuvering to nullify the errors for the flyby of the first moon. Again, it is expected that the predicted transfers provide very good initial guesses.

6.1.1.4 Discussion

Additional loops increase the reachable phase space area and they increase the percentage of the year one can arrive with certain orbital elements. An additional flyby places serious limits on the reachable phase space area, and the percentage of the year one can arrive.

Table 6.1: Difference between the predicted, and the converged initial states for a predictor-corrector scheme changing the arrival states at Deimos, to target an exact flyby of Phobos.

$N_1 - N_2$	t_1 [days]	$i_{\text{MME},1}$ [deg]	$r_{a,1}$ [km]	$r_{p,1}$ [km]	$\omega_{\text{MME},1}$ [deg]	$\Omega_{\text{MME},1}$ [deg]	$\Delta r_{\text{p,Phobos}}$ [km]	$\Delta i_{\text{MME,Phobos}}$ [deg]
1-1								
Predicted	60.5	106.5	662,900	5,983	359.8	282.0	441	1.73
Converged	60.1	106.6	660,958	5,227	359.9	280.2	0.1	1.6e-3
1-2								
Predicted	479.2	15.1	517,739	4,512	0.8	293.2	450	0.93
Converged	479.1	15.0	522,712	4,080	0.0	295.0	0.08	8.1e-4
1-3								
Predicted	117.9	37.3	672,927	3,608	2.2	333.9	179	1.81
Converged	109.9	37.4	673,959	3,838	0.8	332.3	0.09	1.6-5
2-1								
Predicted	659.6	69.7	691,205	43,181	352.1	289.8	441	0.64
Converged	659.6	69.7	669,670	36,862	353.2	284.8	0.10	3.8e-3
2-2								
Predicted	682.5	58.2	704,567	49,743	355.0	312.9	202	1.02
Converged	682.8	57.5	698,909	45,679	354.6	311.1	0.10	2.94e-5
3-1								
Predicted	378.7	33.5	536,306	18,067	358.5	312.9	401	1.03
Converged	378.8	33.5	541,114	17,670	358.2	314.0	0.09	8.2e-4

Table 6.2: Difference between the predicted, and the converged initial states for a predictor-corrector scheme changing the arrival states at Phobos, to target an exact flyby of Deimos.

$N_1 - N_2$	t_1 [days]	$i_{\text{MME},1}$ [deg]	$r_{a,1}$ [km]	$r_{p,1}$ [km]	$\omega_{\text{MME},1}$ [deg]	$\Omega_{\text{MME},1}$ [deg]	$\Delta r_{\text{p,Deimos}}$ [km]	$\Delta i_{\text{MME,Deimos}}$ [deg]
1-1								
Predicted	482.9	6.4	647,379	11,665	358.2	261.8	481.9	1.94
Converged	481.8	6.3	655,429	10,427	1.1	259.9	0.01	0.02
1-2								
Predicted	652.0	66.51	644,505	11,799	356.1	227.0	463.3	1.1
Converged	656.1	66.50	642,629	11,555	357.2	227.9	0.01	1.8e-3
1-3								
Predicted	374.6	10.3	555,394	14,590	355.1	234.5	420	1.3
Converged	375.1	10.3	554,930	14,387	359.1	231.2	0.1	0.008
2-1								
Predicted	20.0	93.5	639,885	10,595	358.3	260.4	360	1.9
Converged	19.2	93.5	639,885	10,781	358.8	260.3	0.07	0.08
2-2								
Predicted	385.9	36.9	580,237	8,035	358.8	253.79	307	1.6
Converged	366.1	36.9	587,321	8,011	358.9	245.7	0.10	0.07
3-1								
Predicted	665.9	64.1	577,088	12,298	356.8	244.6	514	0.3
Converged	667.2	64.1	576,465	12,198	357.2	244.8	0.094	4.4e-4

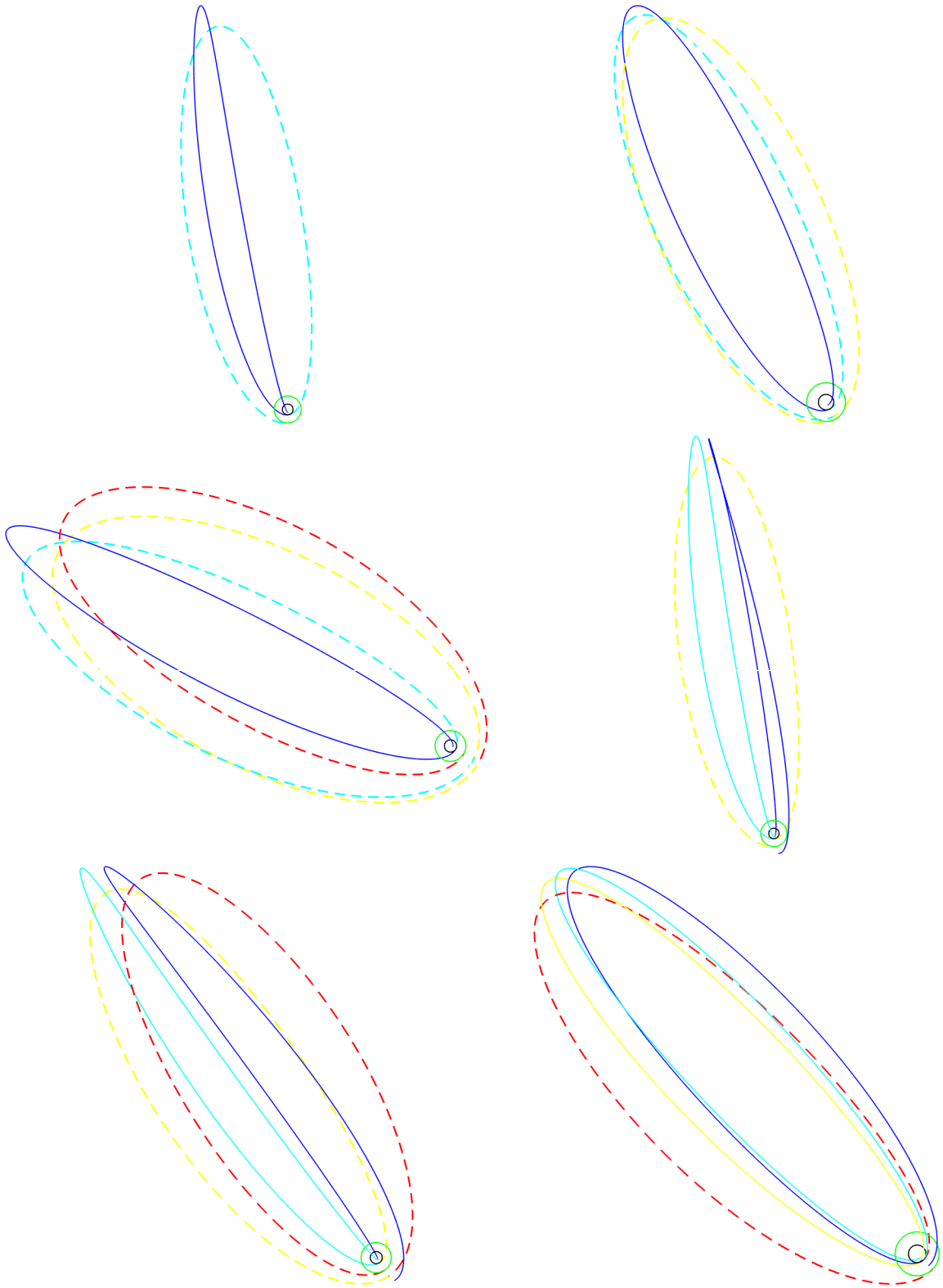

Figure 6.20: Visualization of the converged injection-Phobos(black)-Deimos(green) transfers, mapped on the xy-plane of the MME reference frame. The injection-Phobos segment is indicated with a solid line, the Phobos-Deimos segment with a dashed line. From left to right and top to bottom: 1-1, 1-2, 1-3, 2-1, 2-2, 3-1 transfers.

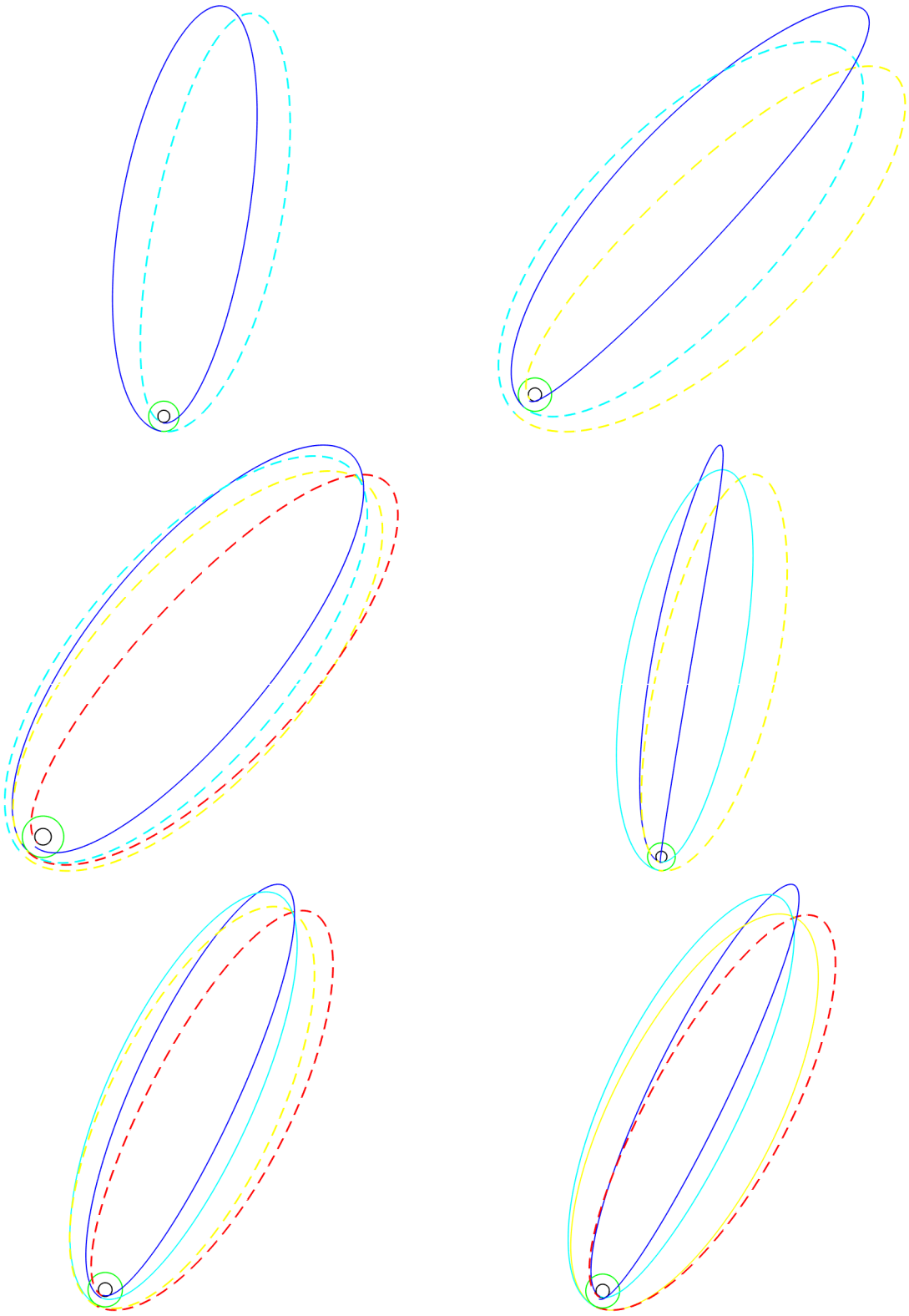

Figure 6.21: Visualization of the converged injection-Deimos(green)-Phobos(black) transfers, mapped on the xy-plane of the MME reference frame. The injection-Deimos segment is indicated with a solid line, the Deimos-Phobos segment with a dashed line. From left to right and top to bottom: 1-1, 1-2, 1-3, 2-1, 2-2, 3-1 transfers.

6.1.2 Transfers with one maneuver

In this section, the initial conditions are determined when one maneuver is allowed at one intermediate periareion. First, the maneuver type and magnitude is discussed. The focus of this research is to solely use solar gravity to perform orbital plane changes. Therefore, the maneuvers are restricted to be in-plane. The maneuvers occur at an intermediate periareion. Therefore, the maneuvers are restricted to be in the velocity direction, solely altering r_a. The required maneuver sizes to decrease and increase the r_a to the lower and upper limits of 440,000 and 720,000 km for any $r_p - r_a$ combination in the considered phase space are plotted in Fig. 6.22. One can see that with solely 25.37 m/s, any r_a state can be achieved, for any initial value of r_a and r_p. Furthermore, one can see that large sections of the phase space require lower maneuver sizes.

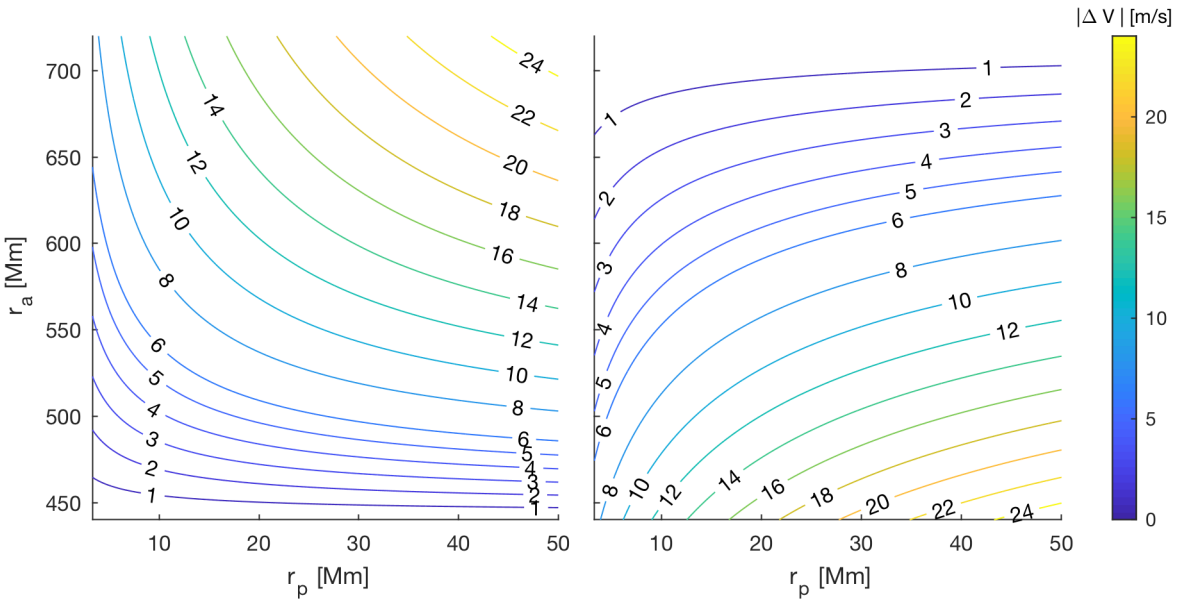

Figure 6.22: $|\Delta V|$ to change r_a to 440,000 (left) and 720,000 (right) for any $r_a - r_p$ combination.

6.1.2.1 Methodology

Target one moon Similar to the ballistic scenario, a sparse grid in $r_{a,f}$ and $\omega_{\text{Hill},f}$ is created and the periareion states post-maneuver are predicted. Then, for every post-maneuver state, 57 pre-maneuver states are selected, differing only by r_a-value. Every value between 440,000 and 720,000 with resolution 5,000 km is used. Those pre-maneuver states are then predicted back

to compute the initial state. A three-dimensional refinement method is employed. The algorithm is summarized in Algorithm 5. This process is again performed for $t_f \in [0, 680]$, with step size 10 days, on scenarios with total loops $N \in [2, 4]$, with maneuvers after loop $M \in [1, N-1]$.

Target both moons on one transfer For the scenario with the additional flyby, a different strategy is followed dependent on the timing of the maneuver.

Maneuver between injection and flyby of first moon: The final states at the second moon that have a flyby with the first moon are already known and the post-maneuver states can be extracted from the ballistic results. Again, for each post-maneuver state, 57 pre-maneuver states are selected and predicted back to compute the initial state. This process is performed for all permutations of N_1 and N_2, and maneuver locations after loop $M \in [1, N_1]$.

Maneuver between flyby of first moon and arrival at second moon: The maneuver directly affects whether or not a trajectory flies by the first moon. Thus, the post-maneuver state can not be extracted from the ballistic results. Again, a grid is created in $r_{a,f}$, $\omega_{\text{Hill},f}$, and t_f. Then, the post-maneuver orbital elements are predicted, and 57 pre-maneuver states are selected and predicted back to the orbital elements near the first moon. A three-dimensional refinement method is employed to find more trajectories that pass close to the first moon. The algorithm is summarized in Algorithm 6. Finally, the trajectories that pass close to the first moon are then mapped back N_1 loops to determine the initial conditions. This process is performed for all permutations of N_1 and N_2, and maneuvers after loop $M \in [N_1 + 1, N_2 - 1]$.

6.1.2.2 Results

Target one moon It is investigated how the maneuvers expand the accessible surface on the $r_{p,1} - i_{\text{MME},1}$ plane for $\Delta V < 1$ m/s, $\Delta V < 5$ m/s, $\Delta V < 10$ m/s, and $\Delta V < 25$ m/s. In Fig. 6.23, a general overview of the results is given for transfers arriving at Phobos or Deimos. The large number of permutations hinders the visualization of the expansion of the area for each individual loop. Therefore, this figure shows the area of the phase space that is accessible for all four loops combined, with only one maneuver for different maximum ΔV-values.

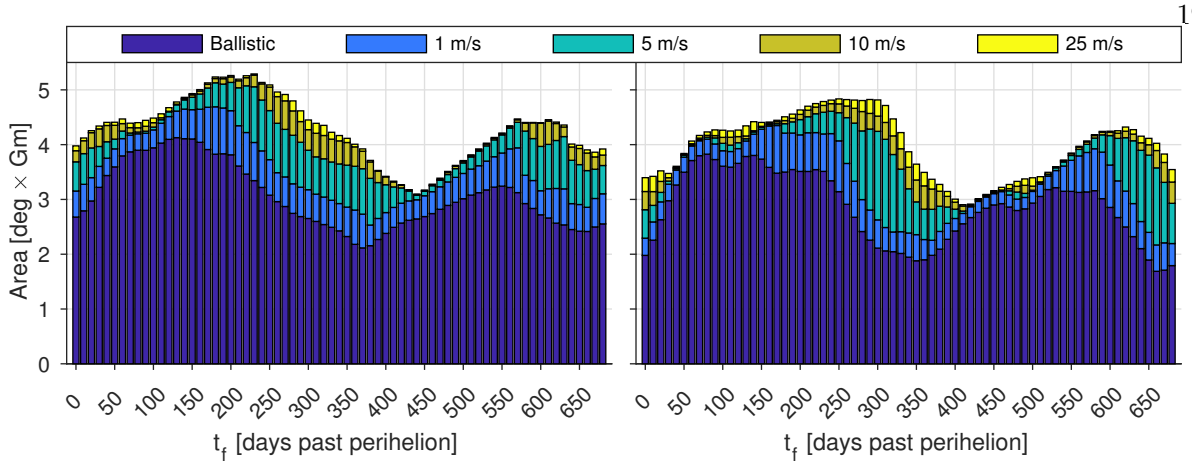

Figure 6.23: Visualization of the effect of one ballistic maneuver on the $r_{p,1} - i_{\mathrm{MME},1}$ plane for transfers arriving at Phobos (left) or Deimos (right) at day 0 through 680.

For each arrival day, the loop number, maneuver location, and maneuver size that results in the minimum TOF or minimum ΔV solution for each region within the $r_{p,1} - i_{\mathrm{MME},1}$ plane can be determined. An example of this procedure is shown in Fig. 6.24. This procedure plots the extrema in the ΔV-TOF trade-off for each region on the $r_{p,1} - i_{\mathrm{MME},1}$ plane, for a specific arrival date. Regions exist with a significant TOF reduction if a maneuver of a few m/s is allowed. An example can be seen for arrival day 0, near 5,000 km and 140°. For the minimum ΔV solution, a nearly ballistic solution with three loops is optimal. By allowing 5 to 10 m/s, a two loop solution with a maneuver after the first loop becomes feasible, saving 120 days.

Finally, one can compute how many days per year one can depart from a certain region in the $r_{p,1} - i_{\mathrm{MME},1}$ plane, for a maximum of 1, 2, 3, and 4 loops, for maximum maneuver sizes of 0 m/s, 1 m/s, 5 m/s, 10 m/s, 25 m/s. The results can be seen in Fig. 6.25.

Target both moons on one transfer These results are significantly trimmed when introducing an intermediate flyby. The initial conditions for the minimum TOF and minimum ΔV transfers for all permutations of N_1, N_2 and maneuver locations are summarized in Fig. 6.26 for injection-Phobos-Deimos transfers and in Fig. 6.27 for injection-Deimos-Phobos transfers. Similar to Fig. 6.25, Fig. 6.28 is created where one can see how many days per year one can depart from a certain region in the $r_{p,1} - i_{\mathrm{MME},1}$ plane, for a maximum of 2, 3, and 4 loops, for maximum maneuver sizes of 0 m/s, 1 m/s, 5 m/s, 10 m/s, 25 m/s.

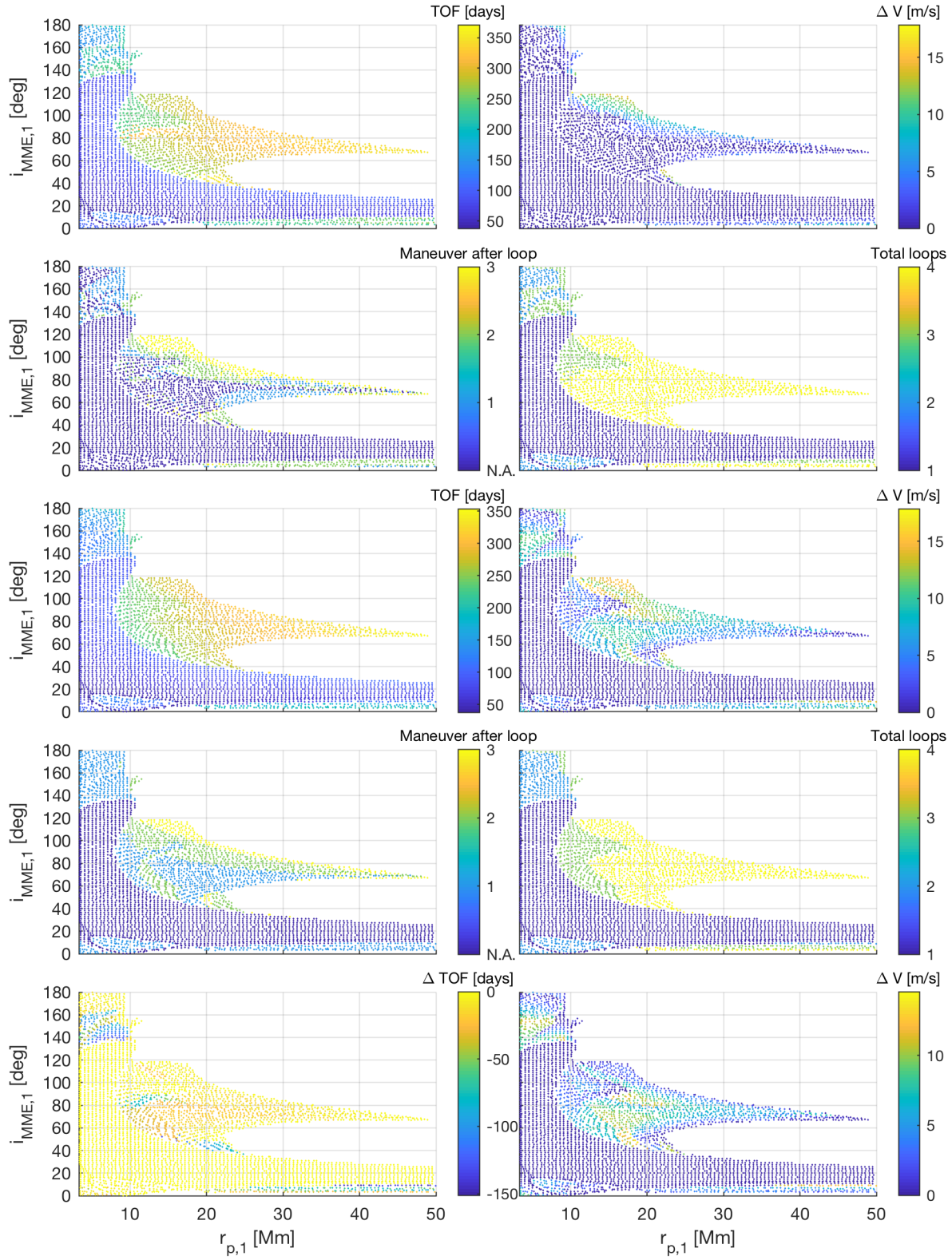

Figure 6.24: Comparison between minimum ΔV (top 2 rows) and minimum TOF transfers (middle 2 rows), and their difference in TOF and ΔV (bottom row) for transfers that arrive at Phobos at day 0.

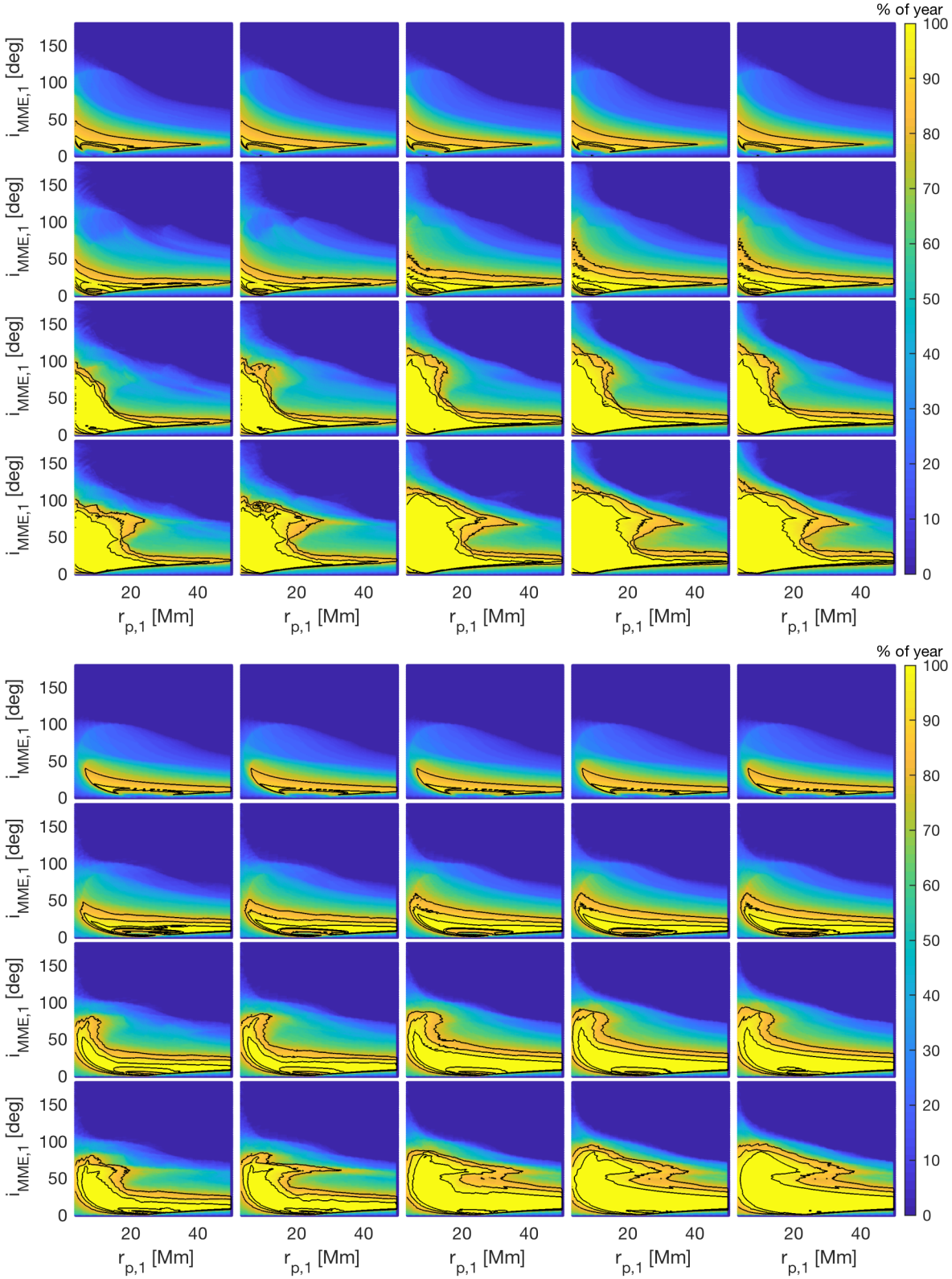

Figure 6.25: Percentage of the year one can arrive at Phobos (top) or Deimos (bottom) within 1, 2, 3, and 4 revolutions (top to bottom). Left to right: ballistic, 1 m/s, 5 m/s, 10 m/s, 25 m/s.

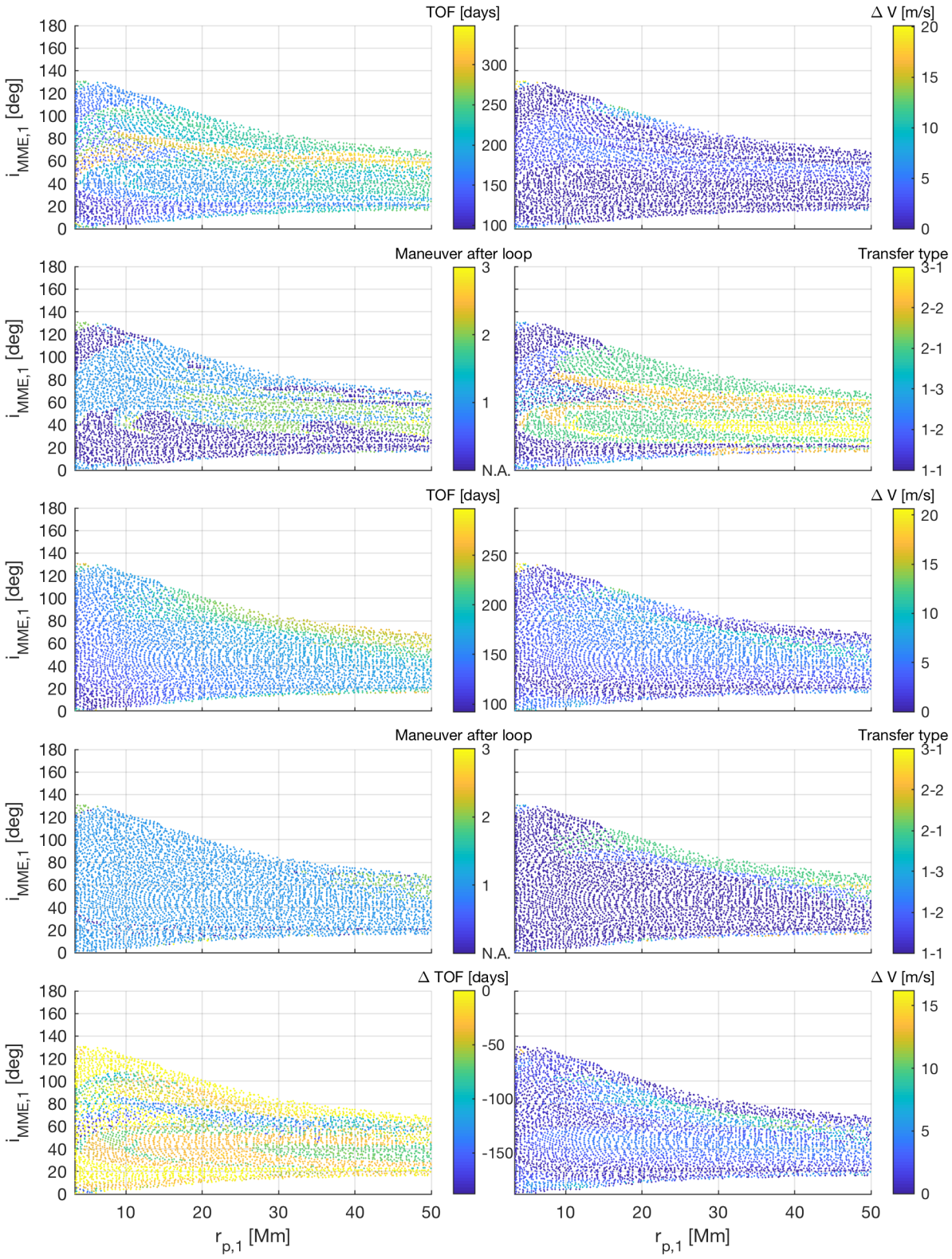

Figure 6.26: Comparison between minimum ΔV (top 2 rows) and minimum TOF transfers (middle 2 rows), and their difference in TOF and ΔV (bottom row) for injection-Phobos-Deimos transfers.

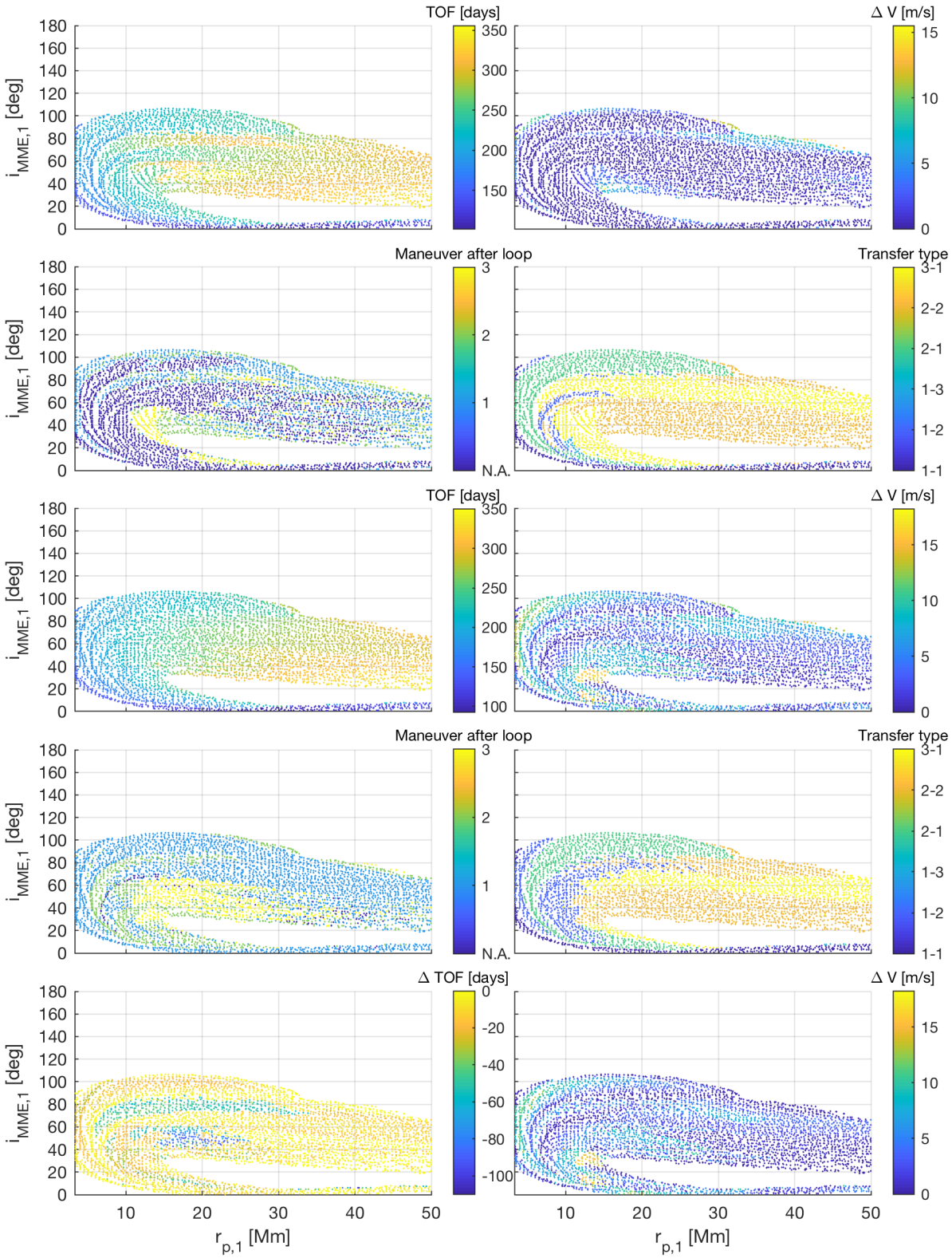

Figure 6.27: Comparison between minimum ΔV (top 2 rows) and minimum TOF transfers (middle 2 rows), and their difference in TOF and ΔV (bottom row) for injection-Deimos-Phobos transfers.

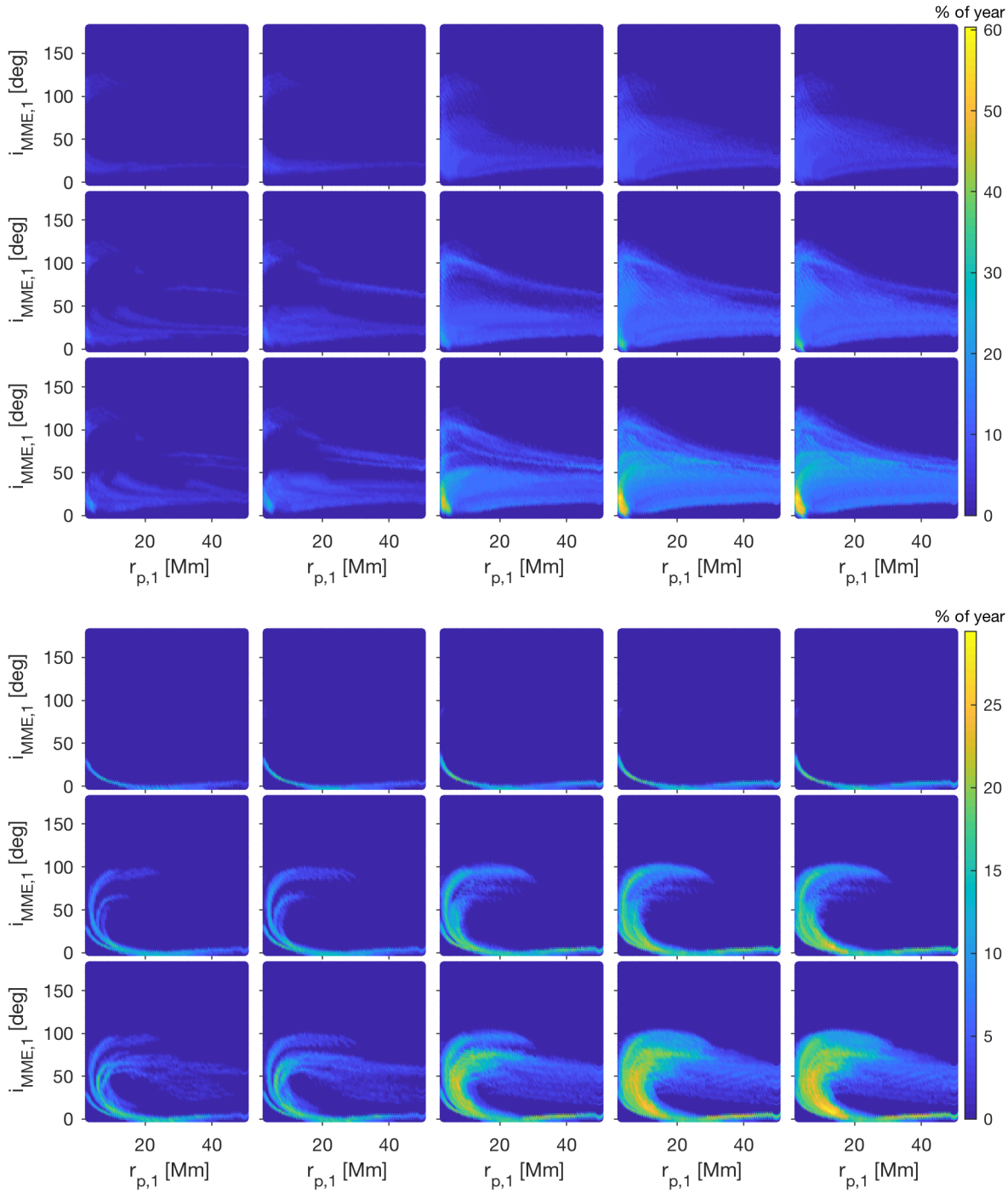

Figure 6.28: Percentage of the year transfers exist within regions of the departable phase space in the $r_{p,1} - i_{\mathrm{MME},1}$ plane for injection-Phobos-Mars (top) and injection-Deimos-Phobos (bottom). Left to right: ballistic, 1 m/s, 5 m/s, 10 m/s, 25 m/s. Top to bottom: 2 through 4 total loops.

6.1.2.3 Validation and correction

Target one moon The identified initial conditions are again validated through backwards numerical integration in the eccentric Hill system. The results for the validation for the minimum TOF transfers arriving at Phobos at day 0 are shown in Fig. 6.29. The results are very similar to the ballistic case, with similar conclusions.

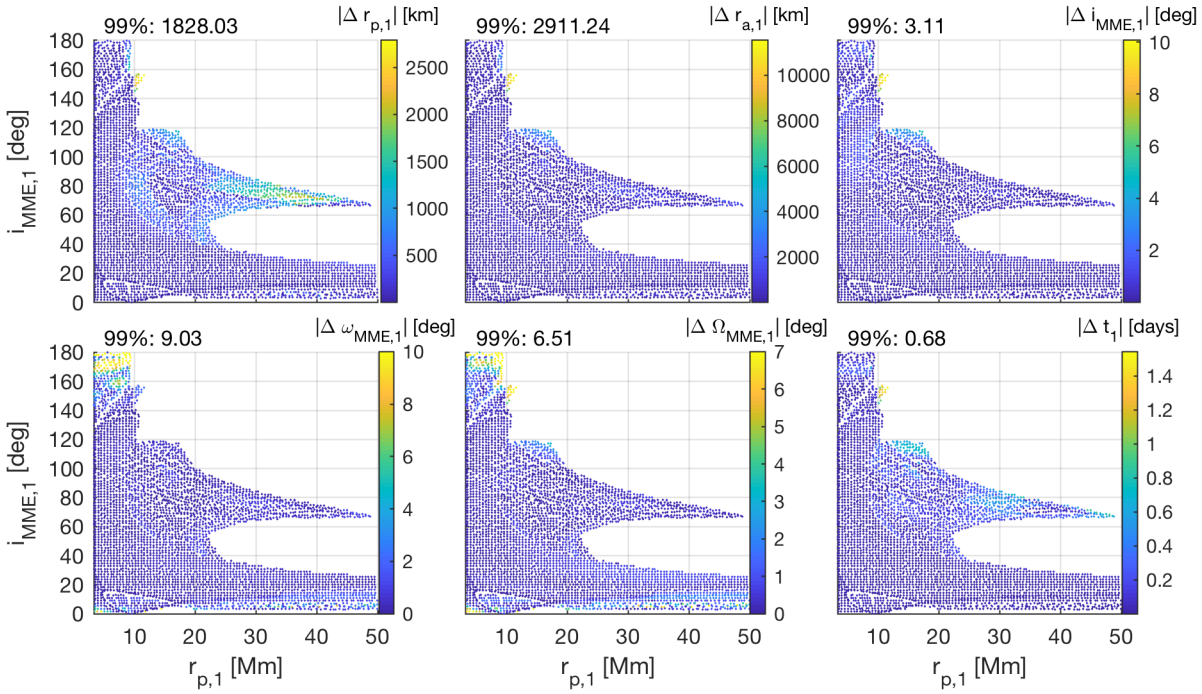

Figure 6.29: Validation of one-maneuver transfers that arrive at Phobos at day 0 with minimum TOF. Deviations between predicted and true initial orbital elements and timing.

Target both moons on one transfer Similarly, the minimum TOF transfers for injection-Phobos-Deimos, and injection-Deimos-Phobos transfers are validated. The results are shown in Fig. 6.30 and 6.31. Compared to Fig 6.18 and 6.19, one can see fewer band structures with small errors at the first moon. However, those band structures are still present, but are hidden by shorter duration transfers at the same location on the $r_{p,1} - i_{\mathrm{MME},1}$ plane. Previously, true ballistic solutions between Phobos and Deimos, and Deimos and Phobos have been identified, and their initial conditions are shown in Tables 6.1 and 6.2. Those ballistic solutions can be re-used to determine the perturbed

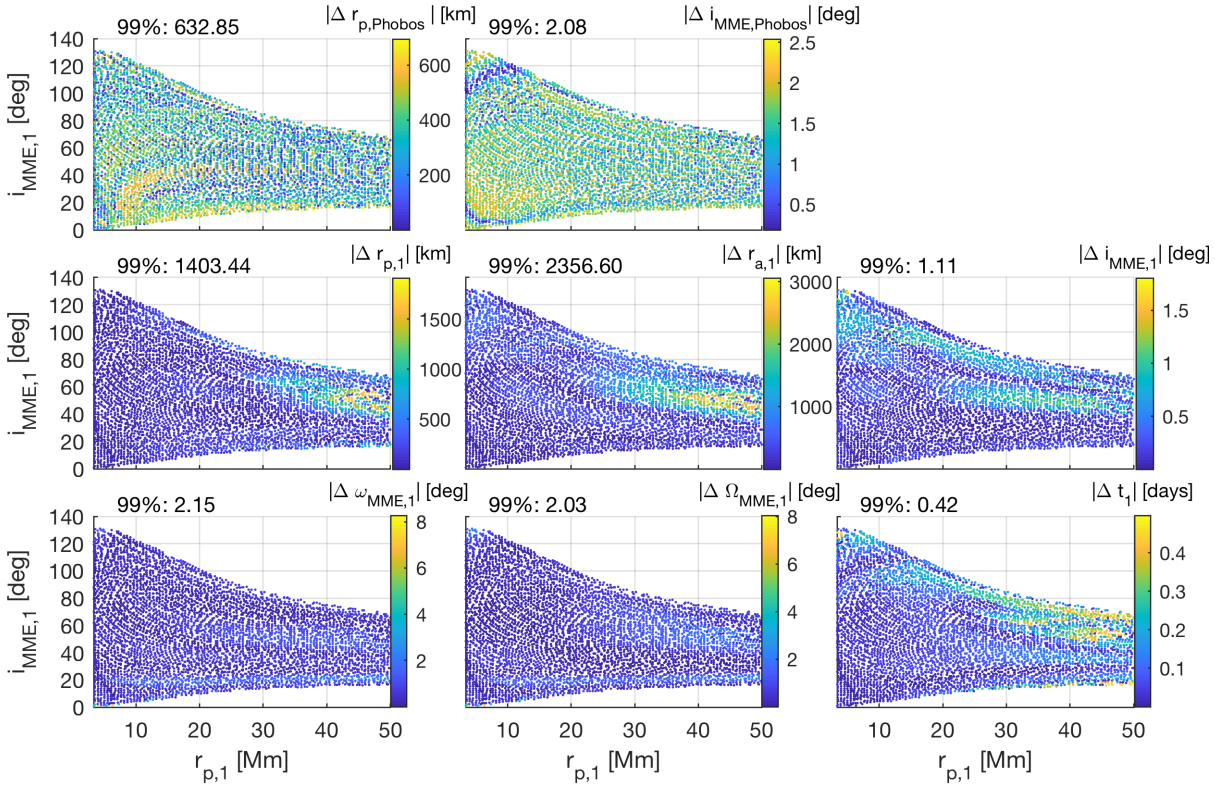

Figure 6.30: Validation of one-maneuver injection-Phobos-Deimos minimum TOF transfers. Top: errors in flyby state. Bottom: error between predicted and true initial orbital elements and timing.

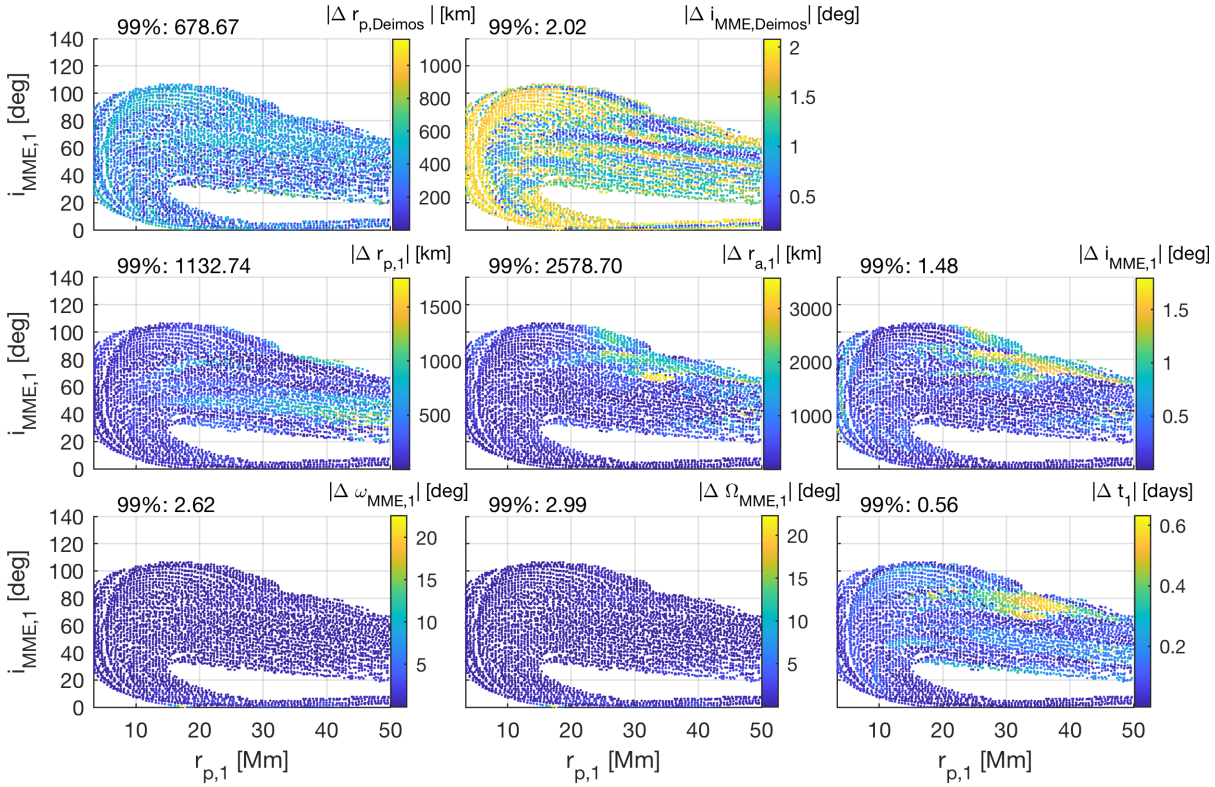

Figure 6.31: Validation of one-maneuver injection-Deimos-Phobos minimum TOF transfers. Top: errors in flyby state. Bottom: error between predicted and true initial orbital elements and timing.

initial conditions for scenarios with maneuvers between injection and the first moon flyby. For all $N_1 - N_2$, and maneuver location permutations, the response for pre-maneuver states between 440,000 and 720,000 with resolution 5,000 km are predicted, and numerically integrated. The results can be seen in Fig 6.32. On the left, it can be seen that for each integrated transfer, a predicted solution exists very close by; within 500 km and 0.5° for injection-Phobos-Deimos. The extrema for injection-Deimos-Phobos are higher; 1500 km and 0.8°. On the right, the integrated response can be seen, for scenarios that do not impact nor escape. The black dots are the ballistic solutions shown in Table 6.1. Note that multiple lines may exist for a $N_1 - N_2$ scenario, differing by the periareion number where the maneuver is applied. As an example, the effect of the maneuver is shown for 2-1 injection-Deimos-Phobos transfers where a maneuver occurs at the Deimos flyby. Six different maneuvers are applied, with maneuver size 14.9 m/s, 7.6 m/s, 4.7 m/s, 2.2 m/s, 1.0 m/s, and 3.3 m/s. Even for such small maneuvers, the effect on the departure conditions on the $r_{p,1} - i_{\text{MME},1}$ are drastic. The integrated transfers are shown in Fig. 6.33. The yellow, Deimos-Phobos segment of the transfer is constant. At the Deimos flyby, a maneuver is applied. Thus, the magnitude of the cyan orbit, which arrives at Deimos, changes, affecting the initial periareion conditions of the blue departure orbit. First, $r_{p,1}$ decreases, and $i_{\text{MME},1}$ increases. The $i_{\text{MME},1}$ keeps increasing past turning point 3, but the $r_{p,1}$-trend reverses direction and starts to increase. Past point 5, the $i_{\text{MME},1}$ levels out and $r_{p,1}$ increases rapidly past this point

For transfers with maneuvers between the first and second moon, one could set-up a predictor-corrector scheme, where the arrival conditions at the second moon, as well as the maneuver are allowed to vary. For this research, it was decided to limit the results to true ballistic solutions between the first and second moon.

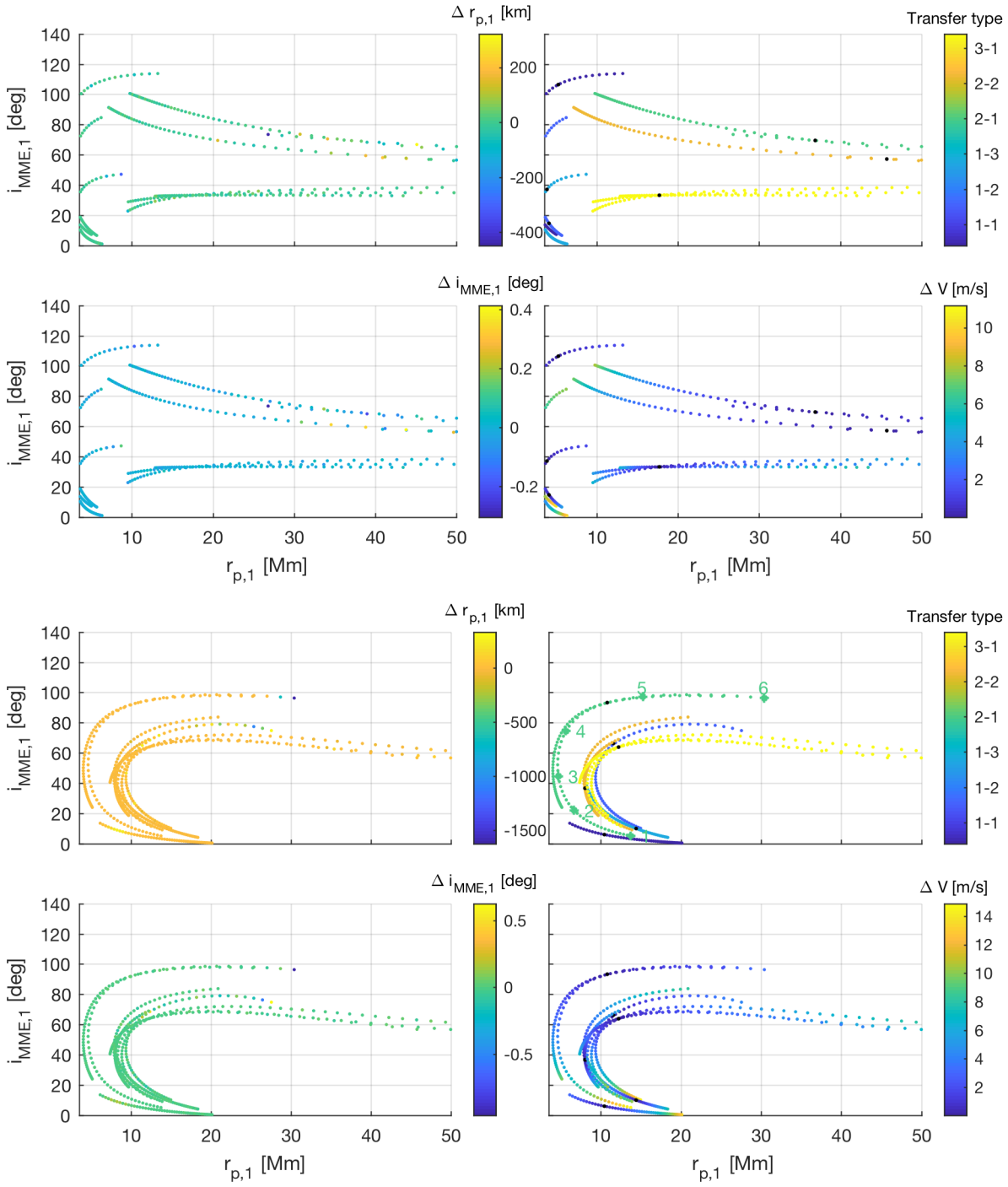

Figure 6.32: Effect of maneuvers on departable phase space for injection-Phobos-Deimos (top) and injection-Deimos-Phobos transfers (bottom). Left: error between predicted and integrated transfer. Right: transfer type and maneuver size with ballistic solutions indicated in black.

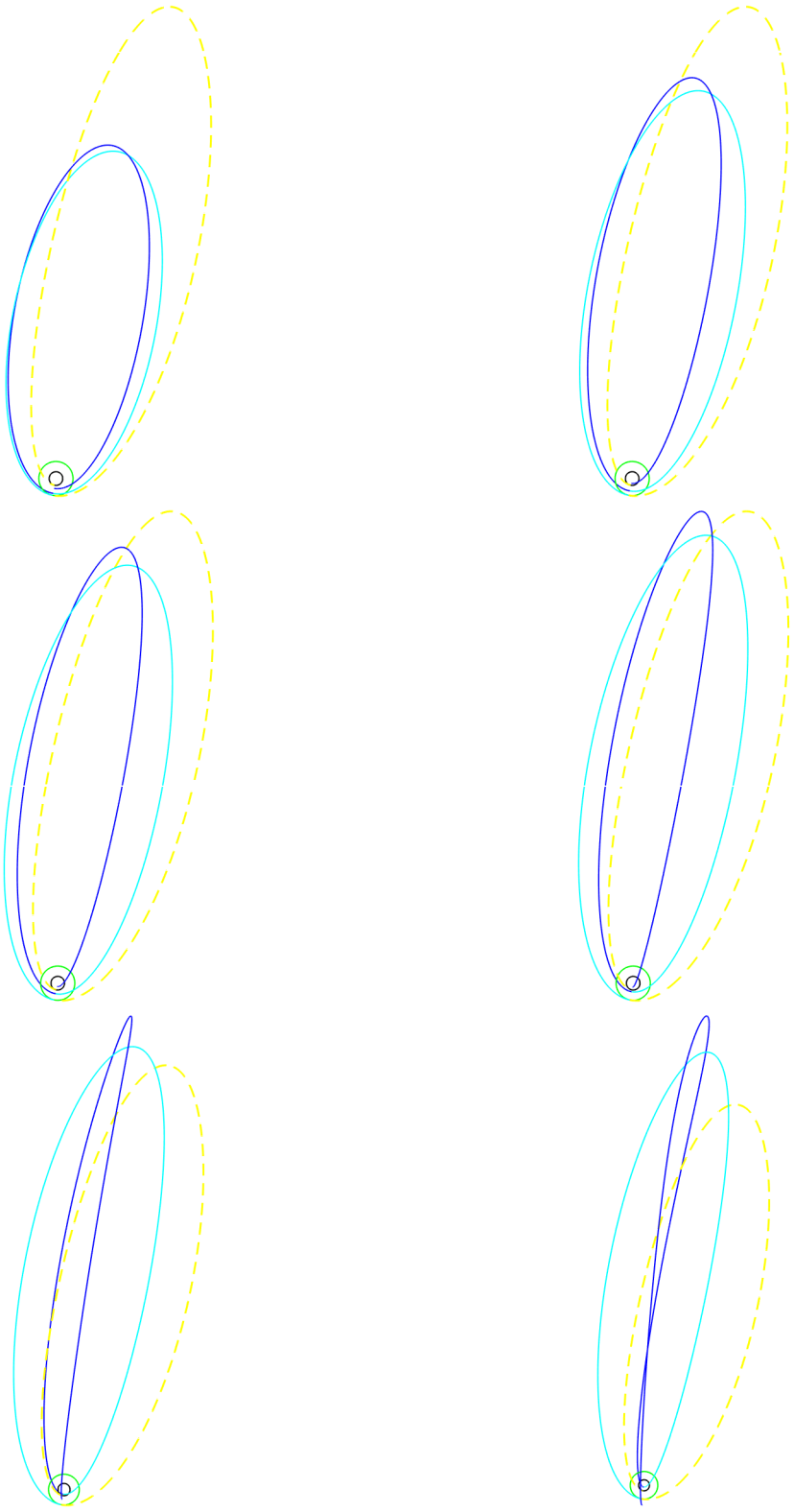

Figure 6.33: Visualization of the effect of maneuvers on the converged injection-Deimos(green)-Phobos(black) transfers, mapped on the xy-plane of the MME reference frame. The 2-loop injection-Deimos segment is indicated with a solid line, the one-loop Deimos-Phobos segment with a dashed line. The maneuvers are placed at the Deimos flyby. From left to right and top to bottom: transfer 1 through 6.

6.1.3 Discussion on computational efficiency

Prior to analyzing the computational efficiencies, it is worth noting that an artificial neural network and a numerical integration approach adhere to two very different philosophies. For the ANN approach, a large upfront investment of computational resources is required to train the ANN. Once trained, each evaluation requires very little computational resources. For the numerical integration approach, no upfront computational resources are required. However, for each new application, a large amount of computational resources are required. Due to their different nature, a fair comparison between both methods is difficult. Three complicating factors can be identified:

(1) The evaluation speed of the ANN allows for a brute-force approach where all potential final states are sampled, with a certain resolution. In the following comparison, it is assumed that the numerical integration method requires the same number of sampling points. In reality, this is not the only numerical integration method one could use to design trajectories; more efficient strategies could be developed. One example is the methodology developed in Chapter 3, another could be an interpolation approach.

(2) The required time for the training and evaluation of the ANN, and for the numerical integration of a single transfer, is highly dependent on the used computational set-up, and the utilized computing language. To make as fair of an analysis as possible, all computations have been performed in the same computing language, Matlab, on the same computational set-up: a 12 core system, each core composed of 1 Intel Xeon E5-2680 v3 @ 2.50GHz CPU. Therefore, the required computational load is expressed in CPU-days on this computational system; a task that takes 2 hours to complete on the 12 cores requires 1 CPU-day. It could be argued that the numerical integration could be significantly sped-up using a parallel system, i.e., using a GPU computational system. However, at the same time, the training and evaluation of the ANN could also be sped-up using a GPU. The individual gains for the integration and the ANN training are impossible to predict and can only be determined by actually implementing a GPU methodology for both architectures.

(3) The computational time of the numerical integration method is highly dependent on the numerical integrator used, and the chosen integration tolerances. In this research, Matlab's ode45 integrator has been used, a variable stepsize Runge-Kutta integrator, with an absolute tolerance of 1e-12, and a relative tolerance of 3e-10.

With these limitations of the comparison method in mind, the actual comparison can be performed. For the creation of the training data, and the training of the backward neural networks, 629.5 CPU-days are required. To predict the initial conditions for transfers that arrive at Phobos at day 0, 1.51 million Poincaré maps are evaluated for the ballistic scenario. Assuming this is representative for the other 68 sampled days, this totals to 104 million Poincaré maps. Adding one intermediate maneuver requires the prediction of an additional 10 million Poincaré maps for day 0. Assuming this is representative for the other 68 sampled days, this adds 690 million Poincaré maps. In total, for Phobos, the Poincaré maps are evaluated 794 million times. This takes approximately 0.48 CPU-days. If one would numerically integrate this with the method listed above, this would require roughly 935 CPU-days.

In conclusion, the most efficient philosophy depends on the number of depth required for each application. For the Phobos application, the transfers were identified with an arrival time resolution of 10 days. In this scenario, the artificial neural network approach is already more efficient with only one application. If one would only identify transfers with a resolution of 50 days, the prediction and integration times are reduced to, respectively, 0.15 and 288 days. In this scenario, if one is only interested in arriving at Phobos, it would have been more efficient to numerically integrate all the solutions. If one is interested in multiple applications, with different target arrival orbits, it is more efficient to use the artificial neural network approach if at least three different applications are considered with a similar number of required Poincaré mappings as for the Phobos application. Again, these conclusions only hold for the specific computational set-up used in this dissertation.

6.1.4 Conclusions

From the previous subsections, it is clear that artificial neural networks are able to identify transfers with specific characteristics such as target a specific final orbit, or transfers that chain multiple target orbits. The initial orbital elements can be predicted, for different mission profiles, with multiple revolutions around Mars and with an intermediate maneuver. This allows a mission designer to quickly generate a global view of the phase space. From the validation, it can be seen that the artificial neural network architecture provide sufficient accuracy to approximate the true initial conditions. Thus, for transfers of interest within the phase space, the designer can easily identify the real transfer in the neighborhood of the predicted transfer.

6.2 Injection error analysis for transfers targeting Phobos

As demonstrated, the backward architecture can support the determination of the initial conditions and timing to target a specific orbit in one or more revolutions. Besides finding this reference trajectory, the forward architecture can be used for a fast evaluation of the effect of injection errors at the first periareion. An example of this application is given in this section.

For this analysis, a few different initial conditions are selected that target Phobos' r_p and i_{MME} at arrival day 0. Two different groups of initial conditions are selected; one group with a constant $r_{p,1} = 5,000$ km at different values of equatorial inclination, and one group with a constant equatorial inclination of 30° and different values of $r_{p,1}$. The orbital elements at the initial periareion are listed in Table 6.3.

For each of the 6 points, 100,000 perturbed initial conditions are created by sampling three position, and three velocity deviations, sampled from normal distributions with mean 0 and standard deviation 10 km and 10 m/s, respectively. The orbital elements for the perturbed initial states of reference trajectory 1 are depicted in Fig. 6.34. $r_{a,1}$ has the largest variation out of the five orbital elements, caused by the large sensitivity of eccentricity to small variations in velocity, in the high eccentric regime for the reference orbits (Fig. 6.22). Using the perturbed initial condi-

Table 6.3: Selected reference trajectories for injection error analysis. Group 1: constant $r_{p,1}$. Group 2: constant $i_{\text{MME},1}$

Parameter	Trajectory 1	Trajectory 2	Trajectory 3	Trajectory 4	Unit
$r_{p,1}$	5000	5,000	5000	5,000	km
$r_{a,1}$	583,977	604,572	620,085	632,467	km
$i_{\text{MME},1}$	50.9	60.7	70.0	80.3	deg
$\omega_{\text{MME},1}$	357.8	357.5	357.2	357.0	deg
$\Omega_{\text{MME},1}$	210.3	208.3	206.0	203.0	deg
$\nu_{M,1}$	318.6	315.4	312.9	310.9	deg

Parameter	Trajectory 5	Trajectory 6	Trajectory 7	Trajectory 8	Unit
$r_{p,1}$	4,999	10,000	14,996	20,002	km
$r_{a,1}$	519,391	558, 632	586,857	611,708	km
$i_{\text{MME},1}$	30.1	30.0	29.9	29.1	deg
$\omega_{\text{MME},1}$	358.5	357.3	356.1	354.7	deg
$\Omega_{\text{MME},1}$	211.5	226.2	231.8	234.2	deg
$\nu_{M,1}$	327.2	321.4	317.0	312.9	deg

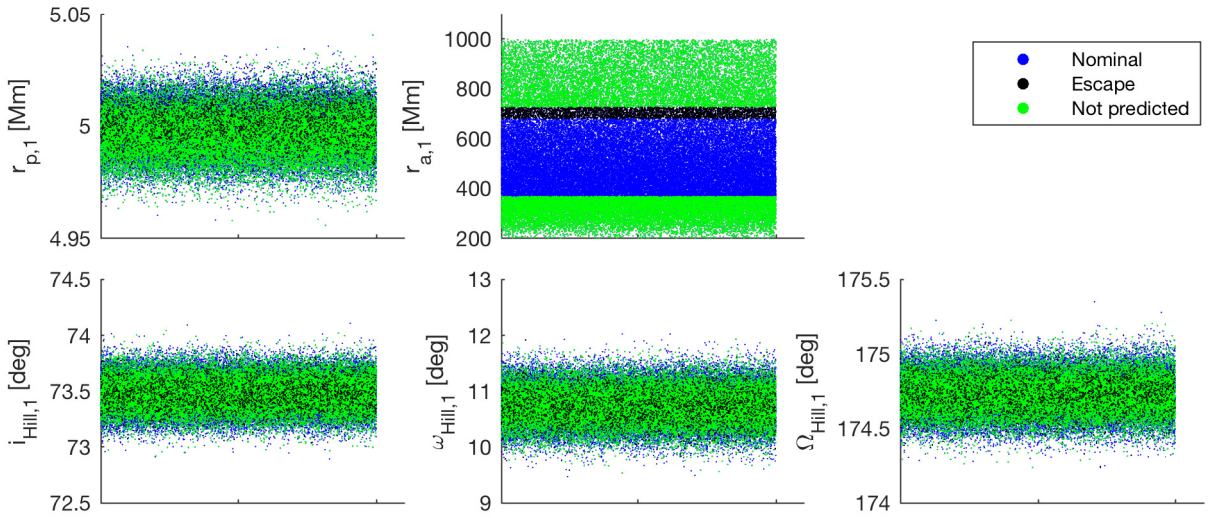

Figure 6.34: 100,000 perturbed orbital elements at periareion one for transfer 1, and the classifications for the next predicted periareion.

tions and the forward ANN architecture, the next periareion is predicted. Figure 6.34 displays the classification for the next periareion. This figure shows the trajectories that impact and escape, as well as the trajectories that cannot be predicted, i.e., the trajectories that are outside the training

region of the ANN. Again, $r_{a,1}$ is the dominating parameter. Therefore, for the other reference trajectories, only the $r_{a,1}$-parameters are shown on the left-hand sides of Figs. 6.35 and 6.36. On the right hand sides of these figures, the predicted $i_{\text{Hill},2}$ and $r_{p,2}$ are shown, color coded by the $r_{a,1}$-value.

Figure 6.35 shows the results for trajectory 1 through 4, for constant $r_{p,1}$ and varying $i_{\text{MME},1}$. These four transfers nominally increase their r_p-value from 5000 km to 9356 km and target $i_{\text{Hill},2} = \varepsilon$, indicated by the grey asterisk. Several trends are observed. First, at very low $r_{a,1}$, the solutions cannot be predicted. However, it can be argued that at these very low $r_{a,1}$-values, the transfers are barely perturbed. Hence, they converge onto the black asterisk, the original, unperturbed initial state. This behavior at low $r_{a,1}$-values is identical to the behavior at low J-values for the LEO-to-GEO transfers' Monte Carlo analysis in Fig. 3.19. For larger $r_{a,1}$-values, the $r_{p,2} - i_{\text{Hill},2}$ values approach the nominal values. At higher $r_{a,1}$-values, the $r_{p,2}$ increases strongly, until the escape criterion at 50,000 km is achieved. A region of escape exists. For even higher $r_{a,1}$-values, the transfers can no longer be predicted. However, it can be argued that those transfers points most likely escape as well. For the $r_{a,1}$-values lower than the nominal value, the $r_{p,2}$-values decrease, before they increase again to reach the unperturbed state (black asterisk). For high enough initial inclination, the lowest value of $r_{p,2}$ crosses the Martian surface (red dashed line), and an impact region occurs. This is very similar to the behavior observed for day 43 in Fig. 3.19.

Figure 6.36 shows the results for trajectory 5 through 8, for constant $i_{\text{MME},1}$ and varying $r_{p,1}$. Similar conclusions can be drawn: low $r_{a,1}$ transfers converge on the original unperturbed state, high $r_{a,1}$-transfers escape. Again, it can be argued that the transfers with very high $r_{a,1}$-values that cannot be predicted, probably escape.

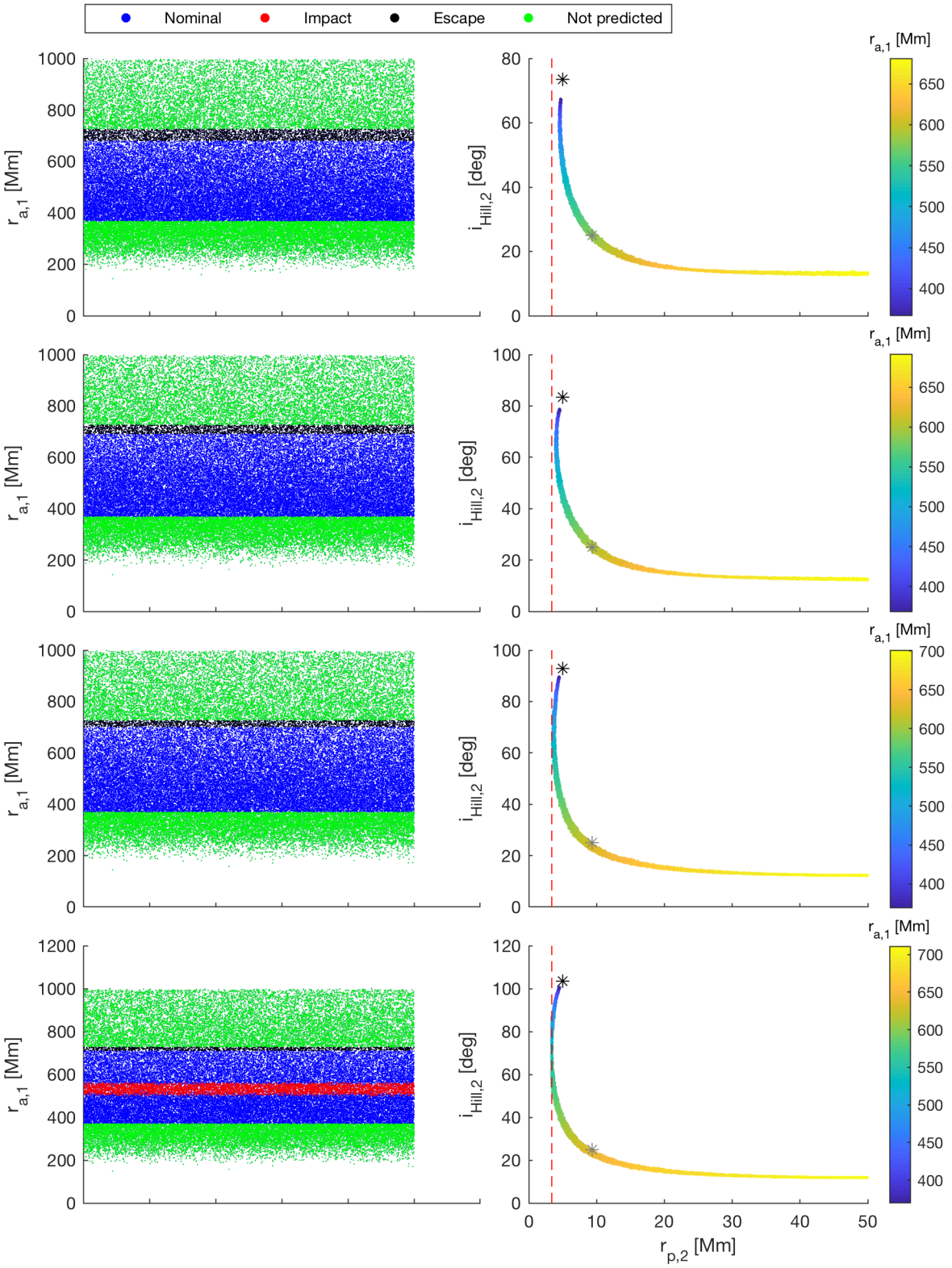

Figure 6.35: Results of the Monte Carlo injection error analysis for group 1 with constant $r_{p,1}$. From top to bottom: trajectory 1 through 4. Left: perturbed $r_{a,1}$ and classifications for the next predicted periareion. Right: $r_{p,2}$ and $i_{\text{Hill},2}$ at the next periareion, in function of original $r_{a,1}$. Red dashed line represents the Martian surface.

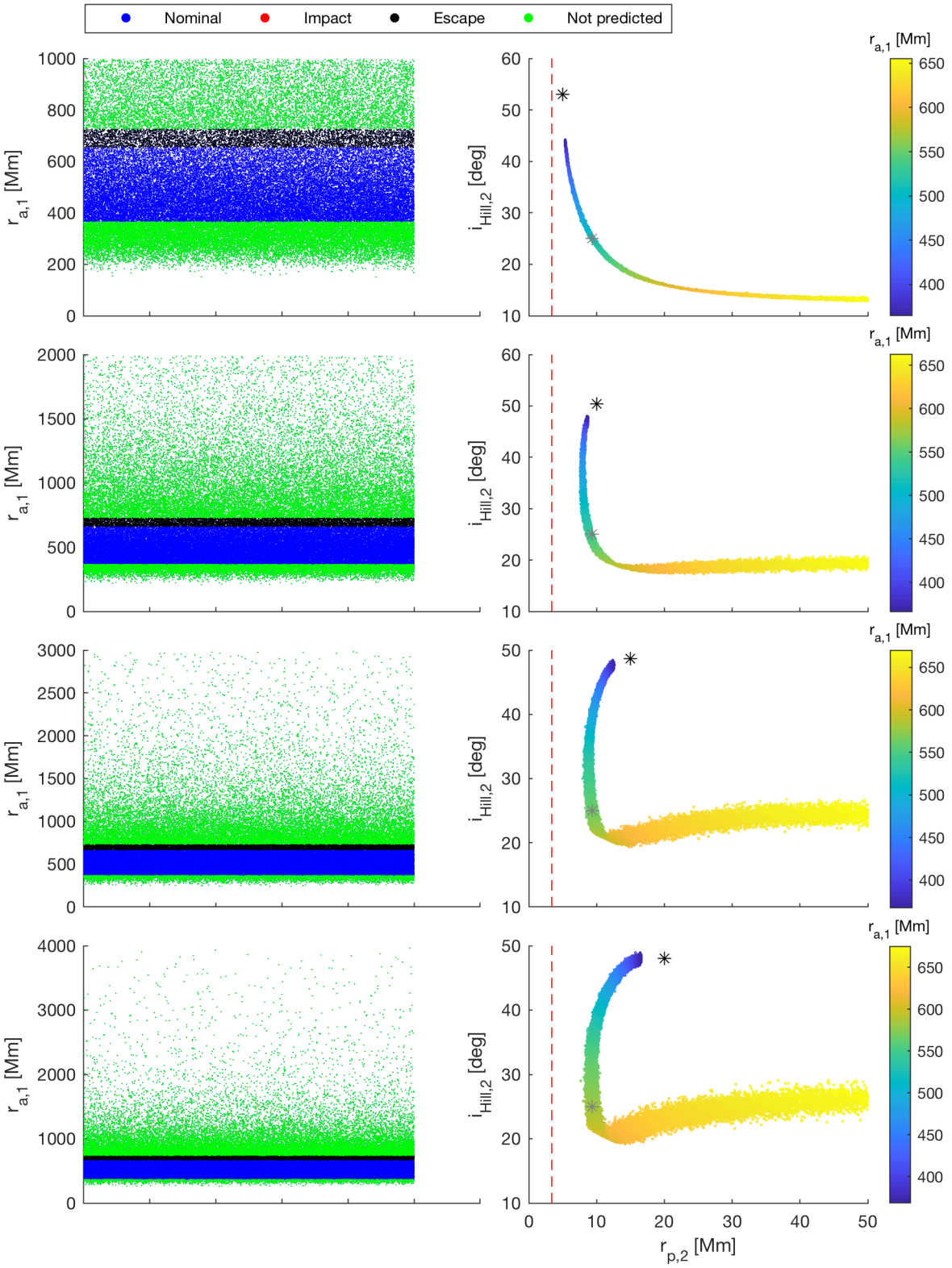

Figure 6.36: Results of the Monte Carlo injection error analysis for group 2 with constant $i_{\text{MME},1}$. From top to bottom: trajectory 5 through 8. Left: perturbed $r_{a,1}$ and classifications for the next predicted periareion. Right: $r_{p,2}$ and $i_{\text{Hill},2}$ at the next periareion, in function of original $r_{a,1}$. Red dashed line represents the Martian surface.

6.3 Missed insertion burn analysis for transfers targeting Phobos

The initial conditions are predicted to arrive at target $r_{p,f}$ and $i_{\text{MME},f}$-values. At these arrival conditions, a maneuver circularizes the transfer into its target orbit, for instance in orbits with Phobos' or Deimos' r_p and i_{MME}. In analogy with Subsection 3.6.1, this section assumes this maneuver does not occur and the transfer continues along its natural dynamics. Through the prediction of the next Poincaré maps using the forward ANN architecture, r_p and i_{MME} at the next periareions can be computed. As an example, the next three periareions are shown in Fig. 6.37 for transfers that nominally arrive at Phobos at day 0 after a one-loop transfer. On this figure, the impacting and escaping transfers are indicated in red and black, respectively. The cyan transfers return to the correct r_p and i_{MME} within a 1000 km and 3$\circ$ tolerance, in accordance with the accuracy of the ANN in Table 5.16 for multiple revolution transfers. The bottom-left figure displays the transfers that satisfy these tolerances, and the periareion number when the tolerances are met. For these transfers, the missed insertion burn can be executed at this later periareion. However, for the vast majority of the transfers, the natural dynamics hinder the recovery of a missed insertion burn.

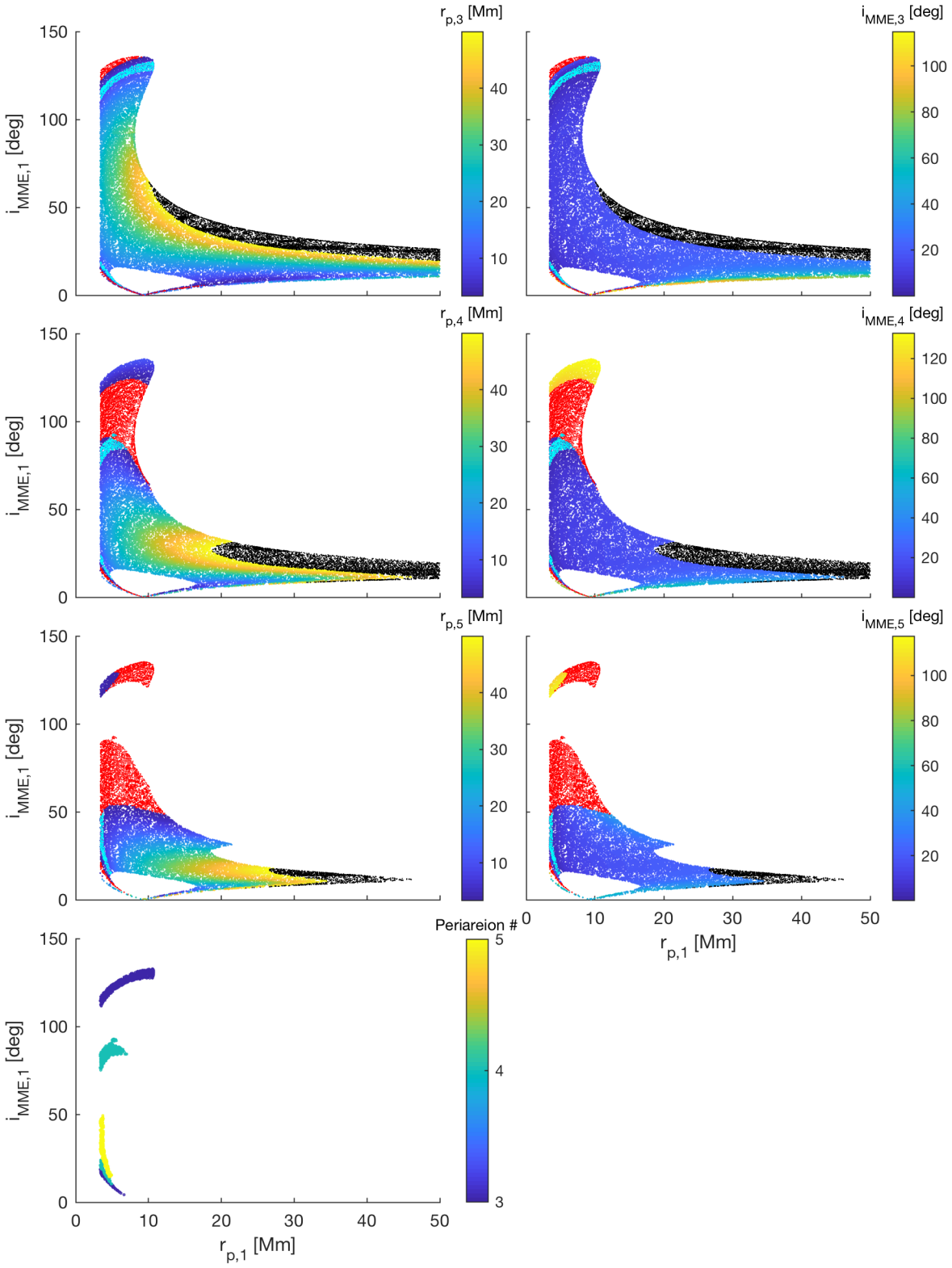

Figure 6.37: Results of the missed insertion burn analysis for one-loop transfers that arrive at Phobos at day 0. Red: impact, black: escape, cyan: transfers that meet tolerances.

6.4 Arrival phase space trade-studies

This dissertation claims to provide global understanding for solar gravity driven orbital transfers around Mars, for all times in the Martian year, any orbital orientation, for a large region of r_p and r_a. However, so far, only transfers that target the equator have been considered. For instance, Section 6.1 performs a detailed analysis of the phase space for transfers targeting Phobos and Deimos. In this section, the feasible initial phase space on the $r_{p,1} - i_{\text{MME},1}$ plane is determined for a wide variety of target orbits with different target $r_{p,f}$ and $i_{\text{MME},f}$-values. This highlights the capability of the developed architecture to predict transfers for a wide variety of target orbits, warranting the claim of global understanding.

Visualizing all existing transfers in compact form is impossible. Therefore, this section focuses on one-loop transfers and ignores the time component; the regions on the $r_{p,1} - i_{\text{MME},1}$ plane are determined for which at least one transfer throughout the Martian year exists for a specific target $r_{p,f}$ and $i_{\text{MME},f}$. This process is performed for a wide range of target $r_{p,f}$ and $i_{\text{MME},f}$ values. The results are computed and visualized for discrete levels of $i_{\text{MME},f}$. For each level of $i_{\text{MME},f}$, 42 values of $r_{p,f}$ are sampled between 4,000 and 45,000 km. It is observed that different regions on the $r_{p,1} - i_{\text{MME},1}$ plane have different intervals of $r_{p,f}$ for which transfers exist. The minimum and maximum target $r_{p,f}$ for each region on the $r_{p,1} - i_{\text{MME},1}$ plane for different final $i_{\text{MME},f}$ are shown in Fig. 6.38 through Fig. 6.40.

A mission designer can use these figures to quickly determine whether or not transfer exists between specific $(r_{p,1}, i_{\text{MME},1}) \rightarrow (r_{p,f}, i_{\text{MME},f})$ combinations. A few examples on how to use these graphs are indicated by arrows on Fig. 6.38. Departing from $r_{p,1} = 4,000$ km and $i_{\text{MME},1} = 100°$ (black arrows), transfers exist to the equator for target $r_{p,f} \in [4000, 37000]$ km. Departing from $r_{p,1} = 20,000$ km and $i_{\text{MME},1} = 100°$ (red arrows), transfers exist to the equator for target $r_{p,f} \in [4000, 25000]$ km. If a transfer exists, the methods developed in Section 6.1 can be used to identify the initial orbital elements and timing for the transfers.

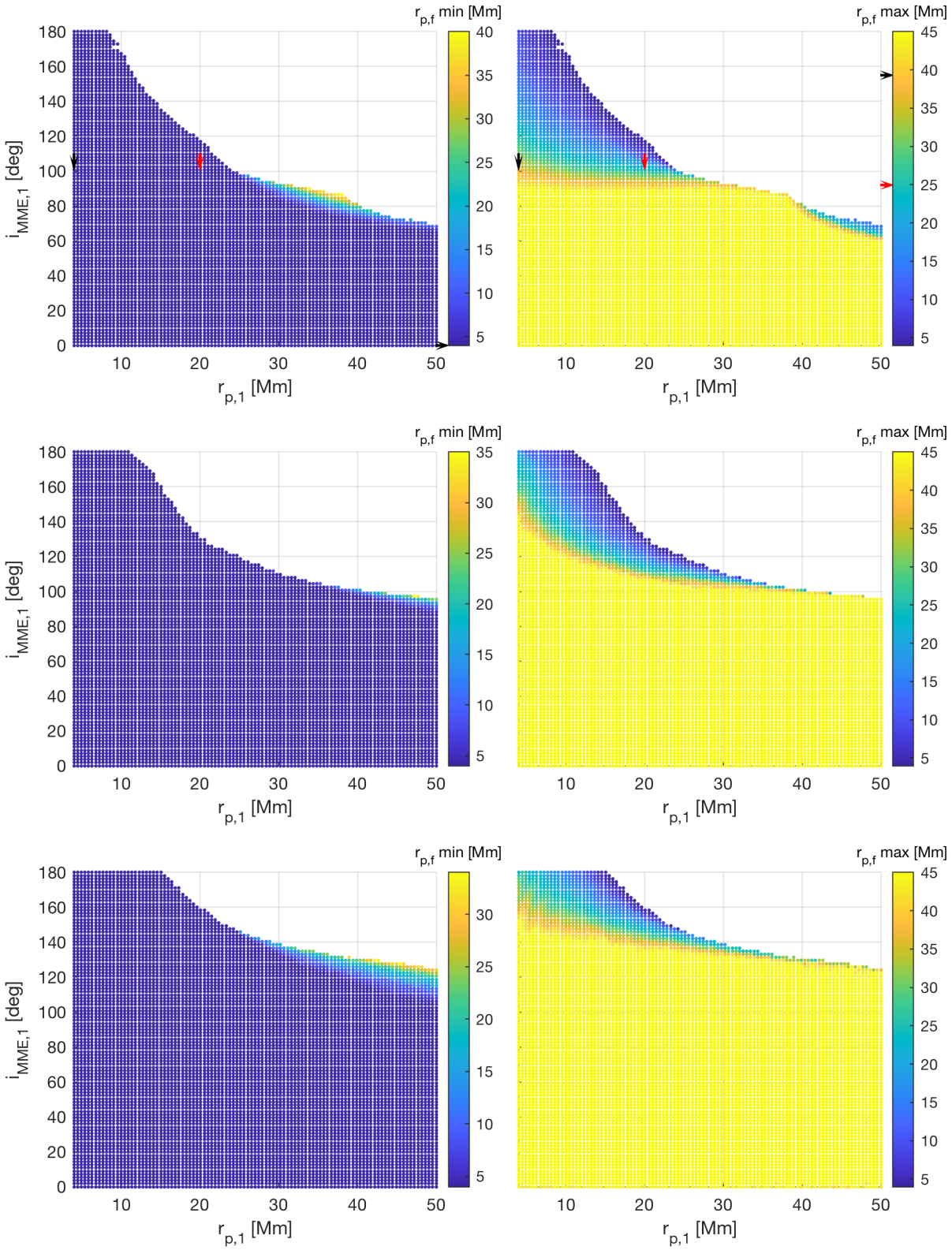

Figure 6.38: Feasible initial phase space for target orbits with arrival $i_{\mathrm{MME},f} = 0°$ (top), 30° (middle), 60° (bottom) for $r_{p,f} \in [4000, 45000]$ km

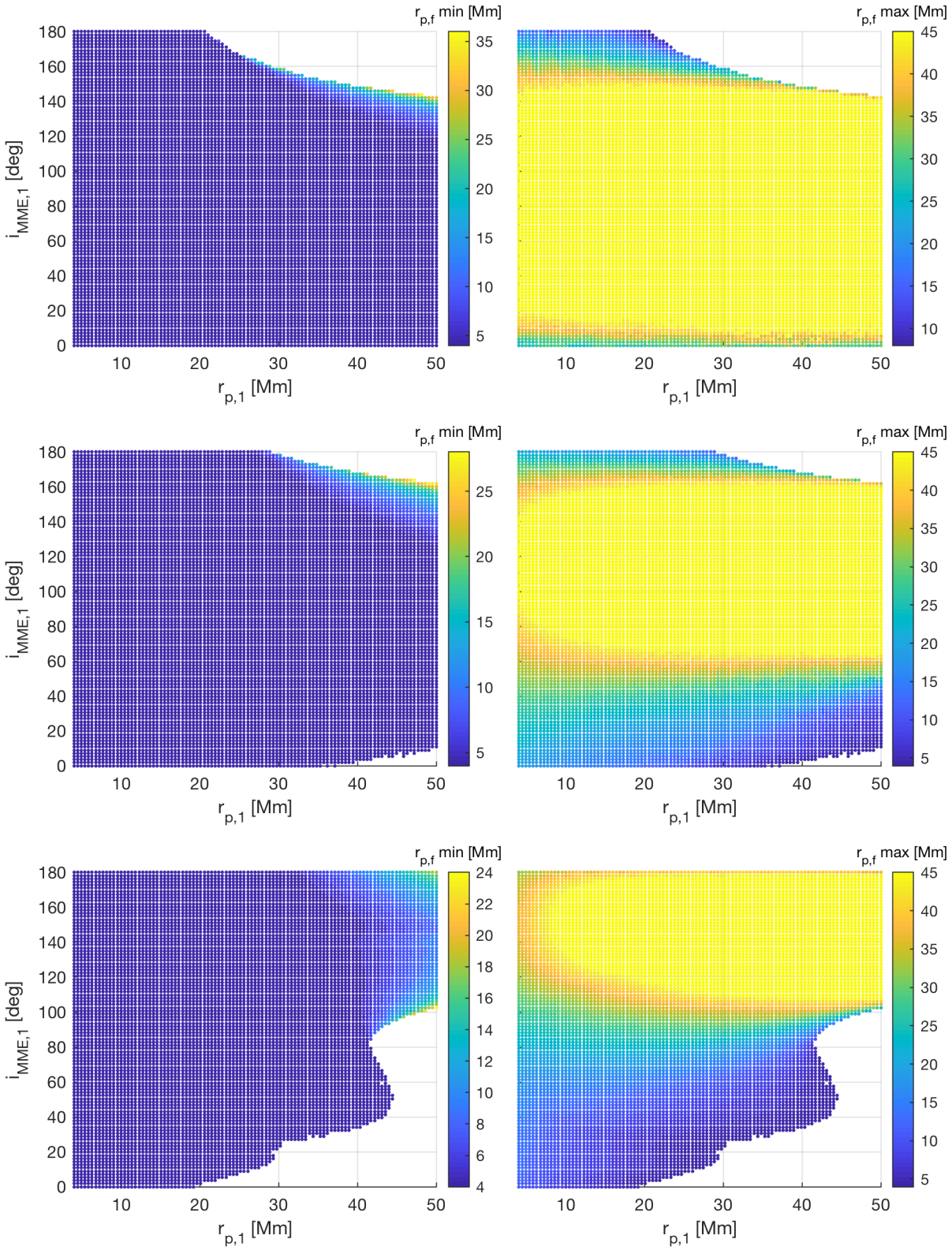

Figure 6.39: Feasible initial phase space for target orbits with arrival $i_{\mathrm{MME},f} = 90°$ (top), 120° (middle), 150° (bottom) for $r_{p,f} \in [4000, 45000]$ km

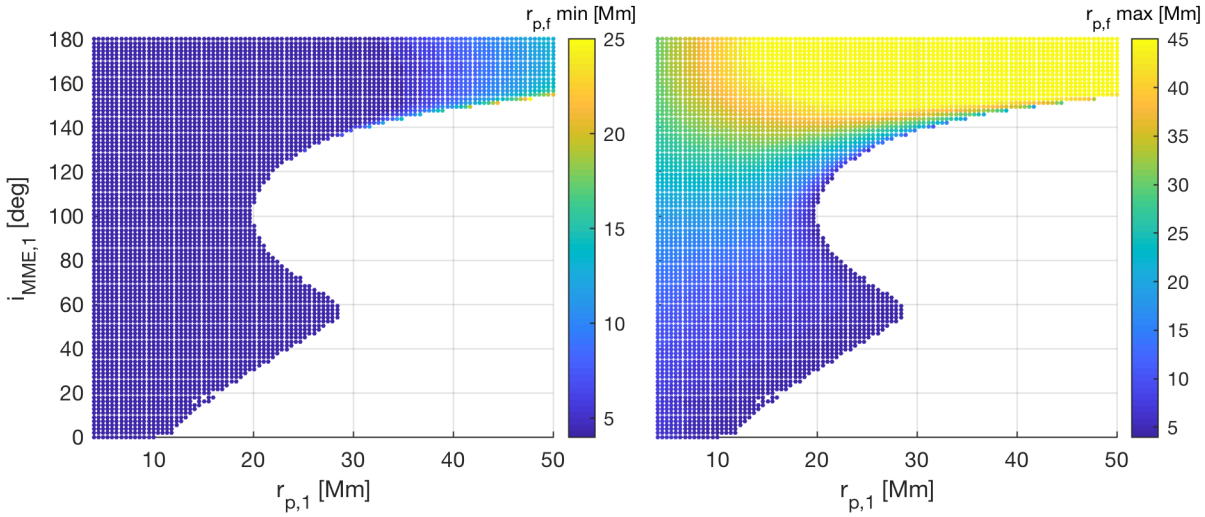

Figure 6.40: Feasible initial phase space for target orbits with arrival $i_{\mathrm{MME},f} = 180°$ for $r_{p,f} \in [4000, 45000]$ km

6.5 Escape and impact stability analysis

The forward architecture can also support general dynamic studies. For instance, the impact and escape stabilities of the phase space can be assessed for multiple revolutions. While the developed networks can be used on the entire phase space in Table 5.7, the results of a six-dimensional phase space are hard to visualize. Therefore, a subset of the phase space is analyzed; the effect of $r_{p,1}$ and $\omega_{\text{Hill},1}$ is investigated. Six different combinations of initial $i_{\text{Hill},1}$ and $\Omega_{\text{Hill},1}$ are used for a fixed $r_{a,1}$ and departure time. The next four periareions are predicted for 100,000 ($r_{p,1}$, $\omega_{\text{Hill},1}$) combinations for each of the six selected combinations. Fig. 6.41 shows how the initial $r_{p,1}$ and $\omega_{\text{Hill},1}$ affect the impact and escape characteristics. All the transfers depart when Mars is at perihelion and have an initial apoapse radius of 700,000 km, while different initial conditions for $i_{\text{Hill},1}$ and $\Omega_{\text{Hill},1}$ are used. Besides impact and escape characteristics, the architecture can also be used to determine how the location of the periareions evolve. In Fig. 6.42, the projections of the periareions on the xy-plane are shown.

The number of subsequent periareions that can be predicted is theoretically unlimited. However, the errors, as quantified in Tables 5.15 and 5.16 will increase. An example where the impact and escape characteristics for the next 16 periareions are predicted can be found in Fig. 6.43. From this, one can see that there is a region in ($r_{p,1}$, $\omega_{\text{Hill},1}$) space where the transfers do not escape nor impact for a large number of orbital revolutions around Mars. To assess the accuracy, the 10,000 initial points are integrated numerically for 16 loops. The results can be seen in Fig. 6.44. While there are 243 transfers that are predicted to not escape nor impact, only 182 really do. Hence, there is only a 73% accuracy. Comparing Fig. 6.43 and Fig. 6.44, one can see that the global structure is captured.

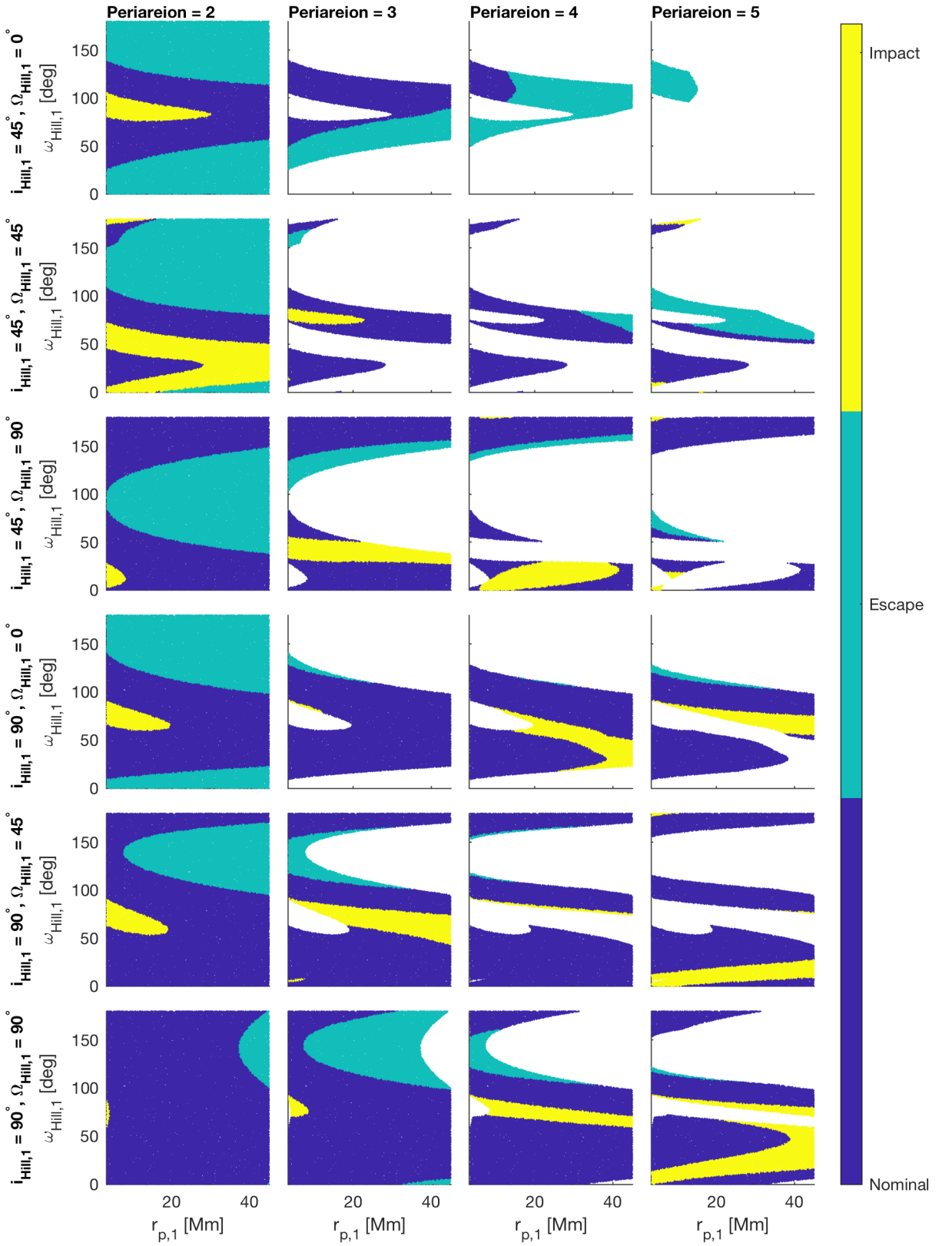

Figure 6.41: Impact and escape characteristics for the next four periareions for multiple combinations of $i_{\text{Hill},1}$ and $\Omega_{\text{Hill},1}$ with $r_{a,1} = 700,000$ km, departing when Mars is at perihelion.

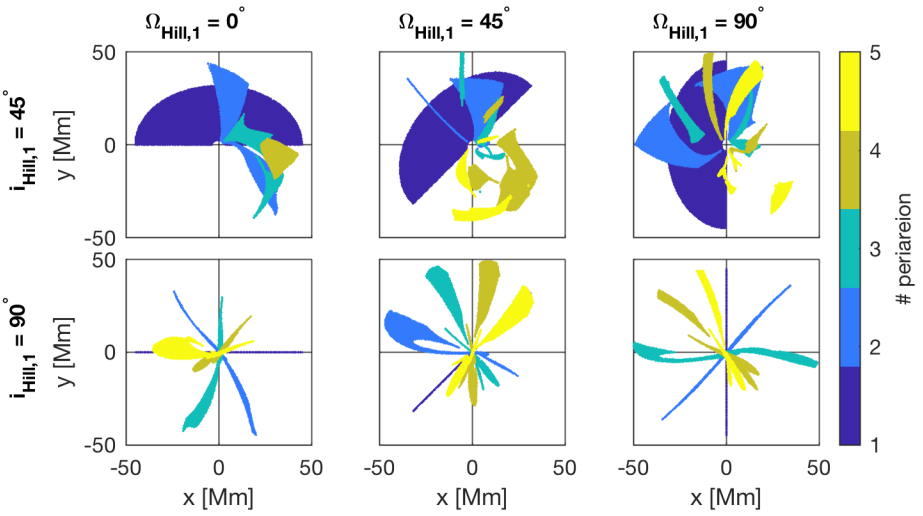

Figure 6.42: xy projection of periareions 1 through 5 for multiple combinations of $i_{\text{Hill},1}$ and $\Omega_{\text{Hill},1}$ with $r_{a,1} = 700,000$ km, departing when Mars is at perihelion.

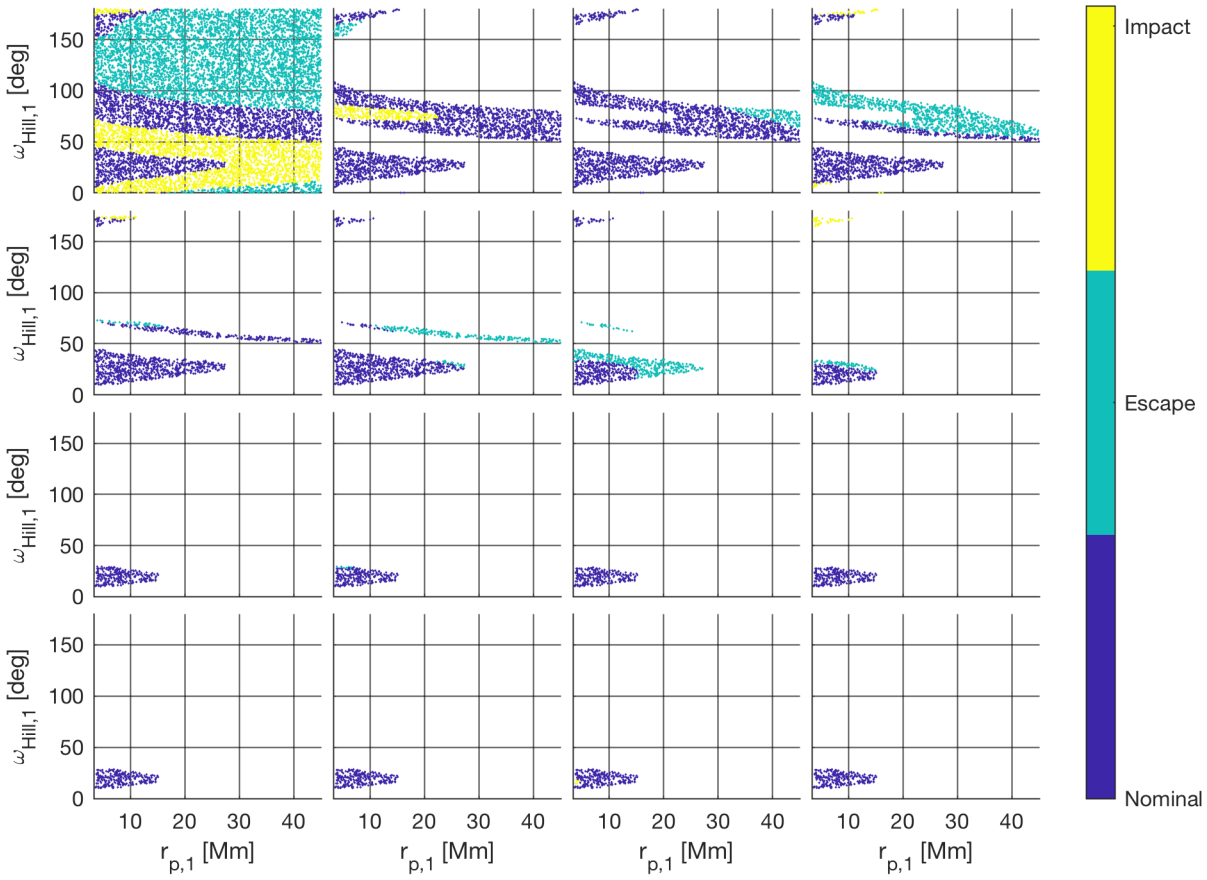

Figure 6.43: Impact and escape characteristics for next 16 periareions for $i_{\text{Hill},1} = 45°$, $\Omega_{\text{Hill},1} = 45°$ with $r_{a,1} = 700,000$ km, departing when Mars is at perihelion.

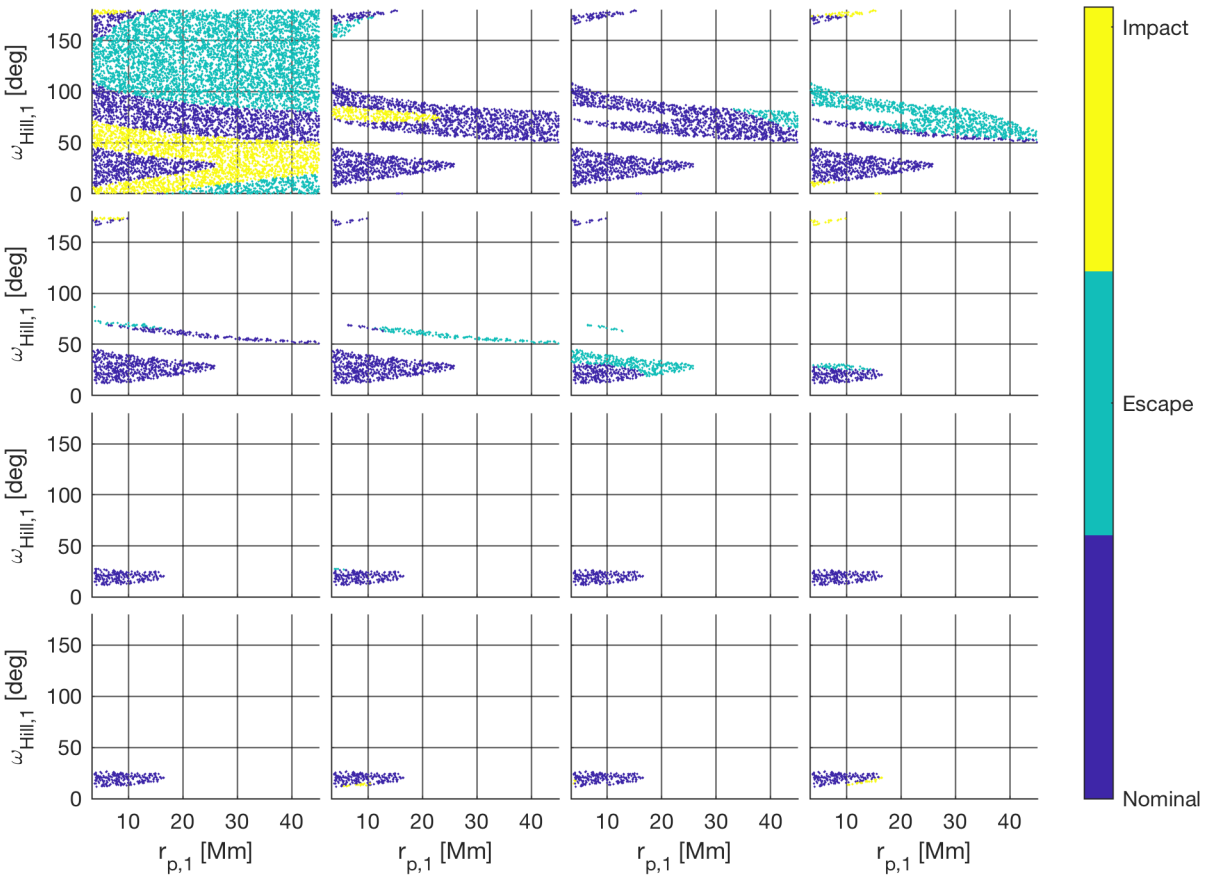

Figure 6.44: Integrated impact and escape characteristics for next 16 periareions for $i_{\text{Hill},1} = 45°$, $\Omega_{\text{Hill},1} = 45°$ with $r_{a,1} = 700,000$ km, departing when Mars is at perihelion.

6.6 Identify heteroclinic connections in the Earth-Moon CRTBP

In this section, first, the heteroclinic connections are predicted using the ANN designed in Section 5.5. Second, a predictor-corrector scheme is used to nullify the position and velocity errors on the predicted connections. This last step also allows to quantify the errors in the predicted connections. Finally, some conclusions are drawn on the obtained results.

6.6.1 Predicting heteroclinic connections

The responses on the Poincaré map for both the L_1 unstable and L_2 stable manifolds for both periapse groups are predicted. A heteroclinic connection only exists between orbits with identical Jacobi constant. Therefore, a Jacobi constant is selected, between 3.07 and 3.17. For this specific Jacobi constant, the τ-phase space is sampled with a 0.1° resolution. The classification neural networks predict if a periapse exists for a specific periapse group and $J - \tau$ combination. If it is predicted to exist, the regression neural networks are used to predict the xy-coordinates of the manifold's intersection with the Poincaré surface of section.

Four different types of connections exist: (1,1), (1,2), (2,1) and (2,2) connections where the first and second number indicate the group numbers of the L_1 and L_2 manifold periapses respectively. Note that because of the difference in chosen Poincaré surface, these connection categories are different from the ones commonly found in literature [3, 109]. For each connection type, the distance between the periapses is computed for all $\tau_1 - \tau_2$ permutations. The permutation with the smallest predicted distance is stored as a potential heteroclinic connection, if the distance is smaller than 2000 km. While in theory, (1,2) and (2,1) connections should be identical, small differences in classification and regression network accuracies give slightly different results. Only the connection with the smallest periapse distance for the (1,2) and (2,1) connections are stored. This process is repeated for $J \in [3.07, 3.17]$ with a 0.001 J-resolution. The results of these computations can be seen in Fig. 6.45. Note that τ_2-values larger than 360° are shown to guarantee a continuous figure. In analogy with an angle, the correct τ_2 values can be found by subtracting 360°. Further note

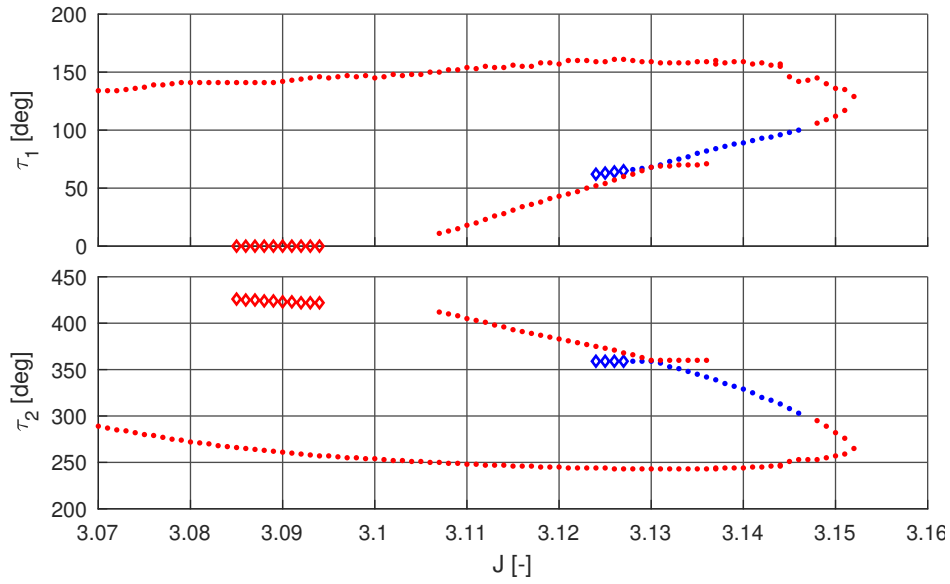

Figure 6.45: Location of the origin of the manifolds along the planar Lyapunov orbits for the predicted heteroclinic connections: (1,1) connection (blue) and (1,2) or (2,1) connections (red).

that all found (2,2) connections impact the Moon. The identified initial conditions are integrated, and the actual position and velocity discontinuities at the predicted connections are computed. It is observed that for some transfers, the error in $\dot{x}$ and $\dot{y}$ is larger than 100 m/s. Those transfers, indicated by diamonds, pass relatively close to the Moon. As a result, small errors in position can lead to large errors in velocity. Those transfers are discarded. Between J=3.095 and J=3.106, the predicted 2-1 transfers impact the Moon and are thus not shown. Note: the heteroclinic connection at 3.147 is not identified. From the results, a heteroclinic connection is expected with a τ_2-value near 300°. Looking at Fig. 5.56, this is on the classification border between group 1 and group 2 of the L_2 stable manifolds. As a result, it is wrongfully predicted that no periapses exists in this region.

6.6.2 Validation and discussion on results

As a final validation, the predicted initial conditions are corrected until the heteroclinic connections are continuous with a position and velocity tolerance of 1 m and 1 mm/s, respectively. In Fig. 6.46, the errors between the predicted and true τ-values are depicted. Note that for a few

transfers, the heteroclinic connections do not converge. Within the correction procedure, at the initial τ-value, the number of required Poincaré mappings to arrive near the predicted periapse is computed. During the correction procedure, this number is held constant, i.e., a fixed number of Poincaré mappings are computed. Sometimes, numerical instabilities can lead to the introduction or removal of a periapse. Since the correction procedure performs a fixed amount of Poincaré mappings, this leads to a jump in the location of this periapse. It is expected that with a more stable correction procedure, these connections would converge.

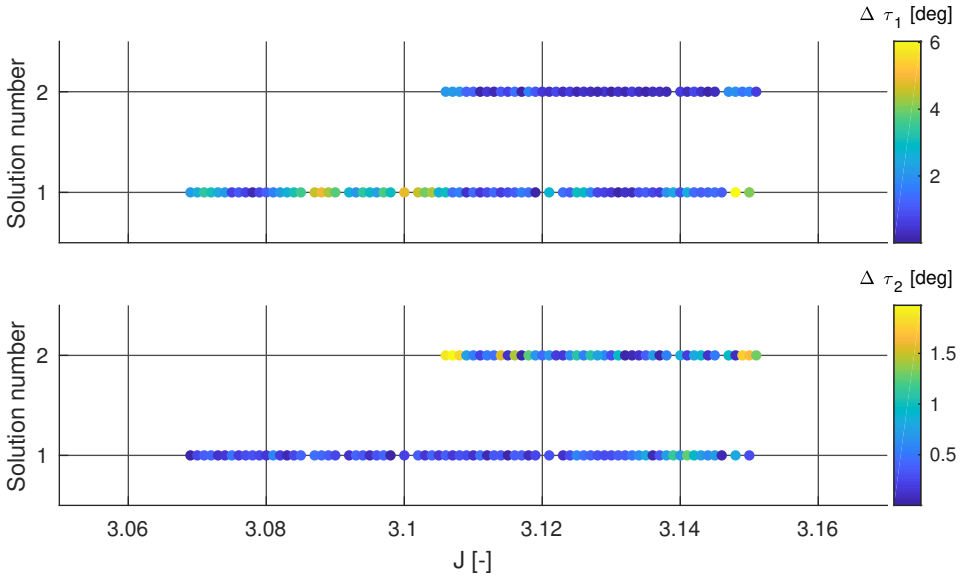

Figure 6.46: Difference between the location of the origin of the manifolds along the planar Lyapunov orbits for the predicted, and corrected heteroclinic connections.

One can see that in general, the predicted τ-values are order of magnitude 1° off. For a few connections, the $\Delta\tau_1$ is significantly larger. At $J = 3.15$, τ_1 is predicted to be 140, while the correct value is 146.21. Looking at the top left of Fig. 5.57, the largest negative errors in x-coordinates are occurring in this neck region. Thus, the neural network predicted connection is not as accurate as for other regions of the phase space. Finally, Fig. 6.47 shows the corrected heteroclinic connections at a few J-values. Haapala identified a transfer at $J = 3.15$ in Ref. [110]. The solution is identical to the heteroclinic connections found in this work. Furthermore, the transfers at $J = 3.134$ in Ref. [3] lie in between the identified transfers at $J = 3.13$ and $J = 3.14$.

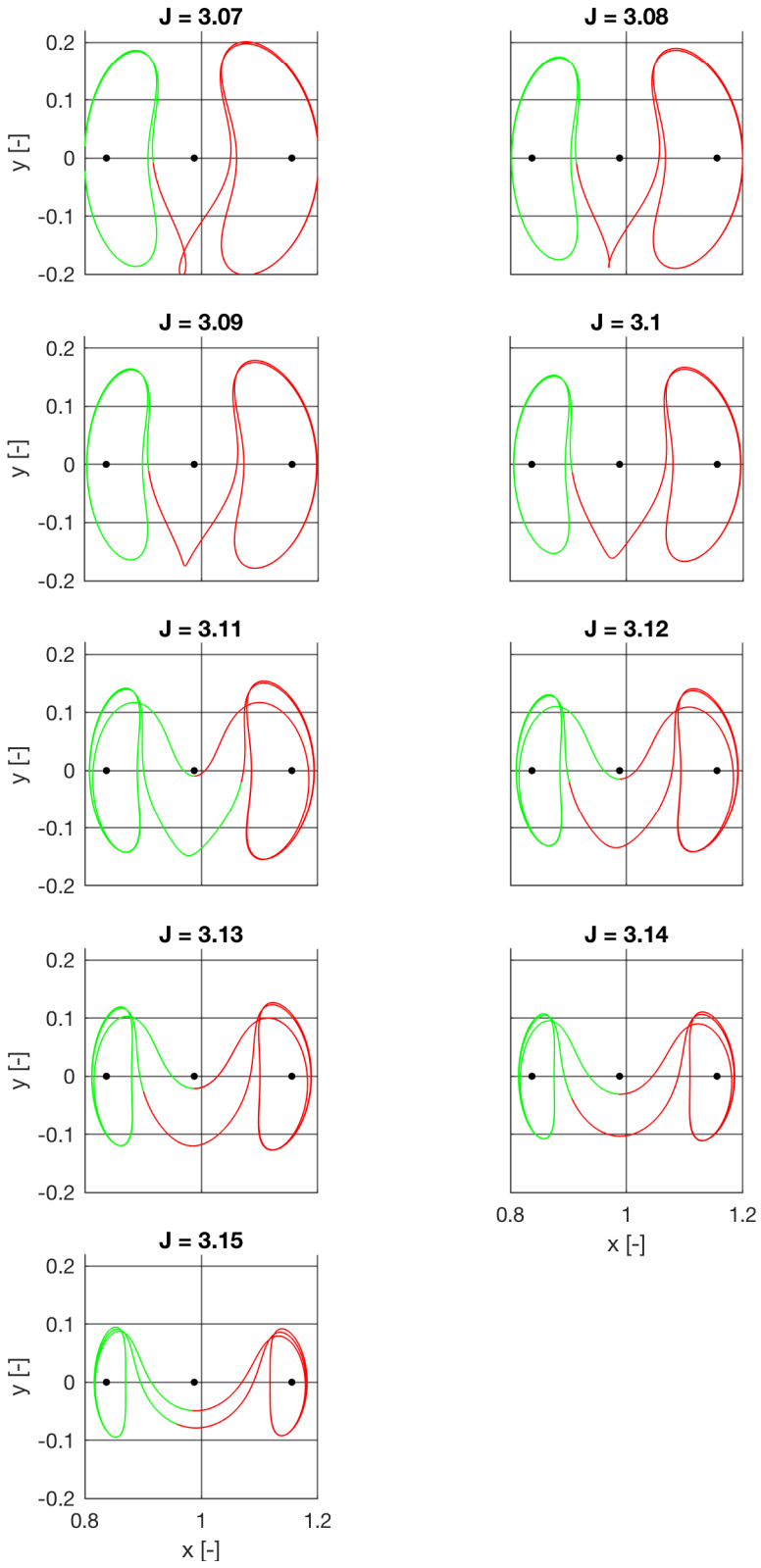

Figure 6.47: Converged heteroclinic connections between planar Lyapunov orbits in the Earth-Moon CRTBP.

6.6.3 Conclusion

This section demonstrates how a combination of classification and regression feedforward neural networks can be used to find heteroclinic connections between planar L_1 and L_2 Lyapunov orbits. To do this, the manifolds are computed for orbits with different Jacobi constants between 3.07 and 3.17, with resolution 0.005, at 36 different locations on each orbit. The developed artificial neural network architecture succeeds in identifying the heteroclinic connections, if they exist, between any orbit with Jacobi constant within the training range. The predictions are within 0.1-1% of the arclength along the periodic orbit.

This research can be extended by computing subsequent periapses, and again, creating classification and regression neural networks to capture the response. This allows the identification of higher order connections, e.g. (1,3), (2,3), (3,3), etc. Furthermore, this methodology can be applied for different departure and arrival orbits. For instance, heteroclinic connections between halo orbits. These orbits are no longer planar, making them an excellent test bed to see if the additional two dimensions of the Poincaré map can still be accurately captured using artificial neural networks.

Chapter 7

Conclusions

7.1 Summary

This thesis deals with the efficient design of solar gravity driven orbital transfers. Early research efforts focuses on developing a systematic methodology to identify transfers from inclined low-earth orbits to the geostationary orbit. Based on the observed control authority of the Sun, it is hypothesized that the solar gravity driven transfers enable a new mission architecture for the injection of multiple spacecraft around Mars. To assess the versatility of the proposed mission architecture, the control authority of the gravitational perturbations needs to be understood for a wide variety of departure and target orbits in the Martian system. This requires a well-defined and easily accessed database of transfers in this system. The framework to build this database is developed on a small subset of the phase space, centered around one specific application. This allows the exploration of different methods for constructing this database, while limiting the required computational resources. Even for this small subset of the phase space, the required number of numerical integrations to compute the database increases due to the time variant effect of the Sun-Mars distance on the control authority.

This issue is alleviated by a pairing of artificial neural networks with an apoareion scaled version of the circular Hill system. This system manages to capture the majority of the time-variant effect of the eccentric system, using only a fraction of the required numerical integrations. When applied to the small subset of the phase space, promising results are obtained, as well as several recommendations to improve the performance of the neural networks. Those recommendations

are implemented in a new artificial neural network architecture to capture the response of a large subset of the phase space. This architecture is comprised of three families of networks. One network predicts if a transfer escapes or impacts. If the transfer is anomaly free, one network predicts the response in the apoareion scaled version of the circular Hill system. While this system captures the majority of the time-variant effect of the eccentric Hill system, the system also has systematic errors compared to the eccentric Hill system. Therefore, another artificial neural network family predicts the difference in response between both dynamical systems.

The developed neural network architecture is applied on a wide variety of applications. First, the architecture is used to identify the initial conditions for transfers with up to four solar perturbed revolutions around Mars, with or without a maneuver at an intermediate periareion. The initial conditions are identified for transfers targeting Phobos or Deimos, as well as transfers that chain multiple targets together; transfers that go to Phobos and Deimos on a single transfer. Second, the architecture is used to compute the effect of missed, or incorrect, maneuver executions on the identified transfers. Third, it is demonstrated how the neural networks can be used to determine the regions of the initial phase space that have at least one transfer per Martian year for a wide variety of target orbits. Finally, the versatility of the artificial neural network architecture is demonstrated by applying it on a different problem; identifying heteroclinic connections between planar Lyapunov orbits in the Earth-Moon circular restricted three-body problem.

7.2 Main contributions

The main contributions of this dissertation are listed below:

(1) Developed a methodology to identify solar gravity driven transfers between a specified departure and target orbit.

(2) Introduced a new mission architecture that can inject multiple spacecraft around Mars in different orbital planes and radii.

(3) Defined a new dynamical system, the apoareion scaled circular Hill system, as an approxi-

mation of the eccentric Hill system.

(4) Developed a general artificial neural network architecture for Poincaré maps, using a combination of regression and classification neural networks.

(5) Demonstrated how artificial neural networks can be used to predict the difference between a more complex, and a simpler dynamical system.

(6) Demonstrated how an artificial neural network architecture functions as a database of solutions to a difficult problem in mission design, without the explicit need to store a large amount of pre-computed transfers.

(7) Demonstrated how the artificial neural networks can be used to predict all the initial conditions that transfer to a specific target orbit, with multiple solar-perturbed revolutions around Mars with or without intermediate maneuvers. Once trained, the computational efficiency of the network architecture gives the mission designer a global understanding of the phase space in a time span of minutes to hours.

7.3 Future work

This dissertation is the first step in the systematic study of planetocentric solar gravity driven orbital transfers. The current artificial neural network architecture enables the design of transfers with multiple revolutions around Mars with maneuvers at intermediate periareions. This dissertation builds the foundation for different categories of follow-up studies.

The first category of follow-up studies leverages the architecture for different applications. The developed methodology to target Phobos or Deimos can be applied to different equatorial target orbits that are of scientific or operational interest, such as an areostationary orbit. Furthermore, new mission concepts can be analyzed. An example would be the deployment of a constellation of satellites around Mars, that are all injected into orbits with the same inclination and orbital radius, but with different right ascensions of the ascending node. The developed methodology can

be readily used, be it with different necessary conditions imposed on the arrival state.

The second category of follow-up studies expands the capabilities of the artificial neural network architecture. A straightforward next step is the design of transfers with maneuvers at intermediate apoareions. This requires the training of periareion-to-apoareion and apoareion-to-periareion ANN. Furthermore, methods could be investigated to include SEP on the solar perturbed transfers. In this dissertation, the analysis was broken off upon arrival at the target orbit. The eccentricity upon arrival is high, and this dissertation assumes it is reduced using an impulsive maneuver. This requires a chemical propulsion system, on top of the SEP system used for the interplanetary transfers. Different ways could be investigated to include SEP. The impulsive transfers could be used as ballistic initial guesses for local optimizers. Adding the co-states to the inputs of the Poincaré map could also allow the addition of the SEP component, while automatically guaranteeing optimal transfers. Those co-states need to be added to the inputs of the ANN. It is expected that the behavior is more strongly non-linear, and thus harder to train.

The third category of follow-up studies extends the analysis to different sun-planet or planet-moon Hill systems. The trained apoareion scaled Hill ANN can be re-used for different Hill systems. Note that the training region of r_p and r_a for Mars' system is mapped to a different r_p and r_a-region, depending on the ratio between the different Hill systems' length scales. The correction ANN are dependent on the eccentricity of the secondary around the primary, and cannot be recycled between different systems. These ANN need to be trained with new data created for every system.

The fourth and final category of follow up studies could address several issues of solar gravity driven transfers that this dissertation identified. For instance, further studies could mitigate the severe effects of a missed final injection burn, as well as the effects of initial injection burn inaccuracies. A study could trade-off navigational requirements, such as required accuracy and urgency of obtaining the navigation solution, with the timing and ΔV budget required to design a trajectory correction maneuver.

Bibliography

[1] J. D. Aziz. Low-Thrust Many-Revolution Trajectory Optimization. PhD thesis, University of Colorado at Boulder, 2018.

[2] C. A. Ocampo. Transfers to Earth centered orbits via lunar gravity assist. Acta Astronautica, 52(2-6):173–179, 2003.

[3] J. S. Parker and R. L. Anderson. Low-Energy Lunar Trajectory Design. Wiley, 2014.

[4] W. S. Koon, M. W. Lo, J. E. Marsden, and S. D. Ross. Low Energy Transfer to the Moon. Celestial Mechanics and Dynamical Astronomy, 81:63–73, 2001.

[5] M. J. Chung, S. J. Hatch, J. A. Kangas, S. M. Long, R. B. Roncoli, and T. H. Sweetser. Trans-lunar Cruise Trajectory Design of GRAIL (Gravity Recovery And Interior Laboratory) Mission. In Proceedings of the AIAA/AAS Astrodynamics Specialist Conference 2010, AIAA 2010-8384, pages 1856–1863, Toronto, Canada, August 2-5, 2010. AIAA.

[6] S. B. Broschart, M. J. Chung, S. J. Hatch, J. H. Ma, T. H. Sweetser, S. S. Weinstein-Weiss, and V. Angelopoulos. Preliminary trajectory design for the Artemis lunar mission. Advances in the Astronautical Sciences, 135(2):1329–1343, 2009.

[7] J. K. Miller and E. A. Belbruno. A Method for the Construction of a Lunar Transfer Trajectory Using Ballistic Capture. In AAS/AIAA Space Flight Mechanics Meeting, AAS91-101, Houston, TX, 1991.

[8] H. Yamakawa. On Earth-Moon Transfer Trajectory with Gravitational Capture. PhD thesis, University of Tokyo, 1993.

[9] K. Uesugi, H. Matsuo, J. Kawaguchi, and T. Hayashi. Japanese first double lunar swingby mission Hiten. Acta Astronautica, 25(7):347–355, 1991.

[10] D. C. Davis and K. C. Howell. Trajectory evolution in the multi-body problem with applications in the Saturnian system. Acta Astronautica, 69:1038–1049, 2011.

[11] B. F. Villac, D. J. Scheeres, L. A. D'Amario, and M. D. Guman. The Effect of Tidal Forces on Orbit Transfers. In Spaceflight Mechanics 2001, volume 108 of Advances in the Astronautical Sciences Series, pages 2049–2070, San Diego, CA, 2001. Univelt.

[12] B. F. Villac and D. J. Scheeres. New Class of Optimal Plane Change Maneuvers. Journal of Guidance, Control, and Dynamics, 26(5):750–757, 2003.

[13] B. F. Villac. Dynamics in the Hill Problem with Applications to Spacecraft Maneuvers. PhD thesis, University of Michigan, 2003.

[14] B. F Villac and D. J. Scheeres. Third-Body-Driven vs. One-Impulse Plane Changes. The Journal of the Astronautical Sciences, 57(3):545–559, 2009.

[15] B. F. Villac and D. J. Scheeres. Escaping Trajectories in the Hill Three-Body Problem and Applications. Journal of Guidance, Control, and Dynamics, 26:224–232, 2003.

[16] M. E. Paskowitz and D. J. Scheeres. Robust Capture and Transfer Trajectories for Planetary Satellite Orbiters. Journal of Guidance, Control, and Dynamics, 29:342–353, 2006.

[17] Geryon Space Technologies. Multi-Body Dynamics Method of Generating Fuel Efficient Transfer Orbits for Spacecraft. US Patent 20120248253, filed March 22, 2012 and issued October 04, 2012.

[18] E. Herrera-Sucarrat. Study of LEO to GEO transfers via the L1 Sun-Earth or Earth-Moon libration points, Master's thesis, Universitat Politècnica de Catalunya, 2008.

[19] K. E. Davis, R. L. Anderson, and G. H. Born. Preliminary Study of Geosynchronous Orbit Transfers from LEO using Invariant Manifolds. Journal of the Astronautical Sciences, 58:295–310, 2011.

[20] B. F. Villac and D. J. Scheeres. On the concept of periapsis in Hill's problem. Celestial Mechanics and Dynamical Astronomy, 90:165–178, 2004.

[21] R. Furfaro, J. Simo, B. Gaudet, and D. Wibben. Neural-based trajectory shaping approach for terminal planetary pinpoint guidance, volume 150 of Advances in the Astronautical Sciences, pages 2557–2574. Univelt, San Diego, CA, 8 2013.

[22] R. Furfaro and R. Linares. Waypoint-Based Generalized ZEM/ZEV Feedback Guidance for Planetary Landing via a Reinforcement Learning Approach. In 3rd IAA Conference on Dynamics and Control of Space Systems, Moscow, Russia, May 30 - June 01, 2017.

[23] A. Mereta, D. Izzo, and A. Wittig. Machine Learning of Optimal Low-Thrust Transfers Between Near-Earth Objects. In International Conference on Hybrid Artificial Intelligence Systems, pages 543–553. Springer, 2017.

[24] A. Das-Stuart, K. C. Howell, and D. Folta. A Rapid Trajectory Design Strategy for Complex Environments Leveraging Attainable Regions and Low-Thrust Capabilities. In 68th International Astronautical Congress -IAC17C1.7.3, Adelaide, Australia, September 25 - 29, 2017.

[25] N. Parrish and D. J. Scheeres. Optimal Low-Thrust Trajectory Correction with Neural Networks. In AIAA/AAS Astrodynamics Specialist Conference, AAS18-397, Snowbird, UT, August 19-23, 2018.

[26] D. Guého, P. Singla, and R. G. Melton. Learning Capabilities of Neural Networks and Keplerian Dynamics. In AIAA/AAS Astrodynamics Specialist Conference, AAS18-427, Snowbird, UT, August 19-23, 2018.

[27] V. Shah and R. Beeson. Rapid approximation of invariant manifolds using machine learning. In AIAA/AAS Astrodynamics Specialist Conference, AAS17-784, Stevenson, WA, August 20-24, 2017.

[28] N. Hyeraci and F. Topputo. Method to Design Ballistic Capture in the Elliptic Restricted Three-Body Problem. Journal of Guidance, Control, and Dynamics, 33:1814–1823, 2010.

[29] G. Gómez, W. S. Koon, M. W. Lo, J. E. Marsden, J. Masdemont, and S. D. Ross. Connecting orbits and invariant manifolds in the spatial restricted three-body problem. Nonlinearity, 17(5):1571–1606, 2004.

[30] K. Yagasaki. Sun-perturbed earth-to-moon transfers with low energy and moderate flight time. Celestial Mechanics and Dynamical Astronomy, 90:197–212, 2004.

[31] K. C. Howell and M. Kakoi. Transfers between the Earth-Moon and Sun-Earth systems using manifolds and transit orbits. Acta Astronautica, 59:367–386, 2006.

[32] K. A. Bokelmann and R. P. Russel. Halo orbit to science orbit captures at planetary moons. Acta Astronautica, 134:141 – 151, 2017.

[33] N. Bosanac, A. D. Cox, K. C. Howell, and D. C. Folta. Trajectory design for a cislunar cubesat leveraging dynamical systems techniques: The lunar icecube mission. Acta Astronautica, 144:283 – 296, 2018.

[34] GPS GOV Official U.S. Government information about the Global Positioning System. Space Segment - last accessed September 11, 2018 - `https://www.gps.gov/systems/gps/space/`.

[35] Á Mozo-García, E. Herráiz-Monseco, A. B. Martín-Peiró, and M. M. Romay-Merino. Galileo constellation design. GPS Solutions, 4(4):9–15, 2001.

[36] Ariane Space. Launch Kit - VA240 - Galileo FOC-M7 SAT 19-20-21-22 - last accessed September 11, 2018 - `http://www.arianespace.com/wp-content/uploads/2017/12/VA240-launchkit-EN2.pdf`.

[37] J. Benkhoff, J. van Casteren, H. Hayakawa, M. Fujimoto, H. Laakso, and M Novara. BepiColombo Comprehensive exploration of Mercury: Mission overview and science goals. Planetary and Space Science, 58(1):2 – 20, 2010.

[38] R. J. Lillis, S. M. Curry, D. E. Larson, C. T. Russell, D. A. Brain, D. W. Curtis, J. S. Parker, N. Parrish, and J. Puig-Suari. Mars Ion and Sputtering Escape Network (MISEN). In 49th Lunar and Planetary Science Conference - Contrib. No. 2083, Woodlands, TX March 19-23, 2018.

[39] J. S. Parker, N. Parrish, R. J. Lillis, S. M. Curry, D. W. Curtis, J. Luhmann, J. Puig-Suari, C. T. Russell, and D. A. Brain. Mars Ion and Sputtering Escape Network (MISEN) Mission Concept . In AIAA/AAS Astrodynamics Specialist Conference, AAS18-423, Snowbird, UT, August 19-23, 2018.

[40] S. Frey, V. Angelopoulos, M. Bester, J. Bonnell, T. Phan, and D. Rummel. Orbit design for the themis mission. Space Science Reviews, 41:61–89, 2008.

[41] N. Chow, E. Gralla, and N. J. Kasdin. Low Earth orbit constellation design using the Earth-Moon L1 point. In AIAA/AAS Space Flight Mechanics Meeting AAS04-248, Maui, HW, February 8-12, 2004.

[42] R. F. Hoelker and R. Silber. The bi-elliptical transfer between co-planar circular orbits. Journal of Planetary and Space Science, 7(164-175):164–175, 1961.

[43] K. F. Wakker. Fundamentals of Astrodynamics. TU Delft Library, 2015.

[44] A. E. Petropoulos. Low-Thrust Orbit Transfers Using Candidate Lyapunov Functions with a Mechanism for Coasting. In AIAA/AAS Astrodynamics Specialist Conference and Exhibit, Providence, RI, August 16-19, 2004.

[45] S. R. Messenger, F. Wong, B. Hoang, C. D. Cress, R. J. Walters, C. A. Kluever, and G. Jones. Low-thrust geostationary transfer orbit (LT2GEO) radiation environment and associated solar array degradation modeling and ground testing. IEEE Transactions on Nuclear Science, 61(6):3348–3355, 2014.

[46] C. A. Ocampo. Trajectory analysis for the lunar flyby rescue of AsiaSat-3/HGS-1. Annals of the New York Academy of Sciences, 1065:232–253, 2005.

[47] L. Euler. De Motu Corporis Ad Duo Centra Virium Fixa Attracti. Novi commentarii Academiae Scientiarum Imperialis Petropolitanae, 10:207–242, 1764.

[48] J. L. Lagrange. Mécanique analytique. Chez la Veuve Desaint, 1788.

[49] C. G. J. Jacobi. Vorlesungen über dynamik. G. Reimer, 1847.

[50] H. J. Poincaré. Les méthodes nouvelles de la mécanique céleste, volume 1,2, 3. Gauthier-Villars, Paris, 1892, 1893, 1899.

[51] G. W. Hill. Researches in the lunar theory. American Journal of Mathematics, 1(1):5–26, 1878.

[52] V. Szebehely. Theory of orbit: The restricted problem of three Bodies. Academic Press, New York, 1967.

[53] C. G. J. Jacobi. Sur le mouvement d'un point et sur un cas particulier du problème des trois corps. Compt. Rend, 3:59–61, 1836.

[54] A. Miele. Theorem of Image Trajectories in the Earth-Moon Space. Astronautica Acta, 6(51):225–232, 1960.

[55] D. J. Scheeres and F. Marzari. Spacecraft dynamics in the vicinity of a comet. Journal of the Astronautical Sciences, 50(1):35–52, 2002.

[56] H. Schaub and J. L. Junkins. Analytical Mechanics of Space Systems. AIAA Education Series, Reston, VA, 3rd edition, 2014.

[57] B. F. Villac and D. J. Scheeres. Escaping Trajectories in the Hill Three-Body Problem and Applications. Journal of Guidance Control Dynamics, 26:224–232, March 2003.

[58] A. F. Haapala and K. C. Howell. Trajectory Design Using Periapse Poincaré Maps and Invariant Manifolds. In AIAA/AAS Astrodynamics Specialist Conference 2011, AAS 11-131, volume 140 of Advances in the Astronautical Sciences Series, San Diego, CA, 2011. Univelt.

[59] D. J. Grebow. Generating Periodic Orbits in the Circular Restricted Three-Body Problem with Applications to Lunar South Pole Coverage. PhD thesis, Purdue University, 2006.

[60] D. C. Davis, C. Patterson, and K. C. Howell. Solar Gravity Perturbations to Facilitate Long-Term Orbits: Application to Cassini. In AIAA/AAS Astrodynamics Specialist Conference 2007, AAS 07-275, volume 129 of Advances in the Astronautical Sciences Series, pages 383–404, San Diego, CA, 2007. Univelt.

[61] A. L. Samuel. Some studies in machine learning using the game of checkers. IBM Journal of Research and Development, 3(3):210–229, 1959.

[62] S. Landset, T. M. Khoshgoftaar, A. N. Richter, and T. Hasanin. A survey of open source tools for machine learning with big data in the hadoop ecosystem. Journal of Big Data, 2(1):24, 2015.

[63] C. Cortes and V. Vapnik. Support-vector networks. Machine Learning, 20(3):273–297, Sep 1995.

[64] T. M. Mitchell. Machine Learning. McGraw-Hill, 1997.

[65] N. S. Altman. An introduction to kernel and nearest-neighbor nonparametric regression. The American Statistician, 46(3):175–185, 1992.

[66] W. S. McCulloch and W. Pitts. A logical calculus of the ideas immanent in nervous activity. The bulletin of mathematical biophysics, 5(4):115–133, Dec 1943.

[67] F. Rosenblatt. The perceptron: a probabilistic model for information storage and organization in the brain. Psychological review, 65(6):386, 1958.

[68] M. A. Arbib, editor. The handbook of brain theory and neural networks. MIT press, 2 edition, 2003.

[69] T. K. Ho. The random subspace method for constructing decision forests. IEEE Transactions on Pattern Analysis and Machine Intelligence, 20(8):832–844, 1998.

[70] Y. LeCun, L. Bottou, G. B. Orr, and K. R. Müller. Efficient BackProp, pages 9–50. Springer Berlin Heidelberg, 1998.

[71] M. R. Veronez, S. F. de Souza, M. T. Matsuoka, A. Reinhardt, and R. M. da Silva. Regional Mapping of the Geoid Using GNSS (GPS) Measurements and an Artificial Neural Network. Remote Sensing, 3:668–683, 2011.

[72] R. Hecht-Nielsen. Theory of the Backpropagation Neural Network. In International Joint Conference on Neural Networks, pages 593–608, 1989.

[73] M. Nielsen. Neural Networks and Deep Learning. Determination press, 2015.

[74] H. B. Keller. Numerical Solution of Bifurcation and Nonlinear Eigenvalue Problems. In P. H. Rabinowitz, editor, Applications of Bifurcation Theory. Proceedings of an Advanced Seminar Conducted by the Mathematics Research Center at the University of Wisconsin at Madison, pages 359–384, New York, 1977. Academic Press.

[75] T. F. Chan. Newton-Like Pseudo-Arclength Methods for Computing Simple Turning Points. SIAM Journal on Scientific and Statistical Computing, 5(1):135–148, 1984.

[76] J. Kawaguchi, H. Yamakawa, T. Uesugi, and H. Matsuo. On making use of lunar and solar gravity assists in lunar-a, planet-b missions. Acta Astronautica, 35(9):633 – 642, 1995.

[77] G. Tancredi, A. Sánchez, and F. Roig. A Comparison Between Methods to Compute Lyapunov Exponents. The Astronomical Journal, 121:1171–1179, 2001.

[78] C. Froeschlé. The Lyapunov Characteristic Exponents - Applications to Celestial Mechanics. Celestial Mechanics, 34:95–115, 1984.

[79] C. Froeschlé, E. Lega, and R. Gonczi. Fast Lyapunov Indicators. Application to Asteroidal Motion. Celestial Mechanics and Dynamical Astronomy, 67:41–62, 1997.

[80] ULA. Delta IV Launch Services User's Guide, version June 2013 - last accessed August 28, 2018 - `https://www.ulalaunch.com/docs/default-source/rockets/delta-iv-user's-guide.pdf`.

[81] ULA. Atlas V- last accessed August 28, 2018 - `https://www.ulalaunch.com/rockets/atlas-v`.

[82] Space X. Falcon 9 - last accessed August 28, 2018 - `https://www.spacex.com/falcon9`.

[83] E. Berger. ARS Technica - Blue Origin releases details of its monster orbital rocket - last accessed August 28, 2018 - `https://arstechnica.com/science/2017/03/blue-origin-releases-details-of-its-monster-orbital-rocket/`.

[84] Space X. Falcon Heavy - last accessed August 28, 2018 - `https://www.spacex.com/falcon-heavy`.

[85] E. Kyle. NASA's Space Launch System - last accessed August 28, 2018 - `http://www.spacelaunchreport.com/sls0.html`.

[86] C. T. Russell and C. A. Raymond. The Dawn Mission to Vesta and Ceres. Space Science Reviews, 163(1):3–23, Dec 2011.

[87] A. Fujiwara, J. Kawaguchi, D. K. Yeomans, M. Abe, T. Mukai, and T. Okada. The Rubble-Pile Asteroid Itokawa as Observed by Hayabusa. Science, 312(5778):1330–1334, 2006.

[88] Y. Tsuda, M. Yoshikawa, M. Abe, H. Minamino, and S. Nakazawa. System design of the Hayabusa 2 - Asteroid sample return mission to 1999 JU3. Acta Astronautica, 91:356 – 362, 2013.

[89] A. Singh, N. Thakur, and A. Sharma. A review of supervised machine learning algorithms. In 2016 3rd International Conference on Computing for Sustainable Global Development, pages 1310–1315, 2016.

[90] A. Chariatis. Very fast online learning of highly non linear problems. Journal of Machine Learning Research, 8:2017–2045, December 2007.

[91] M. Schuster and K. K. Paliwal. Bidirectional recurrent neural networks. IEEE Transactions on Signal Processing, 45(11):2673–2681, 1997.

[92] T. L. Fine. Feedforward neural network methodology. Springer, 1999.

[93] N. Murata, S. Yoshizawa, and S. Amari. Network information criterion-determining the number of hidden units for an artificial neural network model. IEEE Transactions on Neural Networks, 5(6):865–872, 1994.

[94] M. J. H. Walker, J. Owens, and B. Ireland. A set of modified equinoctial orbit elements. Celestial Mechanics, 36:409–419, August 1985.

[95] K. Hornik, M. Stinchcombe, and H. White. Multilayer Feedforward Networks are Universal Approximators. Neural Networks, 2:359–366, 1989.

[96] H. R. Maier and G. C. Dandy. The effect of internal parameters and geometry on the performance of back-propagation neural networks: an empirical study. Environmental Modelling And Software, 13:193–209, 1998.

[97] K. Levenberg. A Method for the Solution of Certain Non-Linear Problems in Least Squares. Quarterly of Applied Mathematics, 2(2):164–168, 1944.

[98] D. W. Marquardt. An Algorithm for Least-Squares Estimation of Nonlinear Parameters. Journal of the Society for Industrial and Applied Mathematics, 11(2):431–441, 1963.

[99] B. M. Wilamowski and J. D. Irwin, editors. Intelligent Systems. CRC press, 2 edition, 2015.

[100] R. Caruana. Multitask Learning. PhD thesis, Carnegie Mellon University, 1997.

[101] MATLAB Statistics and Machine Learning Toolbox 11.2. The MathWorks Inc., Natick, MA, USA, 2017b.

[102] E. B. Baum and D. Haussler. What size net gives valid generalization? Neural Computation, 1(1):151–160, 1989.

[103] L. L. Rogers and F. U. Dowla. Optimization of groundwater remediation using artificial neural networks with parallel solute transport modeling. Water Resources Research, 30(2):457–481, 1994.

[104] GMAT. GMAT, General Mission Analysis Tool, Software Package, Version R2017a, NASA Goddard Space Flight Center, Greenbelt, MD. 2017.

[105] J. S. Bridle. Probabilistic Interpretation of Feedforward Classification Network Outputs, with Relationships to Statistical Pattern Recognition. In Françoise Fogelman Soulié and Jeanny Hérault, editors, Neurocomputing, pages 227–236, Berlin, Heidelberg, , 1990. Springer Berlin Heidelberg.

[106] P. Golik, P. Doetsch, and H. Ney. Cross-entropy vs. squared error training: a theoretical and experimental comparison. In Interspeech, pages 1756–1760. ISCA, 2013.

[107] F. Topputo and R. Y. Zhang. Approximation of Invariant Manifolds by Cubic Convolution Interpolation. In 25th AAS/AIAA Space Flight Mechanics Meeting, AAS15-322, Williamsburg, VA, Jan 12-15, 2015.

[108] R. Beeson, D. Bunce, and V. Coverstone. Approximation Methods for Quick Evaluation of Invariant Manifolds During Global Optimization. In AIAA/AAS Astrodynamics Specialist Conference, Long Beach, CA, Sep 13-16, 2016.

[109] W. S. Koon, M. W. Lo, J. E. Marsden, and S. D. Ross. Heteroclinic connections between periodic orbits and resonance transitions in celestial mechanics. Chaos: An Interdisciplinary Journal of Nonlinear Science, 10(2):427–469, 2000.

[110] A. Haapala. Trajectory Design in the Spatial Circular Restricted Three-Body Problem Exploiting Higher-Dimensional Poincaré Maps. PhD thesis, Purdue University, 2014.

Appendix A

Publication list

Journal articles:

(1) N. Parrish, D. Scheeres, S. Tardivel, C. Venigalla, J. Aziz, M. Pellegrino, O. Fuentes, **S. De Smet**, "GTOC 9: Results from the University of Colorado at Boulder (team CU Boulder)," Acta Futura, (11), 9197. 10.5281/zenodo.1139268

(2) **S. De Smet**, D. Scheeres, J. Parker, "Dynamics and Stability of Sun-Driven Transfers from Low Earth to Geosynchronous Orbit", Journal of Guidance, Control, and Dynamics, Vol. 41, No. 9 (2018), pp. 2002-2010, DOI:10.2514/1.G003331

(3) **S. De Smet**, D. Scheeres, J. Parker, "Leveraging Artificial Neural Networks to Systematically Explore Solar Gravity Driven Transfers in the Martian System", Journal of Astronautical Sciences, in review

(4) **S. De Smet**, D. Scheeres, J. Parker, "Representing dynamics in the eccentric Hill system using a neural network architecture", Journal of Astrodynamics, in review

(5) C. Venigalla, N. Baresi, J. Aziz, B. Bercovici, D. Brack, A. Dahir, **S. De Smet**, J. Fulton, M. Pellegrino, S. Van wal, "The Near-Earth Asteroid Characterization and Observation (NEACO) Mission to Asteroid (469219) 2016 HO3", JSR, in review

(6) **S. De Smet**, D. Scheeres, J. Parker, "On the design of multiple-revolution solar gravity driven orbital transfers around Mars", in preparation

Conference papers:

(1) **S. De Smet**, J. Parker, J. Herman, and R. Noomen, "Mission Design for a Crewed Earth-Venus-Mars Flyby Mission using Solar Electric Propulsion," 32nd AAS Guidance and Control Conference - Paper AAS 15-091, Breckenridge, CO, January 30 - February 4, 2015.

(2) **S. De Smet**, J. Parker, J. Herman, J. Aziz, B. Barbee, J. Englander, "Identifying Accessible Near-Earth Objects For Crewed Missions With Solar Electric Propulsion," AAS/AIAA Astrodynamics Specialist Conference, Paper AAS 15-598, Vail, CO, August 9-13, 2015.

(3) C. Deccia, J. Parker, **S. De Smet**, J. Herman and R. Noomen, "Preliminary Design of a Multi-Spacecraft Mission to Investigate Solar System Evolution Using Solar Electric Propulsion," AAS/AIAA Astrodynamics Specialist Conference, Paper AAS 15-765, Vail, CO, August 9-13, 2015

(4) J. Aziz, S. Napier, **S. De Smet**, J. Parker, "Trajectory design of the time capsule to Mars student mission," AAS/AIAA Astrodynamics Specialist Conference, Paper AAS 15-658, Vail, CO, August 9-13, 2015.

(5) L. Corpaccioli, R. Noomen, **S. De Smet**, J. Parker, J. Herman, "Preliminary trajectory design for a solar polar observatory using sep and multiple gravity assists," 25th International Symposium on Space Flight Dynamics, Munich, Germany, October 19 23, 2015

(6) **S. De Smet**, J. Parker, N. Parrish, "Designing an asteroid deflection mission using continuous thrust and uncertainty," 26th AAS/AIAA Space Flight Mechanics meeting - Paper AAS 16-435, Napa, CA, February 14-18, 2016.

(7) J.Parker, J. Aziz, D. Case, L. Corpaccioli, C. Deccia, R. Handzo, J. Herman, N. Parrish, **S. De Smet**,"GTOC8: Results and methods of the University of Colorado Boulder," 26th AAS/AIAA Space Flight Mechanics meeting - Paper AAS 16-377, Napa, CA, February 14-18, 2016.

(8) **S. De Smet**, J. Parker, D. Scheeres, "Harnessing the Sun's Gravity for LEO to GEO transfers," 26th International Symposium on Space Flight Dynamics - Paper ISSFD-2017-055, Matsuyama, Japan, June 3-9, 2017

(9) **S. De Smet**, J. Parker, D. Scheeres, "Dynamics and stability of Sun-driven transfers from LEO to GEO," AAS Astrodynamics Specialist Conference, Paper AAS 17-593, Stevenson, WA, August 20-24, 2017

(10) C. Venigalla, N. Baresi, J. Aziz, B. Bercovici, G. Motta, D. Brack, J. Cardosa dos Santos, A. Dahir, A. Davis, **S. De Smet**, J. Fulton, N. Parrish, M. Pellegrino, S. Van wal, "The Near-Earth Asteroid Characterization and Observation (NEACO) mission," AAS Astrodynamics Specialist Conference, Paper AAS 17-744, Stevenson, WA, August 20-24, 2017

(11) **S. De Smet**, D. Scheeres, J. Parker, "Systematic Exploration of Solar Gravity Driven Orbital Transfers in the Martian system using Artificial Neural Networks," AAS Astrodynamics Specialist Conference, Paper AAS 18-216, Snowbird, UT, August 20-23, 2018

(12) **S. De Smet**, D. Scheeres, "Identifying heteroclinic connections using artificial neural networks," 69th International Astronautical Congress, Paper IAC-18-C1-1-8x42401, Bremen, Germany, October 1-5, 2018

(13) **S. De Smet**, D. Scheeres, J. Parker, "On the design of multiple-revolution solar gravity driven orbital transfers around Mars," 29th AAS.AIAA Space Flight Mechanics Meeting, Paper AAS 19-234, Maui, HI, January 13-17, 2019, in preparation

Appendix B

Algorithms

Algorithm 1 Find transfers targeting a final orbit in the circular Hill problem

for $i_{\text{Hill},1}$ **do**
  for e_1 **do**
    create grid in $\omega_{\text{Hill},1}$ and $\Omega_{\text{Hill},1} \rightarrow G$
    PoincareMapping ($r_{p,1}$,e_1,$i_{\text{Hill},1}$, G)
      return Hill orbital elements periareion 2
    SplineInterpolation(G, Hill orbital elements periareion 2)
      return ($\omega_{\text{Hill},1}$, $\Omega_{\text{Hill},1}$) arriving at correct $r_{p,2}$ and $i_{\text{Hill},2} = \epsilon$
    PoincareMapping($r_{p,1}$,e_1,$i_{\text{Hill},1}$,$\omega_{\text{Hill},1}$, $\Omega_{\text{Hill},1}$)
      return $\omega_{\text{Hill},1}$ and $\Omega_{\text{Hill},1}$ confirmed within 1° and 500 km of correct $r_{p,2}$ and $i_{\text{Hill},2}$
    ComputeTiming($\Omega_{\text{Hill},2}$,TOF)
      return initial and final time such that $i_{\text{Hill},2} = \varepsilon$ is mapped to the equator
    RotateStates (initial and final conditions and time)
      return initial and final conditions in MME frame
  end for
end for

Algorithm 2 Find transfers targeting a final orbit in the apoareion scaled circular Hill problem

create grid in $\omega_{\text{Hill},1}$ and $\Omega_{\text{Hill},1} \rightarrow G$
for $\nu_{M,a}$ **do**
    for $r_{a,1}$ **do**
        scaleStates ($r_{p,1}$,$r_{a,1}$,$\nu_{M,a}$)
            return scaled $r_{p,1}$ and $r_{a,1}$
        for $i_{\text{Hill},1}$ **do**
            PoincareMapping ($r_{p,1}$,e_1,$i_{\text{Hill},1}$, G)
                return Hill orbital elements periareion 2, scaled back to true values
            SplineInterpolation(G, Hill orbital elements periareion 2)
                return ($\omega_{\text{Hill},1}$, $\Omega_{\text{Hill},1}$) arriving at correct $r_{p,2}$ and $i_{\text{Hill},2} = \epsilon$
            PoincareMapping($r_{p,1}$,e_1,$i_{\text{Hill},1}$,$\omega_{\text{Hill},1}$, $\Omega_{\text{Hill},1}$)
                return $\omega_{\text{Hill},1}$ and $\Omega_{\text{Hill},1}$ confirmed within 1° and 500 km of correct $r_{p,2}$ and $i_{\text{Hill},2}$
            ComputeTiming($\Omega_{\text{Hill},2}$,TOF)
                return initial and final time such that $i_{\text{Hill},2} = \varepsilon$ is mapped to the equator
            RotateStates (initial and final conditions and time)
                return initial and final conditions in MME frame
        end for
    end for
end for

Algorithm 3 Find initial conditions for N-loop transfers targeting an equatorial final orbit in the eccentric Hill problem, using a backwards method.

$i_{\text{Hill},f} = \epsilon$, $r_{p,f}$ fixed to target orbit, fixed t_f
compute $\Omega_{\text{Hill},f}$: ($i_{\text{Hill},f}$, t_f) $\rightarrow i_{\text{MME},f} = 0$
initialize grid in arrival states ($r_{a,f}$, $\omega_{\text{Hill},f}$) $\rightarrow G_f$
initialize sampling grid on plane of interest: grid in ($r_{p,1}$,$i_{\text{MME},1}$) $\rightarrow G_1$
while $\exists$ undersampled regions **do**
    for loops = 1 to N **do**
        EccentricHillPoincareMapping(G_f, t_f)
            return previous periareion state and time using algorithm in Fig. 5.16
    end for
    determine the undersampled regions in grid G_1
    compute a new set of arrivalStates, G_f, in undersampled regions of G_1
    refine grid G_1
end while

Algorithm 4 Find transfers targeting an equatorial final orbit in the eccentric Hill problem after $N_1 + N_2$ loops, with an intermediate flyby after N_1 loops

$i_{\text{Hill},f} = \epsilon$, $r_{p,f}$ fixed to target orbit, fixed t_f
initialize grid in arrival states $(r_{a,f}, \omega_{\text{Hill},f}, t_f) \rightarrow G_f$
for $t_f \in G_f$ **do**
    compute $\Omega_{\text{Hill},f}$: $(i_{\text{Hill},f}, t_f) \rightarrow i_{\text{MME},f} = 0$,
end for
initialize sampling grid on plane of interest: grid in $(r_{p,1}, i_{\text{MME},1}) \rightarrow G_1$
while $\exists$ undersampled regions **do**
    InitialState(G_f,N_1,N_2)
        return initial and arrival conditions $\in G_f$ in MME frame with close intermediate flyby
    determine the undersampled regions in grid G_1
    compute a new set of arrivalStates, G_f, in undersampled regions of G_1
    refine grid G_1
end while

procedure: InitialState(G_f,N_1,N_2)
    for loopCounter= 1 to N_2 **do**
        EccentricHillPoincareMapping(periapse state, timing)
            return previous periareion state and time using algorithm in Fig. 5.16
    end for
    for transfers $\in G_f$ **do**
        if $|i_{\text{MME},f-N_2} - i_{\text{flyby}}| < 2^\circ$ and $|r_{p,f-N_2} - r_{p,\text{flyby}}| < 500$km **then**
            for loopCounter= 1 to N_1 **do**
                EccentricHillPoincareMapping(periapse state, timing)
                    return previous periareion state and time using algorithm in Fig. 5.16
            end for
        else
            discard
        end if
    end for
return initial and arrival conditions $\in G_f$ in MME frame with close intermediate flyby

Algorithm 5 Find initial condition of a single transfer arriving at equatorial final orbit in the eccentric Hill problem for N loops with maneuver after loop M

$i_{\text{Hill},f} = \epsilon$, $r_{p,f}$ fixed to target orbit, fixed t_f
compute $\Omega_{\text{Hill},f}$: $(i_{\text{Hill},f}, t_f) \rightarrow i_{\text{MME},f} = 0$
initialize grid in $r_{a,f}$,$\omega_{\text{Hill},f} \rightarrow G_f$
initialize grid in $r_{a,\text{preManeuver}} \rightarrow H_f$
initialize sampling grid on plane of interest: grid in $(r_{p,1}$,$i_{\text{MME},1}) \rightarrow G_1$
while $\exists$ undersampled regions **do**
    InitialState(G_f,H_f,N,M)
        return initial and arrival conditions $\in G_f$ in MME frame with intermediate maneuver
    determine the undersampled regions in grid G_1
    compute new, finer sets G_f and H_f in undersampled regions of G_1
    refine grid G_1
end while

procedure: InitialState(G_f,H_f,N,M)
    for loopCounter= 1 to $N - M$ **do**
        EccentricHillPoincareMapping(periapse state, timing)
            return previous periareion state and time using algorithm in Fig. 5.16
    end for
    for transfers $\in G_f$ **do**
        for $r_{a,\text{preManeuver}} \in H_f$ **do**
            update $r_{a,f-M}$ with $r_{a,\text{preManeuver}}$
            for loopCounter= 1 to M **do**
                EccentricHillPoincareMapping(periapse state, timing)
                    return previous periareion state and time using algorithm in Fig. 5.16
            end for
        end for
    end for
return initial and arrival conditions in MME frame for transfers $\in G_f$ and maneuvers $\in M_f$

Algorithm 6 Find transfers targeting an equatorial final orbit in the eccentric Hill problem after $N_1 + N_2$ loops, with an intermediate flyby after N_1 loops and a maneuver after $M > N_1$ loops

$i_{\text{Hill},f} = \epsilon$, $r_{p,f}$ fixed to target orbit, fixed t_f
initialize grid in arrival states $(r_{a,f}, \omega_{\text{Hill},f}, t_f) \rightarrow G_f$
for $t_f \in G_f$ **do**
    compute $\Omega_{\text{Hill},f}$: $(i_{\text{Hill},f}, t_f) \rightarrow i_{\text{MME},f} = 0$,
end for
initialize grid in $r_{a,\text{preManeuver}} \rightarrow H_f$
initialize sampling grid on plane of interest: grid in $(r_{p,1}, i_{\text{MME},1}) \rightarrow G_1$
while $\exists$ undersampled regions **do**
    InitialState(G_f,H_f,N_1,N_2,M)
        return initial and arrival MME $\in G_f$, and maneuvers $\in M_f$ with intermediate flyby
    determine the undersampled regions in grid G_1
    compute new, finer sets G_f and H_f in undersampled regions of G_1
    refine grid G_1
end while

procedure: InitialState(G_f,H_f,N_1,N_2,M)
    for loopCounter= 1 to $N_1 + N_2 - M$ **do**
        EccentricHillPoincareMapping(periapse state, timing)
            return previous periareion state and time using algorithm in Fig. 5.16
    end for
    for transfers $\in G_f$ **do**
        for $r_{a,\text{preManeuver}} \in H_f$ **do**
            update $r_{a,f-M}$ with $r_{a,\text{preManeuver}}$
            for loopCounter= 1 to $N_2 - M$ **do**
                EccentricHillPoincareMapping(periapse state, timing)
                    return previous periareion state and time using algorithm in Fig. 5.16
            end for
            if $|i_{\text{MME},f-N_2} - i_{\text{flyby}}| < 2^\circ$ and $|r_{p,f-N_2} - r_{p,\text{flyby}}| < 500\text{km}$ **then**
                for loopCounter= 1 to N_1 **do**
                    EccentricHillPoincareMapping(periapse state, timing)
                        return previous periareion state and time using algorithm in Fig. 5.16
                end for
            else
                discard
            end if
        end for
    end for
return initial and arrival conditions $\in G_f$ and maneuvers $\in M_f$ with close intermediate flyby

Appendix C

Acronyms

ANN	Artificial Neural Network
CE	Cross Entropy
CRTBP	Circular Restricted Three-Body Problem
EME	Earth Mean Equator and equinox of J_{2000}
EMO	Earth Mean Orbit of J_{2000}
EOM	Equations Of Motion
GEO	GEostationary Orbit
GMAT	General Mission Analysis Tool
LCE	Lyapunov Characteristic Exponent
LCT	Lyapunov Characteristic Time
LEO	Low-Earth Orbit
LPO	Lagrangian Point Orbit
MME	Mars Mean Equator and equinox of J_{2000}
MMO	Mars Mean Orbit of J_{2000}
MSE	Mean Squared Error
RSS	Root Sum Squared
SEP	Solar Electric Propulsion
SLS	Space Launch System
SOI	Sphere Of Influence
TMI	Trans Mars Injection
TOF	Time Of Flight

Appendix D

Nomenclature

Roman

a	semi-major axis	[km]
b	artificial neuron bias	[-]
d	instantaneous Mars-Sun distance	[km]
e	eccentricity	[-]
G	gravitational constant	[$km^3 \cdot kg^{-1} \cdot s^{-2}$]
h	specific relative angular momentum	[$km^2 \cdot s^{-1}$]
i	inclination	[deg]
J	Jacobi constant	[-]
l	length scale	[km]
M_i	mass of body i	[kg]
$[M_n(\alpha)]$	rotation matrix around the n^{th} body axis by angle α	[-]
N	mean motion	[s^{-1}]
N	total number of revolutions around Mars	[-]
N_1	total number of revolutions around Mars before the flyby	[-]
N_2	total number of revolutions around Mars after the flyby	[-]
$\hat{\mathbf{n}}$	normal vector	[-]
P	orbital period	[s]
p	semi-latus rectum	[km]

$\mathbf{r}$	non-dimensional position vector	[-]
$\mathbf{R}$	dimensional position vector	[km]
r_a	apoapse radius	[km]
r_p	periapse radius	[km]
$\hat{\mathbf{t}}$	tangent vector	[-]
t_0	reference time for conversion between MMO and Hill frame	[s]
TOF	time of flight	[days]
TOF_{apo}	time of flight between periareion and apoareion	[days]
u	argument of latitude	[deg]
$\mathbf{V}$	dimensional velocity vector	[km$\cdot$ s^{-1}]
w	artificial neuron weight	[-]
W	total number of weights and biases in ANN	[-]

Greek

α	mass scaling parameter	[-]
α	apoapse location angle	[deg]
β	rate of change of the true anomaly	[s^{-1}]
γ	ratio between arrival and departure orbital radii for co-planar transfers	[-]
ε	small perturbation	[-]
ε	obliquity of the ecliptic	[deg]
ζ	ratio between intermediate and departure orbital radii for bi-elliptic transfers	[-]
η	three-body parameter	[-]
Θ	instantaneous angle between MO and Hill frame	[deg]
λ	true longitude	[deg]
μ	standard gravitational parameter	[km$^3\cdot$ s^{-2}]
ν	true anomaly	[deg]

σ	standard deviation	[-]
τ	angle-like parameter describing position on an LPO	[deg]
τ	time scale	[s]
ϕ	activation function	[-]
Φ	state transition matrix	[-]
ψ	mass scale	[-]
χ	Lyapunov characteristic exponent	[-]
$\boldsymbol{\omega}$	rotation vector	[s^{-1}]
ω	argument of periapse	[deg]
Ω	right ascension of ascending node	[deg]

Miscellaneous

$\Delta\square$	change
$\mathcal{O}\square$	order of magnitude
$\square_1$	state at the first periareion after injection maneuver one
$\square_2$	state at the second periareion before injection maneuver two
$\square_a$	state at the apoareion between periareion one and two
$\square_f$	state at the final periareion
$\hat{\square}$	unit vector
$\dot{\square}$	derivative with respect time
$\ddot{\square}$	second derivative with respect time
$\square'$	derivative with respect to true anomaly
$\square''$	second derivative with respect to true anomaly
$\square_E$	Earth
$\square_M$	Mars
$\square_S$	Sun
$\square_s$	stable manifold
$\square_{us}$	unstable manifold

Appendix E

Physical constants

General		
AU	149,597,870.700	[km]
G	6.67E-20	[$km^3 \cdot kg^{-1} \cdot s^{-2}$]
μ_S	1.3271248287031293E+11	[$km^3 \cdot s^{-2}$]
Earth		
a	1.00	[AU]
e	0.0167	[-]
R_E	6378.136	[km]
μ_E	398600.4415	[$km^3 \cdot s^{-2}$]
ε	23.34	[deg]
epoch alignment EMO and Hill	0	[days past J2000]
Mars		
a	1.52366231	[AU]
e	0.09341233	[-]
R_M	3389.5	[km]
μ_M	42828.372	[$km^3 \cdot s^{-2}$]
ε	25.19	[deg]
epoch alignment MMO and Hill	2460322.6003472232	[JD]
epoch perihelion	2460438.94726728	[JD]

Earth-Moon CRTBP

μ	0.01215	[-]
Length scale	384,401	[km]
Time scale	377,491	[s]